Fabrication of High Aspect Ratio Atomic Force Microscope Tips Using Silicon and Diamond

by

Farheen Nasir

A thesis

presented to the University of Waterloo

in fulfillment of the

thesis requirement for the degree of

Doctor of Philosophy

in

Electrical and Computer Engineering

Waterloo, Ontario, Canada, 2025

© Farheen Nasir 2025

EXAMINATION COMMITTEE MEMBERS

Supervisor: Professor Guo-Xing Miao

Professor, Electrical and Computer Engineering,

University of Waterloo.

Co-Supervisor: Professor Bo Cui,

Professor, Electrical and Computer Engineering,

University of Waterloo.

Internal member: Professor Karim Salludin Karim,

Professor, Electrical and Computer Engineering,

University of Waterloo.

Internal member: Professor Dayan Ban,

Professor, Electrical and Computer Engineering,

University of Waterloo.

Internal-External member: Professor Yuning Li,

Professor, Chemical Engineering,

University of Waterloo.

External member: Professor Bo Tan

Professor, Aerospace Engineering,

Toronto Metropolitan University.

AUTHOR'S DECLARATION

I hereby declare that I am the sole author of this thesis. This is a true copy of the thesis, including any required final revisions, as accepted by my examiners.

I understand that my thesis may be made electronically available to the public

ABSTRACT

Atomic Force Microscope (AFM) is in a family of microscopy called Scanning Probe Microscope (SPM) which also includes Scanning Tunneling Microscope (STM). AFM has become a standard characterization tool for surface topography measurements in most microfabrication. However, in order to obtain accurate representation of high aspect ratio structures such as trenches, the AFM tip must be capable of reaching the bottom of such a trench. This requires the AFM tip to have a high aspect ratio as well as sharp apex. Additionally, for application which require contact with the surface the AFM tip must have very high wear resistance, which is typically obtained using diamond AFM tips . In this work we have designed several methods to obtain high aspect ratio diamond and silicon AFM tips with sharp apex.

Chapter 3 and 4 discuss two methods to obtain high aspect ratio diamond tip with silicon base. We have used ultra-nanocrystalline diamond grown on silicon wafer and have fabricated diamond AFM tips using Reactive Ion Etching. In the first method we use O2/CHF3 gas to etch patterned diamond with shrinking mask. Next, we use pseudo-Bosch etching to fabricate high aspect ratio silicon pillars under the diamond tip. With this method we are able to obtain aspect ratio close to 10 and tip apex of less than 25 nm. In the second method we are able to obtain even smaller apex by fabricating the silicon base first before the fabrication of diamond apex using O2/C4F8 plasma. This method allows for aspect ratio of 7.5 and apex diameter close to 10 nm.

Chapter 5 and 6 focus on the fabrication of silicon AFM tips. In chapter 5 we use (111) oriented silicon wafers, which are first dry etched to form pillars. Next, the sample is etched in alkaline solution using either TMAH or surfactant added TMAH. We have tested two non-ionic surfactants and have obtained aspect ratio close to 14 and tip apex of less than 10 nm without oxidation

sharpening when 1000 ppm Triton X-405 is added to 25 wt% TMAH. We have also studied the effect of surfactant composition and concentration on silicon etching.

In chapter 6, we have developed two method to fabricate tetrahedral AFM tips using a combination of dry and wet anisotropic etching. The first method uses SOI wafer coated with LPCVD nitride. After patterning the silicon is dry etched to form trenches which are then oxidized. Next, the LPCVD nitride is removed to exposed un-oxidized silicon that is anisotropically etched in 25 wt% TMAH to form AFM tips with one side perpendicular to the edge of the cantilever surface. In the second method we remove the need of LPCVD nitride which may not be readily available. In this method, after fabrication of trenches, the entire silicon surface is oxidized along with trench sidewalls. However, before anisotropic wet etching, the surface oxide is selectively removed using angled ion milling. Careful recipe optimization is done in order to fully remove the surface oxide while the oxide on the trench sidewalls remain unharmed. After wet anisotropic etching, this method allows for fabrication of silicon tips with apex as low as 60 nm before oxidation sharpening.

ACKNOWLEDGMENT

First, I want to express gratitude to my supervisors Prof. Bo Cui and Prof. Guo-Xing Miao for their guidance, encouragement and patience while I navigated my PhD journey.

I also want to thank my examination committee members, Prof. Dayan Ban, Prof. Karim S. Karim and Prof. Mustafa Yavuz for taking time out of their busy schedule to review this thesis and for offering valuable feedback.

I also want to acknowledge my colleagues, Dr. Aixi Pan, Zihao Wang, Dr. Chenxu Zhu, and especially, Dr. Xiaoli Zhu for your invaluable help and guidance in navigating various aspects of my PhD. I am grateful to the staff at Quantum Nano and Fabrication and Characterization Facility including Dr. Nathan Nelson-Fitzpatrick, Dr. Lino Eugene, Dr. Greg Holloway, Matthew Scott, Ken Speirs and Rodello Salandanan for providing me with the infrastructure necessary to perform my research.

I am eternally thankful to my husband, Aurangzeb, for your unwavering support and sacrifices during this journey. I'm also grateful for my dad for your prayers and support for my whole life.

Lastly, I thank the Almighty Allah, for giving me the strength and patience to carry on this work and for blessing me with great people who have been my greatest supporter in both my personal and professional life.

DEDICATION

To Aurangzeb, my partner in every joy and challenge, and to our little Jehan, whose laughter, curiosity, and light brightens the world.

TABLE OF CONTENTS

AUTHOR'S DECLARATION IV
ABSTRACT V
ACKNOWLEDGMENT VII
DEDICATION VIII
LIST OF FIGURES XIII
LIST OF TABLES XVIII
LIST OF ABBREVIATIONS XIX

CHAPTER 1: INTRODUCTION TO AFM AND DEVICE FABRICATION...1

1.1. ATOMIC FORCE MICROSCOPE 1
1.1.1. Working Principle 2
1.1.2. Forces in AFM 3
1.2. SCANNING MODES IN ATOMIC FORCE MICROSCOPY 5
1.2.1. Static Mode 5
1.2.2. Dynamic Mode 7
1.2.3. Intermittent Contact/ Tapping Mode 9
1.3. CRITICAL PARAMETERS 10
1.3.1. AFM Tip 11
1.3.1.1. Silicon AFM tips 12
1.3.1.2. Silicon Nitride AFM tips 13
1.3.1.3. Carbon Nanotube (CNT) AFM tips 13
1.3.1.4. Diamond AFM tips 14
1.3.2. AFM Cantilever 14
1.4. RECENT ADVANCES IN ATOMIC FORCE MICROSCOPY 15
1.4.1. Peak Force Tapping AFM 16
1.4.2. Conductive AFM 17
1.4.3. High Speed AFM 19
1.4.4. Scanning Spreading Resistance Microscopy 21
1.4.5. Colloidal AFM 23

1.5. OBJECTIVES OF THIS WORK 24

CHAPTER 2: STANDARD PROBE FABRICATION METHODS 26

2.1. STANDARD METHODS FOR ALL SILICON PROBE FABRICATION 26
2.1.1. All Silicon AFM Probe 26
2.1.2. Silicon Nitride Cantilever 29
2.1.3. Silicon Tetrahedral Tips 30
2.2. METHODS FOR FABRICATION OF SILICON PROBE WITH DIAMOND TIP 32
2.2.1. Pyramid Molded Diamond Tips 33
2.2.2. Plasma Etched Diamond Tips 36
2.3. METHODS FOR HIGH ASPECT RATIO TIP FABRICATION 38
2.3.1. Focused Ion Beam (FIB) Milling/Etching 39
2.3.2. Ion/Electron Beam Induced Deposition (EBID/IBID) 40
2.3.3. Carbon Nanotubes 41
2.3.4. Oxidation Sharpening 42
2.4. PROCESSES USED FOR PROBE FABRICATION 43
2.4.1. Lithography 44
2.4.1.1. Photolithography 44
2.4.1.2. Electron Beam Lithography 46
2.4.2. Liftoff 46
2.4.3. Etching 47
2.4.3.1. Reactive Ion Etching 47
2.4.3.2. Ion Milling 51
2.4.3.3. Wet Etching 53
2.4.4. Deposition 59
2.4.4.1. Physical Vapor Deposition 59
2.4.4.3. Chemical vapor deposition 60

CHAPTER 3: HIGH ASPECT RATIO DIAMOND TIP.....62

3.1. INTRODUCTION 62
3.2. EXPERIMENT 65

3.3. RESULTS AND DISCUSSION 67
3.3.1. Mask Selection 67
3.3.2. Diamond Etching Recipe Optimization 69
3.3.3. Silicon Etching 75
3.4. CONCLUSION 79

CHAPTER 4: NOVEL METHOD FOR FABRICATION OF HIGH ASPECT RATIO DIAMOND TIP 80

4.1. INTRODUCTION 80
4.2. EXPERIMENT 81
4.3. RESULTS AND DISCUSSION 83
4.3.1. Fabrication of Silicon Base 83
4.3.2. Fabrication of diamond apex 88
4.4. CONCLUSION 91

CHAPTER 5: FABRICATION OF HIGH ASPECT RATIO AFM TIPS BY SURFACTANT ADDED TMAH ETCHING 92

5.1. FABRICATION OF HIGH ASPECT RATIO AFM TIPS 92
5.1.1. Experiment 95
5.1.2. Results and Discussion 97
5.1.2.1. Etching in 25 wt% TMAH 97
5.1.2.2. Etching in 25 wt% TMAH + 1000 ppm Triton X-405 100
5.1.2.3. Etching in 25 wt% TMAH + 1000 ppm Triton X-100 102
5.1.3. Summary and Conclusions 105
5.2. ANISOTROPIC ETCHING OF (111) SILICON IN NON-IONIC SURFACTANTS .. 105
5.2.1. Experiment 108
5.2.2. Results and Discussion 110
5.2.3. Conclusion 115

CHAPTER 6: FABRICATION OF TETRAHEDRAL TIP ON SILICON 117

6.1. TETRAHEDRAL AFM TIP 117
6.2. FABRICATION OF TETRAHEDRAL TIP USING Si_3N_4 MASK 118
6.2.1. Experiment 118
6.2.2. Results and Discussion..... 120
6.3. FABRICATION OF TETRAHEDRAL TIP BY ION MILLING 126
6.3.1. Experiment 127
6.3.2. Results and Discussion..... 129
6.4. CONCLUSION 134

CHAPTER 7: CONCLUSION AND FUTURE WORK 135

REFERENCES..... 139

APPENDIX A: SUPPLEMENTARY INFORMATION – DIAMOND SHRINKING MASK 154

APPENDIX B: SUPPLEMENTARY INFORMATION – DIAMOND T-SHAPED MASK 155

APPENDIX C: SUPPLEMENTARY INFORMATION – SI TIP 157

APPENDIX D: SUPPLEMENTARY INFORMATION –TETRAHEDRAL TIP. 158

LIST OF FIGURES

Figure 1.1: STM current dependence on tip-sample distance. Reproduced with permission from Ref.……...1
Figure 1.2 Working Principal of AFM . Reprinted with permission from Ref. ……..3
Figure 1.3: Interatomic force vs. tip-sample distance in AFM. Reprinted with permission from Ref. ……..5
Figure 1.4: Effect of sharp and blunt tip on the scanning results for A),B) hills and C,D) valleys. Reproduced with permission from Ref. ……..…….11
Figure 1.5: a) Standard silicon AFM tip, b) High aspect ratio tip, c) Tetrahedral tip. Reproduced with permission from Ref. ……12
Figure 1.6: Tip Sample interaction curve in PFT-AFM. Reprinted with permission from Ref. …….....17
Figure 1.7: Apex for, a) diamond coated silicon, b) Pt-coated silicon and c) Pt-Si tips. Reproduced with permission from Ref. ……..……..19
Figure 1.8: Comparison of standard AFM cantilever and those used for HS-AFM (circled). Reprinted with permission from Ref. ……20
Figure 1.9: Working Principle of SSRM. The labels show the sharp tip (A), sample cross-section (B) and back-contact (C) respectively. Reprinted with permission from Ref. ...……..22
Figure 2.1: Process flow for fabrication of all silicon AFM probe. Reprinted with permission from Ref. ……...……...27
Figure 2.2: SEM micrograph of cantilever and tip fabricated by the process flow detailed above. Reprinted with permission from Ref. ……...……....28
Figure 2.3: Fabrication steps for Si_3N_4 AFM probe. Courtesy of NanoWorld …….....30
Figure 2.4:Fabrication steps for tetrahedral AFM tip. Reprinted with permission from Ref.…31
Figure 2.5: Tetrahedral AFM tips fabricated using process shown above. Reprinted with permission from Ref.……...32
Figure 2.6: Fabrication process for diamond AFM tips. Reprinted with permission from Ref. ……35
Figure 2.7: Pyramid diamond tip. Reprinted with permission from Ref. ……..…...36

Figure 2.8: Process flow for fabrication on diamond tips using Ga+ ion implantation. Reprinted with permission from Ref. ……..……..38
Figure 2.9: FIB milling process for high aspect ratio trenches. Reprinted with permission from Ref. ……39
Figure 2.10: Schematic illustration of EBID process. b) SEM images of Cobalt structures fabricated by EBID. Reprinted with permission from Ref. …….……41
Figure 2.11: High aspect ratio CNT tip. Reprinted with permission from Ref. ……..…..42
Figure 2.12: a) Oxide sharpened silicon tip with outer oxide visible. b) improved aspect ratio silicon tip with outer oxide removed by HF. Reprinted with permission from Ref. ……43
Figure 2.13: : Photolithography process using maskless lithography system. Reprinted with permission from Ref. …….……45
Figure 2.14: Reactive Ion Etching process. Reprinted with permission from Ref. …….....48
Figure 2.15: Bosch Process. Reprinted with permission from Ref. ……...…..….51
Figure 2.16: Ion Beam Milling system. Reprinted with permission from Ref. ……..…..52
Figure 2.17: a) Si(111) Etch Profile [1], b) Si(100) etch profile. Reprinted with permission from Ref. …….....55
Figure 2.18: a) schematic of various types of surfactants, b) molecular structure of non-ionic (Triton X-100), anionic (sodium dodecyl benzene sulfonate, SDBS) and cationic (1-hexadecylpyridinium chloride, CDC) surfactant. c) etch rate ratios for various silicon orientations with and without a non-ionic surfactant added in TMAH. d) effect of surfactant added TMAH etching for patterned silicon. Reprinted with permission from Ref.……..…..56
Figure 2.19: : (a) Pit Nucleation, (b) Step flow, (c-d) Hillocks, (e-g) Step Bunching. Reprinted with permission from Ref. ……...……..58
Figure 2.20: Schematic Illustration of CVD deposition process. Reprinted with permission from Ref. ……...…....61
Figure 3.1: b) SEM image of diamond film surface. ……66
Figure 3.2: Process flow for diamond tip with silicon base. …….....67
Figure 3.3: SEM image of Reactive Ion Etching of diamond using a) Al_2O_3 and b) Al hard mask. …….69

Figure 3.4: Diamond etching rate (top), and selectivity (bottom) between diamond and Al_2O_3 mask, as a function of oxygen gas flow. Total O_2/CHF_3 gas flow is 52 sccm. ……...….72
Figure 3.5: Selectivity (diamond : Al_2O_3) and sidewall angle with varying RF power in optimized diamond etching recipe. ……...……73
Figure 3.6: Diamond tip fabricated using optimized O_2/CHF_3 recipe. ……...……..74
Figure 3.7: Si RIE with diamond hard mask using a-b) Standard Bosch, and c) non-switching pseudo-Bosch etching. ……..……75
Figure 3.8: Diamond tip after silicon etching using non switching pseudo-Bosch with RF power a) 20 W, b) 30 W. ……...…….76
Figure 3.9: a) Diamond tip with Al_2O_3 apex, b) Diamond tip after silicon base fabrication, c) Apex of tip shown in b). ……...…….78
Figure 3.10: Graphical illustration of diamond tip fabrication using mask shrinkage method. ……...…….78
Figure 4.1: Process flow for diamond tip fabrication using T-gate mask…….…….83
Figure 4.2: SEM image of AFM tip base fabricated using Bosch etching with a) 5 seconds etching 7 seconds passivation; b) 6 seconds etching, 6 seconds passivation and c) 5 seconds etching, 6 seconds passivation……...……86
Figure 4.3: SEM image of AFM tip base fabricated using Pseudo-Bosch etching with RF power being a) 20 W and b) 50 W…….87
Figure 4.4: Sidewall slope of diamond obtained using a) O2/C4F8: 50/5 sccm and b) O2/C4F8: 52/3 sccm. RF: 50 W, ICP: 1000 W, Pressure 10mTorr and Temperature is 40°C for both recipes……...…….90
Figure 4.5: a) AFM tip with silicon base and diamond apex, b) diamond apex of tip shown in a) …….……..91
Figure 5.1: Schematic mask design used for etching Si(111) wafer. ……96
Figure 5.2: TMAH Etching of circular mask with initial dry etching height of a) 20 μm, b) 30 μm and c) 40 μm. ……..98
Figure 5.3: Tips formed after TMAH etching using a) diamond (square rotated by 45°), b) circular mask and c) square shaped mask. Dry-etching height is 30 μm for all masks….……99
Figure 5.4: Tips formed after TMAH + Triton X-405 etching of circle mask with initial dry-etching height of a) 20 μm, b) 30 μm and c) 40 μm. ……100

Figure 5.5: a) Uniformity across array and b) cone angle for tips fabricated using circular shaped mask and dry etching height of 30 μm……101
Figure 5.6: Tips formed after silicon etching in TMAH + Triton X-405 with a) diamond and b) square-shaped masks. The dry-etching height is 40 μm for both masks. ……..…..102
Figure 5.7: Silicon etching in TMAH + Triton X-100 using circular-shaped mask with dry-etching height of a) 20 μm, b) 30 μm and c) 40 μm. ……...……103
Figure 5.8: Silicon etching in TMAH + Triton X-100 using a) diamond and square-shaped mask. The dry-etching height is 30 μm for both masks. …….……104
Figure 5.9: a) Pillars formed on (111) surface after Bosch etching. b) Etching profile after TMAH etching. ……...110
Figure 5.10: Etching profiles after wet anisotropic etching in a-b) 1 ppm, c-d) 10 ppm, e-f) ppm, g-h) 1000 ppm surfactant concentration. The Millar index for various planes are inserted according to our best understanding using stereographic projection of (111) silicon as well as literature…….. ……..…….....112
Figure 5.11: AFM tips fabricated using a) pure 25 wt% TMAH, b) TMAH + 1000 ppm Triton X-100 and c) TMAH + 1000 ppm Triton X-405…….….113
Figure 5.12: Undercut at different surfactant concentrations. ……..……...114
Figure 5.13: Top view of sample etched in pure TMAH.....115
Figure 6.1: Imaging of trench using tetrahedral AFM tip. Reproduced with permission from Oxford Instruments. …….....117
Figure 6.2: Process flow for tetrahedral tip fabrication using Si_3N_4 mask. ……120
Figure 6.3: SEM image after silicon etching in 25 wt% TMAH at 70°C for 20 minutes using a) square, b) diamond and c) V-shaped masks…….121
Figure 6.4: Mask for tetrahedral tip fabrication. …….……122
Figure 6.5: Trend for mask opening angle versus tip apex. ……123
Figure 6.6: Tip obtained after TMAH etching, a) when silicon is not dry etched to expose underlying oxide in SOI wafer and b) silicon is dry etched to the expose underlying oxide in SOI wafer…….124
Figure 6.7: SEM image of tetrahedral tip after TMAH etching. ……..……...125
Figure 6.8: SEM image of tetrahedral tip after cantilever patterning. ……..…….….126
Figure 6.9: Process flow for fabrication of tetrahedral tip by ion milling. ……..…...129

Figure 6.10: SEM image of tip formed after TMAH etching, when tilt angle between ion beam and sample surface is 50°. ……...131
Figure 6.11: SEM image of tip formed after TMAH etching, when tilt angle between ion beam and sample surface is 40°. ……...132
Figure 6.12: SEM image showing uniformity across array after TMAH etching, when angle between ion beam and sample surface is 40°……...133
Figure 6.13: SEM image for cantilever fabricated on tip fabricated in figure 6.11…...……..134

LIST OF TABLES

Table 3.1: RIE Recipe tested for diamond etching.……70

Table 4.1: RIE recipes used for Si, aSi, SiO_2 and PMMA etching……...……..84

Table 4.2: Etching rate of different materials using recipes from table 4.1 ...……...85

Table 4.3: Diamond, Al_2O_3 and Cr_2O_3 etch rate using different O_2/C_4F_8 gas flows……..…….88

Table 4.4: Sidewall angle of patterned diamond and selectivity between diamond and Al_2O_3 for recipes listed in table 4.3…….89

Table 6.2: Etch rate of thermal oxide at various tilt angles between ion beam and sample surface. ……...……..…….130

Table 7.1: Apex, cost and aspect ratio of AFM probes fabricated using this work versus commercially available diamond and silicon AFM tips. …….138

LIST OF ABBREVIATIONS

AFM	Atomic Force Microscope
AM	Amplitude Modulation
APCVD	Atmospheric Pressure Chemical Vapor Deposition
BOE	Buffered Oxide Etch
CAD	Computer Aided Design
C-AFM	Conductive Atomic Force Microscope
CMOS	Complementary Metal-Oxide-Semiconductor
CNT	carbon nanotubes
CVD	Chemical Vapor Deposition
DI	Deionized
DUV	Deep Ultraviolet
EBID	Electron Beam Induced Deposition
EBL	Electron Beam Lithography
ECR	electron cyclotron resonance
EDP	Ethylene Diamine Pyrocatechol
EUV	Extreme Ultraviolet
FDT	Full Diamond Tips
FIB	Focused Ion Beam
FM	Frequency Modulation
FMM	Frictional Force Microscopy
HF acid	Hydrofluoric Acid
HMDS	Hexamethyldisilazane
HS-AFM	High Speed Atomic Force Microscope
HSQ	Hydrogen Silsesquioxane
IBID	Ion Beam Induced Deposition
ICP	Inductively Coupled Plasma
ICP-RIE	Inductively Coupled Plasma Reactive Ion Etching

IPA	Isopropanol
KOH	Potassium Hydroxide
LPCVD	Low Pressure Chemical Vapor Deposition
LPCVD	Low pressure Chemical Vapor Deposition
MEMS	Micro Electromechanical Systems
MWNT	Multi wall carbon nanotubes
OBD	Optical Beam Deflection
PDMS	Polydimethylsiloxane
PECVD	Plasma Enhanced Chemical Vapor Deposition
PEG	Poly(ethylene glycol)
PEO	Polyethylene oxide
PFT-AFM	Peak Force Tapping Atomic Force Microscope
PMMA	poly-methyl methacrylate
PVD	Physical Vapor Deposition
RF	Radio Frequency
RIE	Reactive Ion Etching
RPM	Revolutions per minute
SD	Step-dihydride
SDSS	Sodium Dodecyl Sulfate
SEM	Scanning Electron Microscope
SLM	Spatial Light Modulator
SM	Step-monohydride
SOG	Spin-on-Glass
SOI	Silicon-on-insulator
SPM	Scanning Probe Microscope
SSRM	Scanning Spreading Resistance Microscope
STM	Scanning Tunneling Microscope
TD	Terrace dihydride
TM	Terrace monohydride
TMAH	Tetramethyl Ammonium Hydroxide
TMB	Trimethyl-Boron

UNCD	Ultra Nanocrystalline Diamond
UV	Ultraviolet
XRD	X-ray Diffraction

CHAPTER 1: INTRODUCTION TO AFM AND DEVICE FABRICATION

1.1. ATOMIC FORCE MICROSCOPE

Atomic Force Microscope (AFM) is in a family of microscopy called Scanning Probe Microscope (SPM) which also includes Scanning Tunneling Microscope (STM) [2]. STM was developed by Binning and Rohrer (1981) [3] who later went on to receive the Nobel prize (Physics) for their invention. STM operates under principal of current flow between two metals when they are in very close contact (< 0.5nm) [2]. The current is exponential to tip-sample distance, which is utilized to determine surface topography, as shown in figure 1.1

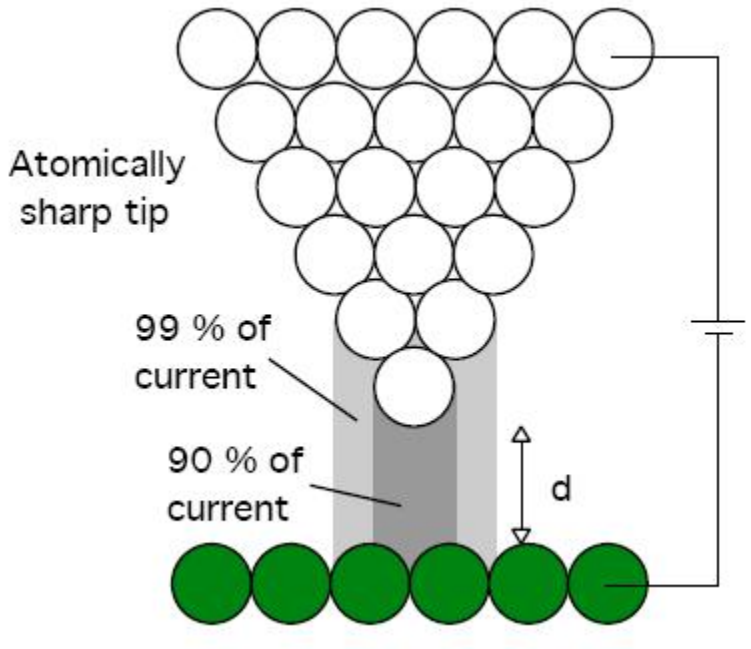


Figure 1.1: STM current dependence on tip-sample distance. Reproduced with permission from [4]

Unlike STM, AFM does not necessitate both tip and sample being conductive. Instead, it uses tip-sample interaction forces [5] to determine surface topography, which opens up possibility of

scanning a wide variety of materials. After the development of AFM in 1985, other variations were developed including Frequency Modulation AFM [6] and tapping mode AFM [7]. Though the possibility of atomic resolution was always possible using AFM, it wasn't until 1995 that the first atomic resolution image was obtained [8].

In recent times, AFM has become a standard characterization tool for surface topography measurements in most microfabrication processes due to its high resolution, ease of application, and minimal sample preparation required. It is also used for obtaining real-time images of biological samples [9], though this is still an emerging field due to various adaptations that are required to operate AFM in liquid environments [10] and on soft biological samples [11].

It has been found that when the AFM tip is biased, it can locally oxidize various materials which can then be used as etching mask during further device processing [12], allowing it to be used to fabricate nanostructures. However, this process requires AFM tip and sample to be conductive [13]. AFM has also be used to selectively move atoms on the surface which can be used to create atomic scale patterns [14]. However, due to the serial nature of AFM nanofabrication, it is not expected to reach commercial success.

1.1.1. Working Principle

The basic principle for Atomic Force Microscope (AFM) is measurement of inter-atomic forces. These forces are divided into short and long-range forces. AFM probe has cantilever with a tip on its end. When the tip interacts with any surface, the forces between the two causes cantilever bending which is most commonly measured by an optical beam deflection (OBD) method [15]. In OBD system, laser beam shines on back of the cantilever and is reflected onto a photodetector. This photodetector has four quadrants which can accurately measure the change in location of reflected laser between quadrants. When cantilever bends (because of tip-sample interaction

forces), the location of laser on photodetector changes, which changes the differential output voltages from the photodetector. The change in output signal is linearly proportional to cantilever bending. Next, feedback system compares output signal to the preset oscillation amplitude of the system and adjusts a piezo driver to maintain constant height/force between sample and cantilever. This can be done by either moving the probe relative to sample or by varying vertical (z-axis) position of sample surface relative to probe.

Output from the photodetector is also fed into a computer system which generates a topographical image of surface. Figure 1.2 shows the operation of AFM.

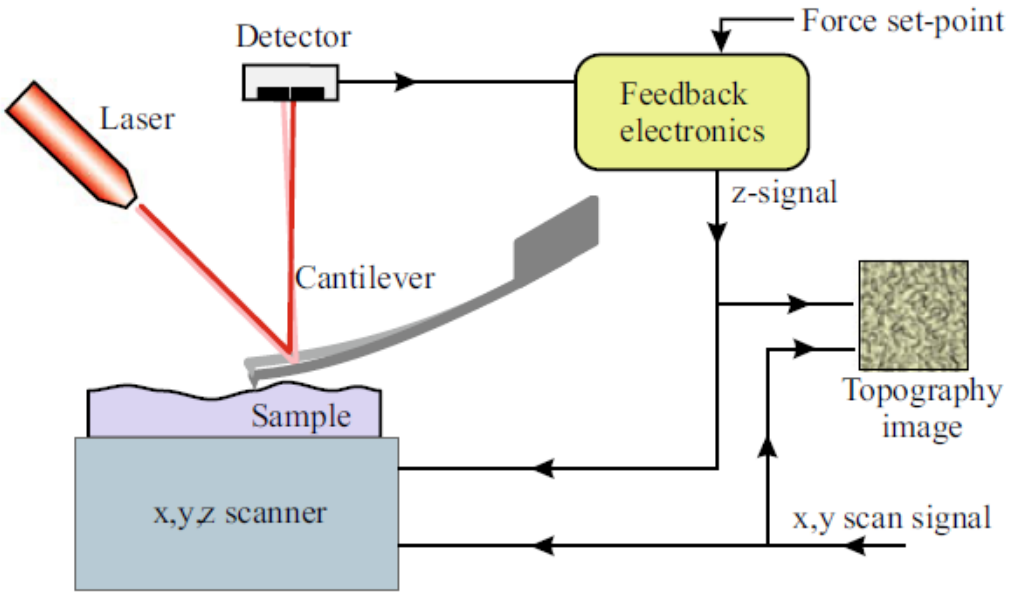


Figure 1.2: Working Principal of AFM . Reprinted with permission from [2].

1.1.2. Forces in AFM

As mentioned in the previous section, AFM detects forces between sample surface and tip. There are two major force categories: i) long range and ii) short range forces.

When tip-sample distance is larger than ~ 1nm, long-range forces dominate, with Van der Waals force having largest amplitude [16]. Other long-range forces detected by AFM are electrostatic [17] and magnetic forces [18], which can be used to study the behavior of charged and magnetic particles respectively. On the other hand, short-range forces occur due to the overlapping of electron wave functions of outermost shells of atoms on sample surface and tip (chemical bonding). They occur when tip-sample distance is less than 1 nm and can be attractive or repulsive in nature depending on the distance [19]. Forces between sample and tip are function of distance between them as shown in figure 1.3. As the tip and sample move closer to each other, the attractive forces increase due to the presence of both short-range and long-range forces. However, if probe-sample distance is very small, electron clouds repel each other, causing an increase in the overall repulsive force. The exact shape of force-distance curve depends on nature of sample surface. For example, for stiff surfaces the repulsive force increases rapidly as tip-sample distance decreases. In samples with very high elastic modulus, repulsive force region in force-distance curve can approximate a straight line. In contrast, softer samples typically exhibit a lower slope, as the tip indents into sample during contact mode [20]. Additionally, the scanning environment and the nature of charge on surface and tip can influence the nature of force distance curve for electrostatic force microscopy [17].

Another important concept in AFM is snap-to-contact. If tip-sample distance is very small (few nm) [21], tip 'snaps' into contact with sample surface. This occurs when the elastic restoring force of the cantilever is not able to balance the attractive forces between tip and sample surface [22]. Snapping-to-contact is considered an instability and is usually avoided by using stiff cantilever (if cantilever spring constant is higher than force gradient) or by using large oscillation amplitude of the cantilever [16].

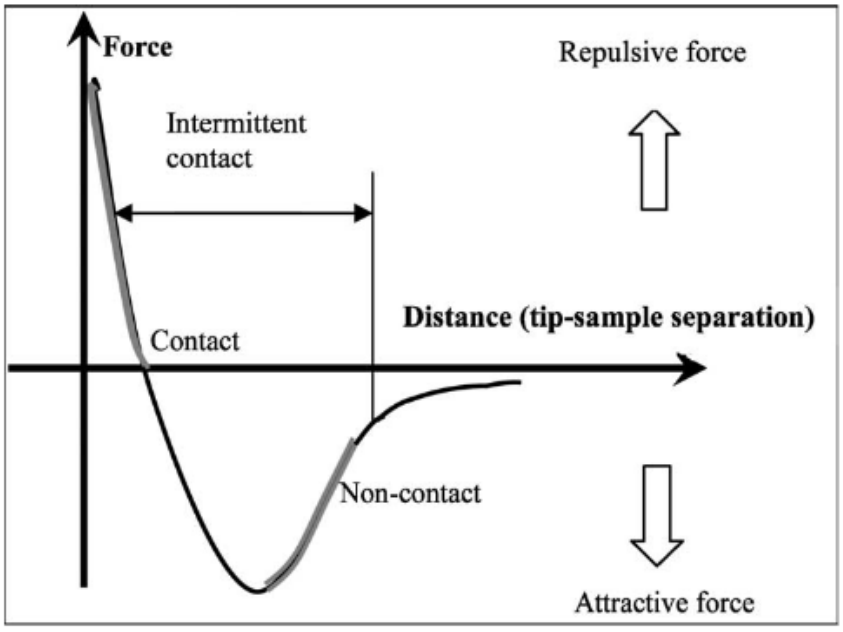


Figure 1.3: Interatomic force vs. tip-sample distance in AFM. Reprinted with permission from [19].

1.2. SCANNING MODES IN ATOMIC FORCE MICROSCOPY

AFM has three distinct excitation modes, named: static, dynamic, and intermittent/tapping mode. The major difference between the three is tip-sample distance, and cantilever vibration during scanning. For static mode, tips are normally in contact with sample (though it can also be done in non-contact mode) and there is no cantilever vibration during scan. On the other hand, dynamic and tapping modes have cantilever that oscillate at a pre-set frequency above sample surface. For tapping mode, tip may come in contact with sample surface during oscillation cycle, but for dynamic mode AFM there is never any contact between the two. Each AFM mode is discussed in more detail below.

1.2.1. Static Mode

In static mode AFM, tip scans the sample at a very small distance. The change in cantilever deflection, caused by tip-sample interaction, is noted. Feedback electronics are set up such that they maintain either constant force between sample and tip (constant force mode) or constant

height between the two. The latter is called constant height mode, where change in total force during scanning is used for creating a topographical map of surface. The cantilever deflection is dependent on cantilever restoring force (F_{cant}) and tip-sample interaction force (F_{ts}). To achieve equilibrium, total force on cantilever must be zero ($F_T = 0 = F_{ts} + F_{cant}$) [20].

Static mode AFM most commonly operates in repulsive force region (contact mode) of force-distance curve but can be made to operate in attractive force regime. In this case static mode is said to be in non-contact mode. It must be noted that the term 'non-contact AFM' is commonly used for dynamic mode AFM, however it can also be done in static mode AFM. The non-contact static mode AFM has a non-oscillating cantilever while dynamic AFM has a cantilever that oscillates at or near a predetermined frequency.

In constant force mode, tip-sample distance is continuously readjusted so that the force between them is constant [23]. The total force is sum of both short and long-range forces. Since magnitude of long-range forces is smaller than short range forces, and they do not vary significantly over tip-sample distance measured by contact mode, they act as background force during scanning. Short-range forces, on the other hand, can vary significantly when tip-sample distance is changed by a small amount, such as 1 Å. However, the total force may still be attractive during contact mode, due to large long-range forces. If the total attractive force becomes too high, it may cause deformation of the tip and/or sample surface, thus the contact area between the two consists of several atoms. This effect inhibits true atomic resolution [20]. However, resolution as low as 0.15 nm has been reported [24]. Since tip and sample are in contact, cantilever must be soft (i.e., spring constant of cantilever must be less than cumulative sample spring constant) to avoid damage to surface.

This mode can also be used to determine friction on the sample surface. Such arrangement is called 'Frictional Force Microscopy (FMM)', or sometimes "Lateral Force Microscopy (LFM) [25]. In this type of AFM, the scanning direction during contact mode is perpendicular to the cantilever length. During the scanning, the cantilever experiences torsional bending which causes change in the location of laser beam on the photodetector, as explained above. This allows for high resolution study of frictional forces present on different areas of the sample surface as well as on different materials and their orientations. For example, in reference [26], researchers used FMM to find the preferred growth orientation of graphene grains on copper.

Static mode AFM may also be operated with constant height of tip above the surface where cantilever deflection is monitored during scanning. Here, the AFM operates in an attractive force regime of force-distance curve and measures long range forces between tip and surface. Since no feedback is required (no change in cantilever position when tip-sample force changes), this type of scanning is fast. However, due to the possibility of tip damage in case of hills on surface, this mode is not commonly used.

1.2.2. Dynamic Mode

Dynamic mode differs from static mode in that it has an oscillating cantilever. In dynamic mode AFM, the probe oscillates at or near a fixed frequency above the specimen. Since tip never makes direct contact with surface, it is more commonly called non-contact mode. Driving frequency ω_{drive} of probe is set (by a piezoelectric actuator) to be near resonant frequency of cantilever. This is because the frequency versus amplitude curve has highest slope near resonant frequency, which translates to smaller magnitude of amplitude or phase/frequency change to be detected in this region [27]. In Amplitude Modulation (AM) scheme of the dynamic mode AFM, the oscillation amplitude is measured with fixed driving frequency (ω_{drive}) and driving amplitude (A_{drive}), and

any changes to the amplitude or phase corresponds to tip sample interaction. On the other hand, in Frequency Modulation (FM) scheme, a change in resonant frequency is measured with the driving and/or oscillating amplitudes being fixed.

In general, it is summarized that when tip sample force is attractive, cantilever's resonant frequency decreases, while it increases for repulsive tip-sample interaction force [28]. It must be noted that this generalization is acceptable only when the interaction force is assumed linear within operating region of oscillating cantilever and the gradient of this force is significantly smaller than cantilever spring constant 'k'. This is called 'small amplitude limit' for dynamic mode AFM (tip-sample interaction force is assumed linear when oscillation amplitude of cantilever remains small) and only occurs during the Amplitude Modulation mode. Tip distance from the sample during oscillation is maintained such that AFM detects Van der Waals or long range forces in this mode. Another important parameter in dynamic force AFM is quality factor 'Q' of cantilever. This depends on mechanical characteristics of cantilever [29] as well as the environment in which the AFM operates [30]. For an AFM, minimum detectable amplitude change depends on slope of resonance curve for a free (non-oscillating) cantilever, which itself depends on Q-factor of the cantilever [31]. Thus, Q-factor directly influences sensitivity of dynamic AFM, and higher Q-factor corresponds to higher sensitivity of the AFM. However, very high Q-factors also correspond to high time constant which causes low scanning speed. As mentioned above, the Q-factor of the AFM also depends on the working environment. A change in the effective Q-factor due to the change of cantilever oscillation may cause erroneous change in the measured amplitude signal. This error may be recognized by measuring the phase of the cantilever oscillation along with its amplitude, since cantilever phase dependance on effective Q-factor is different from amplitude dependence.

As mentioned above, dynamic mode AFM can also operate in frequency modulation scheme. Here, the change in resonant frequency is a function of distance between tip and sample. One of the biggest advantages of this mode is that it can be used with systems that have very large Q. This is commonly the case in ultra-high vacuum conditions where other modes of AFM are not feasible [32]. However, in contrast to AM mode, the FM mode does not operate within the small amplitude limit (oscillating amplitudes are very large). This means that tip-sample interaction forces cannot be assumed linear.

1.2.3. Intermittent Contact/ Tapping Mode

In intermittent contact/tapping mode, the tip periodically touches sample surface as opposed to the non-contact dynamic mode or the constant contact static mode. It is the most utilized mode since it can detect short range forces (thus providing higher resolution) without damaging the surface or tip (longer tip lifetime). In this mode, cantilever oscillates at pre-set frequency (50 – 500 kHz, or higher for fast scan AFM) near the sample surface like dynamic mode AFM. However, amplitude of oscillation in tapping mode is much higher than that in dynamic mode (10 – 100 nm) [33] and driving frequency is set to be at or very near resonant frequency of cantilever. This large driving amplitude results in tip-sample distances with negligible interaction, to distances where interaction force is repulsive (tip being in contact with surface) and there is a non-linear dependence between distance and force between the tip and sample surface. This also means that cantilever oscillation does not follow the small amplitude limit set in the amplitude modulation scheme of dynamic mode. Thus, the system behaves like an anharmonic oscillator (as opposed to harmonic oscillator in dynamic mode AFM) and overall resonance curve has a much different behavior than that in dynamic mode AFM. Large driving amplitude also helps to avoid snap-to-contact conditions. The oscillating amplitude of cantilever is measured to obtain an average tip-sample distance.

Amplitude decreases linearly with distance, when tip is in repulsive force regime i.e. very close to surface [34, 35]. The feedback system is used to keep the oscillating amplitude constant.

Like the dynamic mode AFM, tapping mode AFM also provides phase signal along with amplitude. When the net tip-sample force is attractive, phase of cantilever oscillation will have a value of less than 90°, while for a net repulsive force the phase angle will be greater than 90°. At resonance the phase value is exactly 90°. The AFM tip will visit both extremes of the phase during one cycle, however, for a particular point in the amplitude curve, we can use the phase to determine the nature of the force (attractive/repulsive).

As mentioned above, the tapping mode behaves as an anharmonic oscillator where resonant frequency is strongly dependent on oscillation amplitude, meaning that if oscillation amplitude changes (for example, due to tip-sample interaction) only one part of resonance curve shifts where the amplitude experiences change [36]. Like the case of harmonic oscillator (dynamic mode), when tip-sample interaction force is attractive, resonant frequency decreases, while for repulsive force the shift is towards higher resonant frequency [37]. However, this shift is localized to small areas (certain amplitudes) of resonance curve.

1.3. CRITICAL PARAMETERS

The AFM system can be divided into several parts. The most important of which is the AFM probe, which consists of tip, cantilever and handle. The next part is the detection system which monitors the movement of the probe due to tip-sample interaction. Most commonly used detection system is the Optical Beam Deflection (OBD) [15] as mentioned above. Next, the feedback electronics control the cantilever and/or stage movements by using piezoelectric actuators in accordance with the set scanning parameters.

In this section we look only at the critical parameters of the AFM probe.

1.3.1. AFM Tip

As mentioned above, the AFM tip is the part of the probe which interacts with the sample surface. The shape, dimensions and structural integrity of the tip determines the resolution and lifetime of the probe. The tip must have a sharp apex to allow for accurate representation of the sample surface. A blunt tip results in distorted representation of the surface [38], as shown in figure 1.4. For similar reasons, the tip must also have a high aspect ratio in order to scan deep trenches.

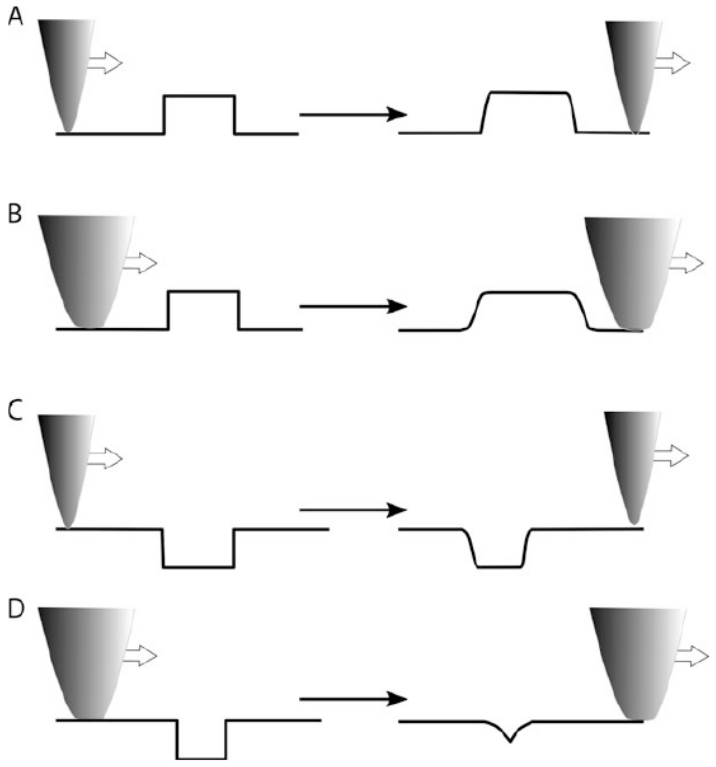


Figure 1.4: Effect of sharp and blunt tip on the scanning results for A),B) hills and C,D) valleys. Reproduced with permission from [38].

Another important parameter for tip is its wear resistance. AFM tips are usually made of silicon, which does not have high wear resistance. Due to the small size of the tip, visual inspection for wear resistance/ tip breakage is not possible. Instead, tip damage is often found out due to erroneous results during sample imaging [38]. To combat this issue, harder materials, such as

diamond, are used for tips which allow for better wear resistance and thus longer tip lifetime. The tip may be fully made of diamond [39] or diamond coating can be done on already-fabricated silicon tip [40]. Other materials have also been used as coating on silicon wafer for various purposes. For example, metals such as platinum [41] can be coated to improve conductivity, which is then used in conductive AFM. However, coated AFM tips often have large apex, and thus lower resolution. Additionally, the profile of the AFM tip can also be used to provide certain advantages. For example, a tetrahedral tip (cone shape close to the edge of the cantilever) allows for better positioning accuracy and reduced adhesion force between tip and sample [42]. Figure 1.5 shows different types of AFM tips. Further details about different materials for AFM tips are explained below.

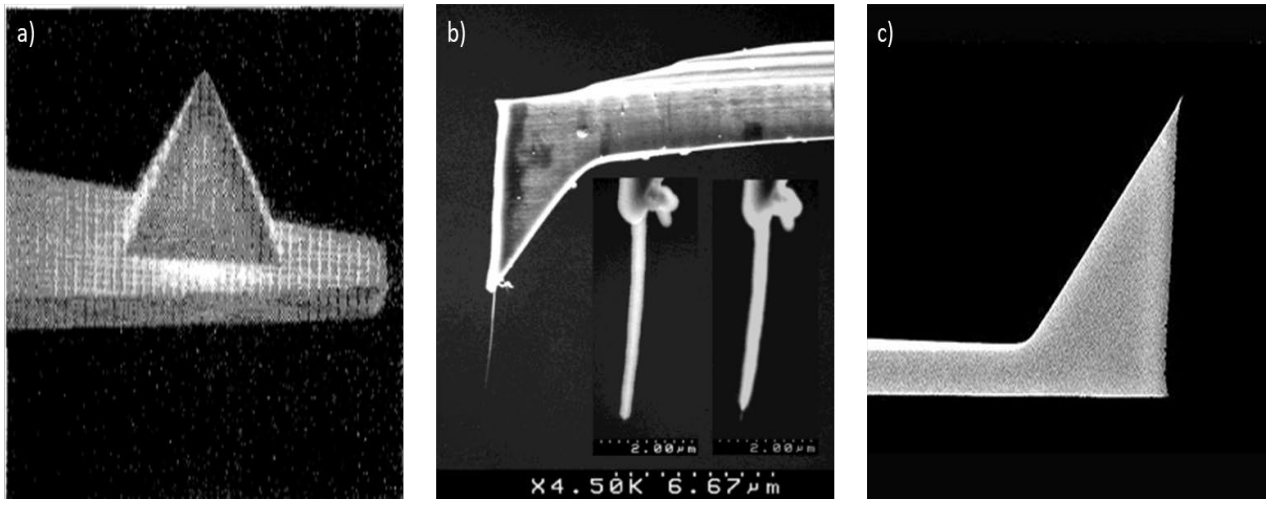


Figure 1.5: a) Standard silicon AFM tip [43], b) High aspect ratio tip [44], c) Tetrahedral tip [45].

1.3.1.1. Silicon AFM tips

Conventional AFM tips are fabricated by monolithic single crystal silicon using lithography and wet anisotropic etching in alkaline solutions. They form pyramidal tips with sloped facets with sidewall half-angles of ~17–25° and apex radii of curvature < 20 nm [46]. The tip height is usually

slightly above 10 micrometers with modest aspect ratio. Silicon tips are very stiff, which yields high force sensitivity on hard surfaces, but they are brittle and wear relatively quickly [47].

1.3.1.2. Silicon Nitride AFM tips

Silicon nitride (Si_3N_4) probes are low-stress thin-film cantilevers with square-pyramidal tips. The tips are fabricated by depositing Si_3N_4 film on anisotropically etched silicon substrate. The radius of curvature for these tips is typically 30 nm [46]. However, the thin-film cantilever gives a much lower spring constant than Si probes, making Si_3N_4 tips better suited to soft or contact-mode imaging. However, the larger tip radius, and moderate aspect ratio, limits resolution and penetration into high-aspect ratio features. Si_3N_4 is much tougher (less brittle) than Si, so these tips survive contact wear better.

1.3.1.3. Carbon Nanotube (CNT) AFM tips

Carbon nanotube probes use a CNT (SWNT or MWNT) attached or grown on a conventional tip. A single CNT has a diameter of only a few nanometers (SWNT) or tens of nm (MWNT) and can be microns long, yielding the highest aspect ratio of any tip. Such CNT tips inherit the tube's properties with extremely high axial stiffness (Young's modulus ~1 TPa). Hafner notes that CNTs have nanometer-scale diameter, long length, high stiffness, and elastic buckling, making them nearly excellent AFM tips [48]. Compared to standard Si or nitride probes, CNT tips have sharper apex, larger aspect ratios, and better resolution [49]. However, CNT tips are hard to fabricate and often multiple tubes are attached to a single silicon tip apex [50], and long CNTs can buckle during scanning, leading to imaging instability. In short, CNT tips offer unmatched aspect ratio and sharpness for high-aspect ratio imaging, but at the cost of complex fabrication, potential buckling artifacts, and usually higher expense.

1.3.1.4. Diamond AFM tips

Diamond AFM probes are generally made by coating a silicon tip with a thin diamond film or by using full diamond substrates. These tips can achieve high-aspect-ratio and sharp tips. For example, single-crystal diamond tips with ~15° cone half-angles and apex radii of ~7–10 nm have been demonstrated [51]. However, most commercially available diamond tips are fabricated using diamond-like-carbon films on Si which are typically a few tens of nanometers thick, giving a macroscopic tip radius of order ~100 nm. Boron doping during CVD diamond growth results in conductive diamond with resistivity between 0.003 – 0.005 Ω·cm [52].

Diamond's material properties yield exceptional stiffness and durability. With Young's modulus ≈1 TPa and hardness ≈100 GPa, diamond tips survive much higher loads and have far lower wear than standard Si or Si_3N_4 tips [53]. Undoped nanocrystalline diamond probes have been reported to outlast silicon nitride probes by roughly an order of magnitude under identical scanning conditions [54]. Boron-doped diamond tips are semiconducting and enable conductive-AFM modes, but even doped diamond remains much less conductive than a metal coating. Diamond-coated and all-diamond AFM tips offer excellent wear resistance, stiffness and chemical inertness which enables long-lifetime and high-resolution imaging. However, these features are obtained at the expense of higher fabrication complexity, cost, and somewhat lower electrical conductance compared to metal-coated tips.

1.3.2. AFM Cantilever

The parameters which must be considered while designing an AFM cantilever are its resonant frequency, Quality factor (Q-factor) and spring constant.

Resonant frequency of cantilever is kept high to avoid interference from surroundings. High resonant frequency also allows for higher sensitivity to tip-sample interaction and faster scanning

[55]. For a cantilever, resonant frequency is determined by choice of material and its dimensions. The relationship between these terms and resonant frequency is expressed by $f = 0.56\ \frac{D}{L^2}\sqrt{\frac{E}{12\rho}}$

Here, E is Young's modulus of the cantilever and ρ its mass density, both of which depend on the material chosen. On the other hand, D and L are thickness and length of the cantilever respectively and depend on cantilever dimensions. Large resonant frequency can be achieved by optimizing the height to length ratio and to use materials with high E:ρ ratio [56].

Spring constant (k) measures the stiffness of the cantilever and depends on the length, width, height and Young's modulus of cantilever. A beam with low spring constant must be used for detection of small tip-sample interaction forces.

Q-factor represents the damping constant of cantilever. It depends on cantilever's resonant frequency (ω), mass (m) and damping coefficient (c) ($Q = \frac{\omega}{c/m}$) . It also depends on the operating environment and tip-sample interactions [57]. Typical value of Q-factor in air range from 100 to 1000, though high Q-factor is required for certain applications such as resonance curve detection [56]. High Q-factor also allows for higher sensitivity, stable oscillations and accurate control of oscillating amplitude [30].

1.4. RECENT ADVANCES IN ATOMIC FORCE MICROSCOPY

Since AFM's development in late 1980s, it has intrigued scientists from all fields of research. Given the simple idea of measuring forces between two materials, it can be used to study various properties of materials, in addition to their topographical information. The non-destructive nature of the characterization and the relative ease of result interpretation also makes AFM an attractive tool for many researchers. This section details some of the most common variants of AFM, their design changes, forces measured, and the results obtained.

1.4.1. Peak Force Tapping AFM

The most widely used variant of AFM in recent years has been the peak force tapping AFM (PFT-AFM). This variant was introduced by Bruker in 2009 [58], and since then has gained popularity for certain applications [59].

The PFT-AFM, though similar to normal tapping mode AFM, has some key differences which allows it to provide gentler imaging. As mentioned above, the tapping mode AFM operates at or near cantilever's resonant frequency. Tip-sample interaction causes change in amplitude of cantilever vibration which is the measured quantity in this mode. Amongst the three primary mode of AFM, this mode provides optimal balance between force exerted on sample and resolution obtained. However, force exerted on the sample surface is not controlled and there is some damage to the sample surface, which can be especially pronounced for soft materials such as biological samples. Peak Force Tapping AFM, on the other hand, carefully controls force exerted on sample and thus provides the least damage to sample surface than any other imaging mode [60]. Additionally, since it directly measures tip-sample interaction force, it can be utilized to measure other material characteristics such as electrical [61] and mechanical properties [62].

Input signal in PFT-AFM is a sinusoidal wave, contrary to triangular waves used in conventional AFM modes [63]. Tip-sample force is set to be near peak value for each pixel scanned [60] as shown in figure 1.6. Additionally, the algorithm of the PFT-AFM has been designed to eliminate the background signal [64] and average the data from long-range forces (non-contact data), which serves as the baseline for the PFT-AFM signal [60]. Given that PFT-AFM operates at a much lower frequency (0.5 – 8 kHz) [63] compared to tapping mode AFM, the scanning speed is generally slower than traditional tapping mode. However, this is accompanied by the consistently high resolution, and less surface damage. Additionally, longer scanning times result in less artifacts than traditional

AFM modes. This is because the peak-force control minimizes the lateral force on the tip which in turn improves its lifetime and reduces tip artifacts [59].

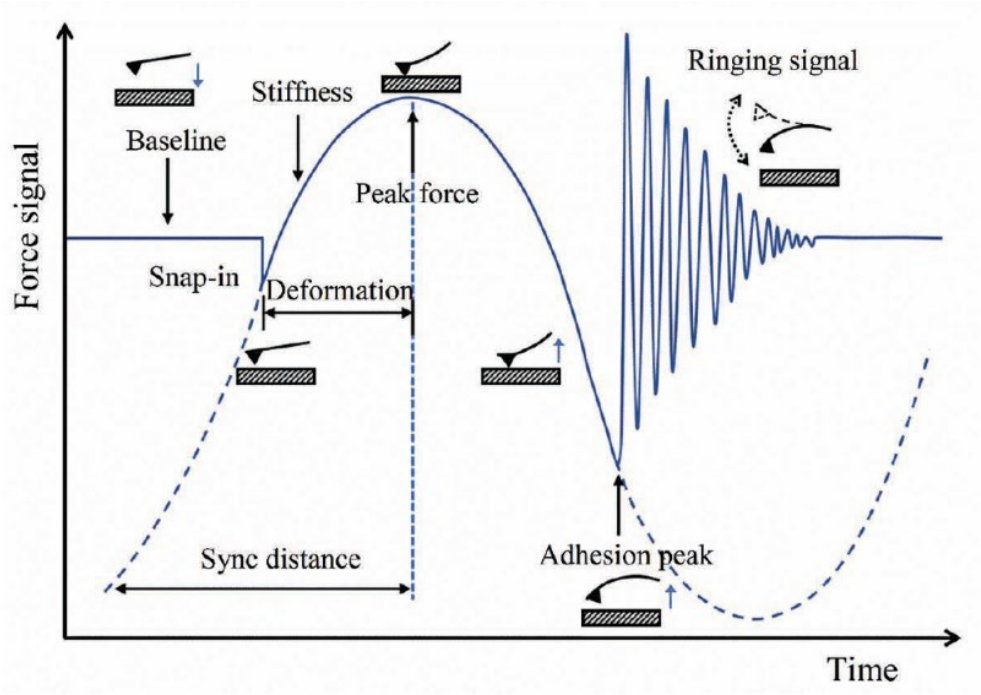


Figure 1.6: Tip Sample interaction curve in PFT-AFM. Reprinted with permission from [60].

1.4.2. Conductive AFM

The use of AFM to measure electrical properties of materials at nanometer scale were first reported in 1993 [65]. By 1996, researchers were able to achieve resolution as low as 8 nm [66, 67]. Since then, Conductive AFM (C-AFM) has been widely utilized to study electrical properties of materials. It utilizes a conductive tip and potential difference between tip and sample, to force a current between the two which is then measured along with the sample topography. The sample is fixed onto the holder by conductive tape and is electrically isolated from external interference. The electric field generated as a result of potential difference causes current to flow between the tip and sample surface. The current follows the equation $I = J.A_{eff}$, where I is total current flowing, A_{eff} is the

effective area for current flow and *J* is current density. It must be noted that the lateral resolution achieved by the C-AFM is determined by the effective area, which can be influenced by experimental conditions such as the contact force between tip and sample surface, and sample conductivity. The current density on the other hand reflects the properties of the material and is very sensitive to inhomogeneities in the material such as local defects, film thickness and doping levels. It is important to note that for C-AFM, effective area (A_{eff}) is not the same as physical contact area between tip and sample surface. This is because the electric field propagates laterally throughout the area which are electrically connected to the tip. This means that a metal sheet with same properties throughout the surface would be considered one electrical entity [68].

The effective area during the C-AFM measurement may be as small as a few nanometers, which can lead to very high current densities even if the current is as small as a few picoamperes. These high current densities can lead to very fast degradation of C-AFM tips resulting in unreliable results [69]. Additionally, the lateral force present between tip and sample is very high for C-AFM measurements which also plays a crucial role in tip degradation [70].

As mentioned above, the tip of C-AFM must be conductive. To achieve this, a standard silicon tip may be coated with a conductive film, or the tip maybe made fully of a conductive material. In the case of the former, the conductive coating maybe a metal, (such as Au [71]), silicide (e.g. PtSi [72]) or alloy (such as TiN [73] or CoCr [74]). Though fully conductive tips are more difficult to fabricate they provide much better mechanical and electrical stability [75].

However, one of the major disadvantages of this type of tip is that the electrical and mechanical wear is very fast which leads to quick loss of conductive characteristics for the C-AFM tip [76]. Additionally, the apex increases with increase in thickness of the coating. Diamond doped with conductive materials has also been used as a coating to provide wear resistance along with

conductive characteristics [76]. However, the conductivity of doped diamond is much lower than metal films and can vary significantly [77]. Additionally, the diamond thickness required to form a closed electrical path, typically leads to apex > 100 nm [40]. Typical apex for different types of conductive tips is shown in figure 1.7.

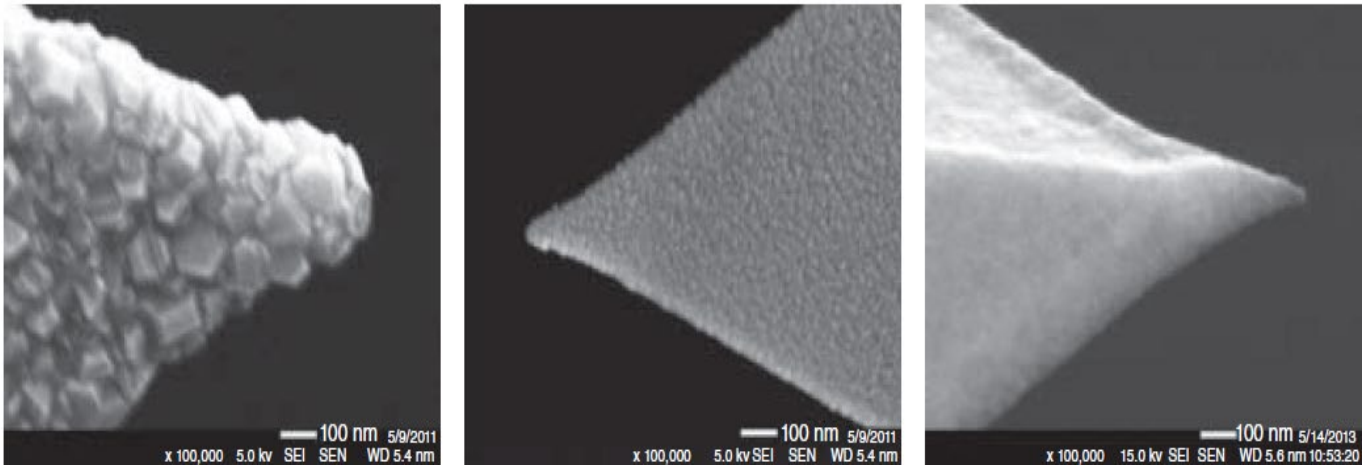


Figure 1.7: Apex for, a) diamond coated silicon, b) Pt-coated silicon and c) Pt-Si tips. Reproduced with permission from [69].

1.4.3. High Speed AFM

High Speed Atomic Force Microscope (HS-AFM) was designed to study biological samples with very high resolution [78]. To achieve this, the cantilever must have very high resonant frequency. The resonant frequency of a cantilever in air is given by:

$$f = 0.56 \frac{D}{L^2} \sqrt{\frac{E}{12\rho}}$$

Where, D is cantilever thickness, L is length, ρ is density and E is the Young's modulus of material used. Since resonant frequency clearly depends on physical dimensions of the cantilever (along with material properties), the cantilever for HS-AFM is very small. A comparison between typical AFM cantilever and HS-AFM cantilever is shown in figure 1.8. Though the decrease in cantilever length can increase the resonant frequency, this introduces other complications such as difficulty

in detection system. As previously mentioned, the detection system for typical AFM uses a laser reflected off the backside of cantilever. If cantilever length is too small, the beam must be focused onto a very small area at the oscillating edge of the cantilever. This is difficult because of the small dimensions of the cantilever. Thus, the OBD detection system used in HS-AFM also include optical lenses to focus the laser beam to the required spot [79]. However, the small size of the cantilever also results in a much higher deflection sensitivity which is useful for high resolution imaging [80].

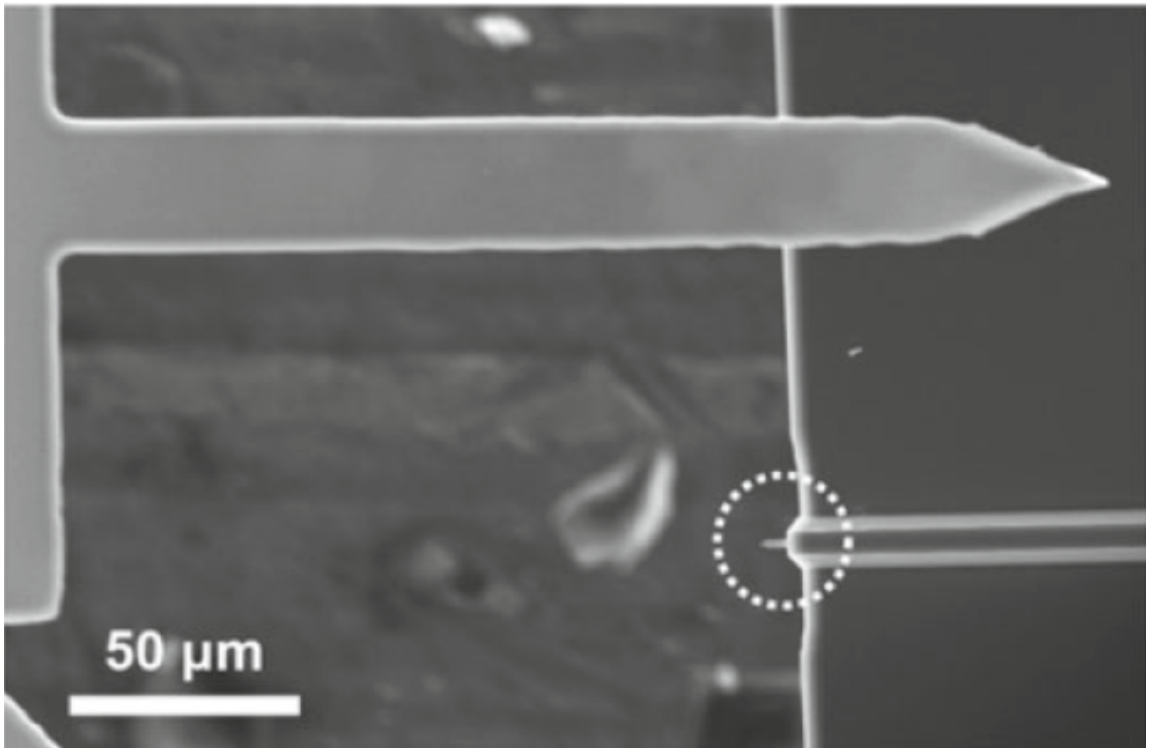


Figure 1.8: Comparison of standard AFM cantilever and those used for HS-AFM (circled). Reprinted with permission from [81].

Another issue encountered during HS-AFM imaging of biological samples occurs due to the liquid environment in which imaging is done. Since the tip must be inside the liquid for at least some of the oscillation cycle, there is significant damping. This effect is more pronounced for high oscillation frequencies and short tip height [80]. This requires that the tip for HS-AFM must be tall

(> 2.5μm) [80]. Tips for HS-AFM, typically use electron beam deposition to grow carbon tips onto already fabricated silicon tips [81]. Though these tips provide good quality imaging without significant damping, the risk of tip breakage is high during high-speed scanning [47].

Though HS-AFM was originally designed for imaging biological samples in liquid environments, some work has also been done on high-speed scanning in air. Due to viscous damping, the Q-factor in liquid is very small (typically between 2 – 4) for small silicon or silicon nitride cantilever, which allows for very high scanning speeds. However, the Q-factor of these materials is much higher in air which leads to significantly slower scanning speeds. For this reason, the cantilever used for high speed scanning in air are typically made of polymer such as SU-8 which have much lower Q-factor than silicon or Si_3N_4 [82].

1.4.4. Scanning Spreading Resistance Microscopy

Scanning Spreading Resistance Microscope (SSRM) was developed by IMEC in 1995 [83, 84] and is used to determine the carrier distribution inside semiconductor materials. It provides very high sensitivity and spatial resolution in 2D and 3D structures. The working principle of the technique is the same as that for spreading resistance profiling [85], however, for SSRM, only one probe is used, and the second contact (back-contact) is provided at the backside of the material being scanned. A conductive probe scans the cross-section of the device, in contact mode. DC bias is applied between the probe and the back-contact. Since the apex of the AFM tip is very small, the current experiences a restriction, followed by a spreading when it passes from the probe to the sample surface. The spreading of the current is associated with a resistance which is called 'spreading resistance' [86]. The working principle is illustrated in figure 1.9.

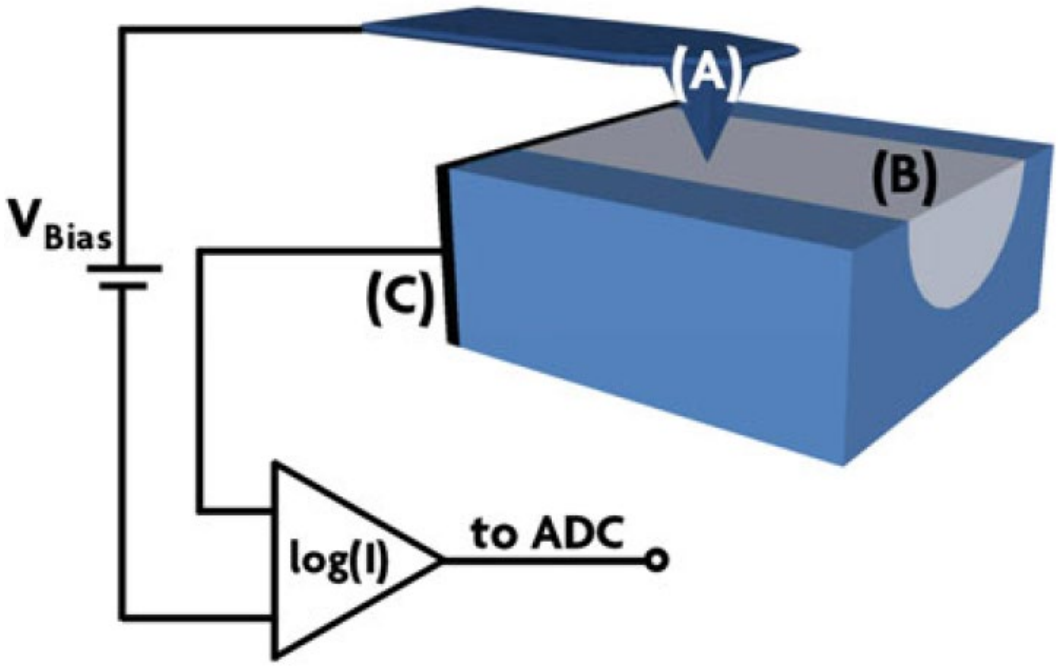


Figure 1.9: Working Principle of SSRM. The labels show the sharp tip (A), sample cross-section (B) and back-contact (C) respectively. Reprinted with permission from [87].

As can be seen in figure 1.9, the electrical contact between the AFM probe and sample is very small (a few nanometers), hence the electrostatic potential drops sharply near the point of contact. This results in a very sharp drop in electric field near the few nanometers at the point of contact, which in turn determines the lateral resolution of the SSRM [87]. Thus, a small contact area is necessary for high resolution.

The probe used for SSRM must be highly conductive so that the spreading resistance dominates the total measured resistance, which in turn is dominated by the local carrier concentration. Additionally, the probe must have very high wear-resistance and must be able to withstand the high mechanical force during scanning. For this reason, boron-doped conductive diamond was first used as conductive tip for SSRM [83]. In the two decades since its development, diamond-coated-silicon [88] and full-diamond tips [89] have emerged as the best suited for SSRM, though diamond-coated-silicon tips experience wear resistance faster than full-diamond-tips [90].

1.4.5. Colloidal AFM

As seen in the previous sections, modifications in AFM are often made to study material properties or apply the fundamentals of AFM in other environments. Another such modification is the colloidal AFM which is used to study the interaction between two colloidal particles or between a colloidal tip and a flat surface [91]. The idea was first studied in 1991 by attaching a sphere to the end of an AFM cantilever [92]. Researchers were able to study the forces occurring between silica particle and silica surface in NaCl solution. Since then, colloidal AFM has been readily used for studying forces between different materials. It has been found that stiffer materials, such as silica, gold etc., serve as better tip material when studying adhesion properties of surfaces [93]. The major difference between a standard AFM and colloidal AFM is the size of the tip. While a typical AFM has a tip apex between 10 – 50 nm, colloidal AFM have tip apex ranges from a few micrometers up to 50 μm. This results in very large adhesion forces between tip and sample surface.

Colloidal AFM tips are commonly fabricated by gluing colloidal particles on an already made AFM cantilever. However, because of the much higher forces involved in the technique, the cantilevers used much be stiff. This is to make sure that colloidal tip can detach from sample surface after interaction. However, this often leads to a loss in resolution. Additionally, hysteresis and creep in the piezoelectric actuator may also cause distortion in the force-distance curves and must be controlled during measurements. This can be done by using piezoelectric actuators having high scanning range [94]. Several techniques have been used to obtain high resolution force curves using colloidal AFM. For example in reference [95], researchers fabricated Polydimethylsiloxane (PDMS) tips on polyimide cantilevers. They used inverted cavities in silicon to act as a mold for PDMS tips while polyimide is patterned and cured to act as a cantilever. This probe was then used for AFM-based printing [95] and imaging [96]. On the other hand, Cho et al. used PDMS tips to study

the frictional properties of monolayers synthesised at different temperatures [97]. They compared the frictional properties using standard silicon tips as well as PDMS tips. They found that since the silicon tips are sharp and hard, they were able to penetrate the organic monolayers, which caused the frictional properties of the layer to be heavily influenced by the silicon tip. However, when using PDMS tips, the friction coefficient of the monolayers was due to their surface properties and not due to viscoelastic deformation.

1.5. OBJECTIVES OF THIS WORK

As discussed in this chapter, the ability of the AFM probe to obtain high resolution imaging is critically dependent on its tip. Most commercial AFM tips are fabricated using wet anisotropic etching of (100) oriented silicon wafer which results in low-aspect ratio pyramid shaped structures. For application such as SSRM and static mode scanning, the AFM tip must have very high wear resistance which is commonly obtained using diamond AFM tip. However, the current fabrication process of diamond AFM tip is complex and serial in nature, as will be discussed in detail in chapter 2.

This work focuses on the fabrication of high aspect ratio, sharp AFM tips. In chapter 3 and 4 we develop methods for fabrication of high aspect ratio diamond tips using reactive ion etching, which can routinely produce < 20 nm apex and provide aspect ratio close to 10. This work allows for low-cost, mass production of diamond AFM tips.

In chapter 5 we fabricate high aspect ratio silicon tips using anisotropic wet etching of (111) oriented silicon wafer, which when dry etched before wet anisotropic etching, can produce very high aspect ratio tips. Using this method, the low-cost advantage of anisotropic wet etching, compared to reactive ion etching, is preserved while the high aspect ratio capability of reactive ion etching is introduced by using pillars on (111) oriented wafer and by careful manipulation of

anisotropy by introduction of non-ionic surfactants, dry etching depths and mask geometry. We have also studied the behavior of non-ionic surfactant adsorption on silicon surface at different concentrations.

Finally, in chapter 6 we have developed two methods for the fabrication of tetrahedral tip which are tips placed at the edge of a cantilever and have one side perpendicular to the cantilever surface. This design provides the advantage of excellent lateral resolution along with ease of alignment with the patterned sample. We use a combination of dry and wet anisotropic etching to obtain the desired profile. The developed methods are capable of mass-producing low-cost tetrahedral tips with very sharp apex.

CHAPTER 2: STANDARD PROBE FABRICATION METHODS

2.1. STANDARD METHODS FOR ALL SILICON PROBE FABRICATION

As mentioned in the previous chapter, AFM probe consists of three parts: the tip, cantilever, and handle. Amongst them, the handle is almost always made by bulk micromachining of silicon [98]. The cantilever is commonly made of silicon [98] or silicon nitride (Si_3N_4) [43, 99], while the tip may be fabricated of several possible materials, depending on the application and requirements of the scan [100]. Most commonly used material for AFM tip is silicon which may or may not be coated with other materials for enhanced conductivity [41], hardness [101] or other properties [102, 103]. Primary reasons for use for silicon in both cantilever and tip fabrication are its good mechanical properties and ease of fabrication using low cost methods such as wet etching [104]. This section reviews the standard fabrication techniques used for all silicon probe fabrication. Additionally, a brief overview will be provided for fabrication of Si_3N_4 cantilever with silicon tips.

2.1.1. All Silicon AFM Probe

Figure 2.1 shows the process flow for fabrication of all silicon AFM probes. First a Silicon-on-insulator (SOI) wafer is thoroughly cleaned using acetone and isopropanol (IPA) followed by rinsing with deionized (DI) water and drying using nitrogen. The wafer is then oxidized (figure 2.1 a) and coated with photoresist. Next, photolithography is done on the back side of the wafer, and the oxide is patterned to function as a mask for the upcoming wet anisotropic etching (figure 2.1 b). Once the oxide is patterned, wet anisotropic etching is done on the back side of the wafer for handle fabrication (figure 2.1 c). Next a layer of photoresist is spin coated and another round of photolithography is performed to define the cantilever structure (figure 2.1 d). The front side

silicon is dry etched to the required cantilever thickness (figure 2.1 e). The front side undergoes another lithography and pattern transfer to oxide hard mask in order to define the tip (figure 2.1 f). Next, silicon is etched using wet anisotropic etching in either Potassium Hydroxide (KOH) or Tetramethyl Ammonium Hydroxide (TMAH) which forms a cone shaped structure to function as a tip (figure 2.1 g). The etching continues until the oxide mask falls off, after which the oxide of the SOI wafer is etched away in HF acid (figure 2.1 h) and the cantilever is released.

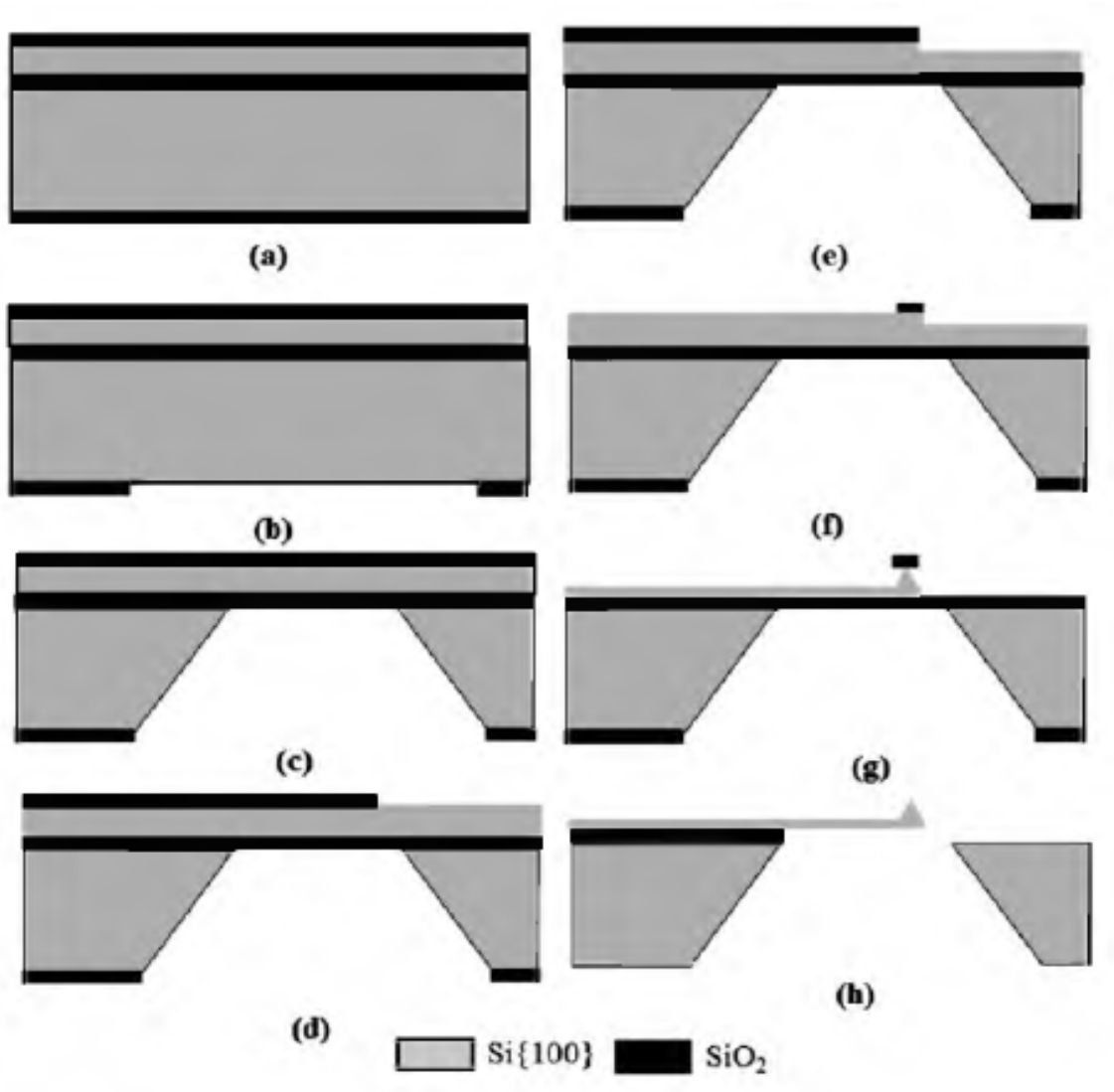


Figure 2.1: Process flow for fabrication of all silicon AFM probe. Reprinted with permission from [104].

This type of probe can also be fabricated by defining the parts of the probe in reverse order (tip, cantilever and lastly handle), however, this requires an additional step of tip and cantilever passivation when wet etching is done for handle fabrication.

It should also be noted that wet anisotropic etching of silicon is a complex process, and care must be taken to obtain the required results. Experimental conditions, such as temperature, etchant type, concentration, contamination, additives etc., all affect the final geometry obtained. Additionally, wafer parameters, such as wafer orientation, mask orientation, miscut etc., must also be carefully adjusted. An example of a tip formed by wet anisotropic silicon etching is shown in figure 2.2. Further details about wet anisotropic etching of silicon are presented in section 2.4.

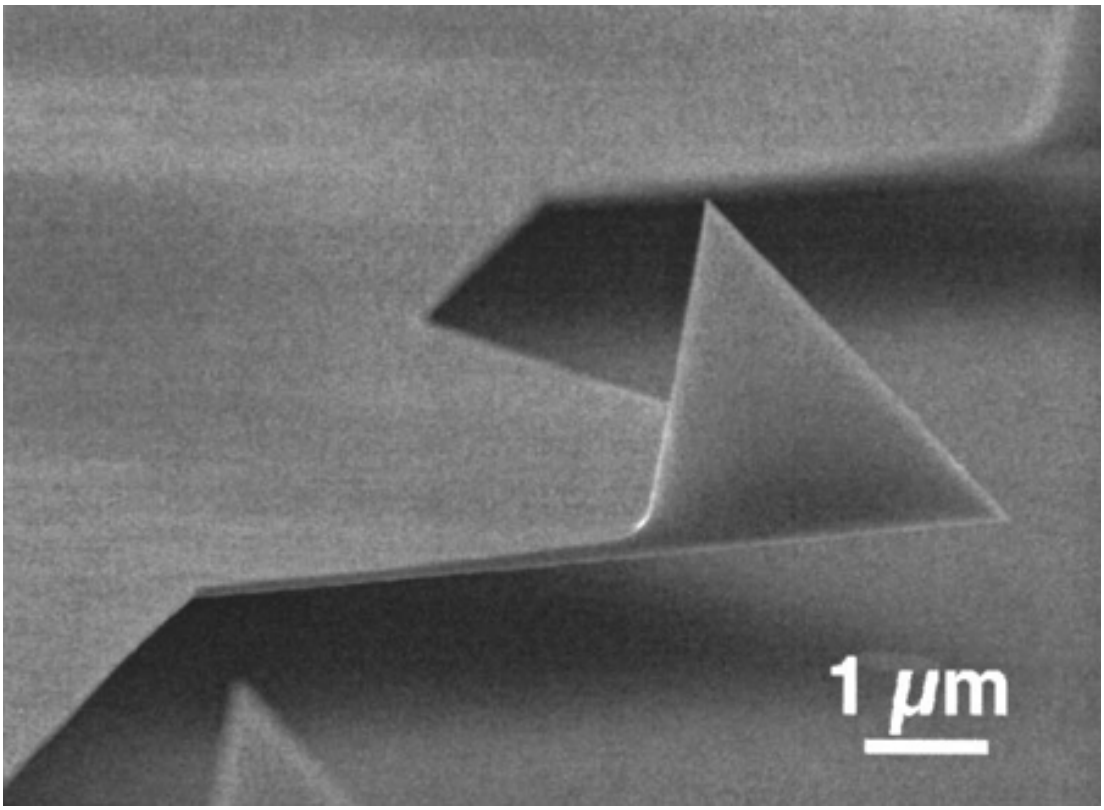


Figure 2.2: SEM micrograph of cantilever and tip fabricated by the process flow detailed above. Reprinted with permission from [105].

2.1.2. Silicon Nitride Cantilever

Figure 2.3 shows the steps for fabrication of silicon nitride (Si_3N_4) AFM probe. In the figure, both the tip and cantilever are fabricated using Si_3N_4. First, a (100)-oriented silicon substrate undergoes thermal oxidation to form an oxide mask on both sides of the wafer (figure 2.3 a). Next, photoresist is spin coated, and photolithography is done to pattern the front side of the wafer (figure 2.3 b), followed by resist development on front side and coating of protective resist layer on the backside of the wafer (figure 2.3 c). The backside resist coating is performed to protect the thermal oxide on the backside of the wafer during BHF etching of front oxide to transfer the pattern from the resist to oxide (figure 2.3 d). Next, resist is removed from both the front and backside of the sample and the oxide acts as a mask during wet anisotropic etching of silicon using KOH (figure 2.3 e). This etching creates V-shaped trenches in the silicon substrate, with an angle of 54.7° with the silicon surface, due to the evolution of slowest etching (111) planes on the trench sidewalls [104]. The oxide from both the top and bottom of the surface is then removed by BHF (figure 2.3 f), and the sample undergoes thermal oxidation again. This oxidation step also oxidizes the newly formed trenches in the silicon substrate (figure 2.3 g). Next, Low-Pressure Chemical Vapor Deposition is done to deposit low-stress silicon nitride on both front and backside of the patterned sample (figure 2.3 h). This nitride acts as both nitride tip and cantilever. The frontside of the sample is then coated with resist while the backside undergoes nitride and oxide removal (figure 2.3 i), which is followed by photolithography on the frontside to pattern the cantilever (figure 2.3 j). After patterning of cantilever, nitride layer is removed from the unpatterned areas and the resist is removed (figure 2.3 k). Next, a diced Pyrex wafer is attached to the patterned silicon using anodic bonding (figure 2.3 l). The Pyrex is further diced to form individual handles for the patterned cantilevers on the silicon substrate (figure 2.3 m). Next, the silicon substrate is etched away using KOH, while the

oxide layer is removed using BHF (figure 2.3 n). This step releases the nitride AFM probe. Finally, the cantilever backside is coated with gold to provide good laser reflectance (figure 2.3 o).

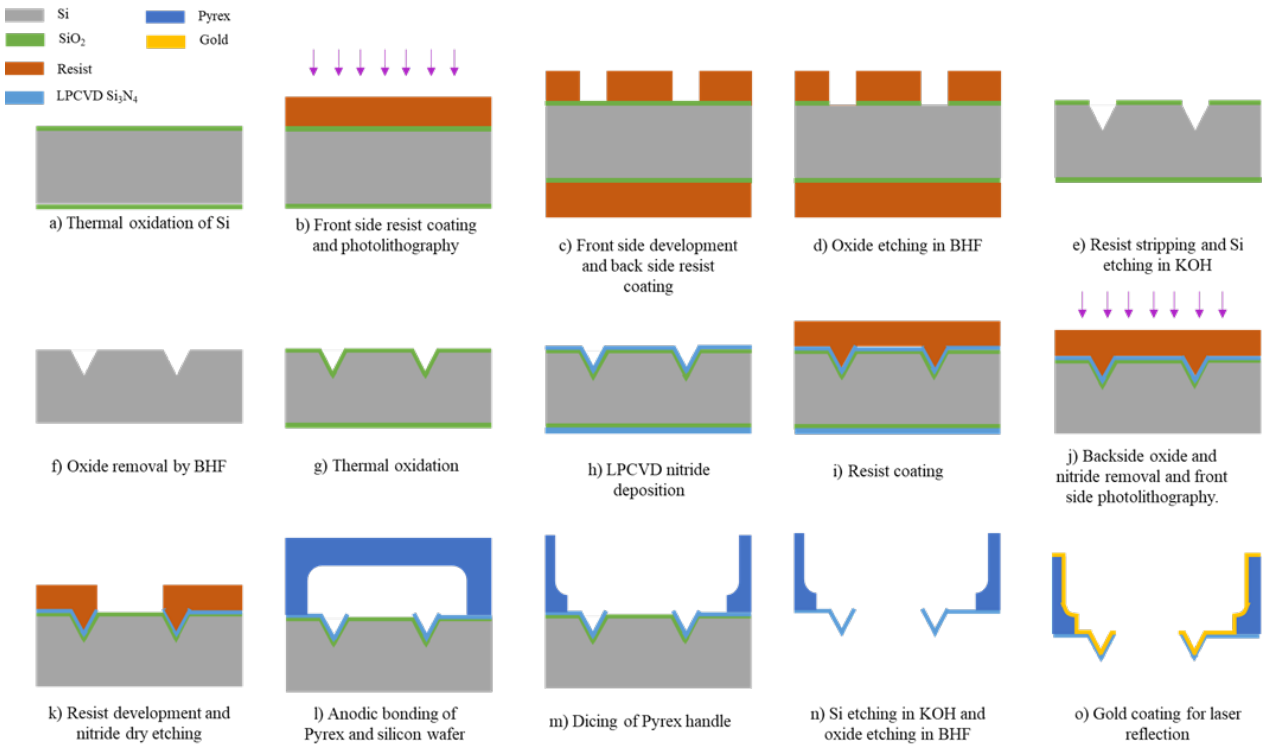


Figure 2.3: Fabrication steps for Si_3N_4 AFM probe. Courtesy of NanoWorld.

The process described in figure 2.3, can be optimized to create the tip of a different material by an additional patterning, deposition, and liftoff step after the pit formation on the silicon substrate.

2.1.3. Silicon Tetrahedral Tips

Tetrahedral AFM tips are fabricated using a combination of dry etching and wet anisotropic etching [106]. To illustrate the process, the fabrication starts with deposition of Si_3N_4 on (100) Si wafer. Next, a square mask is patterned using photolithography and then transferred to Si_3N_4 using RIE (figure 2.4 a). Next, RIE is performed to etch ~10 µm into the silicon substrate (figure 2.4 b). The square mask has corners aligned to <110> direction (figure 2.4 c). The wafer then undergoes thermal

oxidation at 800°C to grow thermal oxide on the exposed silicon surface (figure 2.4 d). The thermally grown oxide growth results in sharp corners of the underlying silicon. The Si_3N_4 layer on top of the square mask inhibits oxidation of silicon on top of the post. Once the Si_3N_4 layer is selectively removed using RIE, the underlying silicon is exposed which is then etched in KOH at high temperatures (figure 2.4 e). After silicon etching the final profile consists of (111) plane with sidewalls covered with thermal oxide (figure 2.4 f). Once the thermal oxide is removed, sharp silicon tips are revealed. However, as the tips formed on all corners of the square shaped mask, the cantilever alignment is a difficult task. Figure 2.5 Shows the tetrahedral tips fabricated using the process described above.

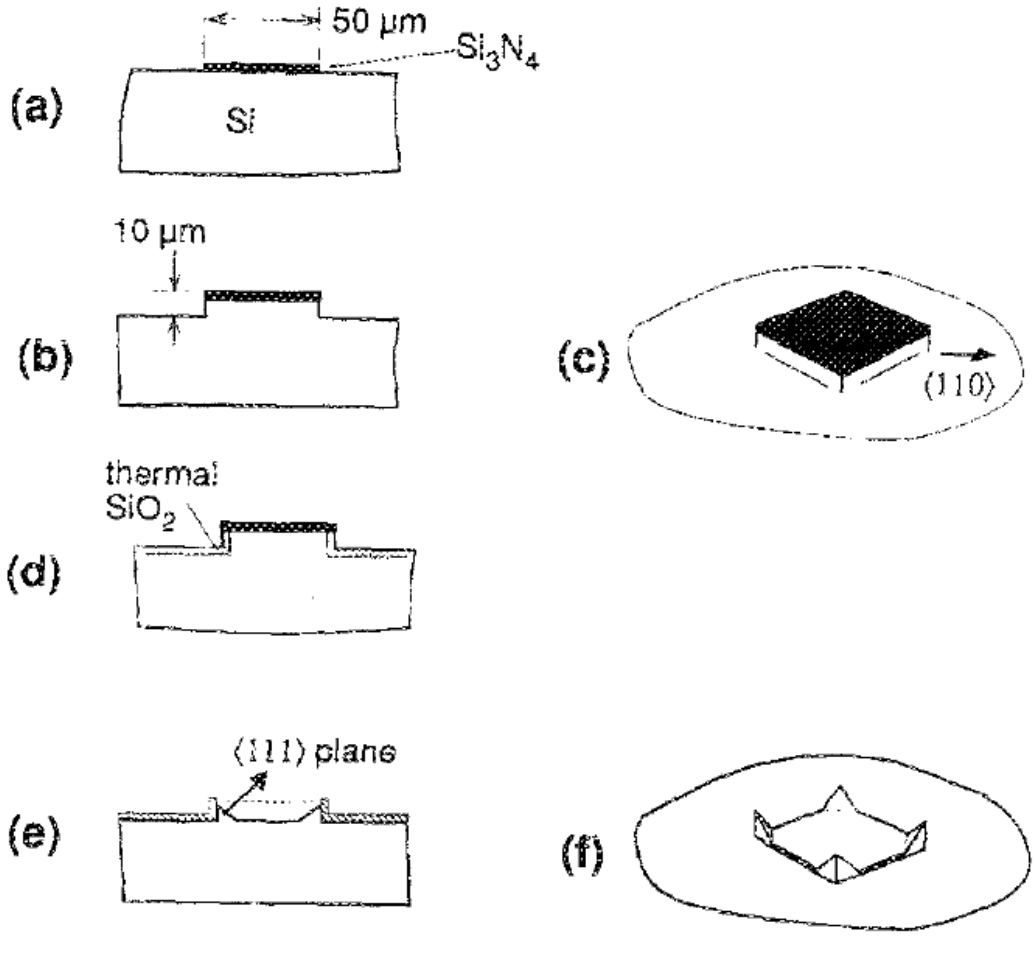


Figure 2.4: Fabrication steps for tetrahedral AFM tip. Reprinted with permission from [106].

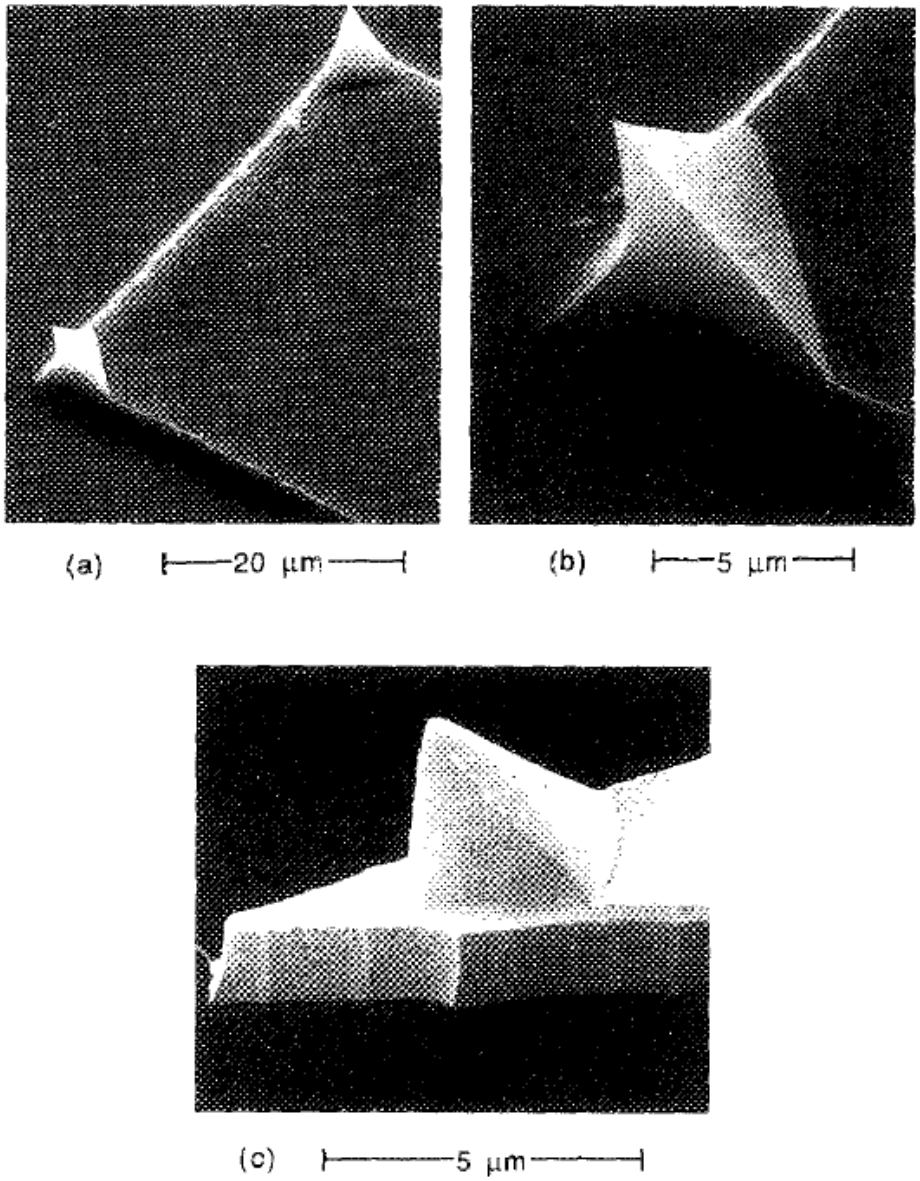


Figure 2.5: Tetrahedral AFM tips fabricated using process shown above. Reprinted with permission from [106].

2.2. METHODS FOR FABRICATION OF SILICON PROBE WITH DIAMOND TIP

Soon after the development of AFM, the requirement for longer tip lifetime emerged. Given diamond's excellent hardness, low friction and its chemically inert nature, it quickly became a front-runner for tips with long lifetimes. Additionally, doped-diamond acts as an excellent electrical conductor [90]. In 1995 sharpened boron-doped diamond crystal, having apex diameter

~100 nm, was used for the first test of Scanning Spreading Resistance Microscopy (SSRM) [107]. However, the resolution of this method was very low. Later, diamond-coated-silicon tips were used to better resolution, though the tip wear was fast due to large forces experienced during SSRM measurements [88]. In recent years, full diamond tips (FDT) have emerged as the best solution to SSRM measurements as well as to provide better wear resistance [89, 108].

Unlike silicon, diamond cannot be wet etched, therefore, diamond AFM tips are fabricated by two main methods: molded pyramid diamond tips [109] and plasma etching of diamond [110]. Other techniques, such as CVD diamond growth combined with selective oxidation, have also been reported to produce high aspect ratio sharp diamond tips [111]. However, the synthesized diamond tips must be manually attached to a cantilever, which makes the process unsuitable for mass production.

2.2.1. Pyramid Molded Diamond Tips

The fabrication process for molded diamond tips is similar to that for Si_3N_4 tips shown in section 2.1.2. The process is also shown in figure 2.6. In the first step, (100) oriented silicon wafer is anisotropically etched in alkaline solution. Next, a seeding step is done, where the silicon substrate is immersed into a seeding solution containing diamond nanoparticles (figure 2.6 a). The nanoparticles provide nucleation sites for diamond growth during the upcoming Chemical Vapor Deposition (CVD) step; thus, this step is crucial for controlled diamond growth. Significant research has been done to show that seeding dispersion has a large impact on the quality of the diamond film [112]. In order to obtain high seeding density, the zeta-potential of the diamond nanoparticles in the solution should be between 20 and 40 mV [113]. To obtain conductive diamond film, the seeding step may be boron-doped [114-116]. Once the silicon substrate is covered by diamond nanoparticles, CVD system, with CH_4/H_2 gases, is used to deposit diamond thin film (figure 2.6

b). For boron-doped diamond film, trimethyl-boron (TMB)/CH_4 is also added to the system. The quality of the diamond film depends on the gas flow and other process parameters such as pressure and temperature [90].

After the deposition of diamond film, the substrate undergoes lithography to pattern the diamond tip (figure 2.6 c). Since diamond is etched in oxygen plasma, which can quickly remove resist mask, pattern is transferred from resist to metal mask (such as Al) after which reactive ion etching is performed to remove the unpatterned diamond film (figure 2.6 d). Next, a metal is electroplated and patterned to function as a cantilever (figure 2.6 e). The release step is done by etching the silicon substrate by wet etching (figure 2.6 f) followed by peeling using tweezers (figure 2.6 g). Finally, a silicon holder is attached to the backside of the cantilever by silver epoxy or lead-free soldering [117] (figure 2.6 h) and the probe is released from the silicon substrate using tweezers (figure 2.6 i). Figure 2.7 shows the diamond tip obtained from the process described above. The authors were able to achieve an average apex of 14.9 nm [90].

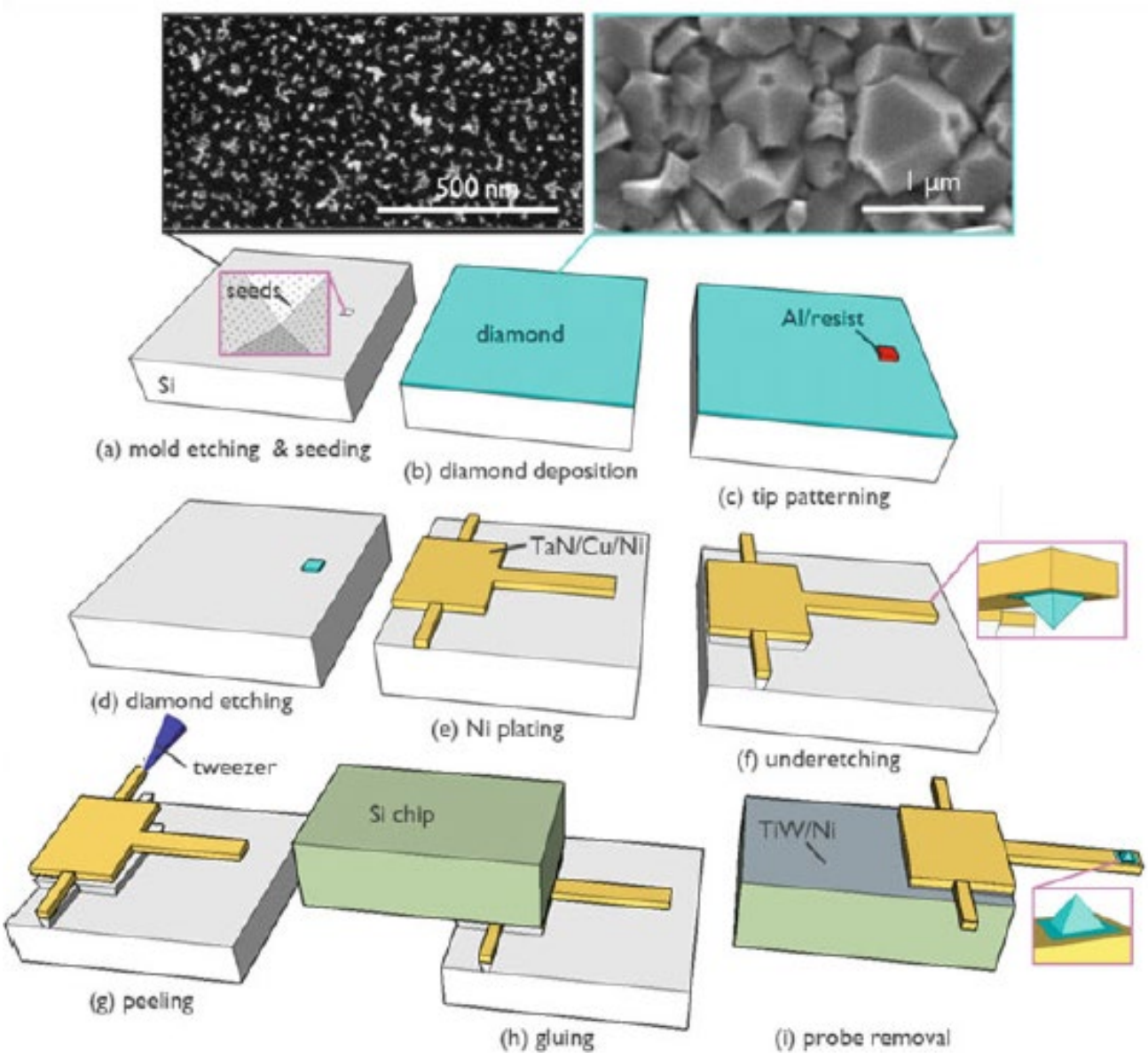


Figure 2.6: Fabrication Process for diamond AFM tips. Reprinted with permission from [90].

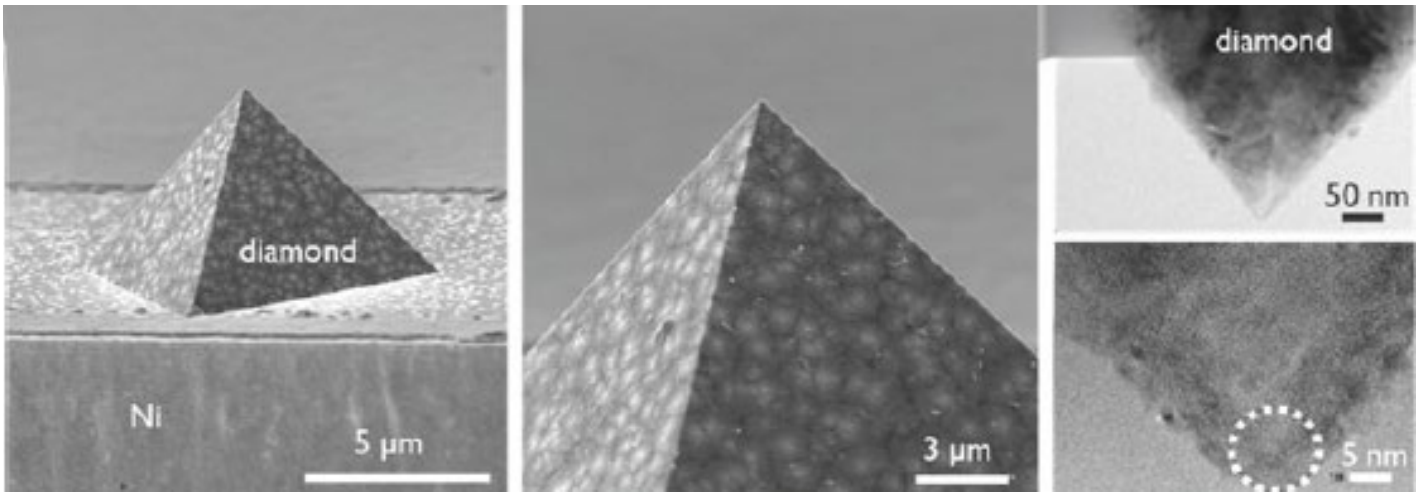


Figure 2.7: Pyramid diamond tip. Reprinted with permission from [90].

2.2.2. Plasma Etched Diamond Tips

Though it is possible to grow diamond layer on prefabricated silicon AFM tips, the film continuity on the tip apex remains challenging. Even if a diamond film is grown successfully on the apex, the growth of film would significantly increase the tip apex [88]. Additionally, processes such as photolithography are required for selective diamond growth on the tip area. However, these processes are unable to handle high aspect ratio tips and would break the fragile processed wafer [90]. To counter these issues, full diamond substrates or diamond thin-film on silicon substrates, are patterned using plasma etching [118, 119]. One such method is gallium ion implantation into diamond to act as a hard mask for plasma etching [119]. This is achieved using focused ion beam (FIB) implantation and allows for mask sizes much smaller than those possible by electron beam lithography and thus the final diamond tip size is much smaller than those etched by patterned hard masks. The process is shown in figure 2.8. It begins with fabrication of tip and cantilever on silicon substrate by patterning (figure 2.8 a) and etching (figure 2.8 b), followed by front side passivation (figure 2.8 c) and backside patterning and etching for handle fabrication (figure 2.8 d). These steps are the same as those followed for silicon probe fabrication. However, once the silicon probe is

fabricated, diamond is grown across the entire probe area using chemical vapor deposition (CVD). Next, gallium ions are implanted in the diamond film using focused ion beam which eliminates the need for sample damaging processes such as spin coating and photolithography [120] (figure 2.8 e). Additionally, precise stage control for FIB system allows for Ga^{+} ions to only be implanted in the tip region. This mask acts as a hard mask to protect diamond on the tip from being etched by subsequent plasma etching [119] (figure 2.8 f).

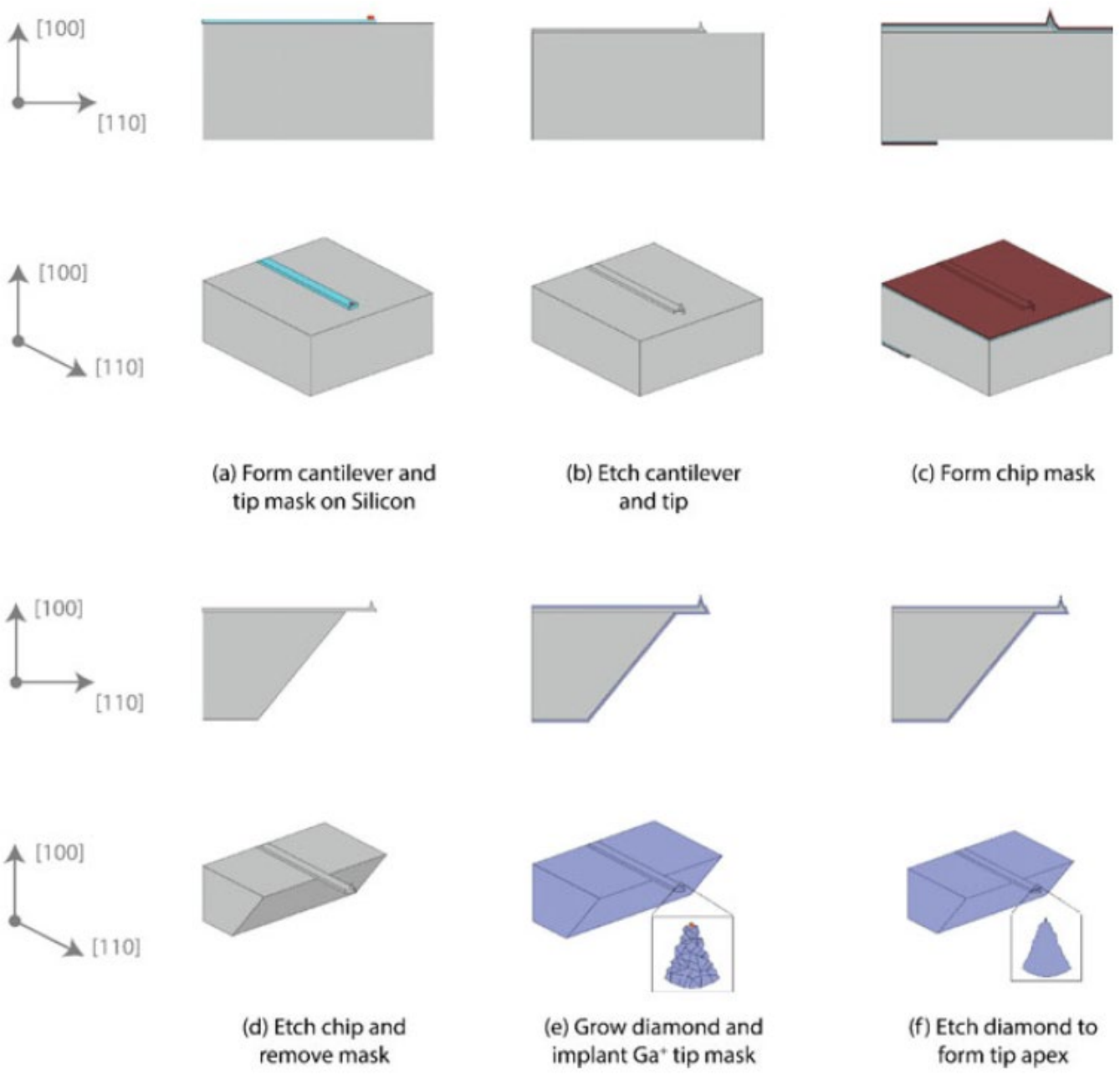


Figure 2.8: Process flow for fabrication on diamond tips using Ga+ ion implantation. Reprinted with permission from [90].

2.3. METHODS FOR HIGH ASPECT RATIO TIP FABRICATION

The previous sections have referred to several processes required to fabricate AFM probe. In this section we detail the processes used to fabricate high aspect ratio AFM tips.

2.3.1. Focused Ion Beam (FIB) Milling/Etching

Ion beam etching employs the removal of surface atoms using high energy ion beams. Typical beam energy used for gallium ion beam is between 5 to 50 keV which is comparable to that used for ion implantation process mentioned in the previous section. Ga^+ ions in this range have a penetration depth of ~10 nm [121], which is much lower than that for electrons in the same energy range, and thus allows for removal of surface atoms. The principal behind this process is the momentum and kinetic energy being transferred from incident ions (such as Ga^+) to surface atoms. Surface atom removal typically takes place using elastic collisions when energy from the incident ion is transferred to the surface atom and causes the atom to dislocate from its position in the lattice. This initial collision gives rise to several secondary collisions eventually leading to surface atom removal. The beam size is typically 5 – 20 nm which allows for fabrication of very high aspect ratio structures [122]. However, material redeposition often occurs during milling process and must be kept in mind when during process design [123]. An example of structure etched by FIB etching is shown in figure 2.9.

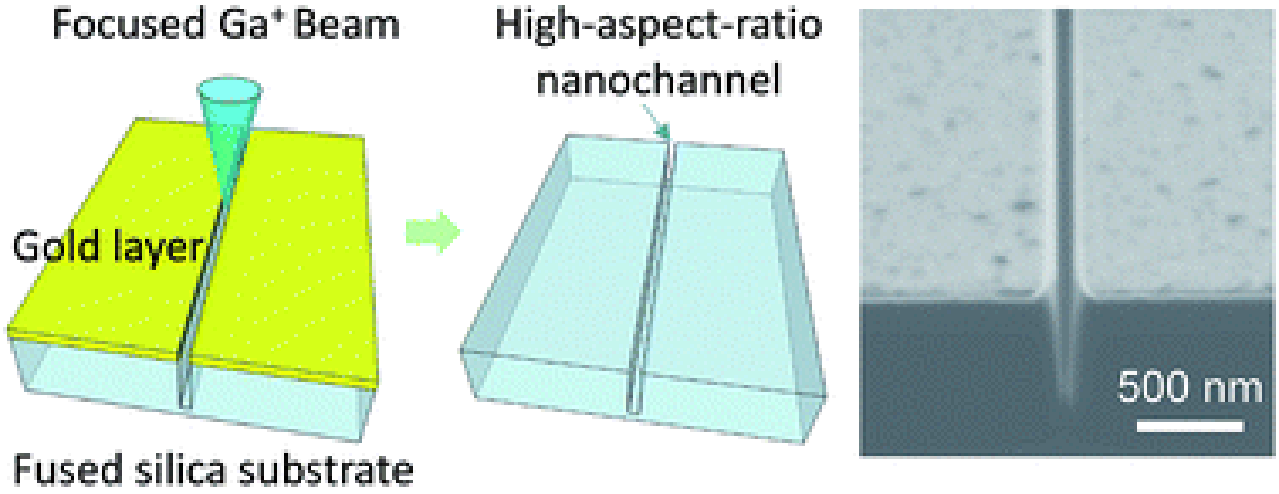


Figure 2.9: FIB milling process for high aspect ratio trenches. Reprinted with permission from [124].

2.3.2. Ion/Electron Beam Induced Deposition (EBID/IBID)

The effect of electron beam induced deposition was first observed in late 1940s by J. H L. Watson [125, 126], who observed that contamination on sample surface after electron microscopy was caused by hydrocarbon vapors from electron microscope pumping system. The vapor was polymerized on the surface by electron beam. Later, this effect was intentionally used to deposit polymer [127] and conducting films [128] onto different surfaces.

Electron and ion beam induced deposition (EBID/IBID) require focused beam (electron or ion) to dissociate gas molecules which are adsorbed onto a sample surface. These dissociated molecules may be volatile or non-volatile compounds. The volatile compounds are removed using the pumping system while the non-volatile compounds deposit onto the surface. As more molecules are dissociated by the electron beam, the thickness of the deposited material increases. By controlling the electron beam dwell time and location of the electron beam, complicated nanostructures can be fabricated. The properties of the deposited material depend on the choice of precursor gas, while the resolution depends on the size of electron beam. When using high energy electrons, patterns as small as 1 nm can be fabricated [129, 130] which is an order of magnitude smaller than those fabricated using electron beam lithography. The pattern size possible by IBID is slightly larger than that by EBID, however, the process is commonly used for mask repair in chip design. Typical beam energy of EBID is between 10 – 20 kV and the process is done in SEM chamber under vacuum. Gaseous precursors are introduced into the chamber using a nozzle injection system in order to maintain high pressure near the surface while having low pressure near the electron beam system [131]. The pressure near the sample surface depends on the distance between sample and the injection nozzle and is relatively constant across the sample. Thus, uniform deposition can be performed across the entire surface by moving the electron beam. Figure 2.10 shows the

schematic diagram of EBID system along with SEM image of high aspect ratio structures fabricated by EBID.

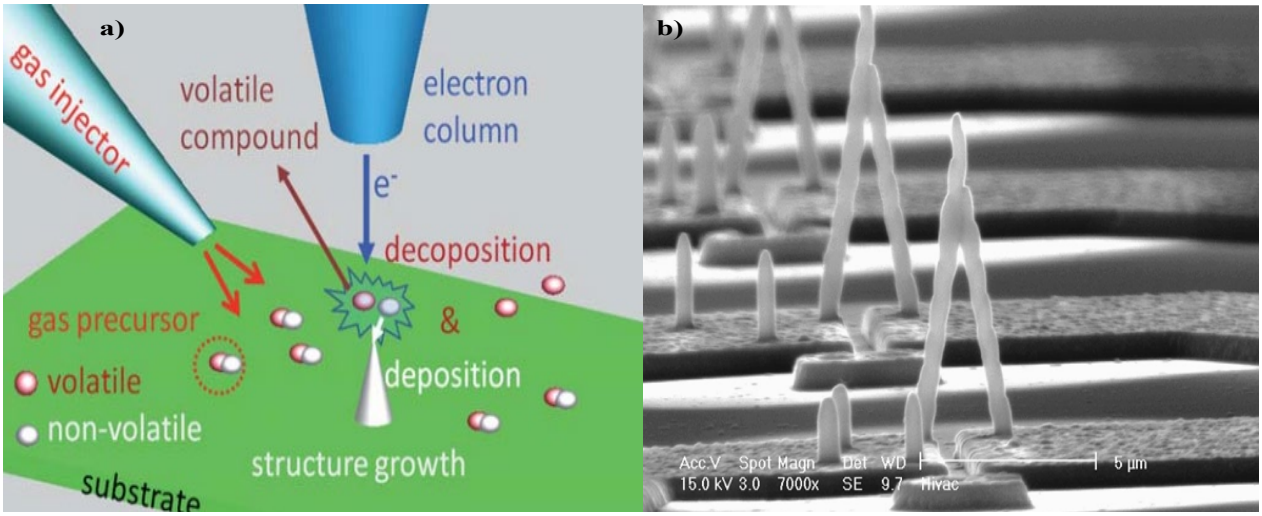


Figure 2.10: a) Schematic illustration of EBID process. b) SEM images of Cobalt structures fabricated by EBID. Reprinted with permission from [132] and [133] respectively.

2.3.3. Carbon Nanotubes

Carbon Nanotubes (CNTs) have long been a topic of interest for AFM tips, given their high aspect ratio, excellent Young's modulus, and good thermal and electrical conductivity among other properties [134]. CNTs may be mounted on an ordinary tip by either direct manipulation [135] or by CVD growth [136]. The simplest method is to manually apply multi-walled CNT (MWNT) to a silicon tip using an adhesion or EBID [137] under a microscope/SEM. However, this method is cumbersome and impractical for mass production. Most CNT tips are made using CVD method to grow CNTs directly on silicon tip using a catalyst on the tip apex [48]. The most important points to consider during CNT growth are its length, orientation, and radius. The CNT tip length can easily be controlled by adjusting growth time [138]. On the other hand, the CNT orientation is difficult to control during growth, though it has been found that application of external electric field can help control the growth orientation [139]. Additionally, FIB irradiation can be used to adjust the CNT

orientation after growth [140, 141]. It was observed that when ion beam pulses were applied to CNTs, their orientation aligned in the direction of irradiation due to irradiation-induced-strain. FIB milling can also be used to shorten CNT length [142].

Though it is generally assumed that higher aspect ratio tips are ideal for AFM imaging, if the aspect ratio is too high, the tips would become brittle. For CNT tips, shorter tips are important for applications on high friction surfaces [143]. As mentioned above, one of the methods to optimize CNT length is by FIB milling [142] or adjusting growth time [138]. Another proposed method is the use of 'nano-knife' where a short CNT attached to a metal tip is used to manually trim the CNT tip [144]. Figure 2.11 shows CNT based AFM tips.

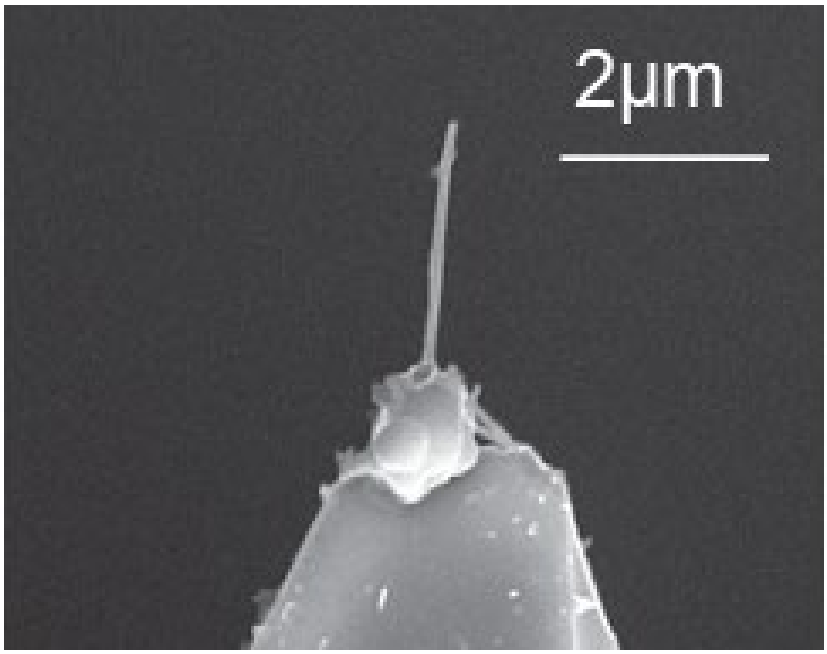


Figure 2.11: High aspect ratio CNT tip. Reprinted with permission from [139].

2.3.4. Oxidation Sharpening

Oxidation sharpening is one of the most common ways to decrease the apex radius of a silicon tip. The process was developed in 1990 by Marcus et. al. [145], and uses oxidation of prefabricated silicon AFM tips to increase the aspect ratio and decrease tip apex. In this method the silicon tip undergoes

thermal oxidation at low temperatures (< 1050 °C) [46]. In this temperature range, the stress between silicon and SiO_2 decreases the rate of oxidation in areas of high curvature (e.g., tip apex). This results in improved aspect-ratio and tip apex, once the thermal oxide layer is removed by HF. Routinely observed tip apex are 5 – 10 nm, though apex of ~1 nm are possible [145]. Figure 2.12 shows silicon tip sharpened by oxidation sharpening.

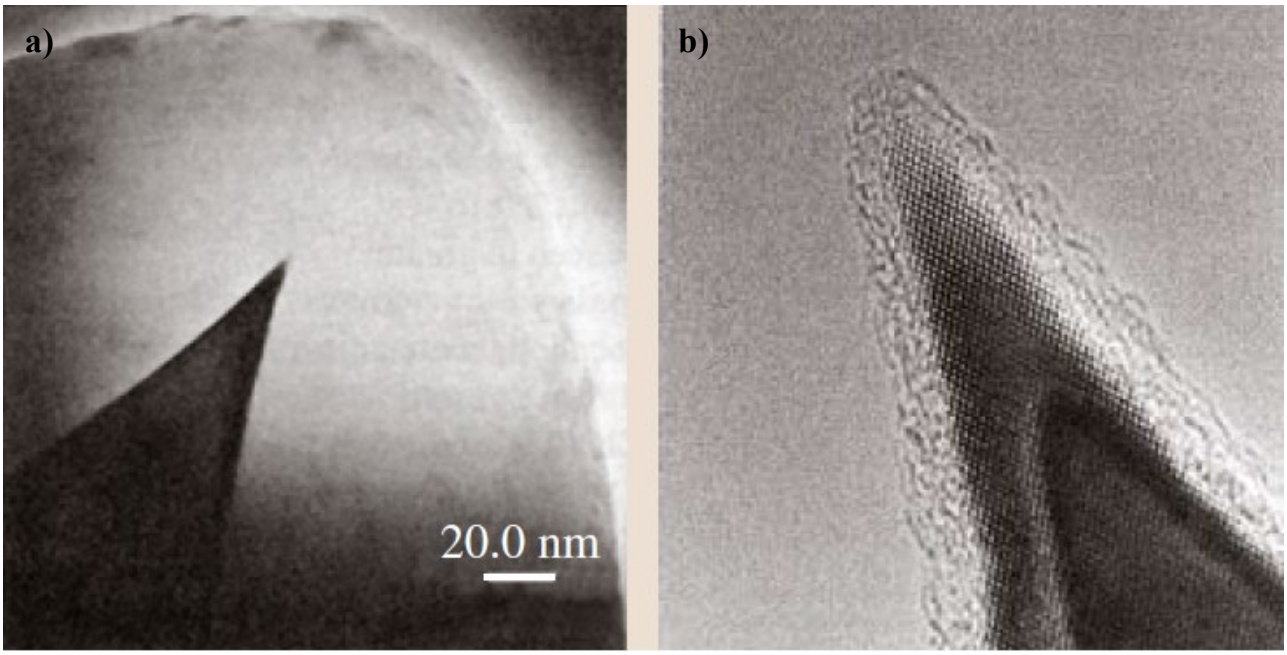


Figure 2.12: a) Oxide sharpened silicon tip with outer oxide visible. b) improved aspect ratio silicon tip with outer oxide removed by HF. Reprinted with permission from [145].

2.4. PROCESSES USED FOR PROBE FABRICATION

As mentioned above, AFM probe has a cantilever with tip attached to one end. Both aspects of the probe have different requirements for achieving good quality results. For the AFM tip, sharp apex, high aspect ratio and wear resistance are important parameters which need to be considered during tip design and fabrication. Sharp apex allows the tip to provide high resolution imaging while high aspect ratio is important to image deep trenches. Wear resistance is crucial because tip is part of

the probe which meets the sample surface and may be worn down by repeated use. Wear resistance is determined by the material used for the tip. Commonly used materials for AFM tips are silicon [146], metals [147], metal-coated-silicon [41], and diamond [89].

For the cantilever, parameters which must be considered during design are resonant frequency, spring constant and surface roughness (especially on backside that reflects laser beam). These parameters are controlled by the cantilever dimensions as well as the material used. For example, spring constant depends on the square of cantilever thickness. Surface roughness must be kept minimum in order to have adequate reflectance of the laser beam from the cantilever. For this purpose, thin metal films may be used to improve reflectance, however, these may affect the spring constant and cantilever resonant frequency. The most popular materials for AFM cantilever are silicon and its nitride (Si_3N_4).

Both tips and cantilever are patterned using lithography (photolithography or electron beam lithography). The cantilever is almost exclusively etched using reactive ion etching (RIE), while the tip may be etched by reactive ion etching, ion milling or wet etching. All these processes will be described in detail below.

2.4.1. Lithography

The term lithography refers to printing or writing on material. For micro and nanoscale devices, lithography can be done by photons (photolithography) or by electrons (electron beam lithography). Photolithography may be further characterized into UV, DUV or EUV depending on the wavelength of the photons. This sections explains the two major classes of lithography.

2.4.1.1. Photolithography

Photolithography is the process of writing on a substrate coated with photoresist, using photons [148]. Light sources lie in the ultraviolet (UV) range (λ = 436 nm, 405 nm, 365 nm), deep ultraviolet

(DUV) (λ = 248 nm, 193 nm) or extreme ultraviolet (EUV) range (13 nm). When photoresist is exposed to photons, it causes chain-scission, cross-linking or other chemical reaction between the polymer chains [149]. The selective illumination of the resist is done using a photomask which has transparent and opaque areas which selectively block light.

Selective illumination may also be done using a laser beam as a light source and a Spatial Light Modulator (SLM) which acts as a programmable mask. This type of lithography is called maskless photolithography since it does not require the use of a physical mask. Instead, the pattern is designed in a Computer Aided Design (CAD) software and transferred to the photolithography system in a format which is readable by it (usually .gds file format) [150]. A typical system for maskless photolithography is shown in figure 2.13. This type of photolithography is commonly used in research laboratories and avoids time consuming and expensive photomask fabrication process and allows for quick redesign of mask file [151].

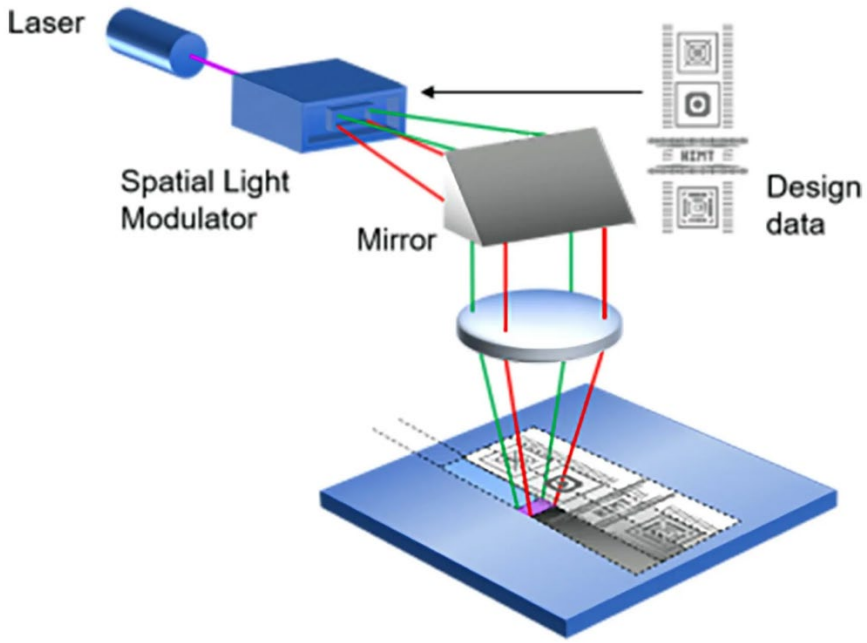


Figure 2.13: : Photolithography process using maskless lithography system. Reprinted with permission from [152].

2.4.1.2. Electron Beam Lithography

When using Electron Beam Lithography (EBL) a user 'writes' on a substrate using electrons [153]. The process is the same as photolithography except that it does not require a mask and the electron-beam resists are different from photoresists. Given that wavelength of electron beam is much smaller than that of photons, EBL can routinely achieve sub-10 nm resolution [154]. The electron beam is focused on sample surface using a series of magnetic lenses, as opposed to optical lenses used in photolithography. Additionally, deflection coils are used to deflect the electron beam from areas where exposure is not required. The entire procedure is done in a high vacuum to avoid electron scattering and to achieve good control of the electron beam.

Most commonly used positive tone resist for EBL are PMMA (poly-methyl methacrylate) [155] and ZEP520 [156], both of which consist of long chain polymers which are broken when exposed to electron beam. On the other hand, HSQ (hydrogen silsesquioxane) [157] is one of the mostly used negative EBL resists which collapses its box-like molecular structure to become oxide-like when exposed to electron beam.

2.4.2. Liftoff

The liftoff process utilizes the ability of easy resist removal, in order to pattern a surface. After lithography , deposition of metals/oxides is carried out using a deposition process having minimal step coverage (e.g., e-beam evaporation) and temperatures lower than ~200 °C [158]. The deposition occurs such that the material is deposited on both the resist and the material surface (only in areas where there is no resist). Next, the resist is removed by a solvent, such as Remover PG, and the deposited material remains only on the exposed areas of the substrate surface.

2.4.3. Etching

Once the substrate has been patterned using lithography, it can undergo selective removal of material using etching process or selective material deposition using liftoff process. In this section we review the etching process. Etching may be isotropic where the etching rate is independent of material's crystallographic direction [159], or anisotropic where the etching rate is heavily dependent on crystallographic direction [160] or is much faster along the vertical direction than lateral direction. Anisotropic etching is usually used for both tip and cantilever fabrication and may be referred to as wet anisotropic etching or dry etching depending on the nature of the etchants. The most widely used dry etching technique is called Reactive Ion Etching (RIE).

2.4.3.1. Reactive Ion Etching

Reactive Ion Etching (RIE) refers to using plasma to obtain reactive species which etch the substrate. Figure 2.14 shows the RIE system and etching of silicon. The RIE system typically uses RF power (13.56 MHz) to generate plasma between two electrodes. When the etching gas is introduced into the system, it is dissociated to produce reactive radicals, monomers and ions which then accelerate towards the sample where they react with the surface [161]. One of the most used systems is the Inductively Coupled Plasma Reactive Ion Etching (ICP-RIE). In this case electric field is generated by inductive coils wrapped around the RIE chamber which allows high density plasma to be formed [162]. Since the bias between the chamber wall and the electrodes is very small, there is negligible erosion of the chamber wall and plasma can be generated at low pressure [163]. Other advantages of ICP-RIE are high etch rate and anisotropy. The sample is biased separately from the plasma generation system and thus the directionality of ion attraction towards the sample can be controlled independently [163].

Since the reactive ions are accelerated towards the sample vertically, the RIE process tends to be very anisotropic. Etching gases are selected such that they have minimum chemical interaction with the mask material, while fast chemical reactions occur at the surface to produce volatile by-products which are removed by the pumping system. For example, SF_6 gas can easily etch silicon while its oxide (SiO_2) has a very low etching rate. CF_4 gas is also used for silicon etching while O_2 gas is used in diamond RIE. In general, most materials can be etched by halogens (fluorine and chlorine being the most popular) [164]. Oxygen gas is used for etching of polymers and other carbon-based materials [165, 166], while argon is used for physical etching of all materials. It should be noted that formation of volatile compounds is necessary for RIE. Metals such as Cu, Ag, Ni etc. which do not produce volatile compounds after reacting with any gas, cannot be etched efficiently using RIE.

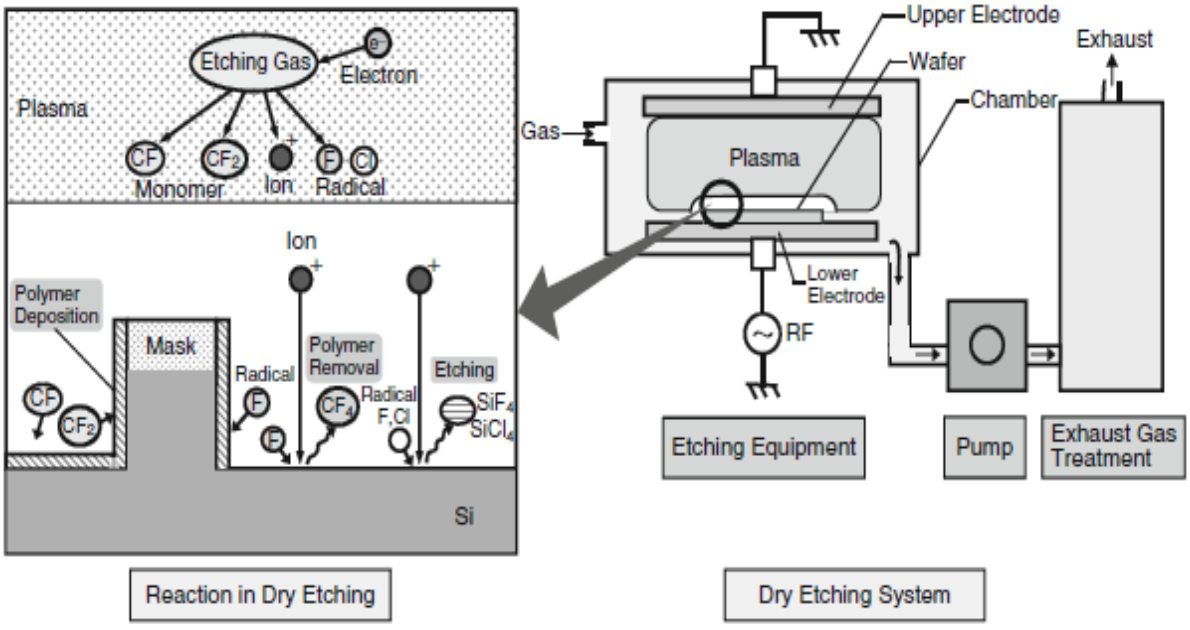


Figure 2.14: Reactive Ion Etching process. Reprinted with permission from [161].

One of the issues that must be addressed in RIE is the deposition of polymers on the surface which form local masks and may inhibit etching of the underlying substrate. However, in some cases (e.g., Figure 2.14) these polymers may further react with the incoming ions and radicals and desorb from the substrate surface after forming volatile compounds.

As mentioned above, diamond is routinely etched using oxygen plasma which produces volatile CO or CO_2 after reacting with carbon atoms [167]. Hydrogen gas can also be used for diamond etching which produces volatile C_xH_x compounds. However, diamond etching rate is much lower in hydrogen plasma than in oxygen plasma [168].

Though oxygen plasma can etch diamond faster than hydrogen plasma, it results in high surface roughness likely due to micro masking effects caused by mask residue sputtered on the diamond surface [169] or due to variation in oxidation rates of different crystallographic orientation of the diamond surface [170]. Roughness is especially pronounced when etching deep into the diamond film. These effects can be controlled by introducing argon into the oxygen plasma [171]. Argon causes physical etching of diamond atoms which then react with O_2 to form CO or CO_2 hence reducing possible preferential etching by O_2 plasma and creating smoother surface [172]. However, the concertation of argon gas must be carefully controlled. It has also been found that Ar/Cl_2 plasma creates very smooth etched diamond surfaces, however the etch rate is very low [173]. Other gases that have been used to reduce surface roughness by etching in oxygen plasma are CF_4 [174], Cl_2 [173], SF_6 [175], CHF_3 [176], $SiCl_4$ [176] etc. However, when selecting additive gases to oxygen or hydrogen plasma, the selectivity of the diamond with the masking material must be considered. For example, while SF_6 and CF_4 may be able to significantly reduce micro-masking, high concentration of these gases can etch away the masking material (e.g., Si) and reduce the aspect ratio of the diamond structures.

The selection of mask material for diamond RIE is another parameter which must be considered during the etching process. The mask material must have high selectivity with diamond in the etching recipe selected [177].

For obtaining high aspect ratio structures in silicon, 'Bosch Process' also called 'deep RIE' is commonly used. Herein, high aspect ratio features are obtained using alternate etching and passivation cycles. SF_6 is used to etch the Si substrate, then a passivation gas (C_4F_8, deposits C-F polymer) passivates the surface and sidewalls of the etched structure. When SF_6 is introduced again, the high energy ions remove passivation layer from the bottom of trench and SF_6 can then etch the exposed silicon. The Bosch process and resulting sidewalls are shown in Figure 2.15. The etching and passivation cycles are kept separate in order to avoid interaction between the two. Due to the alternate etching and passivation cycles, the sidewalls of the high aspect ratio features obtained by Bosch process are rough [178]. This can be avoided using a non-switching pseudo Bosch process [179].

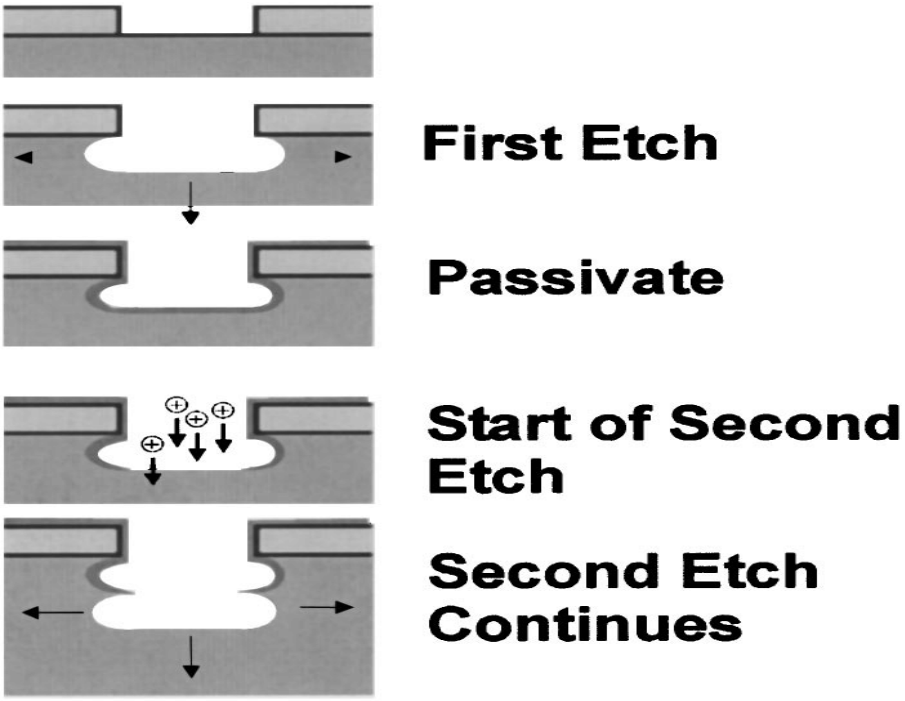


Figure 2.15: Bosch Process. Reprinted with permission from [178].

2.4.3.2. Ion Milling

Another type of dry etching is called ion milling. As the name states, this process etches a material using high energy ions [180]. The process is purely physical etching with no chemical interaction between the high energy ions and substrate, which leads to a low etching rate and low selectivity between the material to etch and the mask. Given the inert nature of Argon, it is the most commonly used gas for ion milling.

Depending on the ion energy, different processes may take place on the substrate surface. For very low energy ions (< 10 eV), ions are absorbed into the substrate surface and cause significant damage to it, which is confined to few atomic layers beneath the surface. Ions with energy greater than 10 keV are implanted deep into the substrate. Ion milling process occurs when the energy of the ions is between 10 eV and 5 keV [180]. Figure 2.16 shows a typical ion milling system.

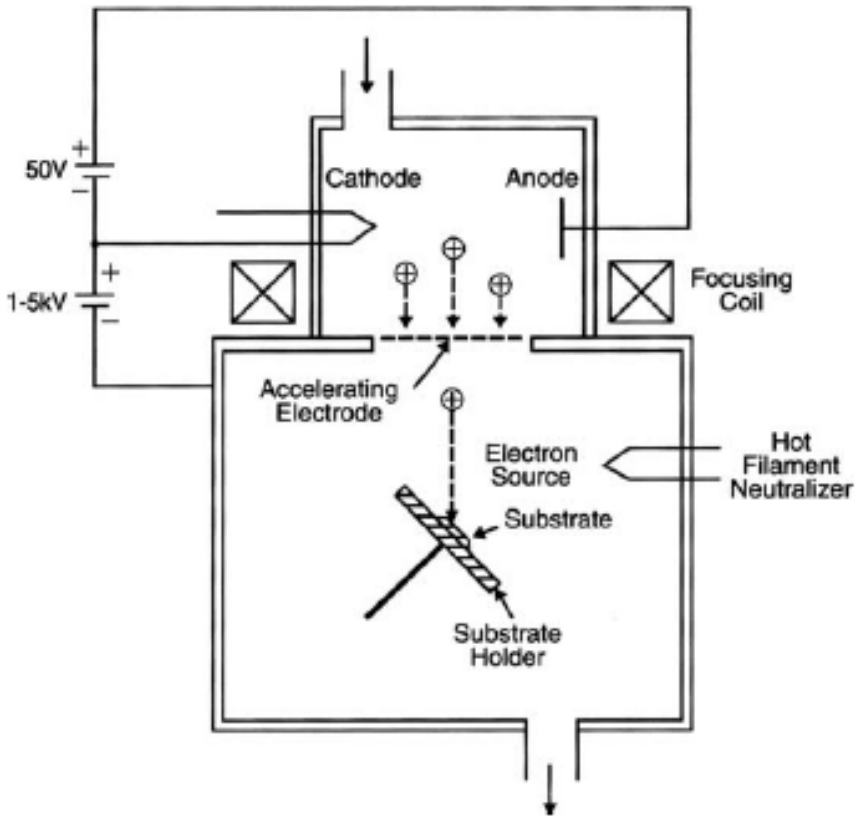


Figure 2.16: Ion Beam Milling system. Reprinted with permission from [180].

Ion beam milling of diamond is often done by adding very small concentration of oxygen gas to milling system [181]. This is called reactive ion beam milling and can be used to increase selectivity. However, this is not the same as RIE because the by-product of the etching is not necessarily volatile [180].

The two biggest issues with ion milling are faceting and redeposition. Faceting is the phenomenon where the corners of the mask are etched faster, making the overall profile very tapered as the process continues. Faceting is a big issue when using polymer resists as mask but may be compensated by using a hard mask [182]. Additionally, given the non-volatile nature of the etched species, ion milling faces the issues of redeposition of etched particles near the pattern surface.

This can be avoided by rotating the sample during milling. Rotation also provides uniform etch rate across the surface [183].

2.4.3.3. Wet Etching

Wet etching is the process of removing materials from a surface using liquid chemicals instead of gases as used in RIE [184]. Wet etching can provide very high selectivity between etched and mask material.

Wet etching may be isotropic or anisotropic depending on whether the rate limiting process during etching is diffusion or chemical kinetics. If the reaction rate of the surface is faster than the transport of reactive species to the surface, then the reaction rate is controlled by diffusion process [185]. If all surface atoms are etched at the same rate, then the reaction is isotropic [186]. On the other hand if the etching rate of atoms on surface have a large difference this implies that the etching rate is controlled by chemical kinetics and the reaction is anisotropic [187]. In this case the surface orientation plays a big role in the reaction rate as well as the evolution of different etching planes [188]. Silicon may be etched both isotropically and anisotropically, depending on the nature of the etchant. Diamond, on the other hand, is chemically inert and cannot be etched by wet etching.

One of the biggest advantages of wet etching of silicon is anisotropic etching when etched in alkaline solutions like Potassium Hydroxide (KOH) [189], Ethylene Diamine Pyrocatechol (EDP) [190] and Tetra-methylammonium Hydroxide (TMAH) [191]. While other etchants such as NaOH [192] and LiOH [189] have the ability to provide anisotropic silicon etch, they do not have sufficient selectivity with the commonly used silicon masks and hence are rarely used. The etching rates of different planes depend on processing conditions such as etchant concentration [193], temperature [193], addition of surfactants [194] etc. Doping level of the silicon wafer also plays a role in overall etch profile [195]. Amongst these methods surfactant addition has been found to be excellent for obtaining smooth

surface, reducing mask undercutting as well as obtaining desired profile [196] when small amount (< 2%) of surfactant is added to the silicon etchant.

Surfactants are organic compounds having a hydrophilic group attached to one end (head) of a hydrophobic group (tail). While the tails of many surfactants are made of hydrocarbon chains, they differ in the chemical composition of their heads. There are two major types of surfactants that can be used in silicon etching. These are i) non-ionic (having uncharged hydrophilic compound) , and ii) ionic (having charged hydrophilic compound). Ionic surfactants are further classified into anionic and cationic surfactants having negative and positively charged hydrophilic groups, respectively. It has been found that anionic surfactants provide the highest etching rate of silicon surface, however, non-ionic surfactants can provide much smoother silicon surfaces especially when etching in TMAH [196]. While the preceding statement helps narrow down the class of surfactants, it is important to note the chemical composition of the surfactant as well as other processing parameters such as surfactant concentration and temperature affect the final profile of the etched structure. For example, a non-ionic surfactant, NCW601-A (30% poly-oxyethylene-alkyl-phenyl-ether) was found to change the etching rate ratio of (110) and (100) Si and decreasing the etching rate of other planes so that (100) plane was not the local minimum etching rate plane [197]. On the other hand, addition of Triton X-100, another non-ionic surfactant, reduces the etching rate of certain planes compared to (100) plane [198]. These changes in anisotropy due to surfactant addition results in change in the final profile achieved.

The reason for the anisotropic etching behavior of silicon is attributed to the complex interplay between the number and spatial arrangement of free bonds on different crystallographic planes [199]. . The planes with the strongest bonds amongst atoms are the most difficult to etch and hence have the slowest etching rate [185]. In general it may be summarized that (111) is the slowest etching plane

in all above mentioned etchants [199, 200]. Typical etch profiles for Si(100) and Si(111) wafer are shown in figure 2.17, while figure 2.18 shows the effects of surfactant modified etching. The anisotropic etching of silicon etching makes it very appealing for Micro Electro Mechanical Systems (MEMS) because of its low cost fabrication and its ability to provide smooth surfaces without changes/damage to the underlying substrate [201].

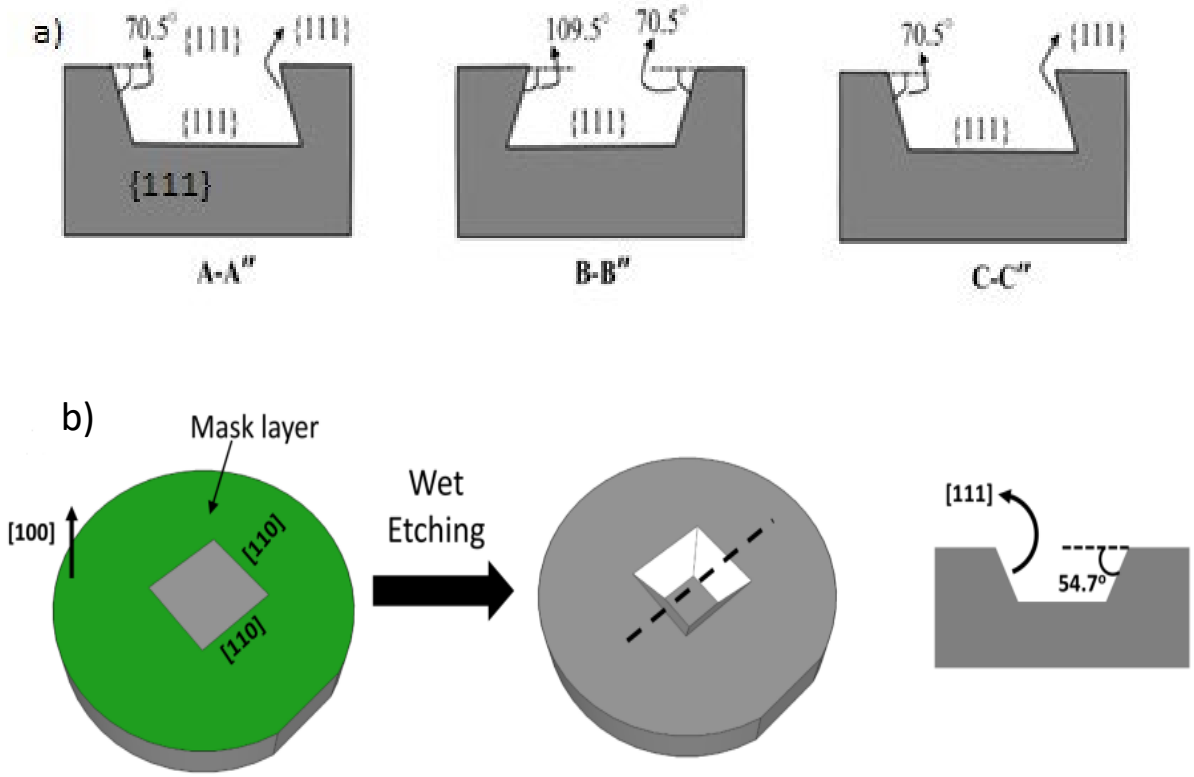


Figure 2.17: a) Si(111) Etch Profile. Reprinted with permission from [1], b) Si(100) etch profile. Reprinted with permission from [202].

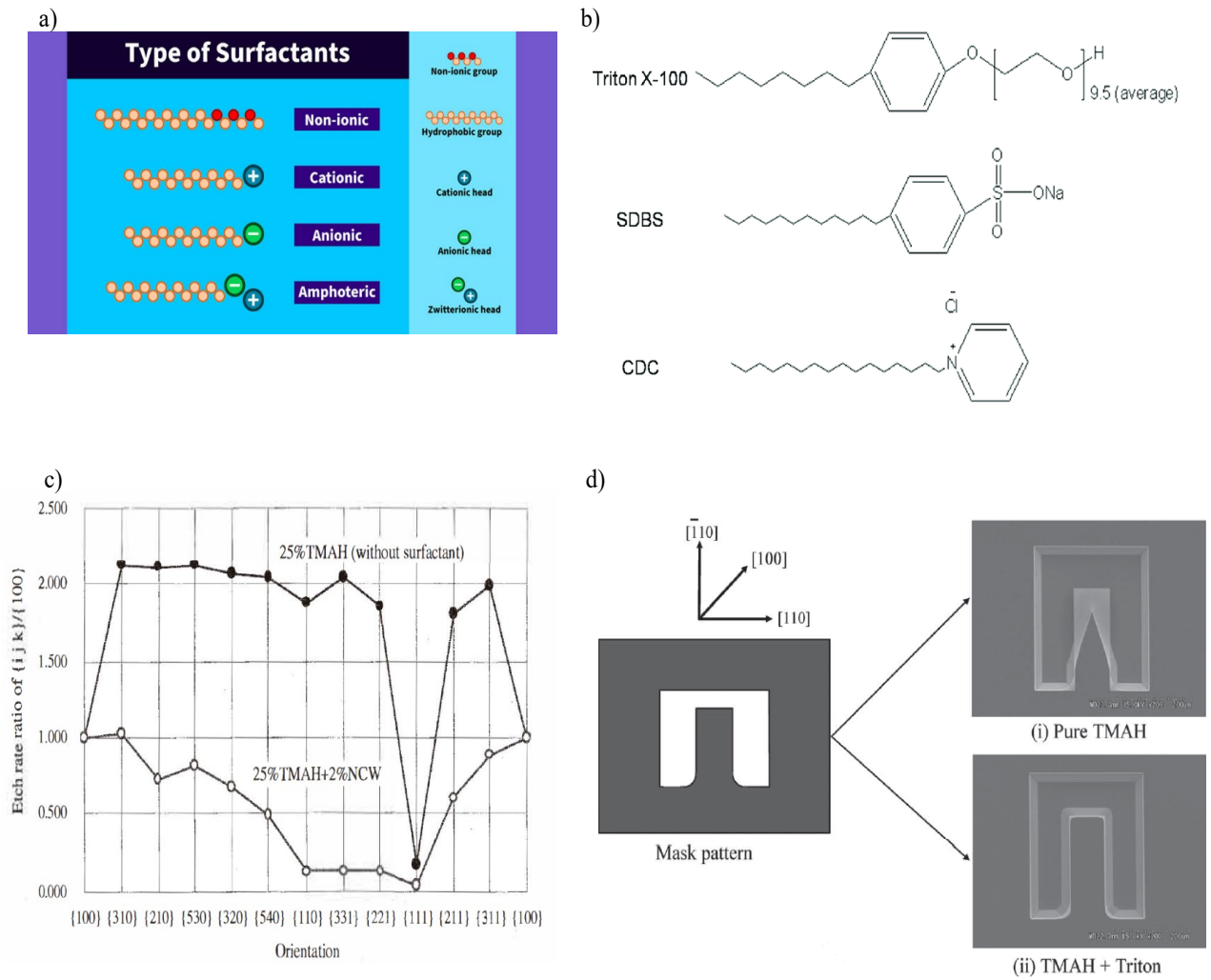


Figure 2.18: a) schematic of various types of surfactants, b) molecular structure of non-ionic (Triton X-100), anionic (sodium dodecyl benzene sulfonate, SDBS) and cationic (1-hexadecylpyridinium chloride, CDC) surfactant. c) etch rate ratios for various silicon orientations with and without a non-ionic surfactant added in TMAH. d) effect of surfactant added TMAH etching for patterned silicon. Reprinted with permission from [197, 203, 204].

During anisotropic wet etching of silicon, Si_3N_4 and SiO_2 are commonly used as masks because they have very high selectivity in alkaline silicon etchants (KOH, TMAH and EDP). Another interesting phenomenon in anisotropic wet silicon etching is that for concave structures (e.g. trench), the sidewall planes are dominated by the slowest etching plane [205], while for convex structures (e.g. tips, islands) the fastest etching planes appear on the sidewall [206]. Mask alignment

with the surface orientation also plays a huge role in the etching process and the resulting shape of the micro-structure. One important factor during processing is determining the etch stop. Most often the etching is stopped by removing the sample from the etchant according to the etch rate measured earlier. Other more sophisticated approaches may also be used such as controlling the local doping concentration since heavily p-doped silicon etches much slower [207], or by passivating the silicon using Si_3N_4 or SiO_2 etch stops.

While the anisotropic wet silicon etching appears simplistic there are several issues that occur during the etching process. These are summarized in figure 2.19. One of the most encountered issues is micro-masking which refers to several microscopic impurities on the surface of the wafer that act as mask and hinder silicon etching. These masks maybe made of polymer residue on the surface, reaction byproduct, mask residue or even hydrogen bubbles formed during the alkaline etching of silicon [208]. While the masks themselves may be micron-sized, they can cause pyramids/hillocks to form on the silicon surface (particularly (100) and (110)) if the etching time is long enough [188].

While micro-masking is not a significant issue for (111) oriented silicon wafer, pit nucleation is. Si(111) is etched by removing atoms from steps formed between two (111) terraces. As the atoms are etched from the steps, they are said to move, and the terrace may be etched away. In case there are no steps, the alkaline etchants etch the stable surface atoms and form pits on the surface. The rate of pit formation may be enhanced by lattice defects in the wafer which behave like pit nucleation center. If the rate of pit nucleation is small, the step propagation dominates the etch profile and the resulting etched surface is smooth. However, for large rate of pit nucleation the surface is rough and appears to have several steps.

Another commonly encountered issue occurs due to diffusion of etchant species to and from the reaction site. As mentioned before, anisotropic etching occurs due to different etching rates of silicon planes. This means that local depletion regions or temperature gradients may be formed in areas of high etch rate. This is referred to as etchant inhomogeneity and is more pronounced in high etch rate areas such as steps. In Si(111) these inhomogeneity can cause step bunching [209], while in Si(110) they cause zigzag structures [210].

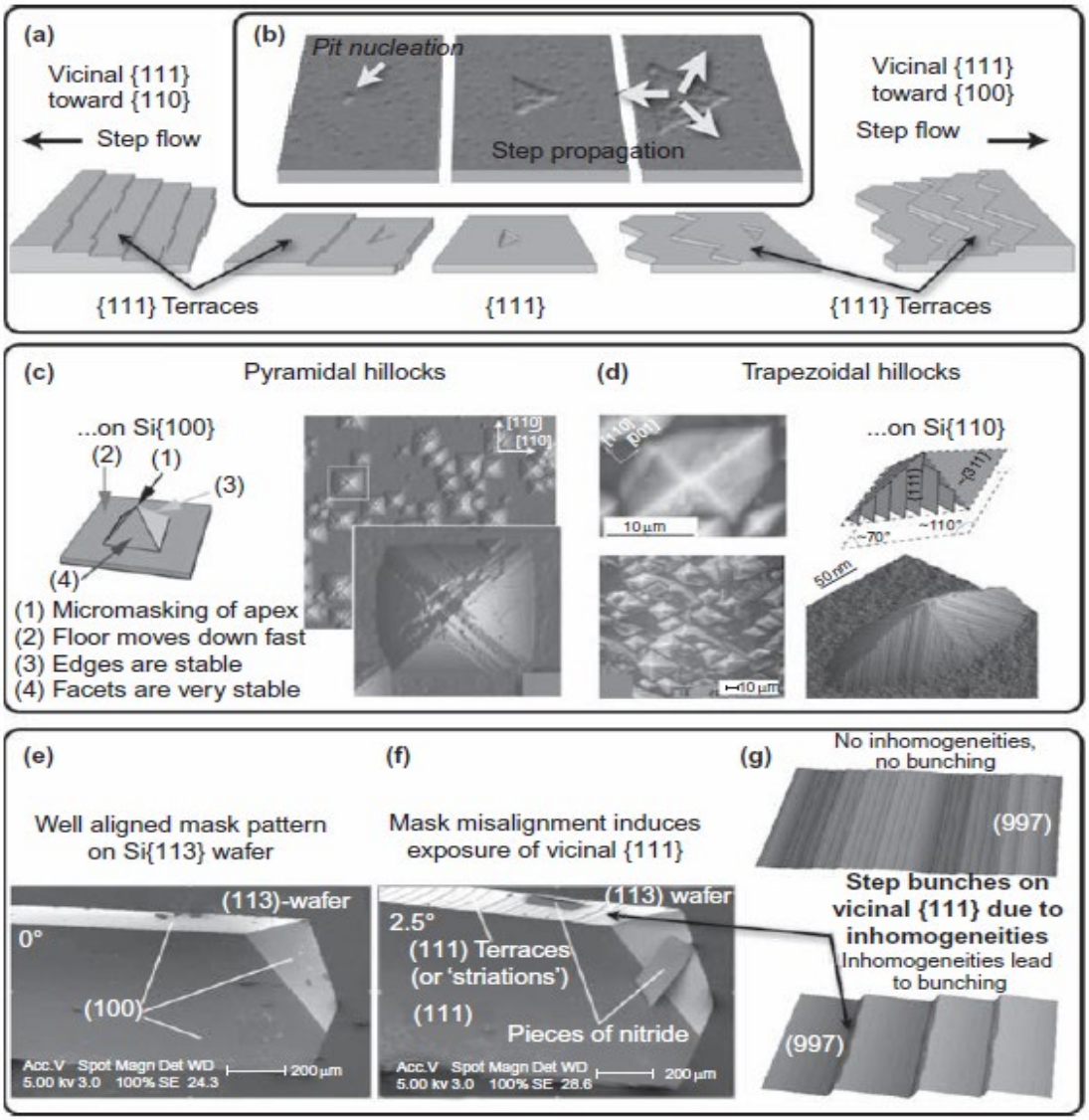


Figure 2.19: : (a) Pit Nucleation, (b) Step flow, (c-d) Hillocks, (e-g) Step Bunching. Reprinted with permission from [185].

*2.4.4. **Deposition***

Deposition is the process of adding material, as opposed to etching which involves material removal. There are two main classes of deposition: i) Physical Vapor Deposition (PVD) and ii) Chemical Vapor Deposition (CVD). As the names suggest, physical vapor deposition involves purely physical transfer of material from target (e.g., crucible) to source (sample surface) and is almost always line of sight deposition. On the other hand, chemical vapor deposition involves chemical reactions at the sample surface which leads to deposition.

Though there are several types of both physical and chemical vapor deposition, this section only explains those commonly used in our work.

2.4.4.1. Physical Vapor Deposition

Physical vapor deposition refers to material deposition with no chemical reaction between substrate and the deposited material. Two major types of PVD deposition techniques are: i) evaporation and ii) sputtering.

Evaporation is the method of depositing material on substrate by converting it from solid to vapor phase. The vapors then travel to and condense onto the substrate forming a thin film. Conversion from solid to vapor phase (sublimation) can be done by either resistive heating of the crucible containing the source material, or by directly heating the source material by electron beam. Though evaporation provides very high-quality films, deposition is usually limited to metals and oxides. Additionally, due to the different sublimation points of materials, it is difficult to deposit compounds using evaporation.

Sputtering process is similar to ion milling, however, in sputtering the target material is bombarded instead of the substrate. The atoms removed from the target material then impinge onto the

substrate, forming a film. One of the main advantages of sputtering over evaporation is the better step coverage and ability to deposit compounds, ceramics, alloys, and polymers.

2.4.4.3. Chemical vapor deposition

As the name suggests, Chemical Vapor Deposition (CVD) involves chemical reactions on a substrate surface which leads to film growth. In CVD system, a precursor gas (diluted with inert carries gas) is pumped into the reaction chamber, where it reacts at the substrate surface to deposit a film. CVD systems provide better step coverage than most PVD systems and allows precise control over film parameters such as grain size, stoichiometry etc.

Detailed deposition process in CVD system is shown in figure 2.20. First, reactant and carrier gases are transported from inlet to the deposition zone (1). Next, homogenous gas-phase reactions lead to formation of film precursors and by-products (2). While the by-products are pumped away, the precursor gas is transported to the substrate surface (3) where it undergoes adsorption and reaction (4). On the substrate surface the molecules undergo diffusion to the growth sites (5), where they undergo surface reactions (6) to form a continuous film. During the surface chemical reaction, by-products are formed which desorb from the surface (7) and are removed from the reactor (8).

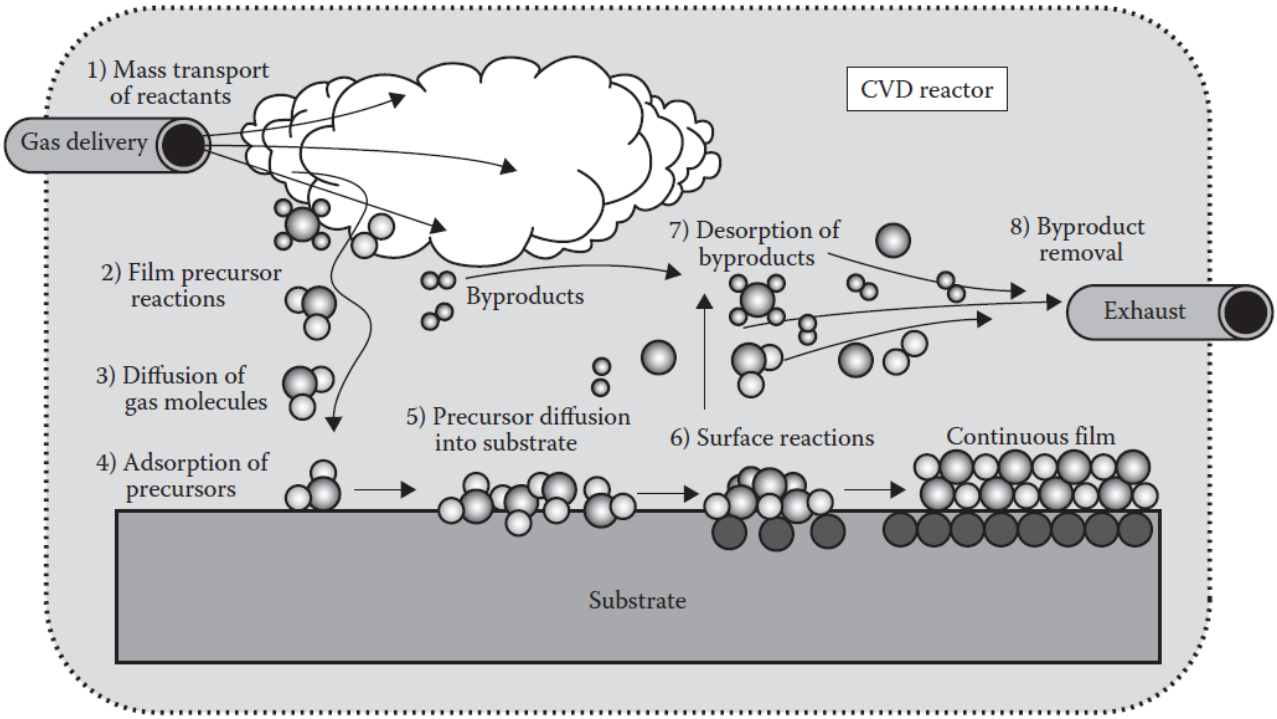


Figure 2.20: Schematic Illustration of CVD deposition process. Reprinted with permission from [211].

In a typical CVD system, a temperature gradient exists such that gaseous precursors are formed at high temperatures, and film formation occurs at slightly cooler substrate surface. The process can also be performed at lower temperatures, however, the energy required for precursor formation would then be provided by other sources such as RF plasma. In this case the process is referred to as Plasma Enhanced CVD (PECVD) [211].

Other variants of CVD system also exist. One of these is Atmospheric Pressure CVD (APCVD) where deposition occurs at atmospheric pressure or slightly lower pressure (100 – 10 kPa).

On the other hand, there is the Low-Pressure CVD (LPCVD) system where deposition takes place at very low pressure (< 10 Pa) with very good film quality. LPCVD results in excellent film uniformity and step coverage.

CHAPTER 3: HIGH ASPECT RATIO DIAMOND TIP

The main body of Chapter 3 is reprinted with permission from Ref. [212]

Nasir, Farheen, Aixi Pan, and Bo Cui. "Fabrication of high aspect ratio diamond tip using reactive ion etching." Diamond and Related Materials 152 (2025): 111950.

3.1. INTRODUCTION

As mentioned in chapter 1, AFM utilizes interaction force between tip and sample surface to create a topographical map of the surface [2]. AFM tips are commonly fabricated from silicon; however, these tips often experience wear after several uses [47, 213] which can lead to distorted results [214]. To combat this issue, several alternative tip materials have been explored. Tips can be fabricated by coating wear-resistant materials on a silicon tip [215] or by fabricating high aspect ratio tips fully made of wear-resistant material [147]. Enhanced wear-resistance and conductivity can be achieved by using metals, such as tungsten [216] and platinum [75]; alloys, such as Pt-Ir [217], carbon nanotubes [218] or diamond [53]. Diamond doped with phosphorous [219] and boron [89] can be used to provide conductivity as well as good wear resistance.

The fabrication process of diamond AFM tips is difficult, because, unlike silicon, diamond cannot be etched by wet chemistry. Commercially available diamond tips are typically fabricated using focused ion beam (FIB) [220, 221], to create sharp tips that are then attached to a silicon cantilever. The serial nature of this process results in longer fabrication times, increasing the cost. Additionally, the tips are made on several microns thick diamond substrate – which adds to the cost – or on diamond thin films deposited on silicon substrates – which do not produce high aspect ratio tips. Other methods include diamond growth on pre-fabricated silicon tip by chemical vapor deposition [111], and Reactive Ion Etching (RIE) [110, 118, 222].

Reactive Ion Etching of diamond is done in oxygen [223] or hydrogen plasma [224]. The etching rate of diamond is slower in hydrogen plasma [167], and since hydrogen gas is considered dangerous, oxygen plasma is usually preferred. When etching is done in pure oxygen plasma, the resulting diamond surface is often rough [225] due to micromasking [226]. However, if small amounts of certain gases are added to the oxygen plasma, surface roughness can be decreased [227]. Depending on the type and concentration of the additive gas, the etch rate and slope of the features can also be controlled. For example, Leech et. al. [225] compared the etching rate and surface morphology of diamond film etched in pure O_2, O_2 + Ar, O_2 + CF_4 and pure Argon plasma. The total gas flow was maintained at 45 sccm. They found that physical sputtering (etching in Ar plasma) resulted in very slow etching. The addition of Ar to O_2 plasma provided a smoother surface compared to etching done in pure O_2 plasma, however, the etching rate of O_2 + Ar plasma was lower. Additionally, they noted that high concentrations of CF_4 (44 sccm) compared to O_2 (1 sccm) provided high etching rate along with smooth surface. On the other hand, Marie et. al. [228] used O_2 + Ar plasma to etch single crystal diamond samples. They noted that the surface roughness becomes a significant problem when etching deep structures. Adding a cyclic cleaning step, using Ar/Cl_2, after diamond etching, allowed them to achieve etching depth of up to 10 μm with smooth surface. In reference [226], Zheng et. al. used several combinations of additive gases in oxygen plasma and found that the smoothest diamond surface was obtained using O_2/CHF_3 plasma. In another work [118] authors fabricated diamond AFM tip using two step RIE process. They used pure O_2 plasma to etch diamond film with Spin-on-Glass (SOG) as a mask. Next, they added a small amount of CF_4 to the oxygen plasma which caused the shrinkage of SOG mask resulting in a sharp tip. They obtained an aspect ratio of 3 and an apex of less than 50 nm. However, due to initial etching in pure O_2 plasma and the consequent micromasking, the surface was very rough even after etching in O_2/CF_4

plasma. In reference [229] Hasan et. al. studied the effects of RIE parameters for diamond tip fabrication in O_2/CHF_3 plasma. They noted that etching rate and slope of the etched diamond structure depends on the ICP and RF power. Higher ICP and RF power provided fast etching and larger slope of the diamond tips. However, the authors noted that at high RF power (250 W), the etching rate of the Hydrogen silsesquioxane (HSQ) mask became much higher than that of diamond, leading to shorter tips. Similar effects were observed with increased pressure. This work emphasizes the importance of mask selection for diamond etching.

The selectivity between the mask and diamond must be suitable to fabricate the required tip dimension. Etching is considered complete when the diamond forms a sharp apex, causing the mask to fall off, which in turn causes the diamond tip to become slightly blunt. This is similar to the process of wet anisotropic etching of silicon in alkaline solution [230]; however, unlike silicon, once diamond RIE is complete, the tip cannot be further sharpened.

It must be noted that along with the etching parameters (gas flow, RF/ICP power, pressure, temperature), the quality of the diamond film and the equipment used for etching also affect the etching results. In reference [110], Uetsuka et. al. etched three types of diamond film in O_2/CF_4 plasma. They found that free standing boron doped polycrystalline diamond films had higher surface roughness than single crystal boron doped diamond, due to formation of nano-whiskers. The authors noted that nano-whiskers form along grain boundaries and on certain crystal orientations, and can be prevented by optimizing the bias power. Whiskers were also noticed by researchers in reference [222] when ultra nanocrystalline diamond (UNCD) was etched in O_2/SF_6 plasma. In reference [231] Toros et. al. provided a catalog of diamond etching recipes and compared several etching parameters.

Commercially available diamond AFM probes are more expensive than their silicon counterparts. This is in part due to the complexity of the tip fabrication process [90] as well as the cost of diamond synthesis. To compete with high aspect ratio silicon tips, the diamond tip must be at least ~10 micrometer tall which adds to the cost of diamond AFM probe. However, as mentioned above, the purpose of diamond tip is to improve the wear resistance of AFM tip. This means that only the tip/apex part needs to be made of diamond. In this work we design a process to fabricate AFM tips with diamond apex and silicon base. We use RIE with shrinking mask, to achieve sharp diamond tips; followed by dry etching of silicon to obtain high aspect ratio structures. Our process would lower the cost for high aspect ratio diamond tip fabrication, since the required diamond film thickness is much lower and we use polycrystalline diamond.

3.2. EXPERIMENT

A 700 nm diamond film is deposited on (100)-oriented silicon wafer using chemical vapor deposition (CVD). The silicon wafer first undergoes nucleation in diamond solution to provide growth sites for CVD diamond. The sample is then transferred to a CVD chamber operating at a frequency of 2.45 GHz. During deposition, the chamber is maintained at a pressure of 2 – 3 kPa and a temperature of approximately 750 °C (1023.15 K). Hydrogen gas at a flow rate of 300 sccm, with 6–8% methane, is introduced into the chamber. During the growth process, methane acts as a carbon source, while the hydrogen is responsible for preferential removal of sp^2 bonded carbon (e.g. graphite) over sp^3 bonded carbon (diamond), as well as creating adsorption sites on the surface for methyl adsorption [232]. Surface analysis using scanning electron microscopy (SEM) imaging (Figure 3.1), reveals that the average grain size is less than 200 nm.

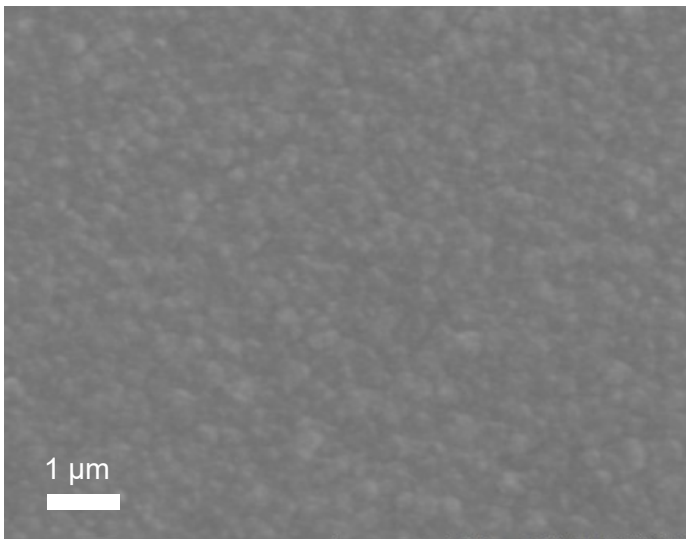


Figure 3.1:SEM image of diamond film surface.

The CVD diamond film is then coated with ZEP520A resist, followed by Electron Beam Lithography (EBL) using JEOL JBX-6300FS Electron Beam Lithography System. Circular patterns ranging from 400 to 900 nm are transferred to a hard mask by liftoff. Mask deposition is performed by electron beam evaporation using Intlvac Nanochrome II e-beam evaporation system. Next, Reactive Ion Etching of diamond and silicon is performed in dedicated Oxford Instruments ICP380 systems. Characterization of the fabricated AFM tips is done by JEOL Scanning Electron Microscope (JSM-7200F). The process flow for fabricating diamond tip with a silicon base is illustrated in Figure 3.2.

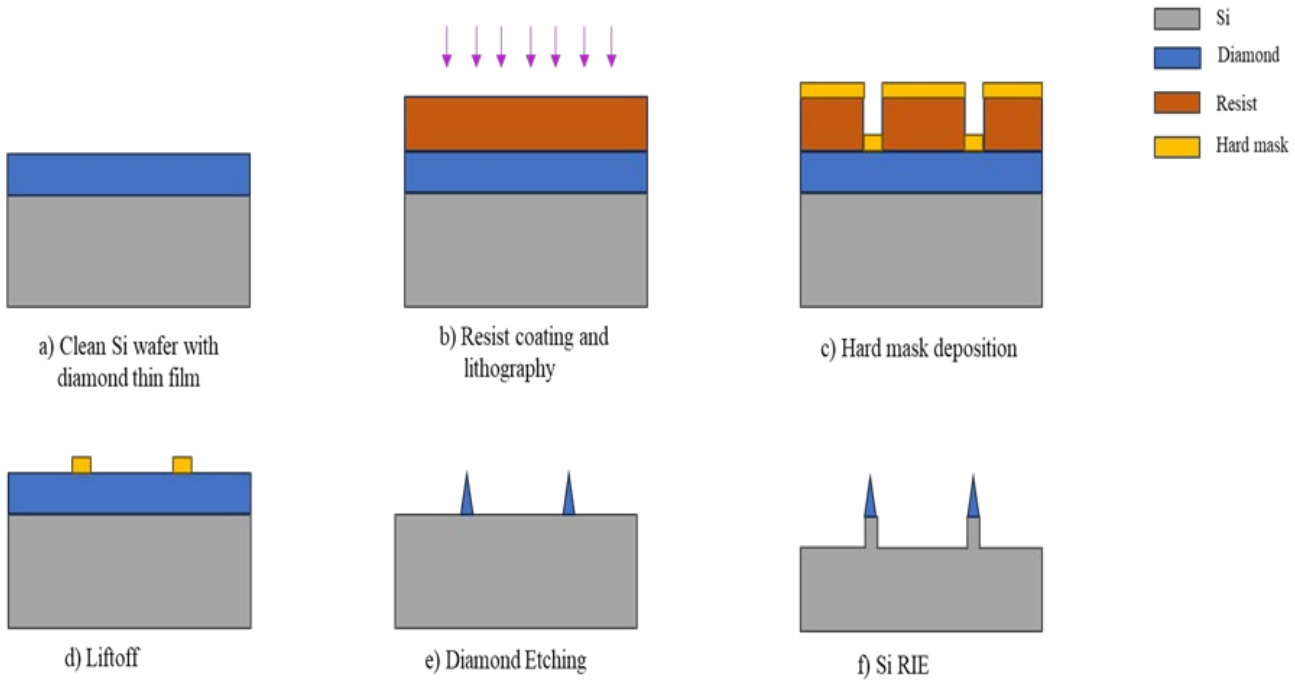


Figure 3.2: Process flow for diamond tip with silicon base.

Oxygen is selected as the primary etchant for diamond during RIE process. The choice of secondary gas lies between Ar, CF_4, SF_6 and CHF_3. As mentioned above, our RIE process requires the mask to shrink laterally, which is difficult to obtain using O_2/Ar plasma [177]. SF_6 is also ruled out as a secondary gas due to risk of increasing surface roughness of the underlying silicon substrate when using O_2/SF_6 plasma [233]. Due to unavailability of CF_4 gas in our RIE system, diamond etching is done in O_2/CHF_3 plasma.

3.3. RESULTS AND DISCUSSION

3.3.1. Mask Selection

Several mask materials are tested in O_2/CHF_3 plasma (O_2: 50 sccm, CHF_3: 5 sccm, RF: 100W, ICP: 1000W, 10mTorr). The tested masks are Cr_2O_3, Cr, SiO_2, Al_2O_3 and Al. SiO_2 was deposited using Plasma Enhanced Chemical Vapor Deposition (PECVD), while all other materials were

deposited using electron beam evaporation. The material thicknesses range from 100 to 500 nm. Amongst them SiO_2, Al_2O_3 and Al provide high selectivity with diamond film. However, the rate of mask-shrinkage required for our RIE process is best achieved by Al_2O_3 mask which is consequently chosen as the mask for diamond RIE. Figure 3.3 illustrates the effects of using Al and Al_2O_3 and Al hard masks for diamond RIE. The slope angle of the diamond cone, with respect to the surface normal, was measured at 25° – for the Al_2O_3 mask – and 19° – for the Al mask – respectively. Both masks experience lateral etching; however, the mask shrinkage rate is higher for Al_2O_3 (14.5 nm/min) than for Al (7.7 nm/min). This difference in shrinkage resulted in a sharper apex for the Al_2O_3 mask (53 nm) than for the Al mask (425 nm), given the same etching time. In both cases, the apex of the cone-shaped structures consists of the remaining mask material (Al_2O_3 or Al).

For our recipe, Al_2O_3 etching occurs in fluorine plasma (CHF_3) [234] with oxygen playing a supplemental role [235]. As shown in Figure 3.3a, residual Al_2O_3 remains atop the cone-shaped structure. This phenomenon has been explained by researchers in reference [234], who suggested that during Al_2O_3 etching in CHF_3 plasma, a fluorocarbon polymer forms on the Al_2O_3 surface. This polymer reduces the vertical etching rate of Al_2O_3 while leaving the lateral etching rate unchanged. This gives Al_2O_3 a unique advantage to act as a shrinking mask for diamond etching using O_2/CHF_3 plasma. On the other hand, the etching mechanism for Al in O_2/CHF_3 plasma is complicated. Authors in reference [236] found reduction of Al etching rate due to formation of AlF_3 on pillar sidewalls when exposed to CHF_3 plasma. In reference [237], researchers found that Al_2O_3 is grown on top of Al surface when exposed to oxygen plasma. The combined effect of O_2/CHF_3 plasma requires further study and is beyond the scope of this work.

Another important factor in etching behavior is the quality of the deposited film [238].In our study, the poor density and structural quality of the as-evaporated Al_2O_3 film, compared to polycrystalline Al, contributed to the favorable etching outcomes.

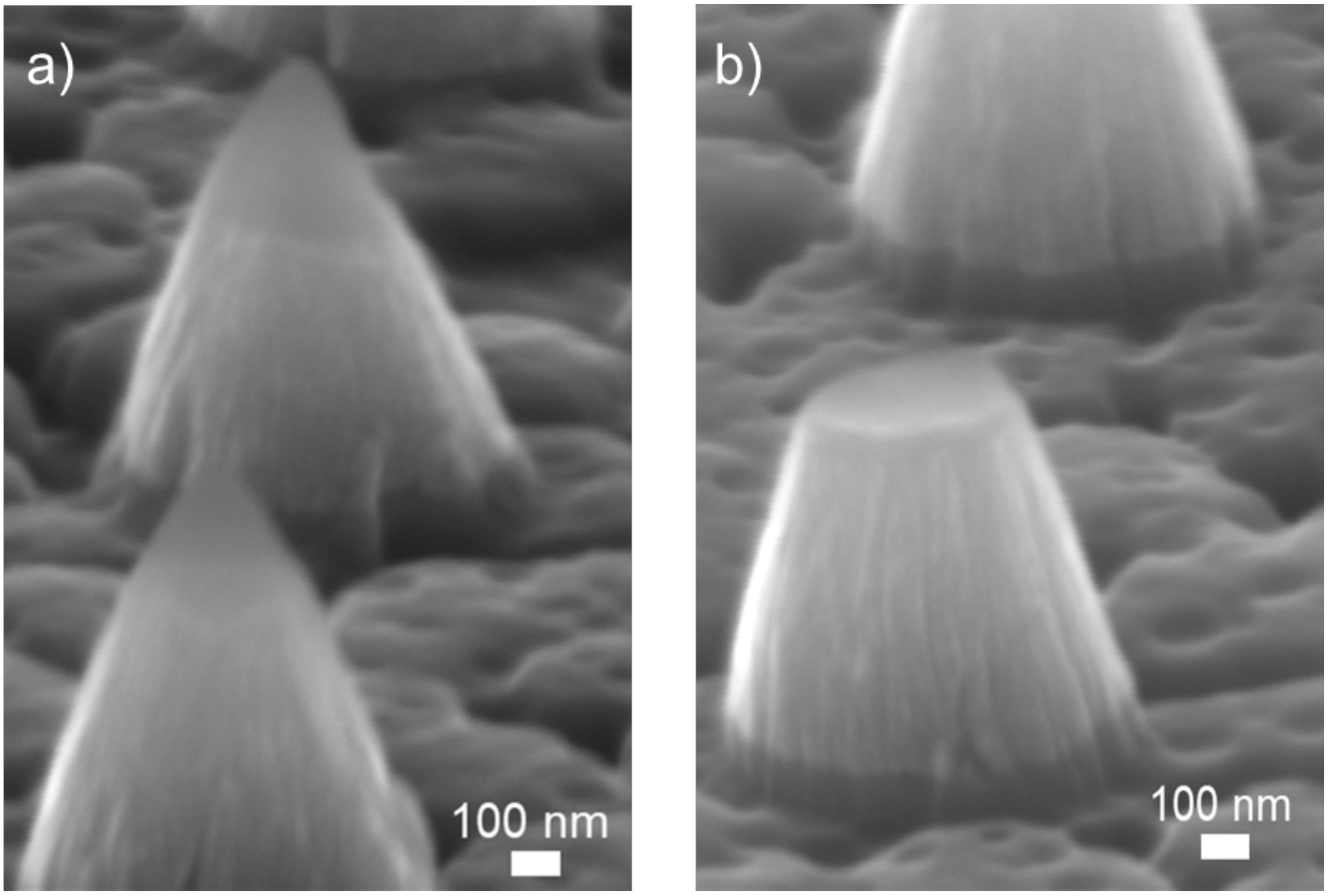


Figure 3.3: SEM image of Reactive Ion Etching of diamond using a) Al_2O_3 and b) Al hard mask.

*3.3.2. **Diamond Etching Recipe Optimization***

The first step for diamond RIE is to optimize the gas flow to achieve fast diamond etching, appropriate selectivity with Al_2O_3 and low surface roughness. Several etching recipes were tested for this purpose. The inductively coupled plasma (ICP) power was maintained at 1000 W, and the chamber pressure was held constant at 10 mTorr. Various O_2/CHF_3 gas flow ratios were tested under RF powers of 50 W and 100 W, as detailed in Table 3.1.

O2 (sccm)	CHF3 (sccm)	Ar (sccm)	RF (W)	ICP (W)	Pressure (mTorr)	Diamond etch rate (nm/min)	Al2O3 etch rate (nm/min)	Selectivity
5	47	0	50	1000	10	13.8	17.6	0.784
5	50	0	50	1000	10	16.6	23	0.72
26	26	0	50	1000	10	37.5	16	2.343
47	5	0	50	1000	10	53	11	4.818
52	0	0	50	1000	10	73	5	14.6
0	52	0	50	1000	10	12	8	1.5
0	0	52	50	1000	10	12	6.2	1.93
47	5	0	100	1000	10	81	18	4.5
50	3	0	100	1000	10	120	28.3	4.25

Table 3.1:: RIE Recipe tested for diamond etching.

The results of the etching tests are summarized as follows:

1. At low oxygen concentrations, the diamond etching rate decreases sharply, becoming comparable to the rate observed in pure Ar plasma. Additionally, the diamond etching rate in pure CHF_3 plasma is nearly identical to that in pure Ar plasma, suggesting that etching in CHF_3 plasma lacks a chemical component and is dominated by physical sputtering.
2. The diamond etching rate is highest in pure oxygen plasma; however, the surface roughness increases significantly due to micromasking by the Al_2O_3.
3. Al_2O_3 is etched through a combination of O_2 and CHF_3. The etching rate of Al_2O_3 is low in both pure O_2 and pure CHF_3, with both rates comparable to that in pure Ar gas. This suggests that the etching mechanism of Al_2O_3 in pure CHF_3 or pure O_2 is primarily physical sputtering, with minimal contribution from chemical reactions.

4. When a combination of O_2 and CHF_3 gases is used, the Al_2O_3 etching rate increases, with higher CHF_3 concentrations leading to a greater etch rate. This is attributed to the formation of a fluorocarbon polymer on the Al_2O_3 surface upon exposure to CHF_3 plasma, which inhibits etching [234]. However, the introduction of oxygen gas removes this polymer [239], allowing etching to proceed. As shown in Table 3.1, a slight increase in CHF_3 gas flow, while keeping the oxygen flow constant, results in an increase in the Al_2O_3 etching rate. This suggests that the rate-limiting factor is the chemical reaction between CHF_3 and Al_2O_3, rather than the removal of the fluorocarbon polymer by oxygen.

Since our process requires mask shrinkage during diamond RIE, achieving very high selectivity is not necessary. Instead, the goal is to obtain optimal selectivity between the Al_2O_3 mask and the diamond film. For this purpose, the optimal gas flow was determined to be O_2: 47 sccm and CHF_3: 5 sccm. The resulting selectivity values were 4.8 and 4.5 at RF powers of 50 W and 100 W, respectively. Diamond etching rate and selectivity as a function of oxygen gas flow are shown in figure 3.4.

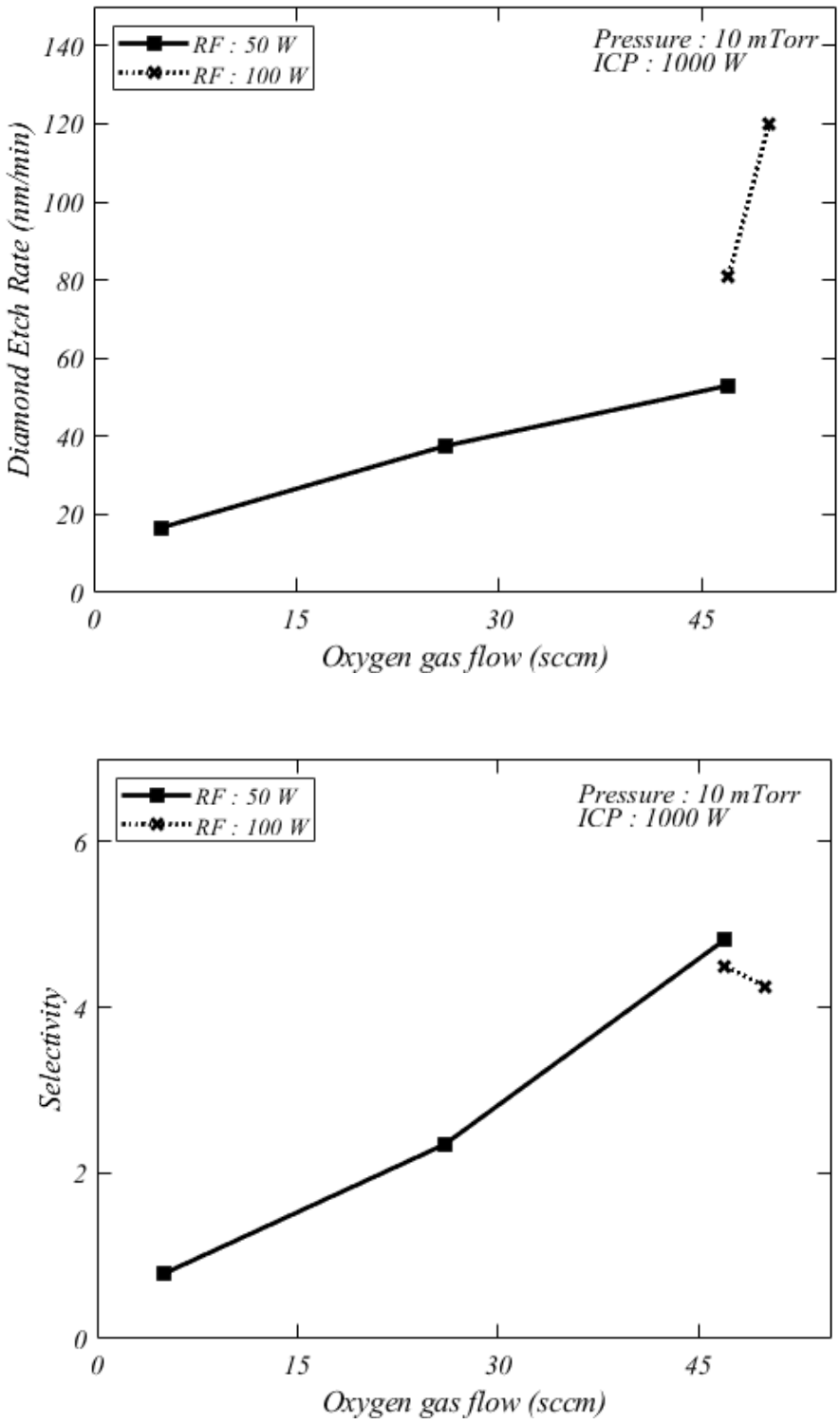


Figure 3.4: Diamond etching rate (top), and selectivity (bottom) between diamond and Al_2O_3 mask, as a function of oxygen gas flow. Total O_2/CHF_3 gas flow is 52 sccm,

The next step is to optimize the RF power to achieve an adequate sidewall slope for the diamond tip. It is well-established that increasing the RF power results in a more vertical sidewall profile [229, 240]. For the 700 nm thick diamond film used in this work, the target sidewall angle is between 20° and 30° from the surface normal which would allow for cone shaped apex to be formed when using circular shaped mask having diameter between 400 and 800 nm. RF power ranging from 50 W to 100 W is tested to determine the optimal sidewall angle and to ensure high selectivity between the diamond and the Al_2O_3 mask. The gas flow, pressure, and ICP power were held constant at O_2/CHF_3: 47/5 sccm, 10 mTorr, and 1000 W, respectively. The results are shown in figure 3.5.

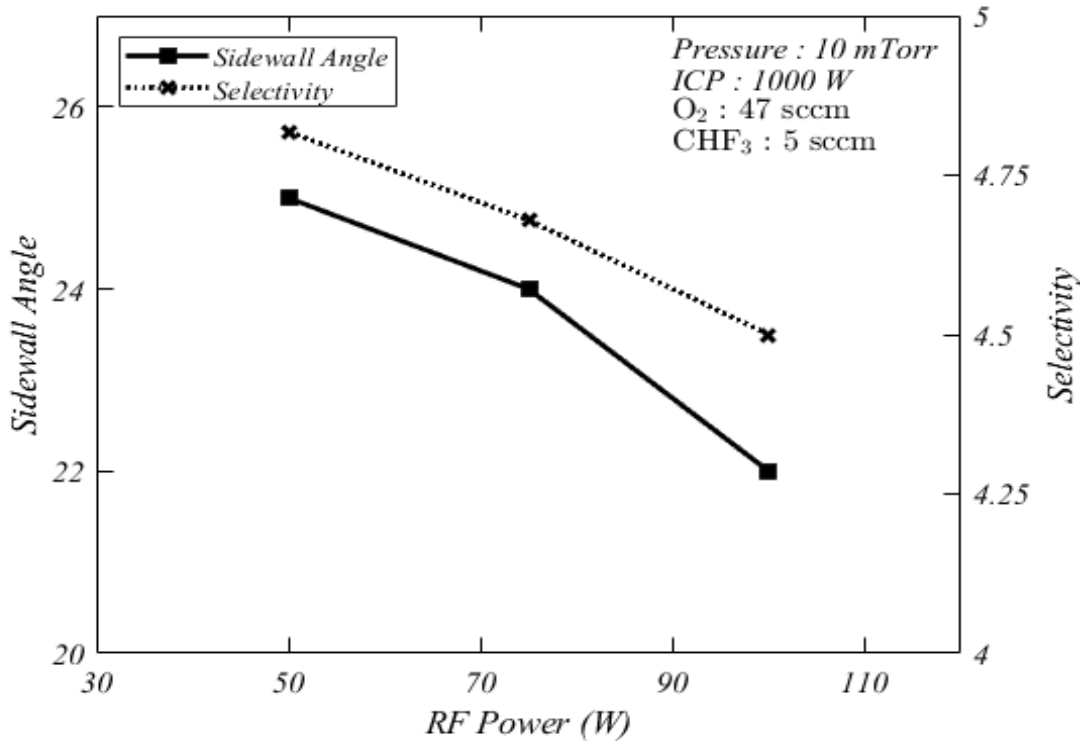


Figure 3.5: Selectivity (diamond : Al_2O_3) and sidewall angle with varying RF power in optimized diamond etching recipe.

We found that the sidewall angles are in the acceptable range for all tested RF power; however, the selectivity between diamond and Al_2O_3 mask decreases with increase in RF power from 50 W to 100 W. Consequently, the optimized RF power is determined to be 50 W.

Next, the ICP power is optimized. A decrease in ICP power from 1000 W to 500 W reduces the etch rate of diamond film from 53 nm/min to 40 nm/min while significantly increasing the Al_2O_3 etch rate from 11 nm/min to 31.66 nm/min (hence decrease in selectivity from 4.8:1 to 1.26:1). Thus, the ICP power is kept constant at 1000 W. These results are in line with those previously reported in literature [229, 231, 240].

The optimized diamond etching recipe is O_2/CHF_3: 47/5 sccm, RF: 50 W, ICP:1000 W, 10 mTorr. With this recipe, the etching rate for diamond is 53 nm/min, while the etching rate for Al_2O_3 is 11 nm/min, with a lateral etching rate of 15 nm/min. Figure 3.6 shows a diamond tip produced using a 400 nm diameter circular mask, etched for 13 minutes. As can be seen from the figure the 260 nm thick Al_2O_3 mask is fully consumed. The average tip apex in this case is 23.5 nm while the diamond tip height is 650nm and the sidewall angle respective to surface normal is 25°. It should be noted that for smaller diameter circles (< 450 nm), the Al_2O_3 is fully consumed due to lateral shrinkage of the mask during the RIE process.

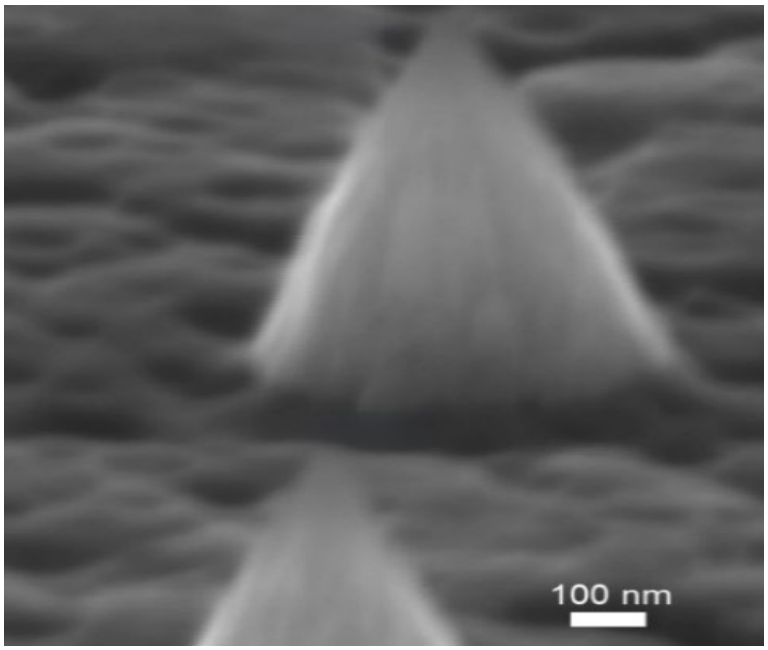


Figure 3.6: Diamond tip fabricated using optimized O_2/CHF_3 recipe.

3.3.3. Silicon Etching

Once the diamond apex is fabricated, the next step is to etch the underlying silicon substrate to act as the high aspect ratio tip base. The required tip height is 10 µm. The already fabricated diamond apex acts as a hard mask during this process. Several dry etching recipes are tested for this purpose. The first test recipe for silicon etching is standard Bosch with 5 seconds deposition and 7 seconds etching cycles (Deposition: SF_6/C_4F_8: 1/160 sccm, RF: 5 W, ICP: 1000 W, 20 mTorr; Etching: SF_6/C_4F_8: 160/1 sccm, RF: 20 W, ICP: 1000 W, 25 mTorr). However, the etched silicon is negatively tapered (figure 3.7a). To improve the silicon sidewall slope, the deposition time is increased to 6 seconds. Though the taper angle is improved – from 2.8° to 1.9° – the sidewall had scalloping effect which is typical of Bosch etching [241] (figure 3.7b). To achieve smooth sidewalls with vertical or slightly positively tapered profile, a non-switching pseudo-Bosch etching recipe is used [242]. The etching recipe is optimized to provide smooth and vertical profile (C_4F_8/SF_6: 40/20 sccm, RF: 50 W, ICP: 1200 W, 10 mTorr, 15 °C) (figure 3.7c).

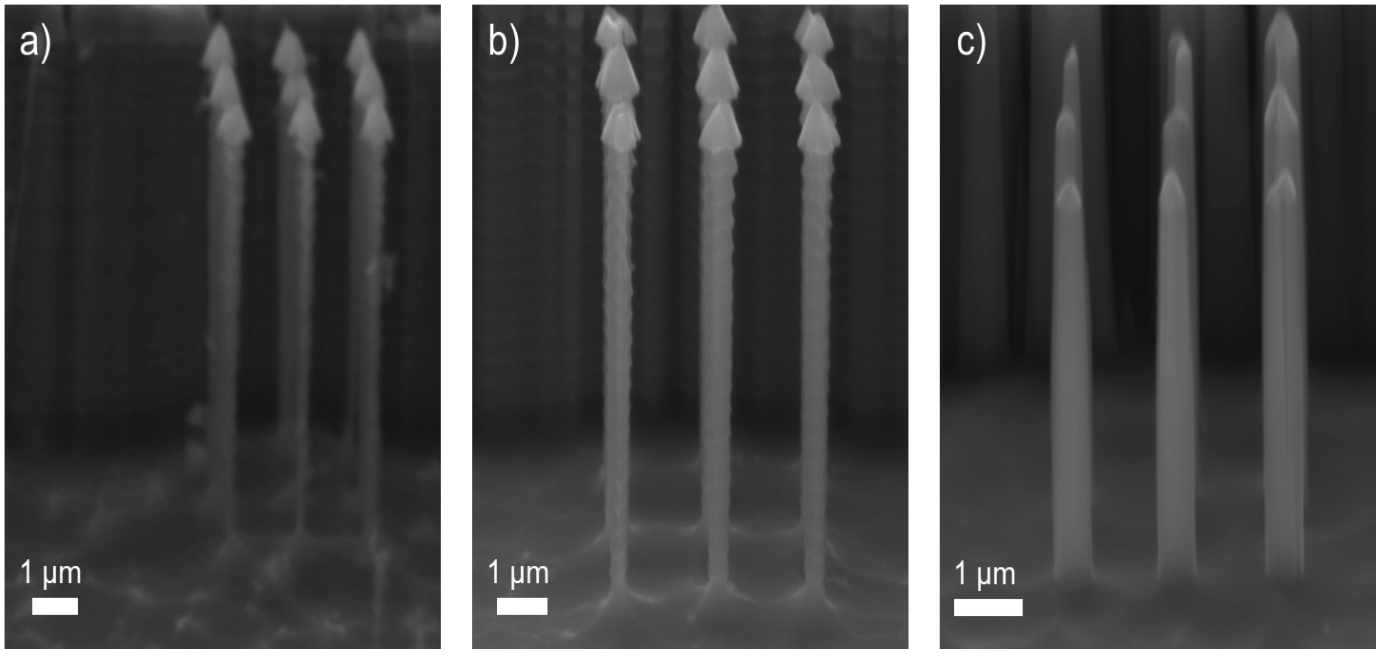


Figure 3.7: Si RIE with diamond hard mask using a-b) Standard Bosch, and c) non-switching pseudo-Bosch etching.

We observed that the diamond apex becomes blunt during the Si RIE process, regardless of the etching recipe used. It is suggested that the cause of this effect is physical sputtering of diamond, rather than chemical reaction occurring between diamond and etching gas. It is well understood that the ion energy during the RIE process is dependent on the RF power of the system [243]. To test this hypothesis, RF power is decreased from 50 W to 30 W and 20 W (figure 3.8 a, b). As expected, the sharpest tip is achieved with the lowest RF power (20 W). However, even when using the lowest stable RF power allowed by the system (20 W), the diamond apex still becomes blunt. During 9 µm silicon etching by non-switching pseudo-Bosch, the diamond tip apex diameter increases twofold following silicon etching.

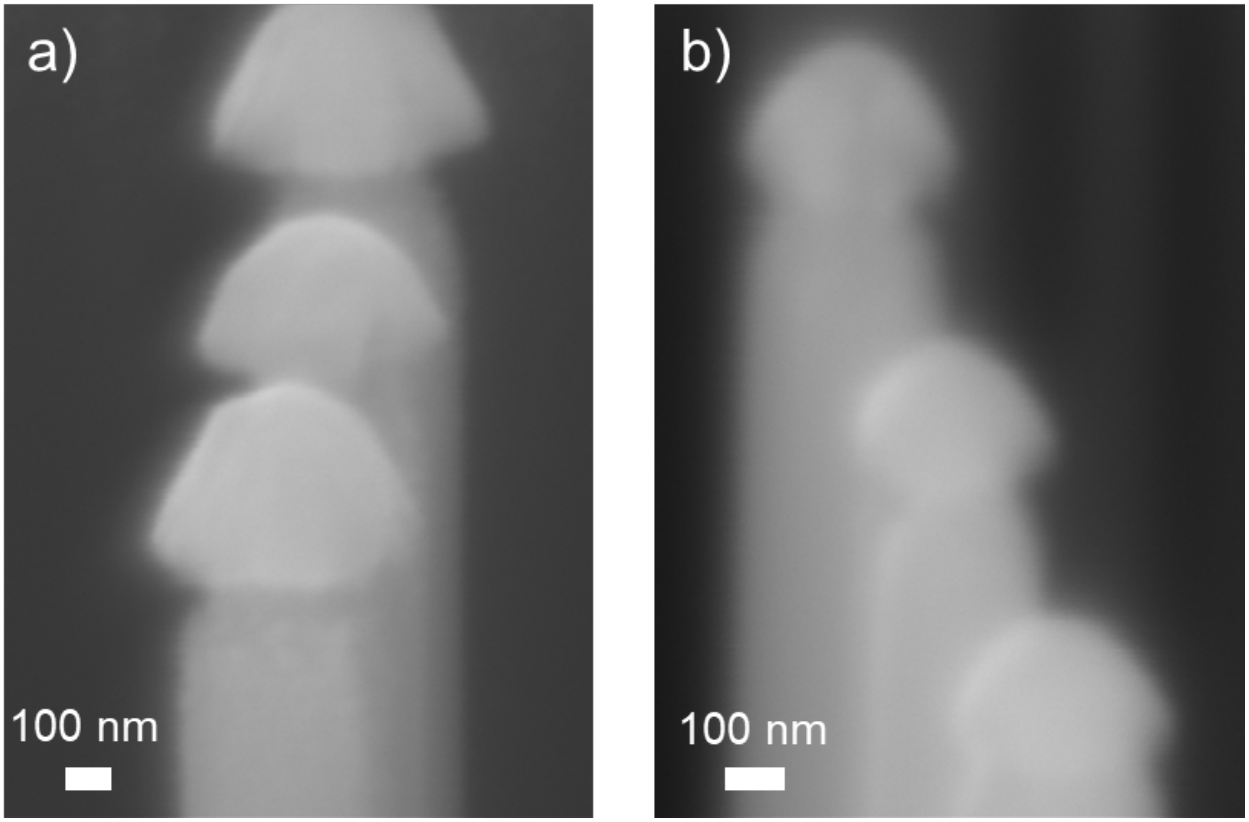


Figure 3.8: Diamond tip after silicon etching using non switching pseudo-Bosch with RF power a) 20 W, b) 30 W.

To combat this issue, the thickness for Al_2O_3 mask is increased such that after diamond RIE, the mask Al_2O_3 is still present (Al_2O_3 apex). The Al_2O_3 acts as a barrier to physical sputtering of diamond tip during silicon etching. However, the mask thickness must be carefully optimized such that when the silicon is etched to the required depth, the Al_2O_3 mask must be completely etched away, and the final tip apex must be diamond. For our tip, this is achieved by using 550 nm thick Al_2O_3. It should be noted that even with increased thickness, lateral etching of Al_2O_3 during diamond RIE causes the mask to be fully removed from smaller diameter circles (< 450 nm) before silicon etching. Using an 800 nm diameter circular mask and diamond RIE for 13 minutes, the tip apex diameter is measured to be 58.5 nm, as shown in Figure 3.9a. During the silicon reactive ion etching (RIE) process, employing a non-switching pseudo-Bosch process with 20 W RF power for 25 minutes, the Al_2O_3 mask undergoes physical sputtering and is gradually etched away. This process exposes a diamond tip with an average apex diameter of 29.5 nm after the silicon RIE. The resulting aspect ratio of the fabricated tip is 9.63. Using larger diameter patterns, or thicker Al_2O_3 mask leads to apex material being Al_2O_3 instead of diamond once the silicon base is formed. The final AFM tip with diamond apex is shown in figure 3.9b and the apex of the fabricated tip is shown in figure 3.9c. As can be seen in figure 3.9b, the tip fabrication using shrinking mask has excellent uniformity across the array. The average apex diameter is 29 nm with an error of ± 5nm. The process is graphically illustrated in figure 3.10.

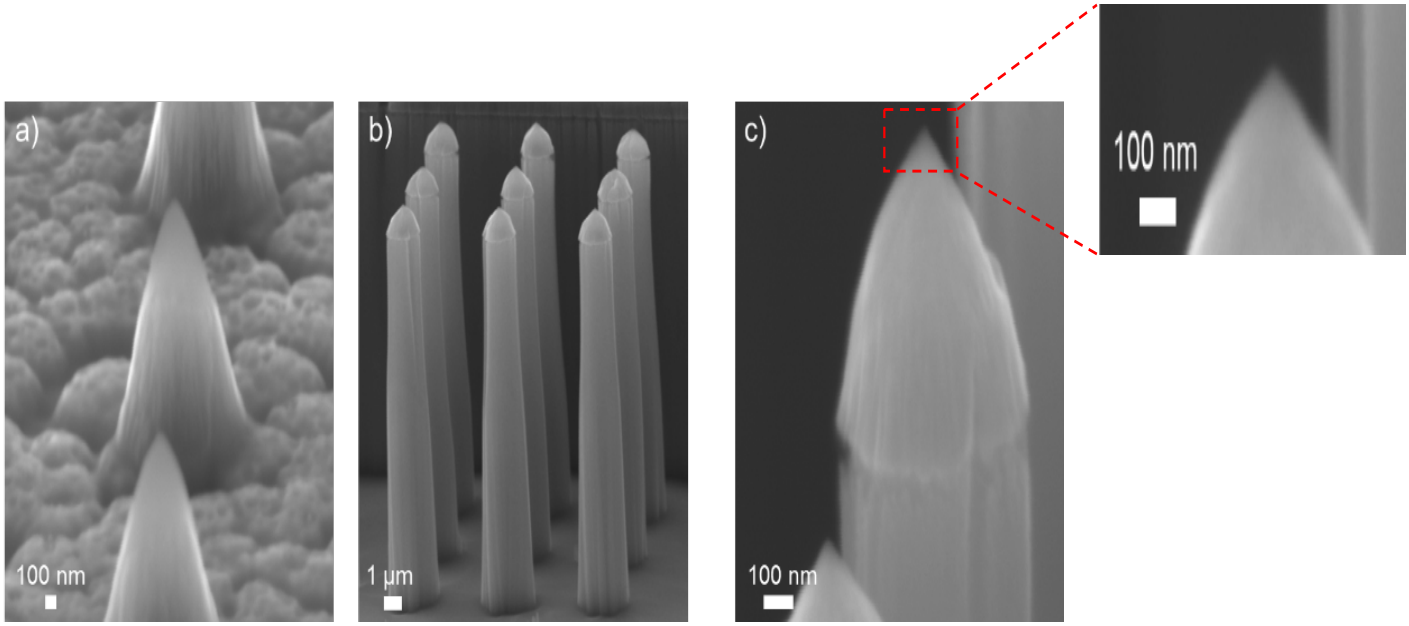


Figure 3.9: a) Diamond tip with Al_2O_3 apex, b) Diamond tip after silicon base fabrication, c) Apex of tip shown in b).

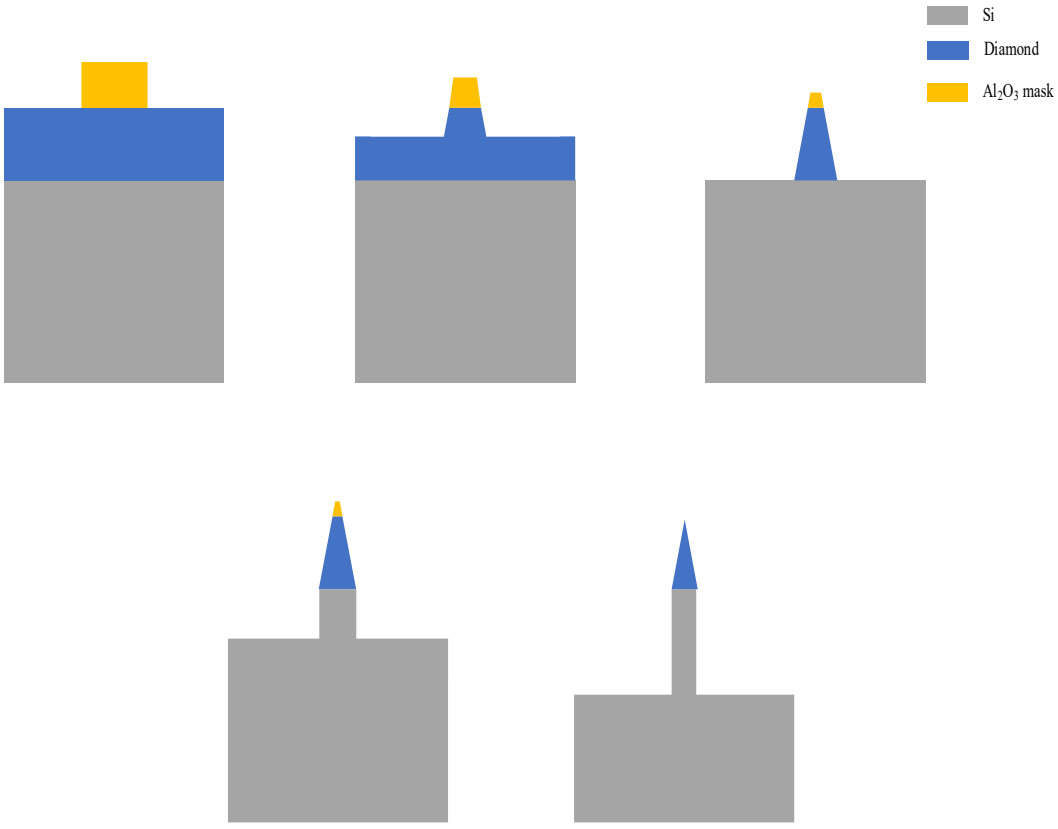


Figure 3.10: Graphical illustration of diamond tip fabrication using mask shrinkage method.

The method developed in this work produces diamond tips with an average apex diameter of less than 30 nm, which is significantly smaller than what is typically achieved using conventional RIE processes [110, 118, 244]. The apex size of our tips is comparable to those obtained through CVD diamond growth on silicon tips [101, 245]. However, the aspect ratio of the diamond-coated silicon tips is much higher in our work.

3.4. CONCLUSION

High aspect ratio, sharp diamond tips are fabricated on silicon base using dry etching. The method developed in this work allows for low-cost fabrication of high aspect ratio sharp tips. The base of the tip is made of silicon, which is dry etched using non switching pseudo-Bosch recipe, while the apex is made of ~650nm thick diamond allowing for harder tip. Given that the diamond film is grown directly on silicon wafer, there is no need for complicated and time-consuming transfer of diamond tip onto silicon cantilever. However, due to the complexity introduced by the diamond RIE, and physical sputtering during silicon dry-etching, careful optimization of mask parameters (material, thickness, width) must be carried out. The fabricated tip has an average apex diameter of 29 nm and aspect ratio of 9.63.

CHAPTER 4: NOVEL METHOD FOR FABRICATION OF HIGH ASPECT RATIO DIAMOND TIP

4.1. INTRODUCTION

As mentioned in the previous chapter, one of the issues during fabrication of diamond AFM tip with silicon base, is the physical etching of diamond during Si-RIE, which causes the tip to become blunt. In the previous chapter, we mitigated this issue by using thicker Al_2O_3 mask. However, this is a complex task, since the etch rates may fluctuate over a period of time, and may leave behind Al_2O_3 as tip apex rather than diamond.

In this chapter, we design a novel method for fabrication of diamond tip, which first fabricates the silicon base, followed by diamond apex. This method eliminates the risk of physical bombardment of diamond apex during base fabrication, and results in sharp apex, along with high aspect ratio obtained during the previous chapter.

The fabrication process is designed in close resemblance to T-gate structures used to fabricate high electron mobility transistors [246]. In traditional T-gate devices, the gate structure has two components, with the bottom part of the gate being very small (< 100 nm wide) to provide high operating frequency [247]. However, the small width of the gate causes an increase in gate resistance and noise [248], which is countered by the wide top. In our work, we have used the dual T-shaped structure to form the mask for our device patterning. First the wider top part of the T-shaped mask is used to pattern the silicon base of our tip. This top part is then selectively removed, and the bottom narrower part of the T-shaped mask is used to pattern the diamond apex. This allows for sharp diamond apex to form and does not require several lithography steps.

4.2. EXPERIMENT

Figure 4.1 shows the process flow for fabrication of diamond AFM tip using T-shaped mask. First an SOI wafer with 300 nm diamond thin film is coated with 350 nm of amorphous silicon (aSi) and 100 nm of SiO_2 using PECVD, at 250°C and 330°C respectively (figure 4.1 a). The design requirements state a smaller opening in the resist for the bottom part of the T-shaped mask, while a wide opening is required for the top. For this reason, a resist stack is spin coated on the substrate. First 500 nm of PMMA is spin coated at 2000 RPM, and baked at 180°C for 10 minutes, followed by 80 nm PMGI coating at 5000 RPM which is baked at 180°C for 5 minutes. The PMGI provides undercut necessary for the forthcoming liftoff process [249, 250]. Finally, 500 nm, undiluted ZEP520A resist is spin coated at 2000 RPM and baked at 180°C for 5 minutes. EBL is then performed using JEOL JBX-6300FS Electron Beam Lithography System. The beam voltage is 100 kV, while the current used is 8 nA. The dose for top layer (ZEP520A) is 350 $\mu C/cm^2$, while for the bottom layer (PMMA) it is 2000 $\mu C/cm^2$. After EBL, the resists are developed as follows: first the top layer (ZEP520A) is developed in ZED-N50 developer for 90 seconds at room temperature, followed by rinse in IPA for 30 seconds and drying by nitrogen. Next, PMGI is developed in MF-319 for 60 seconds and rinsed in DI water for 30 seconds before being dried by nitrogen. Finally, PMMA is developed in MIBK:IPA (1:3) for 90 seconds and rinsed in IPA for 30 seconds before being dried by nitrogen (figure 4.1 b). All RIE steps are done using Oxford Instruments Plasma lab 100 ICP380 RIE system. First, SiO_2 is etched by RIE for 30 seconds (C_4F_8/O_2: 40/5 sccm; RF: 100 W; ICP: 2500 W; 10mTorr ; 50C), followed by isotropic etching of aSi using pure SF_6 plasma (SF_6: 160 sccm ; RF: 10 W ; ICP: 1000 W ; 15 mTorr ; 15C) for 19 seconds. The aSi is etched through to expose the underlying diamond thin film. Isotropic etching is preferred over anisotropic silicon etching, in order to obtain undercut necessary for adequate hard mask patterning and liftoff (figure

4.1 c). Next, remaining PMMA is etched using oxygen plasma (O_2: 50 sccm, RF: 500 W; 800mTorr ; 25 C) for 2 minutes (figure 4.1 d). This is done to ensure deposition of Al_2O_3 mask on the shoulders of the T-shaped design. Finally, hard mask is deposited using Intlvac Nanochrome II e-beam evaporation system (figure 4.1 e). The resist stack is then removed by liftoff in PG remover at 80°C for 20 minutes and the T-shaped mask is transferred to the hard mask (figure 4.1 f). Due to the patterning done by RIE in the above-mentioned steps, the mask is deposited on top of diamond thin film – to form bottom of the T-shape mask – as well as on SiO_2 which forms top of the T-shaped mask. This mask is then used to pattern the base of the AFM tip in a series of RIE processes. First, unpatterned SiO_2 is etched (C_4F_8/O_2: 40/5 sccm; RF: 100 W; ICP: 2500 W; 10mTorr ; 50C) for 30 seconds to expose underlying aSi, which is etched using Bosch etching for 5 cycles (Etch: 20 W RF power, 1000 W ICP power, C_4F_8/SF_6 : 1/160 sccm, 25 mTorr for 6s; Passivation: 5 W RF power, 1000 W ICP power, C_4F_8/SF_6 : 160/1 sccm, 20 mTorr for 6s**)** to create anisotropic profile. The aSi is etched through to expose the diamond thin film, which is then etched in O_2/C_4F_8 plasma. The purpose of this RIE step is not to form a cone shape in the diamond film, but rather to etch through the diamond to reach the Si substrate which would form the base of the AFM tip. Finally, the Si is etched by RIE. The height of the base after etching is 4.5 μm (figure 4.1 g). Once the AFM tip base is formed, the need for the top of the T-shaped mask is finished. This mask is selectively removed by removing the oxide thin film on which it rests. The oxide is removed by placing the sample in 1:10 BOE for 10 minutes with gentle agitation (figure 4.1 h). After oxide and Al_2O_3 removal is done, the remaining a-Si is removed using Bosch etching (Etch: 20 W RF power, 1000 W ICP power, C_4F_8/SF_6 : 1/160 sccm, 25 mTorr for 6s; Passivation: 5 W RF power, 1000 W ICP power, C_4F_8/SF_6 : 160/1 sccm, 20 mTorr for 6s**)** to again create an anisotropic

profile (figure 4.1 i). Finally, diamond is patterned in O_2/C_4F_8 plasma to form cone shape on top of Si base (figure 4.1 j).

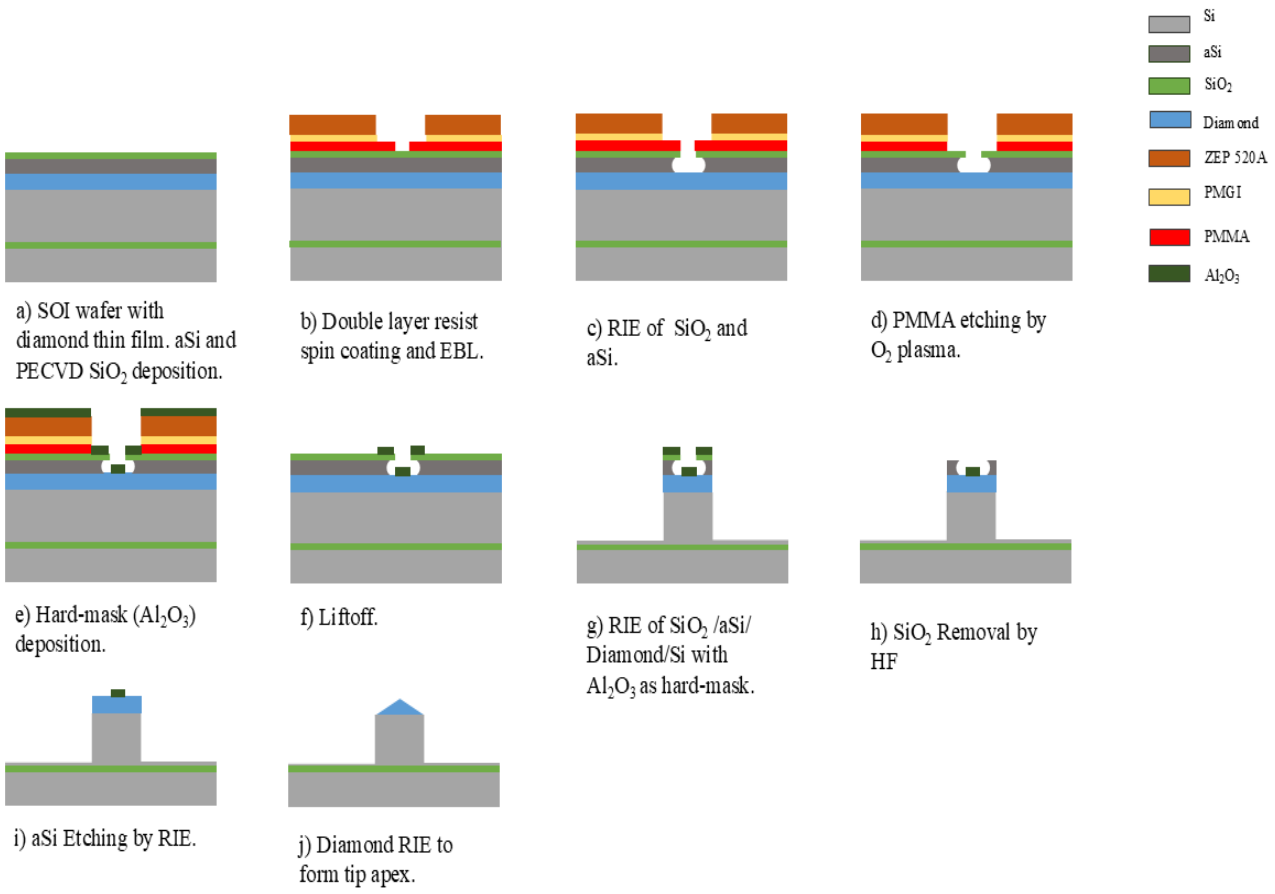


Figure 4.1: Process flow for diamond tip fabrication using T-gate mask.

4.3. RESULTS AND DISCUSSION

4.3.1. Fabrication of Silicon Base

Table 4.1 shows the various recipes tested for Si, SiO_2, and aSi etching, while table 4.2 shows the etch rate of relevant materials with the recipes listed in table 4.1.

	Gas flow (sccm)	RF Power (W)	ICP Power (W)	Pressure (mTorr)	Temperature (°C)
i. Si isotropic etch	SF_6 : 160	10	1000	15	15
ii. Bosch etching (etch: 6 sec;	Etching: SF_6/C_4F_8: 160/1	20	1000	20	15
passivation: 6 sec)	Passivation: SF_6/C_4F_8: 1/160	5	1000	20	15
iii. Pseudo-Bosch etch	SF_6/C_4F_8: 20/40	20 – 50	1200	10	15
iv. SiO_2 etch	C_4F_8/O_2: 40/5	100	2500	10	50
v. Oxygen plasma ashing	O_2: 50	500	-	800	25

Table 4.1: Recipes used for Si, a-Si, SiO_2 and PMMA etching.

Recipe	Etch rate (nm/min)						
	PMMA	**ZEP**	**Si**	**aSi**	**SiO_2**	**Al_2O_3**	**Cr_2O_3**
i.	456	390	2700	1218	66	-	-
ii.	-	-	250 nm/cycle	80 nm/cycle	2.5 nm/cycle	< 1 nm/cycle	< 1 nm/cycle
iii.	-	-	480	60	132	< 1	< 1
iv.	600	394	174	-	222	60	-
v.	64	20	-	-	-	-	-

Table 4.2: Etching rate of different materials using recipes from table 4.1.

During the first batch of RIE, silicon is etched isotropically which results in undercut which allows for easy liftoff of Al_2O_3 mask. The resists thicknesses are decided in-line with the etching rates obtained in table 4.2. After liftoff, second batch of RIE is performed to fabricate the silicon base of the AFM tip. During this step, aSi is etched anisotropically by Bosch etching (Etch: 20 W RF power, 1000 W ICP power, C_4F_8/SF_6 : 1/160 sccm, 25 mTorr for 6s; Passivation: 5 W RF power, 1000 W ICP power, C_4F_8/SF_6 : 160/1 sccm, 20 mTorr for 6s**)** for 5 cycles, while diamond is etched by O_2/C_4F_8:52/3 sccm; 50 W ; 1000 W ; 10mTorr ; 40C, which provides an almost vertical profile (section 4.3.2). To fabricate the silicon base, Bosch and Pseudo-Bosch recipes are tested, the gas flow, RF power, ICP power, pressure and temperatures used are mentioned in table 4.1. Parameters such as etching vs. passivation times are manipulated for Bosch etching in order to obtain vertical profile, while for Pseudo-Bosch etching, RF power is changed to obtained appropriate sidewall profile. The results are shown in figure 4.2 and figure 4.3.

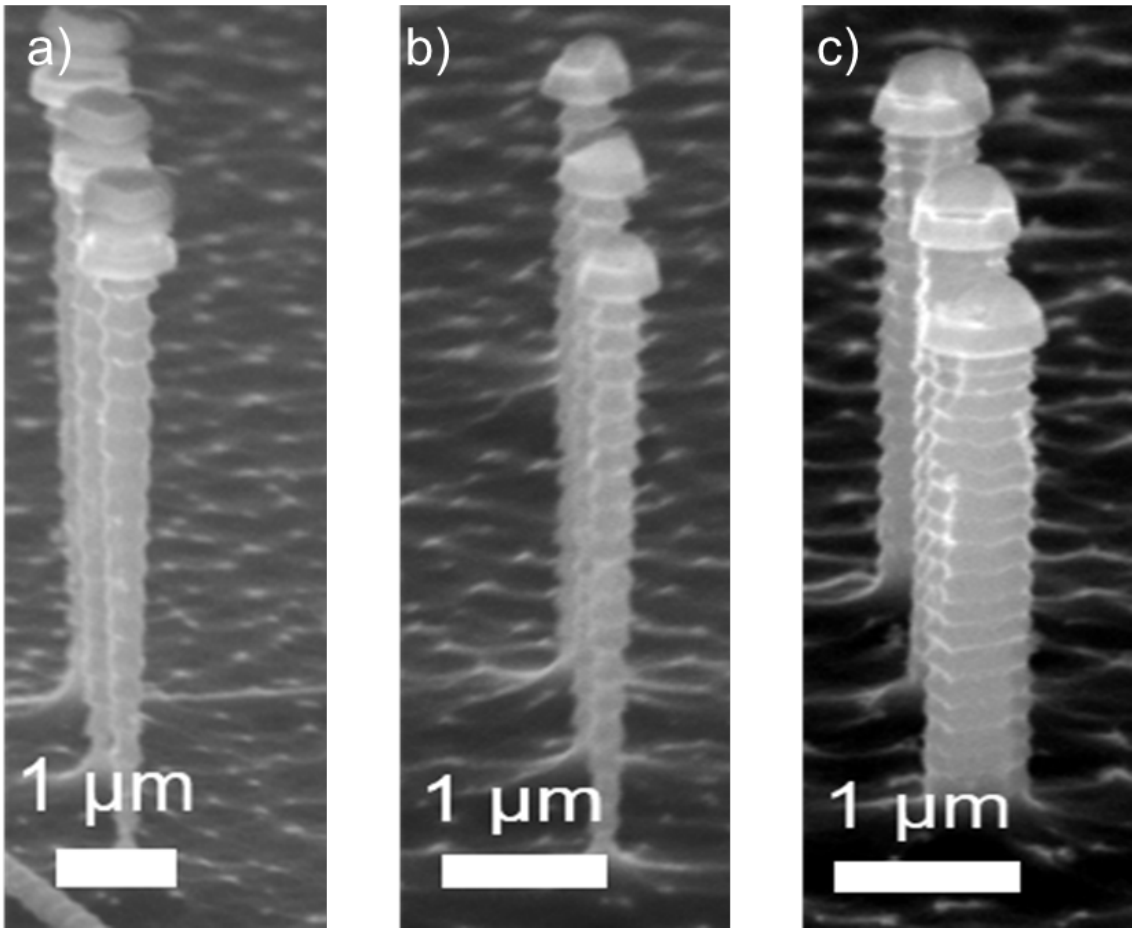


Figure 4.2: SEM image of AFM tip base fabricated using Bosch etching with a) 5 seconds etching 7 seconds passivation; b) 6 seconds etching, 6 seconds passivation and c) 5 seconds etching, 6 seconds passivation.

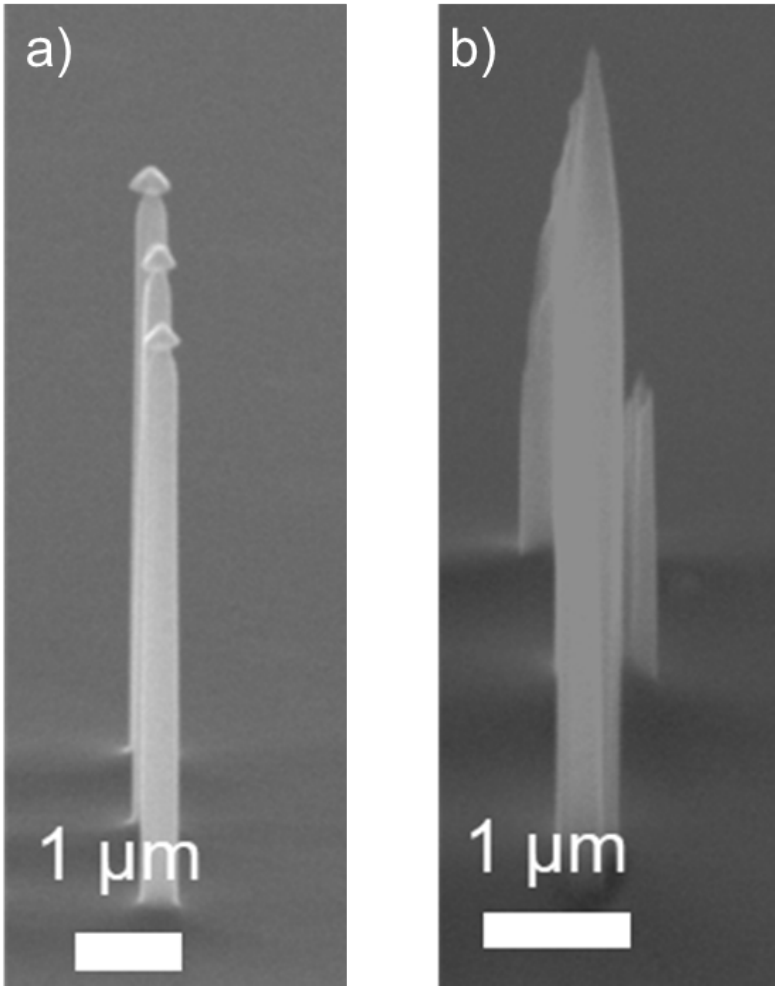


Figure 4.3: SEM image of AFM tip base fabricated using Pseudo-Bosch etching with RF power being a) 20 W and b) 50 W.

It can be seen from figure 4.2, for Bosch etching the vertical sidewalls are obtained with 5 seconds of etching and 6 seconds of passivation. All other etching vs. passivation ratios provide negatively tapered profiles. On the other hand, for Pseudo-Bosch etching, RF power of 20 W and 50 W are tested, both of which give positively tapered profile (figure 4.3). Thus, Bosch etching with 5 seconds of etching and 6 seconds of passivation is chosen as the recipe of choice for fabrication of silicon base. The optimized recipe is: Etch: C_4F_8/SF_6 : 1/160 sccm, 20 W RF power, 1000 W ICP power, , 25 mTorr for 5s; Passivation: C_4F_8/SF_6 : 160/1 sccm, 5 W RF power, 1000 W ICP power, , 20 mTorr for 6s, and the etching rate of silicon with this recipe is 150 nm/cycle.

4.3.2. Fabrication of diamond apex

As mentioned in chapter 3, diamond is etched by oxygen plasma, with some additive gases to prevent micromasking. In this chapter we use O_2/C_4F_8 plasma to etch diamond. The diamond used in this work is 300 nm thick on SOI substrate. For our work, we require the sidewall angle to be between 20 – 30° from the surface normal. Additional requirements are of high diamond etch rate and high selectivity with the masking material. For this work the etching was performed on an RIE system which does not allow any metal masks. Due to the requirement of SiO_2 removal using BOE after fabrication of tip base, it cannot be used as a mask. We tested Cr_2O_3 and Al_2O_3 as masking materials for various gas flow of O_2/C_4F_8 plasma. The results are shown in table 4.3. The RF power is fixed at 50 W, the ICP power is 1000 W, and the pressure is 10 mTorr for all recipes. The total gas flow is maintained at 55 sccm for recipe 1 – 3 and 52 sccm for recipe 4 – 5.

Recipe	**O_2/C_4F_8 (sccm)**	**Etch rate (nm/min)**		
		Diamond	**Al_2O_3**	**Cr_2O_3**
a)	50/5	82	50	> 150
b)	52/3	120	24	> 150
c)	48/7	86	56	> 150
d)	50/2	120	34	53
e)	43/9	87	140	> 150

Table 4.3: Diamond, Al_2O_3 and Cr_2O_3 etch rate using different O_2/C_4F_8 gas flows.

Due to very high etch rate of Cr_2O_3 for all tested recipes, Al_2O_3 was selected as a mask material. Next step is to determine the sidewall angle of the diamond using the recipes listed in table 4.3. The sidewall angle of the patterned diamond and selectivity with the Al_2O_3 mask is shown in table 4.4.

Recipe	O_2/C_4F_8 (sccm)	Sidewall Angle (°)	Selectivity (Diamond/Al_2O_3)
a)	50/5	65	1.64
b)	52/3	86	5
c)	48/7	61	1.53
d)	50/2	89	3.53
e)	43/9	59	0.6

Table 4.4: Sidewall angle of patterned diamond and selectivity between diamond and Al_2O_3 for recipes listed in table 4.3

While recipe b) and d) in table 4.3 provide very high selectivity, the sidewalls for both are nearly vertical. On the other hand, recipe a) and c) provide sidewall angle in the required range (between 20 – 30°). Due to higher selectivity between diamond and Al_2O_3 when using recipe a) (O_2/C_4F_8:50/5 sccm; 50 W ; 1000 W ; 10mTorr ; 40C), it is used as the recipe of choice for fabrication of diamond apex. On the other hand, recipe b) (O_2/C_4F_8:52/3 sccm; 50 W ; 1000 W ; 10mTorr ; 40C) is selected for near vertical diamond etching required during the fabrication of silicon base, due to its high selectivity and nearly vertical sidewall profile. Figure 4.4 shows the sidewall profile of diamond using recipe a) and b).

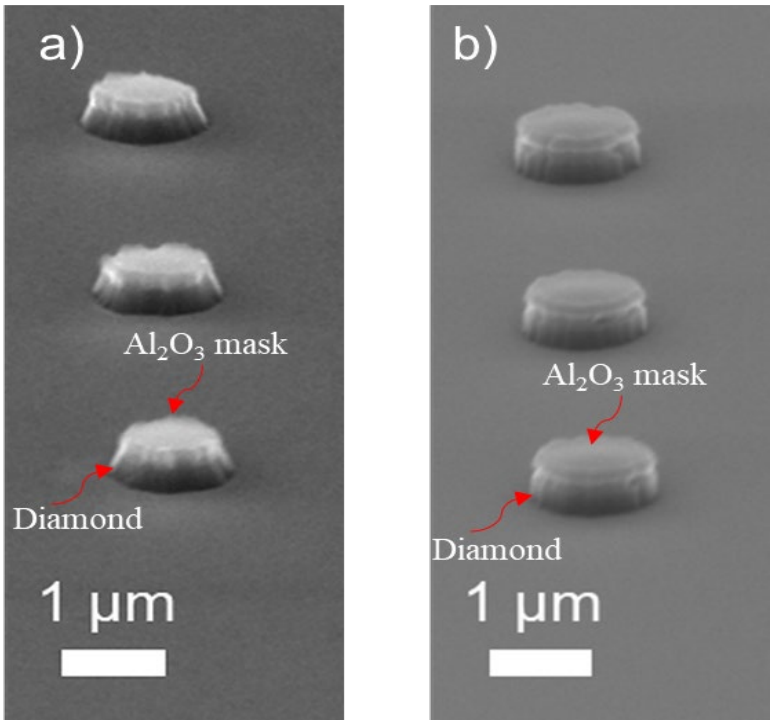


Figure 4.4: Sidewall slope of diamond obtained using a) O_2/C_4F_8: 50/5 sccm and b) O_2/C_4F_8: 52/3 sccm. RF: 50 W, ICP: 1000 W, pressure 10mTorr and Temperature is 40°C for both recipes.

After fabrication of AFM base using Bosch etching (Etch: 20 W RF power, 1000 W ICP power, C_4F_8/SF_6 : 1/160 sccm, 25 mTorr for 5s; Passivation: 5 W RF power, 1000 W ICP power, C_4F_8/SF_6 : 160/1 sccm, 20 mTorr for 6s), the oxide thin film is removed by immersing the sample in 1:10 BOE for 10 minutes at room temperature with gentle agitation to facilitate mask removal. After the oxide is removed, sample is rinsed with DI water for ~ 6 minutes and dried with nitrogen before the last batch of RIE is performed. First aSi is removed by Bosch etching (Etch: 20 W RF power, 1000 W ICP power, C_4F_8/SF_6 : 1/160 sccm, 25 mTorr for 6s; Passivation: 5 W RF power, 1000 W ICP power, C_4F_8/SF_6 : 160/1 sccm, 20 mTorr for 6s) for 5 cycles, followed by the fabrication of diamond apex using the recipe O_2/C_4F_8:50/5 sccm; 50 W ; 1000 W ; 10mTorr ; 40C for 3 minutes. The tip fabricated by this method has an average apex diameter of ~10 nm and is shown in figure 4.5. It should be noted that the mask size of the diamond film during this etching step is crucial for obtaining sharp apex. This is because there is no significant mask shrinkage of Al_2O_3 using O_2/C_4F_8

plasma according to our tests. The optimal mask design for our work is 200 nm diameter (thickness 300 nm) in order to obtain sharp apex using 300 nm thick diamond film. On the other hand, the mask size for fabrication of silicon base is 600 nm. It can be seen from figure 4.5 that the diamond apex is perfectly aligned on top of the silicon base. This is because of one-step patterning using EBL which eliminates the need for complex alignment steps.

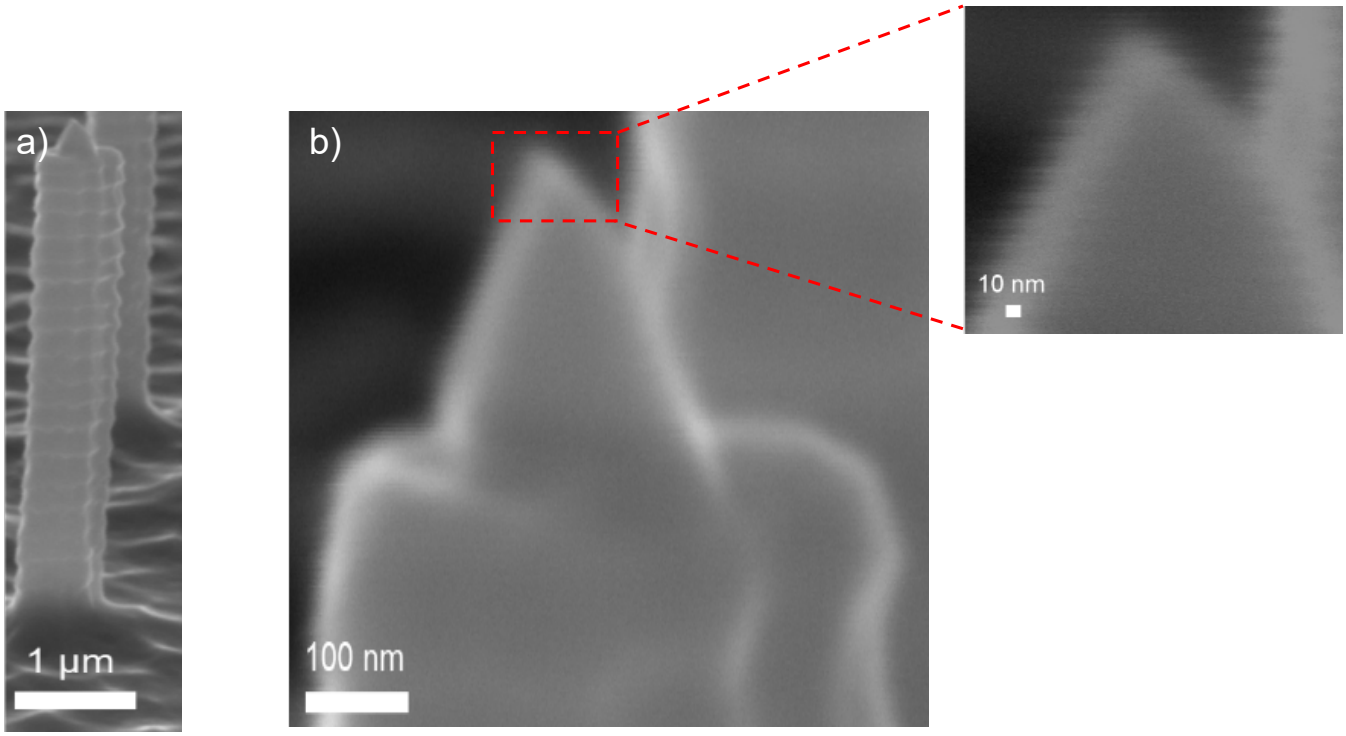


Figure 4.5: a) AFM tip with silicon base and diamond apex, b) diamond apex of tip shown in a)

4.4. CONCLUSION

This work shows the fabrication of high aspect ratio diamond AFM tip. The process results in a tip with average diamond apex of ~10 nm and the silicon base has an aspect ratio of 7.5. Higher aspect ratio can be easily fabricated without affecting the apex diameter. This process does not require complex alignment steps between diamond and silicon base masks and also does not require mask thickness control since the diamond tip apex is formed with the Al_2O_3 mask falling off rather than being consumed as a result of mask shrinkage.

CHAPTER 5: FABRICATION OF HIGH ASPECT RATIO AFM TIPS BY SURFACTANT ADDED TMAH ETCHING

This chapter focuses on fabrication of high aspect ratio silicon AFM tips. The first part of this chapter (Section 5.1) discusses design parameters optimized for tip fabrication, while the second part (Section 5.2) discusses the process parameters and effects of surfactant concentrations on the etching properties of (111) oriented silicon wafers.

The main body of Section 5.1 is reprinted with permission from Ref. [251] (*Farheen Nasir and Bo Cui. "Fabrication of high aspect ratio AFM tips by surfactant added TMAH etching." Sensors and Actuators A: Physical 388 (2025): 116477.)*

5.1. FABRICATION OF HIGH ASPECT RATIO AFM TIPS

Atomic Force Microscope (AFM) has become an important tool for characterizing nanoscale devices and structures in various domains such as nanoelectronics, material sciences and biology [9]. An AFM probe includes a tip attached at the end of a thin cantilever. The other end of the cantilever is attached to a handle. The dimensions and material of the cantilever determine the detection sensitivity of the AFM [252]. For highly sensitive AFM probes, the cantilever experiences detectable bending, even for small tip-sample interaction forces. However, the most important part of the AFM probe is the tip that directly interacts with the sample surface and experiences long- and short-range forces. The tip must be sharp and ideally have high aspect ratio, in order to provide adequate representation of the scanned surfaces [38]. Most commercially available AFM tips are made by anisotropic etching of silicon in alkaline solution which can yield sharp tips at remarkably low cost [104]. Common alkaline etchants for silicon are Potassium Hydroxide (KOH) [189] and Tetramethylammonium Hydroxide (TMAH) [191], with KOH being more frequently used due to its

higher etch rate and pronounced anisotropy between the (100)/(110) and (111) planes [253]. TMAH, however, offers the advantage of compatibility with CMOS technology [254].

Silicon-based AFM tips dominate the commercial market, with most being fabricated on (100)-oriented silicon wafer, as this orientation is easier to etch in alkaline solution [255, 256]. However, anisotropic etching of (100)-oriented silicon wafer results in low aspect ratio (0.5 – 2), pyramid shaped tips [257]. (111) oriented silicon has also been explored for tip fabrication, though it requires an additional dry etching step to expose higher miller index planes on the (111) surface [258, 259]. Tang et. al. demonstrated this approach by fabricating high aspect ratio tips with 20 nm radius of curvature on (111) oriented silicon wafer [146].

Critical parameters to monitor during wet anisotropic etching for silicon tip fabrication include radius of the tip apex, aspect ratio, surface roughness and reproducibility. Several methods have been used to improve these factors. For example, Chang et. al. [260] used a two-step process involving KOH etching followed by etching in HNA (mixture of nitric acid, acetic acid (or water), and hydrofluoric acid) to form silicon tips with (311) sidewall planes on (100)-oriented silicon wafers. Additionally, different mask designs and orientations have also been used. For example, Burt et. al [261] used triangular masks to obtain high aspect ratio tips using KOH and (100) silicon wafer. They found that rotating a triangle mask 63° relative to the <110> wafer flat resulted in the sharpest tip. This is because the (313) plane is exposed during the KOH etching when using this mask orientation. On the other hand, Pradeep et. al. [262], fabricated 158 μm tall silicon tips using square mask and optimized TMAH: H_2O: isopropyl alcohol (IPA) etchant.

Certain additives to alkaline etchant have also been used to improve wet etching results. For example, Zubel et al. [263] studied the effects of IPA concentration on the etching characteristics of TMAH and KOH. They found that at medium solution concentrations (e.g. 3 – 7 M KOH) and

IPA concentrations (5 – 9 % percent), IPA molecules adsorb preferentially only on certain planes, thus blocking the etching from taking place on those planes and improving anisotropy. They also found that for both TMAH and KOH, the surface roughness decreases with increase in IPA concentration. In reference [264], authors studied the effect of several types of surfactants on the surface roughness of Si(100) surface using TMAH. They concluded that cationic ASPEG (ammonium salt of poly(ethylene glycol)) provided the smoothest surface for (100)-oriented silicon wafer (mean roughness : 3.5 nm), although the etch rate (0.4 μm/min) was significantly lower compared to etching in pure TMAH or when other types of surfactants were added to TMAH. They also found that when non-ionic PEG (poly(ethylene glycol)) was added to TMAH, the undercut of the patterned structure was significantly lower. Similarly, Tang et. al. [265] added small amount of non-ionic Triton X-100 surfactant in TMAH to create high aspect ratio, sharp tips on (100) and (111) oriented silicon wafers.

Surfactants are classified based on the charge of their head group. The three main types of surfactants commonly used in silicon etching are non-ionic, cationic, and anionic surfactants. Detailed information on their chemical composition and properties is available in the literature [266]. The role of surfactants during wet anisotropic etching of silicon has been studied in detail [196, 197, 267, 268]. It has been observed that surfactant molecules preferentially adsorb onto specific crystallographic planes, reducing the access of OH^- ions to these surfaces. As a result, the etch rates of these planes decreases, while the etch rates of other planes remain largely unaffected. This selective adsorption ultimately alters the anisotropy of silicon etching. In the case of convex corner etching of silicon for AFM tip fabrication, the addition of surfactants alters the local slowest etching planes, which subsequently affects the final sidewall plane, potentially leading to the formation of higher aspect ratio tips. The specific changes depend on several factors, including the

type and concentration of the surfactant, the choice of alkaline etchant, and the etching temperature [197, 198, 264]. It has been observed that adding anionic surfactants to KOH solutions results in the lowest surface roughness and fastest etching of Si(100) [194]. Conversely, in TMAH etching, cationic and non-ionic surfactants generally produce the smoothest surfaces, while anionic surfactants yield the fastest etching rates but with increased surface roughness [196]. Additionally, non-ionic surfactants provide better etching control and stability compared to cationic surfactants. For this reason, non-ionic surfactants are the most widely used type of surfactant in alkaline etching of silicon. Various non-ionic surfactants exhibit different effects on anisotropy and etch rate reduction. Among them, Triton X-100 (100% iso-octylphenoxy polyethoxyethanol) is the most widely used [269], while Triton X-405, another non-ionic surfactant, has gained attention in recent years.

In this work, we compare etching characteristics of pure 25 wt% TMAH, 25 wt% TMAH + 1000 ppm Triton X-405 and 25 wt% TMAH + 1000 ppm Triton X-100 for the fabrication of sharp, high-aspect-ratio tips (height-to-width ratio ≥ 5) using Si(111) wafers. Additionally, three different mask designs were investigated to determine the optimal configuration for Si(111) etching. Each design underwent dry etching at three different heights to evaluate the effect of etching depth on the final structure.

5.1.1. Experiment

AFM tips are fabricated from 125 mm diameter, 600 μm thick, (111)-oriented silicon wafers (n-doped, 1–2 Ω-cm), sourced from Sumitomo Sitix Silicon, Inc. The wafers undergo a selective dry etching step using the standard Bosch process, which is followed by wet anisotropic etching in TMAH or TMAH with added surfactants.

The Si (111) wafer is first cleaned using oxygen plasma for 60 seconds. Next, 1 µm SiO_2 is deposited using plasma-enhanced chemical vapor deposition (PECVD), followed by spin coating of photoresist (S1811) for photolithography. Photolithography is performed using UV direct write system (MLA150, Heidelberg Instruments). The mask designs selected for this study are square (sides parallel to the wafer flat <110> direction), diamond (sides 45° rotated square with respect to <110> wafer flat) and circle shaped with 15 – 20 µm diameter/side length (figure 5.1). The patterns are subsequently transferred to an oxide hard mask by Reactive Ion Etching (RIE). The silicon is then etched using standard Bosch etching for 46, 73, and 97 cycles, resulting in pillar heights of 20 µm, 30 µm, and 40 µm, respectively. The Bosch etching parameters are as follows: deposition with SF_6/C_4F_8 : 1/160 sccm, ICP: 1000 W, RF : 5 W, 20 mTorr for 5 seconds; and etching with SF_6/C_4F_8 : 160/1 sccm, ICP: 1000 W, RF: 20 W, 25 mTorr for 7 seconds.

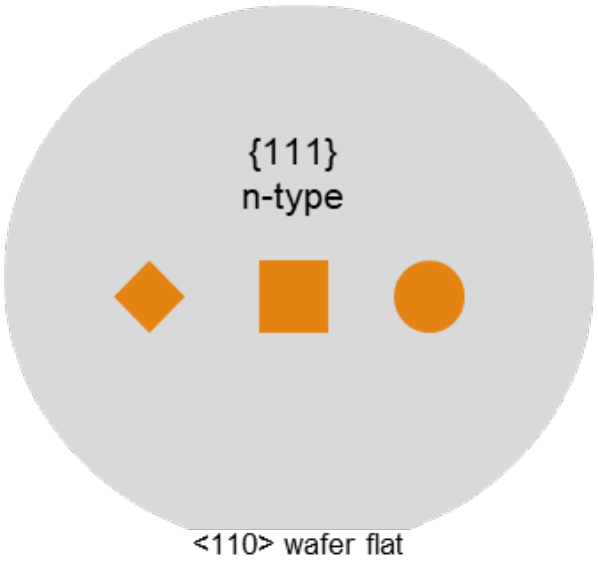


Figure 5.1: Schematic mask design used for etching Si(111) wafer.

After dry etching, the samples are again cleaned using oxygen plasma etching for 60 seconds to remove any fluorocarbon residues. They are then immersed in a 1:10 HF solution for 30 seconds to remove native oxide from the surface, followed by rinsing with deionized water and drying with

nitrogen. This process is completed immediately before transferring the samples into the liquid etchant.

The etchant used is either pure 25 wt% TMAH (Acros Organics) or a mixture of 25 wt% TMAH + 1000 ppm surfactant. The surfactants chosen for this study are Triton X-100 (100% iso-octylphenoxy polyethoxyethanol) and Triton X-405 (70% polyoxyethylene alkyl phenyl ether), both from Sigma Aldrich. All etching tests are done at 70°C and the samples are placed horizontally in the etchant.

Characterization of the fabricated AFM tips is done by JEOL Scanning Electron Microscope (JSM-7200F).

5.1.2. Results and Discussion

5.1.2.1. Etching in 25 wt% TMAH

The final height of the AFM tip required for our application is between 10 and 15 μm. As previously mentioned, the (111) wafer must be dry etched to expose fast-etching planes before being placed in liquid etchant. The Si(111) samples are dry etched to 20 μm pillar height before wet etching in pure 25 wt% TMAH (i.e. without surfactant addition). However, it is found that no high aspect ratio tips were formed after wet anisotropic etching, regardless of the mask shape used. Thus the pillar height of 20 μm is unsuitable for tip fabrication when etching in pure 25 wt% TMAH.

Previously, Tang et. al. [265] has simulated the etching progression of (111) wafer for tip fabrication. They noted that during the etching process, two distinct sets of planes emerge, leading to formation of a neck in the upper region of the dry-etched pillar, which eventually breaks to form a tip-shaped structure. The researchers used a 50 μm dry etching height for this process.

We hypothesize that in our case – for all mask shapes (square, diamond and circle) having 15 µm side-length/diameter – the 20 µm height of the dry-etched pillar is insufficient to form the neck-like structure, preventing the formation of sharp tips, regardless of the mask shape. To address this issue, all mask designs are subsequently dry etched to 30 µm and 40 µm before wet etching. We found that the final tip shape improved significantly once the dry-etched pillar height reached at least 30 µm. The results for tips etched in pure TMAH using a circular mask for 10 minutes at different initial dry-etching heights are shown in Figure 5.2. Once the pillars achieved sufficient height after dry etching, the wet etching process led to the formation of a neck-like structure, which narrowed and eventually broke, forming a high-aspect-ratio tip. The apex of the tips formed is measured using SEM. After TMAH etching, a 30 µm dry-etched circular pillar results in an apex of 16 nm without oxidation sharpening, with an aspect ratio (height-to-diameter at half height) of 8.9. The tip height is 15 µm. For the circular pattern, neck formation occurred at approximately 20 µm from the surface, as shown in Figures 5.2 b and 5.2 c. Once the neck breaks, the tips become self-sharpening.

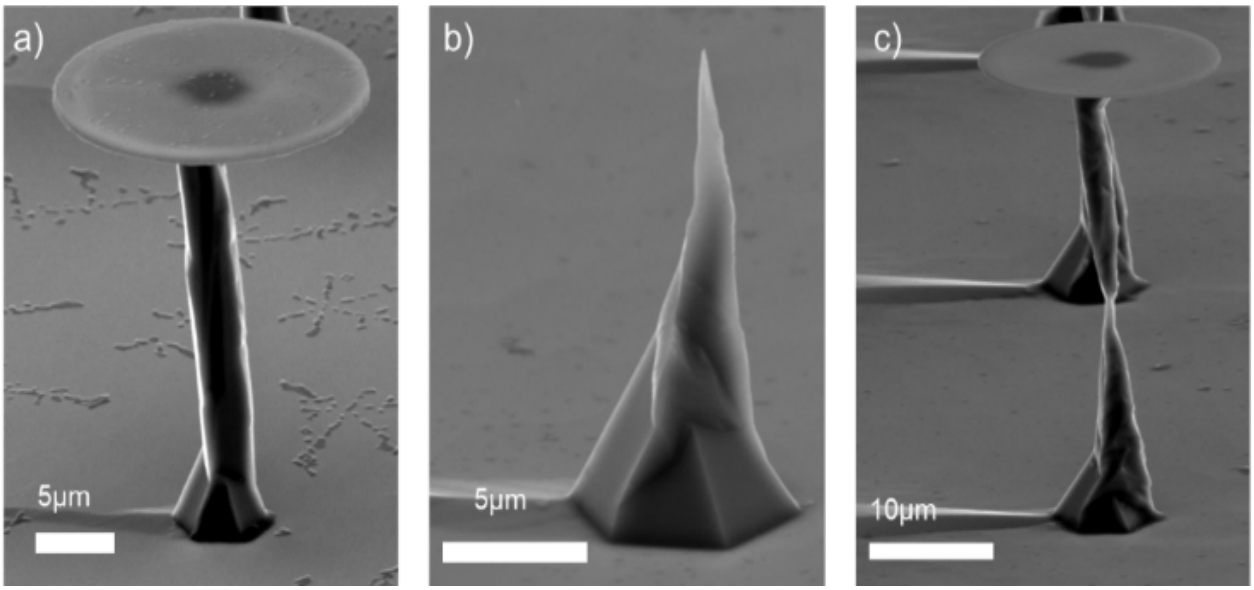


Figure 5.2: TMAH Etching of circular mask with initial dry etching height of a) 20 µm, b) 30 µm and c) 40 µm.

Similar tests are done using square and diamond-shaped masks. It is observed that neck formation was negligible for square shaped masks, regardless of the dry-etching height. In contrast, diamond-shaped masks produce results similar to those of circular masks, though the shape of the tip base differed. Figure 5.3 compares the tips formed after TMAH etching of a 30 μm dry-etched pillar for circular and diamond-shaped masks. The difference in the appearance of the two tips is attributed to different crystallographic planes being exposed during dry etching, which subsequently lead to distinct shapes after anisotropic wet etching [270, 271].

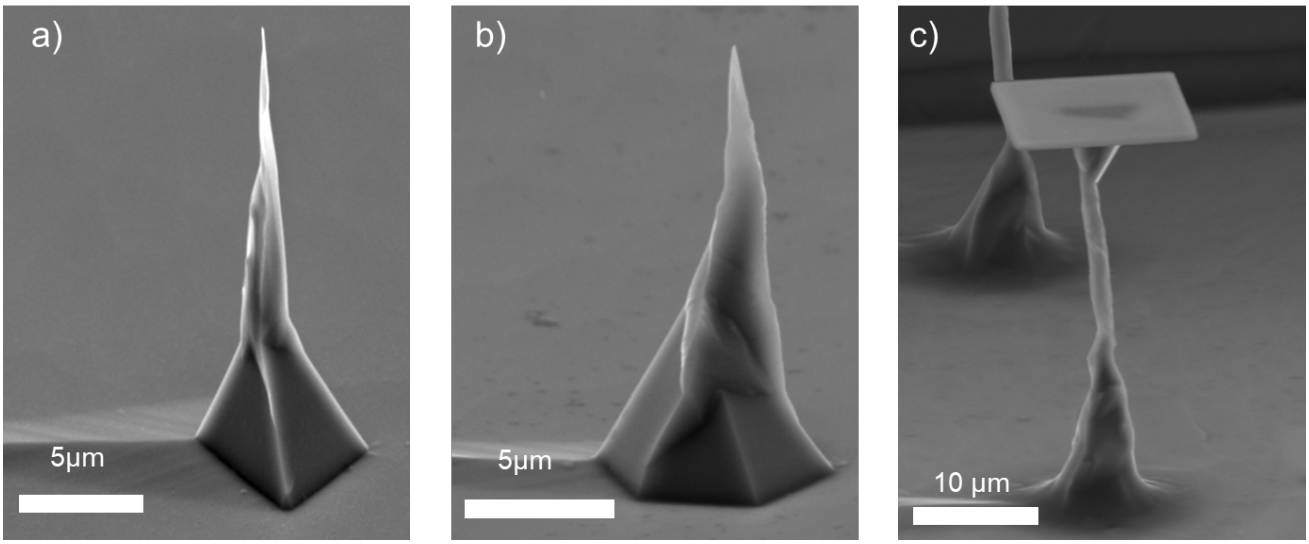


Figure 5.3: Tips formed after TMAH etching using a) diamond (square rotated by 45°), b) circular mask and c) square shaped mask. Dry-etching height is 30 μm for all masks.

Characterization of the fabricated AFM tips is done by JEOL Scanning Electron Microscope (JSM-7200F). Although high aspect ratio and tip apex of less than 20 nm are achieved using pure TMAH etching, the sidewalls of the tips remain rough. To obtain smoother sidewalls while maintaining a high aspect ratio and small apex, the Si(111) samples are etched in surfactant-enhanced TMAH.

5.1.2.2. *Etching in 25 wt% TMAH + 1000 ppm Triton X-405*

When 1000 ppm Triton X-405 is added to TMAH, both the roughness of sidewall and the diameter of the tip apex significantly decreased. Again, etching tests are done for three different dry-etching heights and three different mask shapes. It is found that the circular-shaped masks produce the best tip shape. Unlike in pure TMAH etching, tips are formed at a dry etching height of 20 µm for circular-shaped masks (figure 5.4a). However, at this height, the intersection between tip base and sidewall is very thin, causing the tips to break easily. Once the dry-etched pillar height is at least 30 µm, the final tip shape becomes independent of the dry-etched height. SEM images of tips formed after etching of circular-shaped masks in TMAH + 1000 ppm Triton X-405, with the dry-etching heights of 30 µm and 40 µm are shown in figure 5.4 b and 5.4 c respectively. The tips are self-sharpening after the mask breaks off. The average tip apex diameter achieved using circular-shaped masks with dry-etching height of at least 30 µm is 8 nm without oxidation sharpening. The aspect ratio is 11.4 and 13.8 when the dry etching heights are 30 µm and 40 µm respectively.

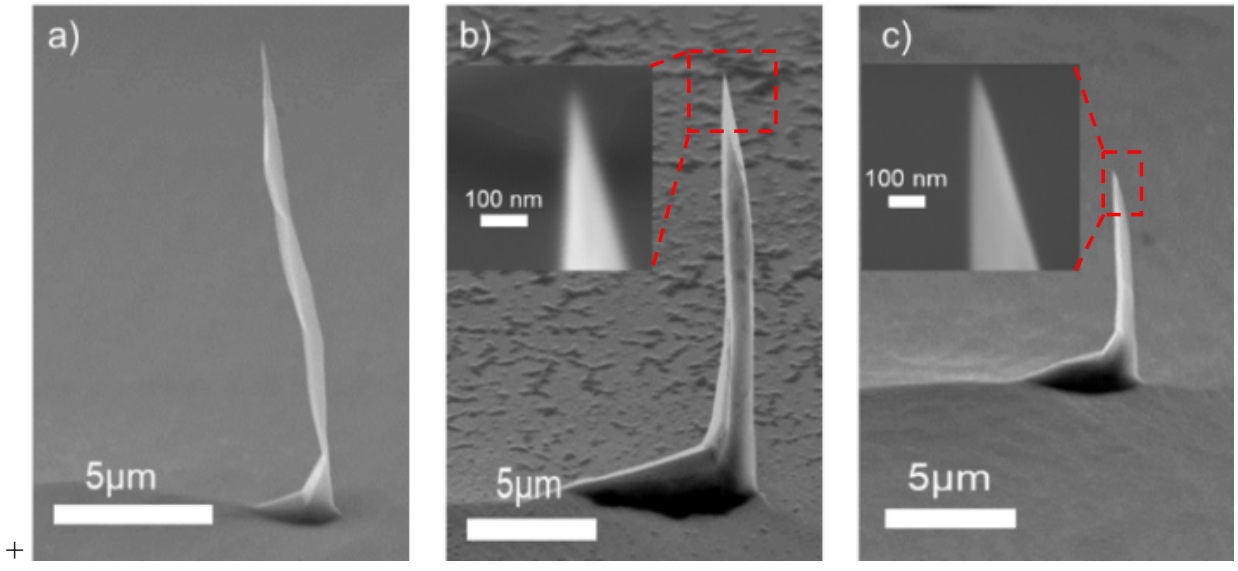


Figure 5.4: Tips formed after TMAH + Triton X-405 etching of circle mask with initial dry-etching height of a) 20 µm, b) 30 µm and c) 40 µm.

In contrast, for square and diamond-shaped masks, tips are only formed when the dry-etching height is 40 µm. For both 20 µm and 30 µm tall pillars, neck formation occurs near the intersection of the tip base and sidewall, causing the tips to break without forming high aspect ratio structures. This effect is attributed to differences in surfactant adsorption on different crystallographic planes [196, 197]. For the diamond-shaped mask, when the dry-etching height is 40 µm, the resulting tip shape closely resembles that of circular-shaped masks, however the apex of the tip is larger than that obtained with the circular shaped mask. Figure 5.5 shows uniformity across array and cone angle for the tips fabricated using 1000 ppm Triton X-405 in 25 wt % TMAH. As mentioned above, the average apex of the tip is < 10 nm with an error range of ± 20 nm.

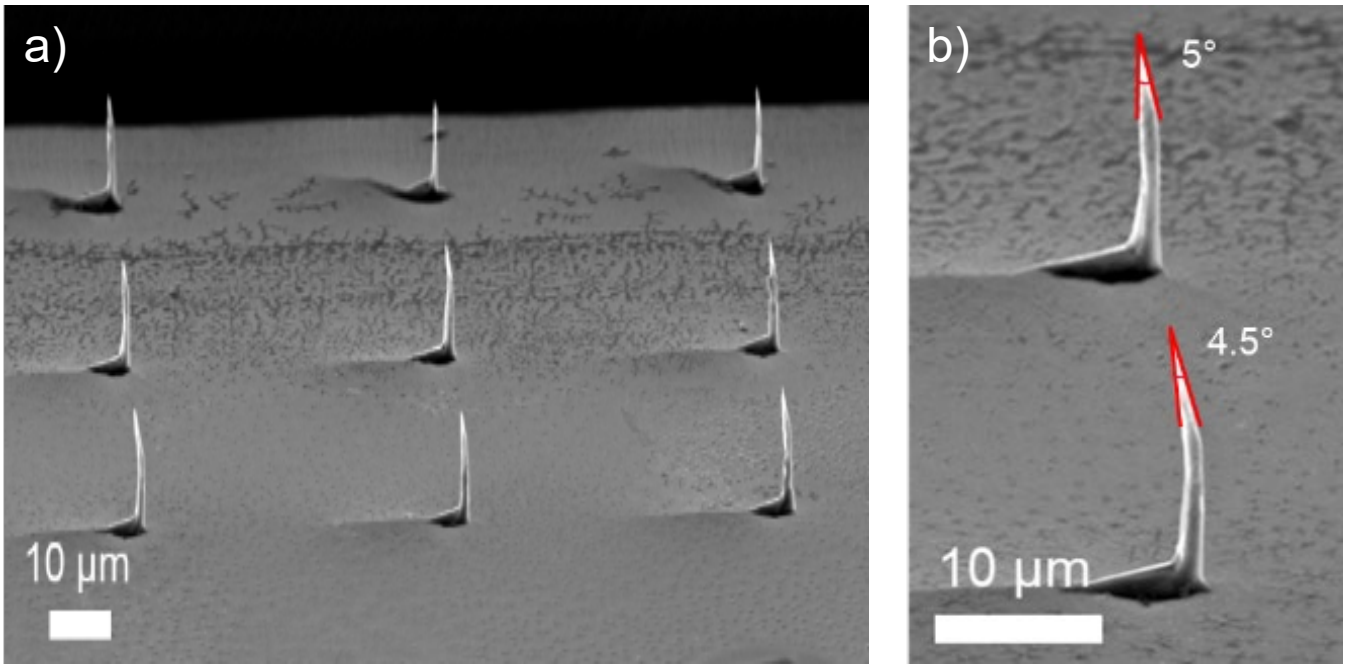


Figure 5.5: a) Uniformity across array and b) cone angle for tips fabricated using circular shaped mask and dry etching height of 30 µm.

Figure 5.6 shows the tips formed using diamond and square-shaped masks when the dry-etching height is 40 µm.

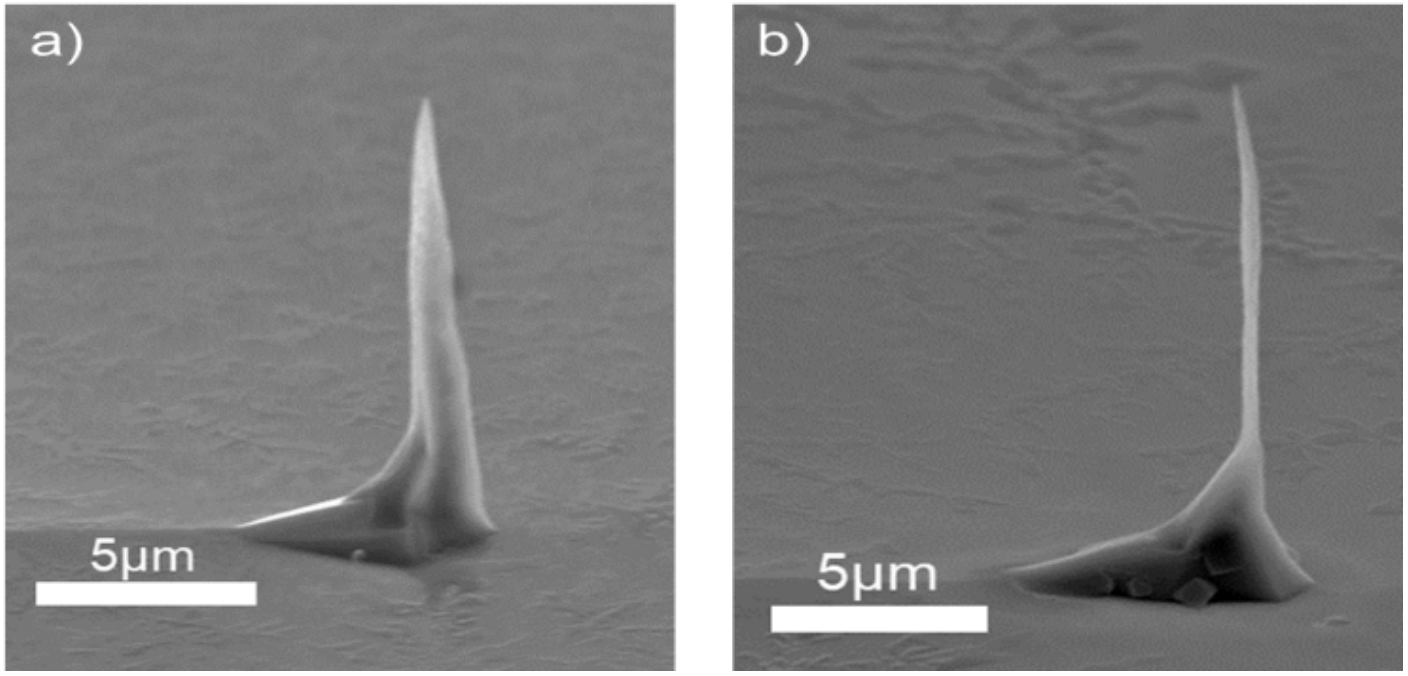


Figure 5.6: Tips formed after silicon etching in TMAH + Triton X-405 with a) diamond and b) square-shaped masks. The dry-etching height is 40 µm for both masks.

5.1.2.3. Etching in 25 wt% TMAH + 1000 ppm Triton X-100

When 1000 ppm Triton X-100 is added to TMAH, the results are different from those obtained by etching in TMAH + 1000 ppm Triton X-405. For a circular-shaped mask, when the dry-etching height is 20 µm or 30 µm, the neck formation occurs at approximately 7 µm from the sample surface which leads to the tip height of ~ 6.5 – 7 µm, with tip apex being 8 nm and aspect ratio of 6. On the other hand, when the dry-etching height is 40 µm, the average tip height is 14 µm, with an apex of ~ 8 nm and aspect ratio of 6.4. These results are shown in figure 5.7 with the inset showing the apex of the respective tips.

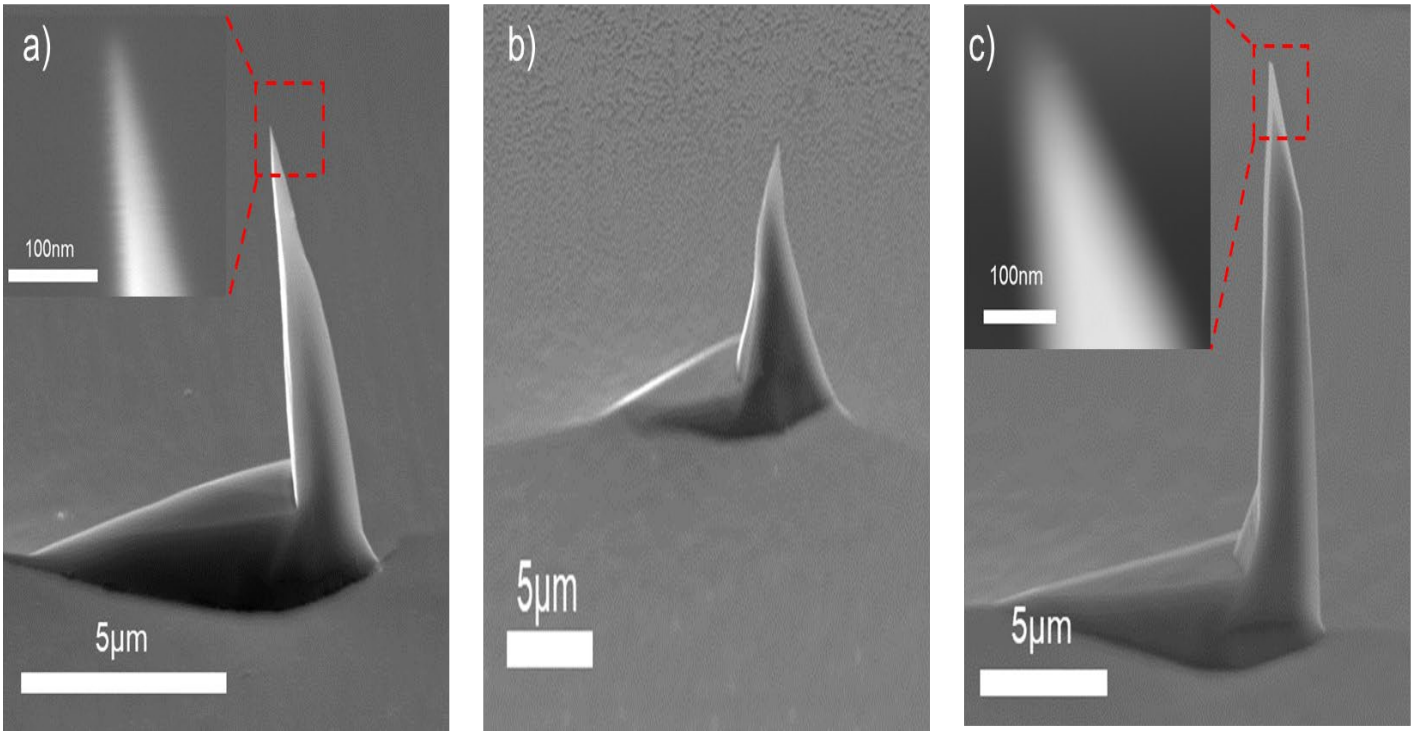


Figure 5.7: Silicon etching in TMAH + Triton X-100 using circular-shaped mask with dry-etching height of a) 20 µm, b) 30 µm and c) 40 µm.

For the square and diamond shaped mask, etching in TMAH + 1000 ppm Triton X-100 leads to neck formation occurring near the interface of the base and tip regardless of the dry-etching height which leads to low aspect ratio structures to form, as shown in figure 5.8.

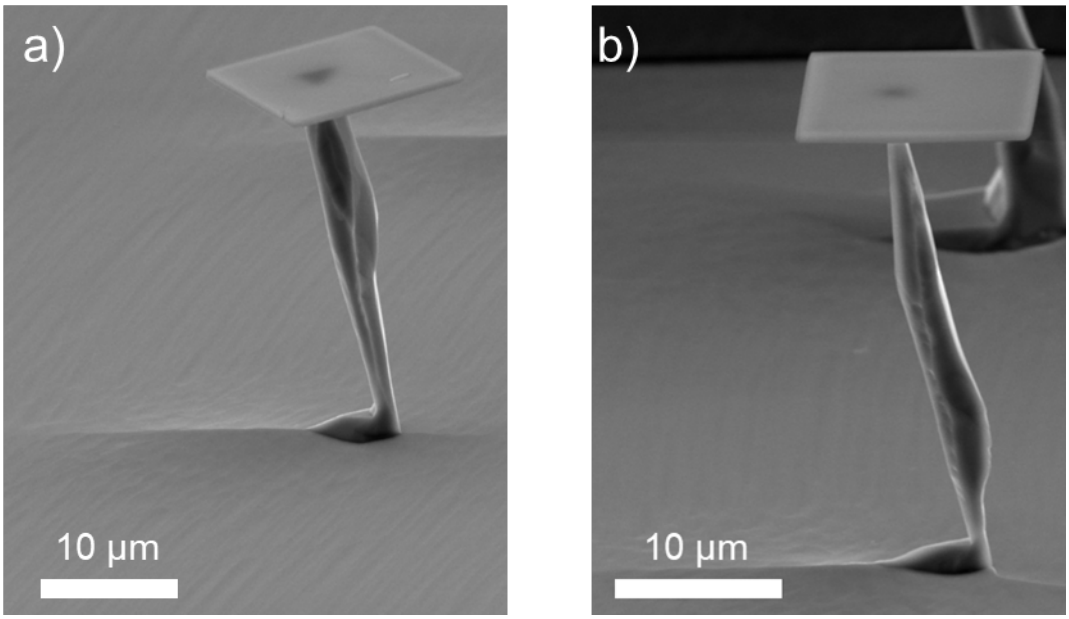


Figure 5.8: Silicon etching in TMAH + Triton X-100 using a) diamond and b) square-shaped mask. The dry-etching height is 30 µm for both masks.

It is interesting to note that all structures etched in TMAH + 1000 ppm Triton X-100 are slightly tilted. It is suggested that this occurs because of a combination of very high selective adsorption of the Triton X-100 on certain crystallographic planes [268], and a slight miscut of the Si(111) wafer which causes slightly different planes to be exposed during dry-etching on either side of the mask. This miscut is also responsible for the formation of tail-like structure to form near the etched structure as explained by Oosterbroek et. al.[258].

As can be seen in the previous two sections, the etching results vary drastically between Triton X-405 and Triton X-100, although both are non-ionic surfactants, with a similar molecular structure and identical concentration used in TMAH. The difference between the two surfactants lies only in their polyethylene oxide (PEO) chain length, with Triton X-405 having a longer PEO chain than Triton X-100 [272], thus making it more hydrophilic. The differences in the etching characteristics of the two surfactants were also noted by Goh et. al. [273]. Further study on the behavior of the two surfactants for AFM tip fabrication will be done in future work.

5.1.3. Summary and Conclusions

Various mask shapes and dry etching heights are studied for fabrication of AFM tips using (111)-oriented silicon wafers. Etching tests are conducted in pure 25 wt% TMAH, TMAH with 1000 ppm Trion X-405 and TMAH with 1000 ppm Trion X-100. The highest aspect ratio (11.4 and 13.8) and sharpest tips (apex < 10 nm) are obtained using circular-shaped mask with dry-etching heights being 30 μm or 40 μm and using 25 wt% TMAH + 1000 ppm Triton X-405 as the etchant. However, surface quality from TMAH + Triton X-405 was more rough compared to etching in pure TMAH or TMAH + Triton X-100. The smoothest surface was obtained with the addition of 1000 ppm Triton X-100 to TMAH.

Additionally, wafer miscut leads to formation of tails near the etched tips for all etchants [258]. This effect was more pronounced when surfactants were added, with Triton X-100 causing more prominent tails than Triton X-405.

5.2. ANISOTROPIC ETCHING OF (111) SILICON IN NON-IONIC SURFACTANTS

Wet anisotropic silicon etching is widely utilized to fabricate Micro Electro-Mechanical Systems (MEMS) for various applications [274-277] . Anisotropy is achieved using alkaline solutions, such as tetramethyl ammonium hydroxide (TMAH) or potassium hydroxide (KOH), which exhibit differential etch rates depending on the crystallographic orientation of the silicon substrate [104]. As discussed by Zubel [199], the origin of anisotropy in these systems is attributed to the complex interplay between the number and spatial arrangement of free bonds on different crystallographic planes. Surface atoms on silicon crystallographic planes can be categorized based on their position (step or terrace sites) and number of hydrogen-terminated bonds they possess, typically one or

two. These configurations are conventionally described using the following nomenclature: step-monohydride (SM), step-dihydride (SD), terrace-monohydride (TM), and terrace-dihydride (TD). Among the low-index silicon planes, atoms on the (100) surface are predominantly characterized as SD-type, possessing two hydrogen-terminated bonds. In contrast, atoms on the (110) and (111) planes are primarily identified as SM and TM types, respectively, each exhibiting a single hydrogen-terminated bond at step or terrace sites respectively. In alkaline solutions, terrace atoms exhibit significantly lower reactivity compared to step atoms [104], which contributes to the (111) plane having the slowest etch rate. Additionally, it has been observed by Zubel [199] that surfaces composed predominantly of SM-SM bonds, such as the (110) plane, etch more rapidly than those with SD-SD bonds, as observed on the (100) plane, despite SD atoms possessing two hydrogen-terminated bonds. This counterintuitive behavior is attributed to the influence of surface atomic configurations, including the distribution and nature of reactive sites, which may facilitate enhanced etching kinetics on certain planes. Variations in etch rates among crystallographic planes are therefore governed by the specific arrangement, bond saturation, and hydration characteristics of the surface silicon atoms.

Applications such as micro-needles, or tips for atomic force microscopy (AFM) require high aspect ratio structures [278], which can be realized through careful control of various design parameters, such as mask shape [251], orientation [261, 270], as well as by manipulation of etchant properties such as temperature [191], concentration [279], and addition of tensioactive compounds [194, 251, 274]. When silicon surface is masked, the final shape of the etched structure is heavily influenced by the mask geometry and orientation. In general, if the mask geometry has convex corners, the final profile of the etched structure will be composed of fast etching planes, while in the case of mask having concave corners, the final structure will be composed of planes having the slowest etching plane

[270]. The emergence of different planes as a result of mask geometry is explained in detail by Pal et. al. [270]

The addition of tensioactive compounds, such as alcohols [280, 281], or surfactants [264] to alkaline etchants can significantly influence the anisotropy [264, 282] i.e. the slowest local etching rate plane may be changed and thus the final stable profile can be manipulated. This effect arises from the preferential adsorption of these compounds on crystallographic planes rich in step-monohydride (SM) sites, which have lowest density of hydrogen terminated sites, such as (111), while minimal adsorption occurs on planes dominated by step-dihydride (SD) configurations [185, 197]. Adsorbed tensioactive molecules act as barriers, restricting the access of etchant species to the surface and thereby reducing the etch rate of the affected planes. In practice, isopropyl alcohol (IPA) is commonly used as an additive in KOH-based etchants, whereas surfactants are typically employed with TMAH solutions. The effectiveness of alcohols in manipulating etch behavior is contingent upon the saturation of the etchant with the tensioactive species [283]. However, in order to achieve saturation in TMAH, significantly higher amount of alcohol is required compared to KOH [199]. Addition of high concentration of alcohol decreases TMAH concentration which equally decreases etch rates of all planes, thus the anisotropy remains unaffected [199, 284]. On the other hand, a small concentration of surfactant in TMAH can cause pronounced change in anisotropy [194]. The degree and nature of the modification are highly dependent on both the type and concentration of surfactant, as well as specific properties of the etchant. For example, Yang et. al. reported that cationic ASPEG, when added to 10 wt% TMAH, results in the lowest surface roughness for (100)-oriented silicon [264]. On the other hand, researchers in [194] found that anionic SDSS, when added to KOH, produced the smoothest (100) surface, while the same surfactant in TMAH resulted in highest roughness. An interesting feature of non-ionic surfactant addition to TMAH when etching

pillars on (111)-oriented silicon wafer, is the formation of neck-like feature along the pillar length. Since both the top mask and bottom (111) plane are etch-stop, the neck should theoretically lie at the mid-point of the pillar height. This behavior has been discussed in our earlier work [251] and has also been noted by others [265]. The presence of this neck-like feature facilitates the fabrication of structures with higher aspect ratios than those achievable through etching in pure TMAH alone. It has also been reported that non-ionic surfactants in TMAH provide the smoothest surface along with high anisotropy [196]. Among these, Triton X-100 is one of the most widely used non-ionic surfactants in TMAH. It shares structural similarity with Triton X-405, with both being polyethylene oxide (PEO)-based non-ionic surfactants with octylphenol hydrophobic head group [285]. The primary difference lies in the length of their PEO chains, with Triton X-100 containing an average of 9.5 PEO units and Triton X-405 containing an average of 35 PEO units.

Previous studies have shown that when (100)-oriented silicon is etched in KOH containing these surfactants, Triton X-405 results in a lower etch rate for the (100) plane than Triton X-100 at concentrations between 1–10 ppm, suggesting greater surface coverage due to the longer PEO chain [273]. However, at higher concentrations (e.g. 100 ppm), Triton X-100 decreases the (100) etch rate more effectively than Triton X-405. In this study, we investigate the influence of varying concentrations of Triton X-100 and Triton X-405 on the etching behavior of silicon pillars on (111) oriented wafer using 25 wt% TMAH.

*5.2.1. **Experiment***

(111)-oriented silicon wafer is cleaned in oxygen plasma for 1 minute, after which 1 μm silicon dioxide (SiO_2) is deposited using Plasma Enhanced Chemical Vapor Deposition (PECVD). Next S1811 resist is spin coated and patterned using UV direct write system (MLA150, Heidelberg Instruments) to pattern 15 μm diameter circular masks on the wafer. RIE is used to transfer patterns

to oxide hard mask. Given that (111) plane is almost resistant to wet anisotropic etching, Reactive Ion Etching (RIE) is performed to expose the sidewall surface which then undergoes lateral wet etching. Si RIE is done with oxide hard mask using standard Bosch etching for 73 cycles (deposition: SF_6/C_4F_8 : 1/160 sccm, ICP: 1000 W, RF : 5 W, 20 mTorr, 5 seconds; etching: SF_6/C_4F_8 : 160/1 sccm, ICP: 1000 W, RF: 20 W, 25 mTorr, 7 seconds), resulting in 30 μm tall pillars.

After Bosch etching, samples are cleaned in oxygen plasma again to remove fluorocarbon residue. Before wet anisotropic etching, the samples are dipped in 1:10 HF for approximately 10 seconds in order to remove native oxide. The samples are then rinsed with deionized water and dried using nitrogen before being placed in the alkaline etchant. Etchants used in this work are 25 wt% TMAH obtained from Acros Organics, TMAH + Triton X-100 (100% iso-octylphenoxy polyethoxyethanol) and TMAH + Triton X-405 (70% polyoxyethylene alkyl phenyl ether). Both surfactants are obtained from Sigma Aldich and their concentration is varied from 1 to 1000 ppm. Etching is done at 70 °C for 5 minutes without stirring.

The surfactant modified etchants are prepared by first making a stock solution of 1000 ppm by adding 0.15 mL of surfactant to 150 mL of TMAH, followed by manual stirring for 15 min. The 100-ppm solution was obtained by mixing 5 mL of the 1000 ppm stock solution with 45 mL of TMAH and stirring manually for 15 min. Similarly, the 10-ppm solution was prepared by diluting 5 mL of the 100-ppm solution with 45 mL of TMAH, and the 1 ppm solution was prepared by diluting 5 mL of the 10-ppm solution with 45 mL of TMAH. Both were stirred manually for 15 min.

*5.2.2. **Results and Discussion***

Circular masks are chosen to eliminate the complexity which arises due to mask shape and orientation [286, 287]. After dry etching the pillars have an angle of 90° with respect to the (111) surface, thus revealing the $(1\bar{1}0)$ plane and other planes.

Figure 5.9 shows the pillars after Bosch etching (figure 5.9 a) and after 5 minutes of subsequent TMAH etching (figure 5.9 b). It is observed that in pure TMAH (i.e. 25 wt% TMAH solution without surfactant), etching proceeds uniformly along the pillar length, resulting in a broader base that reveals the fastest etching $(1\bar{1}3)$ planes. Continued etching under these conditions leads to the dominance of this plane, ultimately producing a low aspect-ratio pyramid-like structure. This is in line with results obtained by others where (311) has the local highest etching rate in TMAH [191, 288].

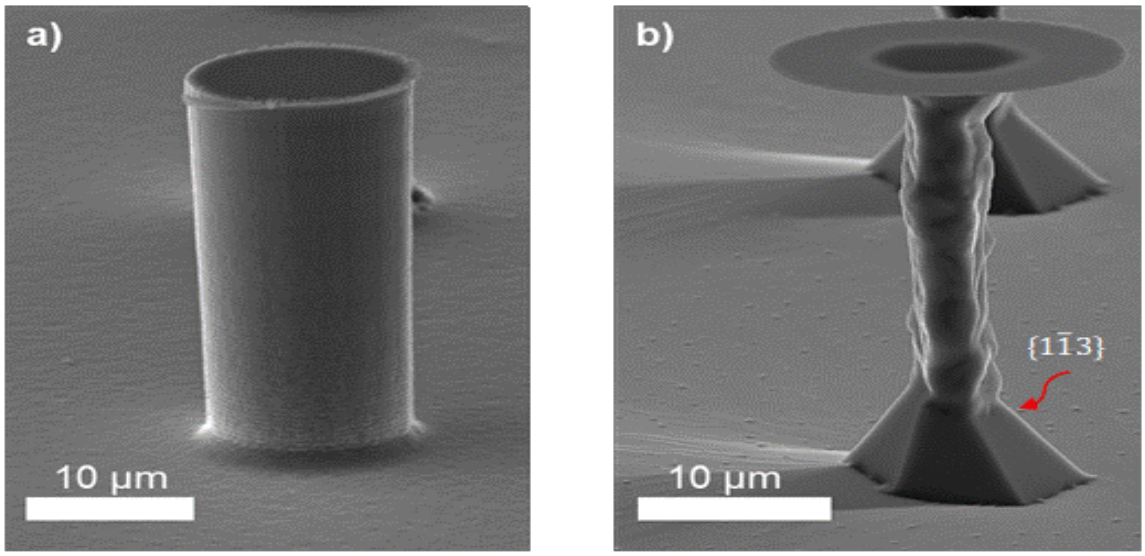


Figure 5.9: a) Pillars formed on (111) surface after Bosch etching. b) Etching profile after TMAH etching.

Figure 5.10 shows the etching results for surfactant added TMAH etching. With surfactant-added-TMAH (figure 5.10), etch profile becomes non-uniform along the pillar length. This deviation is attributed to the significant alteration in anisotropy caused by selective surfactant adsorption on different crystallographic planes. Consequently, the final etched geometry is significantly different

from that produced by pure TMAH. Notably, for both surfactants examined, a characteristic neck-like feature forms along high index planes, enabling the realization of higher aspect ratio structures. At 1 ppm surfactant concentration, the etching is visibly non-uniform across the length of the pillars for both Triton X-100 and Triton X-405, indicating incomplete adsorption and insufficient surface saturation by the surfactant molecules. This problem is substantially mitigated at higher surfactant concentration ($\geq$ 10 ppm). At this concentration, the $(1\bar{1}3)$ plane remains the dominant etching facet for both surfactants; if etching proceeds, the final morphology will comprise of low-index, pyramid-like structures, consistent with pure TMAH.

As surfactant concentration increases, greater adsorption on the $(1\bar{1}0)$ pillars suppresses etching, yielding a more uniform profile along the pillar height and revealing clear dominant sidewall planes. For Triton X-100 the sidewall evolves to $(1\bar{3}3)$ plane whereas for Triton X-405 in TMAH it evolves to $(2\bar{1}0)$. Because adsorption on $(1\bar{1}0)$ alters etch anisotropy, the profiles deviate from those in pure TMAH. At 10 ppm, Triton X-405 yields a $(2\,\bar{1}\,0)$ sidewall, even after mask detachment, whereas 10 ppm Triton X-100 produces either $(1\bar{3}3)$ or $(1\bar{1}3)$, indicating similar etch rates for these planes. Importantly, the low-concentration X-100 response more closely resembles pure TMAH, consistent with its shorter PEO chain being less effective at blocking etchant species; by contrast, the longer-chain X-405 more strongly perturbs anisotropy. It is important to note that at 10 ppm, the surfactant concentration remains below the saturation threshold for surface adsorption, with this saturation likely occurring between 100 and 1000 ppm [285, 289].

At higher surfactant concentrations, $(1\,\bar{1}\,3)$ plane is suppressed for both surfactants and the sidewalls are composed solely of high index planes: $(2\bar{1}0)$ for TMAH + Triton X-405, $(1\bar{3}3)$ for TMAH + Triton X-100. This suggests that Triton X-100 can produce slightly steeper tips than Triton X-405.

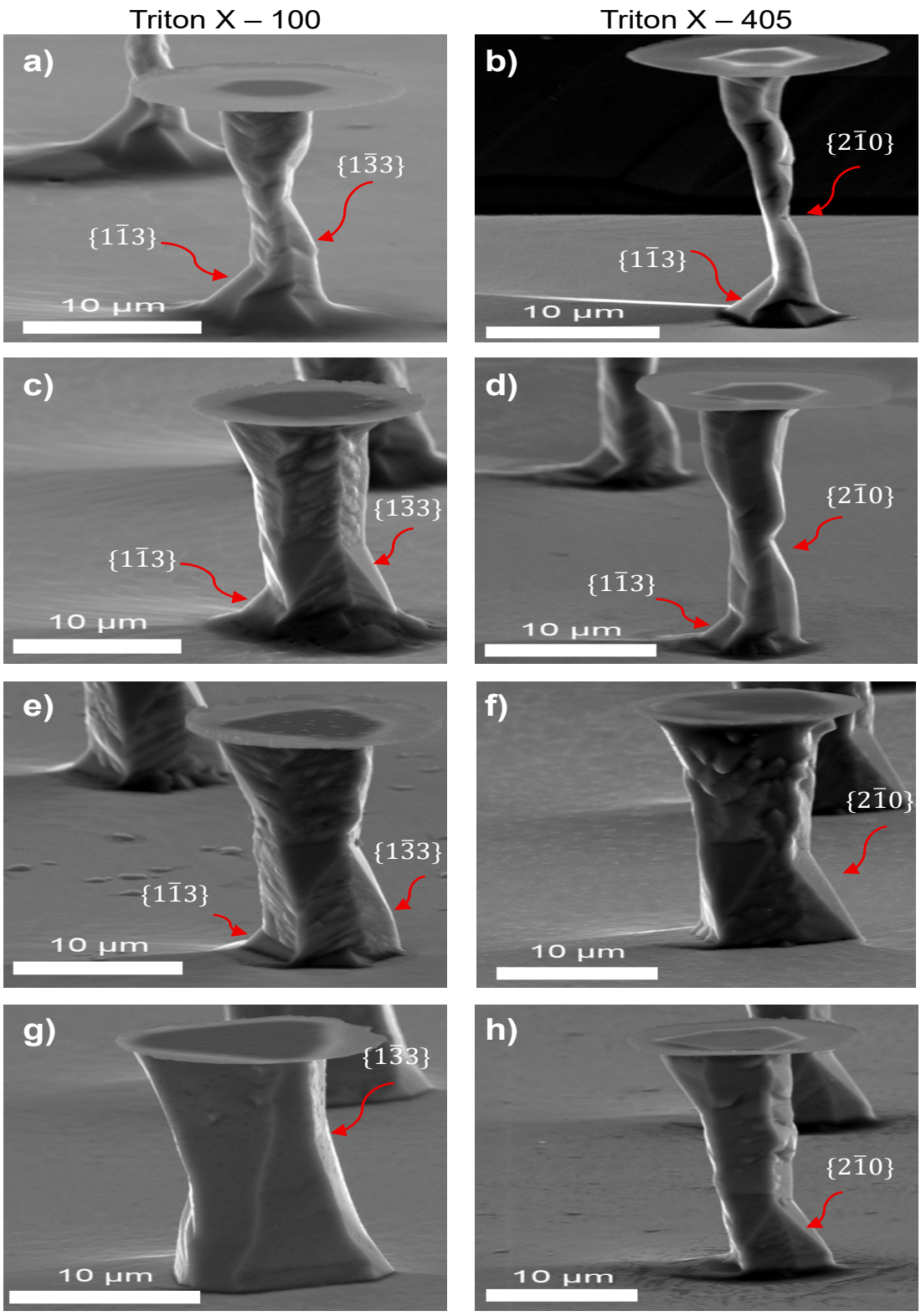


Figure 5.10: Etching profiles after wet anisotropic etching in a-b) 1 ppm, c-d) 10 ppm, e-f) 100 ppm, g-h) 1000 ppm surfactant concentration. The Millar index for various planes are inserted according to our best understanding using stereographic projection of (111) silicon as well as literature.

Figure 5.11 shows the AFM tips fabricated using pure TMAH as well as TMAH + 1000 ppm Triton X-100 and Triton X-405. As evident from the figure, pure TMAH etching results in very low aspect ratio tips having $(1\bar{1}3)$ plane as the sidewall. However, the addition of both Triton X-100 and Triton X-405 results in higher aspect ratio compared to that obtained by pure TMAH.

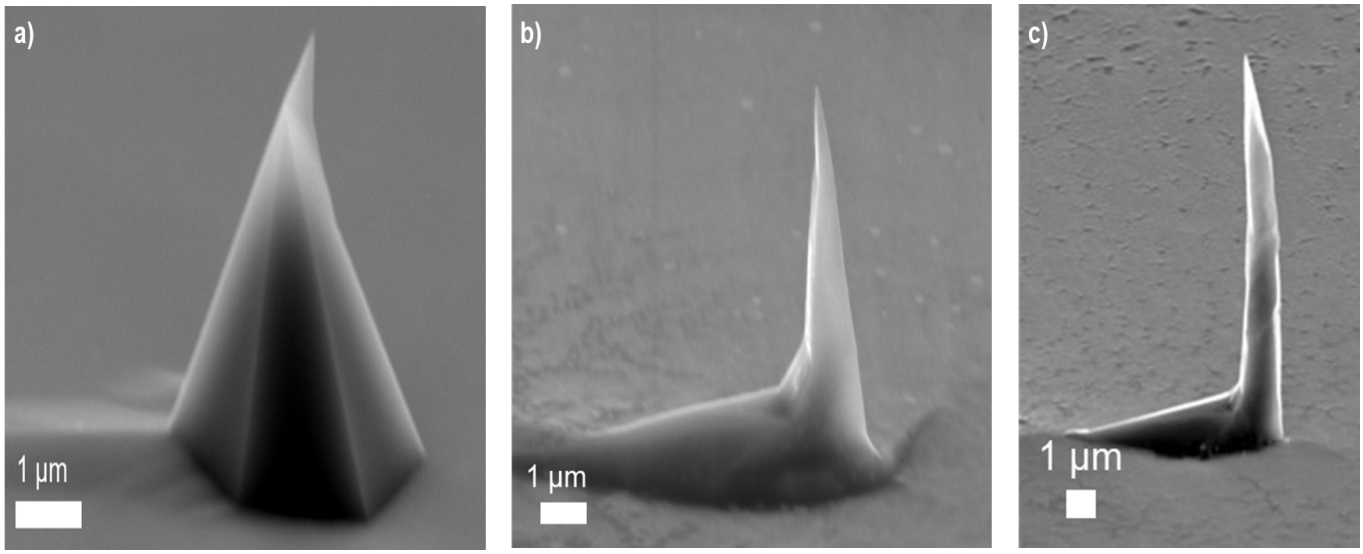


Figure 5.11: AFM tips fabricated using a) pure 25 wt% TMAH, b) TMAH + 1000 ppm Triton X-100 and c) TMAH + 1000 ppm Triton X-405.

Figure 5.12 shows a decrease in undercut as surfactant concentration increases, indicating higher surfactant adsorption. For this work, undercut is the difference between mask dimensions and the pillar width immediately below the mask. For Triton X-100, the reduction in undercut is gradual and uniform, whereas Triton X-405 exhibits a sharp decline in undercut between 10 and 100 ppm, as shown in figure 5.12. These results are in agreement with those reported by Goh. et. al. [273], and likely indicate a change in adsorption mechanism of Triton X-405 between this range.

A clear distinction occurs between Triton X-100 and Triton X-405 in terms of undercut, and sidewall smoothness across all tested concentrations. Triton X-100 consistently results in lower undercut but produces rougher sidewalls compared to Triton X-405. This is attributed to the longer PEO chains in Triton X-405 which are more effective at facilitating hydrogen bubble removal

during etching, leading to smoother sidewall profiles compared to the shorter-chain Triton X-100. At higher surfactant concentration (≥ 100 ppm), the etch rate suppression is higher by Triton X-100 compared to Triton X-405. This behavior is likely attributed to the greater steric hindrance associated with the longer polyethylene oxide (PEO) chains of Triton X-405, which limit the number of surfactant molecules that can effectively adsorb onto the silicon surface. Additionally, both surfactants exhibit saturation in their undercut profile between 100 and 1000 ppm, as evidenced by the plateauing of undercut values in this concentration range. These findings are consistent with previously reported results by other researchers [273, 285].

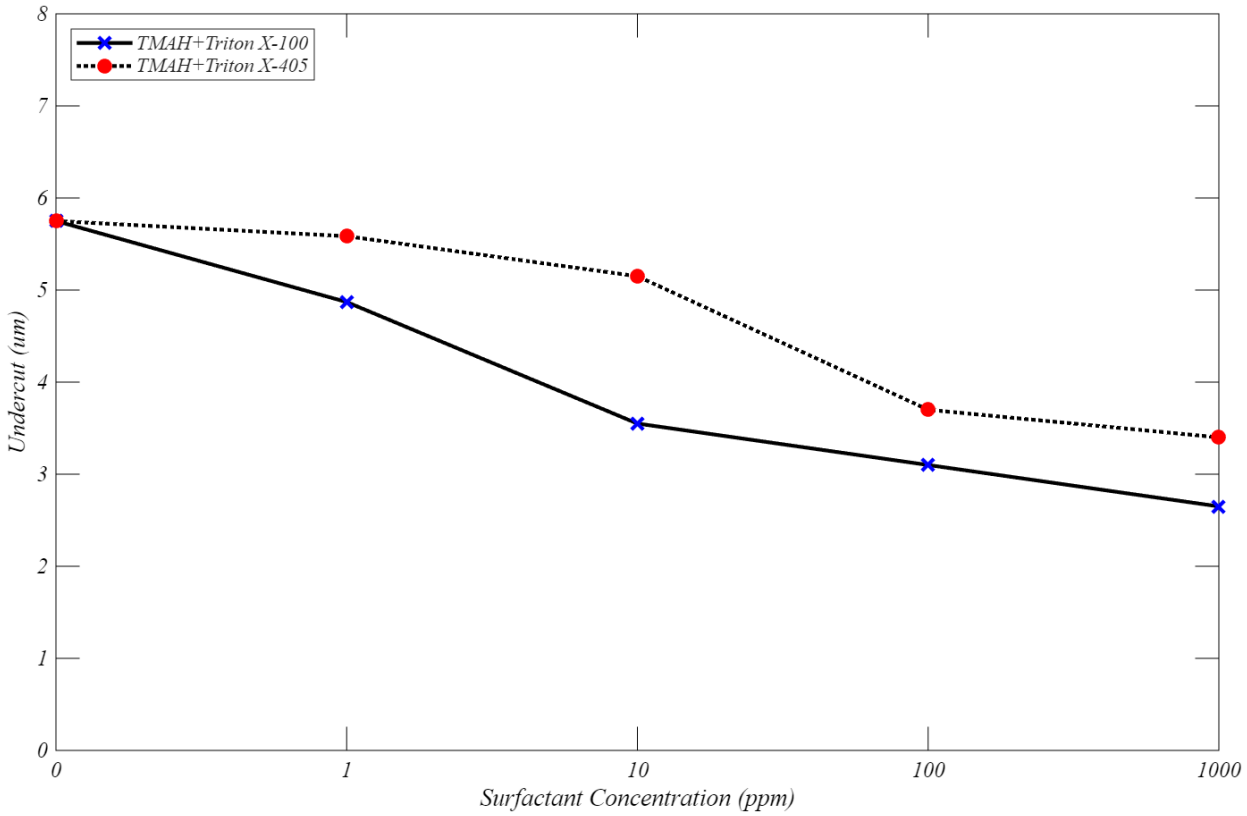


Figure 5.12: Undercut at different surfactant concentrations.

A tail-like feature is also observed at the base of the wet-etched pillars, as shown in Figure 5.13. This structure likely arises due to the off-axis orientation of the (111) silicon wafers [258]. This tail-

like feature is most pronounced in samples etched with pure TMAH and progressively diminishes with increasing surfactant concentration. This trend suggests enhanced surfactant adsorption on the (111) surface, which suppresses the formation of the tail-like structure by reducing etch rates along the miscut planes.



Figure 5.13: Top view of sample etched in pure TMAH.

*5.2.3. **Conclusion***

The effects of non-ionic surfactants Triton X-100 and Triton X-405 on the anisotropic wet etching behavior of (111)-oriented silicon in 25 wt% TMAH were systematically investigated. Both surfactants enabled the formation of high aspect ratio pillar structures. At low concentrations (1 ppm), incomplete surface coverage led to non-uniform etching profiles. This issue is resolved at higher surfactant concentrations (≥ 10 ppm).

When surfactant concentration reaches ≥ 100 ppm, Triton X-100, characterized by a shorter polyethylene oxide (PEO) chain, exhibits greater etch rate suppression due to higher adsorption

density. In contrast, Triton X-405, with its longer PEO chain, was less effective in etch-rate suppression but resulted significantly smoother sidewalls, likely due to better removal of hydrogen bubbles. A sharp decrease in undercut was observed for Triton X-405 between 10 and 100 ppm, suggesting a change in adsorption behavior within this concentration range.

Additionally, the formation of tail-like structures at the pillar base, which was previously attributed to wafer mis-cut, was most prominent in pure TMAH and significantly reduced with surfactant addition, indicating effective surfactant adsorption even on the (111) plane.

Overall, this study demonstrates that tuning surfactant type and concentration can provide etch profiles with desirable structural characteristics, such as smoother sidewalls, higher aspect ratios, and controlled undercut.

CHAPTER 6: FABRICATION OF TETRAHEDRAL TIP ON SILICON

6.1. TETRAHEDRAL AFM TIP

Tetrahedral tips are specialty AFM tips having tip at the very end of the cantilever. One end of the tip is usually perpendicular to the cantilever while the other side is sloped. This architecture allows for accurate imaging of near-vertical steps [290], with exceptional lateral resolution [291], as well as having ease of positioning on the sample surface. As shown in figure 6.1, the tip positioned at the edge of the cantilever allows easy positioning of the tip with the area of interest on the sample surface while the vertical sidewall of the tetrahedral tip allows for accurate measurement of the trench aspect ratio. However, the accuracy of measurement is strongly dependent on the sidewall angle of the vertical side of the tip which must be close to 90° to allow for accurate measurement of the trench.

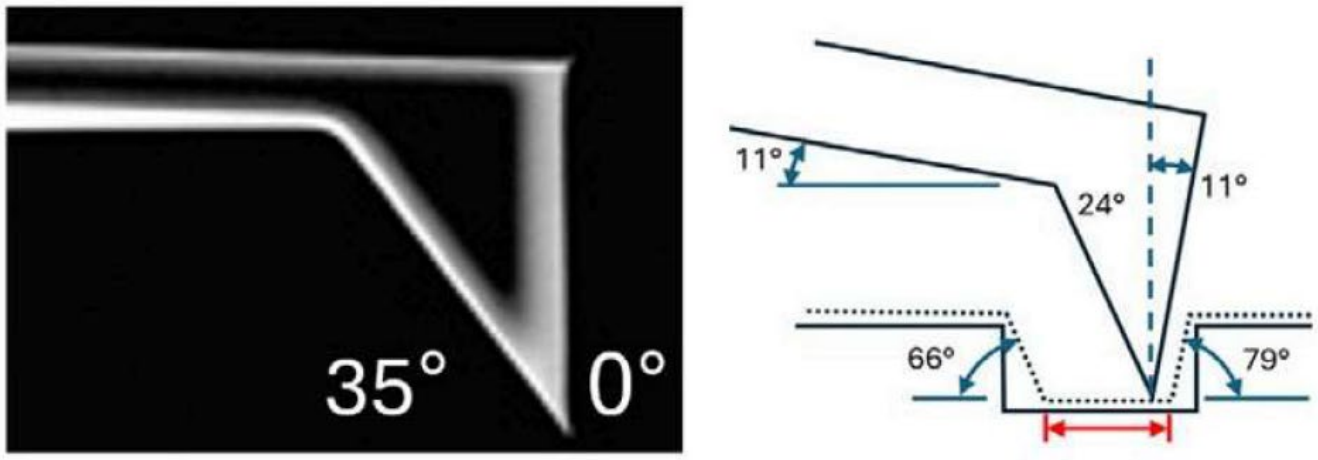


Figure 6.1: Imaging of trench using tetrahedral AFM tip. Reproduced with permission from Oxford Instruments [292].

The requirement for vertical sidewall makes the fabrication of tetrahedral tip difficult – if not impossible – by mask manipulation or additives to the etchant. This is because the vertical sidewalls on (100) surface would be formed by either {021}, {002}, {110} or {022} planes, all of which do not emerge as stable planes during anisotropic etching in alkaline solutions such as TMAH or KOH [288] or by any additives used in literature so far [194, 293]. Although (110) silicon wafer can be wet etched to form very high aspect ratio structures [277], the requirement for one side of the tip to be sloped, makes use of (110) silicon unfeasible. This is why dry etching cannot be used to fabricate tetrahedral tips. For this reason, tetrahedral tip is fabricated using a combination of dry etching, to form vertical sidewalls, and wet etching to form the slope and to provide cone shape to the tip. This work is typically carried out using (100) silicon wafer which anisotropically etches to expose (111) plane having an angle of 54.7° from the wafer surface. Additionally, (111) plane is exposed during concave corner etching [270] of the (100) planes and is almost exclusively the plane which is exposed when (100) silicon is anisotropically etched to form a trench [294], regardless of the type of alkaline etchant used [189]. This fact removes the need for manipulation of process parameters. However, the need for vertical sidewalls does require some design manipulation.

In this chapter, we have developed two methods for the fabrication of tetrahedral tips using (100) oriented silicon wafers.

6.2. FABRICATION OF TETRAHEDRAL TIP USING Si_3N_4 MASK

6.2.1. Experiment

Figure 6.2 shows the fabrication of tetrahedral tip using 50 nm LPCVD Si_3N_4 as mask. First, HMDS is coated on the sample, followed by resist coating of 3 μm NLOF-2035 (figure 6.2 b). The sample is then patterned by photolithography using direct write UV lithography system (MLA150, Heidelberg Instruments) using 375 nm laser, 220 mJ/cm^2 dose and -10 defocus. Next the sample

undergoes post exposure bake at 110°C for 1 minute. The pattern is then transferred to Si_3N_4 by RIE (SF_6: 45 sccm, RF: 20 W; ICP: 2000 W; 10mTorr; 5C) (figure 6.2 c), and trenches are formed in the (100) oriented silicon using a combination of pseudo-Bosch (C_4F_8/SF_6: 40/20 sccm, RF: 50W, ICP:1200W, 10mTorr, 15C) and standard Bosch etching (Etch: 20 W RF power, 1000 W ICP power, SF_6/C_4F_8 flow 160/1 sccm, 25 mTorr, 6s; Passivation: 5 W RF power, 1000 W ICP power, SF_6/C_4F_8 flow 1/160 sccm, 20 mTorr, 6s) (figure 6.2 d). This combination allows for smooth sidewalls to be formed on the top of the trench which is useful in oxidation sharpening of the final formed tip. The silicon is etched down to the oxide etch stop. Remaining resist is then removed by Remover PG. Next the substrate undergoes thermal oxidation at 1000°C for 3 hours which results in 200 nm oxide formation on the sidewalls of the silicon substrate (figure 6.2 e), but not on the top surface since the nitride layer blocks the oxidation process. The Si_3N_4 is then removed using RIE (figure 6.2 f) and the silicon undergoes wet etching in 25 wt% TMAH at 70°C (figure 6.2 g). The oxide is then removed by 1:10 BOE for 10 minutes (figure 6.2 h). After tip fabrication, 10 μm of AZ4602 resist is spin coated on the front side of the sample. This resist acts as protection for the tip as well as used to pattern the cantilever using photolithography (405 nm laser, 1000 mJ/cm^2 dose and 0 defocus) (figure 6.2 i). The large width of the cantilever mask allows room for misalignment. Next the sample undergoes 3 μm deep reactive ion etching to pattern the cantilever (figure 6.2 j).

For handle fabrication, both front and backside of the sample are coated with 10 μm AZ4620 resist (figure 6.2 k). The front side coating acts as a passivation layer during backside patterning and etching. After coating, the backside resist is patterned by photolithography (laser 405 nm, dose: 900 mJ/cm^2, -10 defocus). After development, the sample is hard baked at 120°C for 5 minutes before undergoing dry etching for handle fabrication. Dry etching is performed by 700 cycles of

Bosch etching (Etch: 20 W RF power, 1000 W ICP power, SF_6/C_4F_8 flow 160/1 sccm, 25 mTorr, 6s; Passivation: 5 W RF power, 1000 W ICP power, SF_6/C_4F_8 flow 1/160 sccm, 20 mTorr, 6s) (figure 6.2 l). Finally, the resist is removed from front and backside of the sample, and the tip is released (figure 6.2 m).

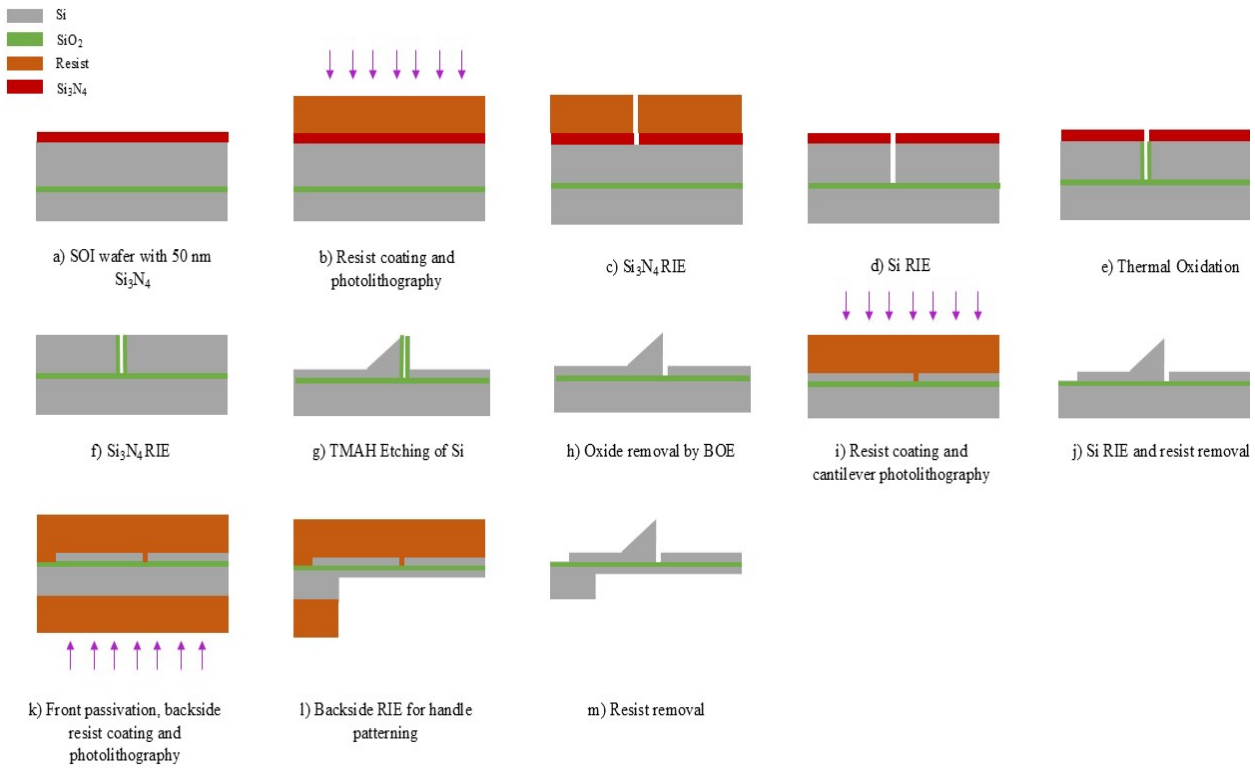


Figure 6.2: Process flow for tetrahedral tip fabrication using Si_3N_4 mask.

*6.2.2. **Results and Discussion***

As mentioned above, the tetrahedral tip has different profile on two sides of the mask. For this reason, a symmetrical mask cannot be used. Instead we require a mask with at least one side that can produce vertical sidewalls. For this purpose several mask designs were tested, such as square (two sides parallel to <110> flat), diamond (two sides having 45° angle with <110> flat), and V-shaped masks. The results after silicon etching in TMAH are shown in figure 6.3. As detailed by authors in reference [270], when four sides of a square-shaped mask are aligned with the (110)

direction, the (111) planes emerge as slopes along the sides but not at the corners. Since tip formation requires the slope to originate from the corner, a square mask aligned in this manner is not suitable. In contrast, the diamond-shaped mask exposes corners from which the (111) planes develop, enabling the formation of a tetrahedral tip. However, because the diamond-shaped mask produces tips at all four corners, it is not suitable for cantilever fabrication. Thus we chose a V-shaped mask for tip formation, which is shown in figure 6.4.

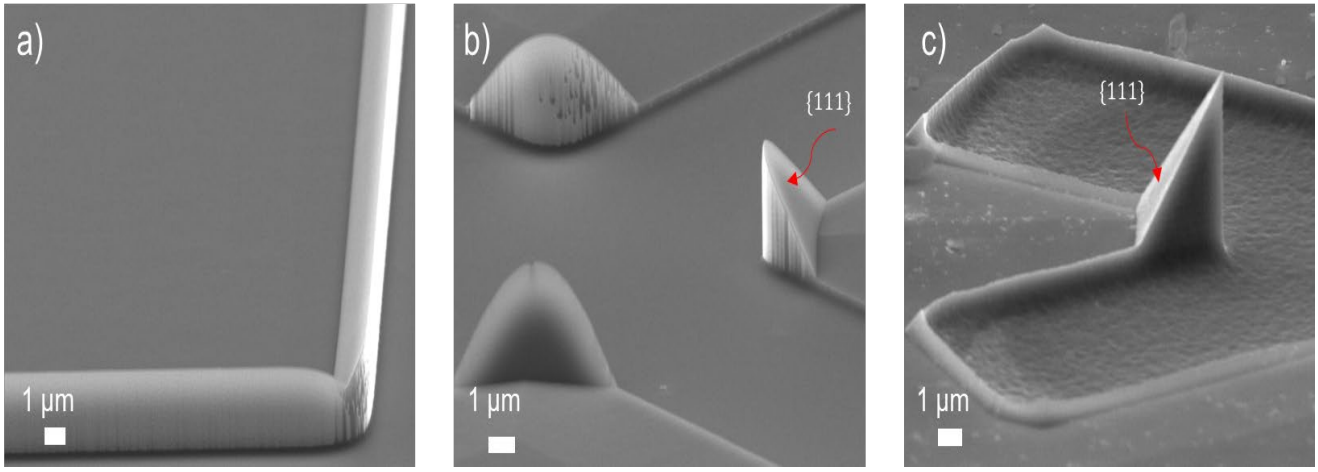


Figure 6.3: SEM image after silicon etching in 25 wt% TMAH at 70°C for 20 minutes using a) square, b) diamond and c) V-shaped masks.

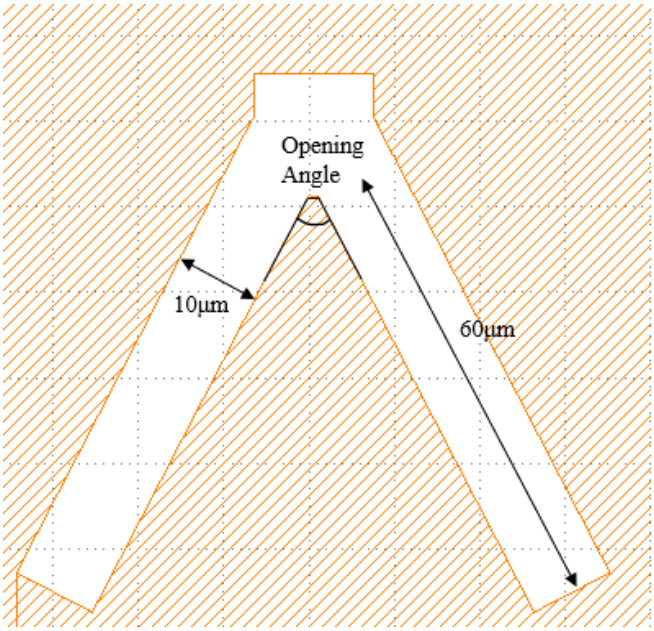


Figure 6.4: Mask for tetrahedral tip fabrication

The width of the V-shaped mask is fixed at 10 µm, while the length is fixed at 60 µm with neither parameter affecting the shape of the tip. The tip apex is solely determined by the opening angle of the V-shaped mask. For this purpose, several opening angles were tested between 40° to 80°. It was found that the sharpest tip was formed when the opening angle of the V-shaped mask was 50°. Figure 6.5 shows the trend for apex size versus mask opening angle.

The larger apex diameter observed for smaller opening angles is likely due to the bird's beak effect during masked oxidation [295]. This arises from the lateral diffusion of oxygen beneath the Si_3N_4 mask, which oxidizes the underlying silicon. As the silicon at the apex is consumed, the remaining silicon becomes less sharp, with the effect being more pronounced at smaller opening angles where lateral oxide growth beneath the V-shaped corner is more severe. Although this effect decreases as the tip mask becomes wider, increasing the opening angle also leads to a broader, less sharp silicon apex. Consequently, the smallest apex diameter is obtained at a moderate opening angle of 50°.

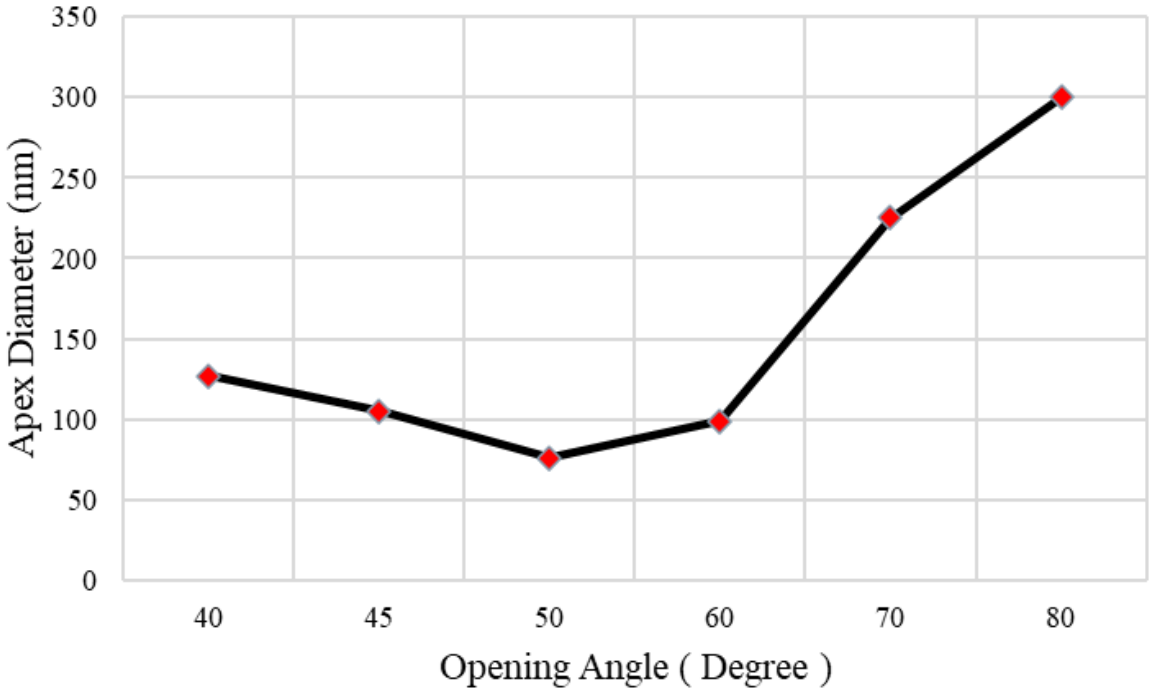


Figure 6.5: Trend for mask opening angle versus tip apex diameter.

To evaluate the effect of V-shaped trench etching depth, we considered cases where the silicon was not etched completely to the buried oxide layer of the SOI wafer. In such cases, because the cantilever pattern cannot be perfectly aligned with the V-shaped tip pattern, the tip must be included within the cantilever design. This requires the cantilever to extend beyond the tip apex, leaving a thin silicon base beneath and around the tip tetrahedral pyramid. Furthermore, insufficient trench depth allows lateral etching beneath the silicon at the trench bottom, which can attack the silicon on the inner side of the V-shaped opening. The effects of this effect is shown in figure 6.6

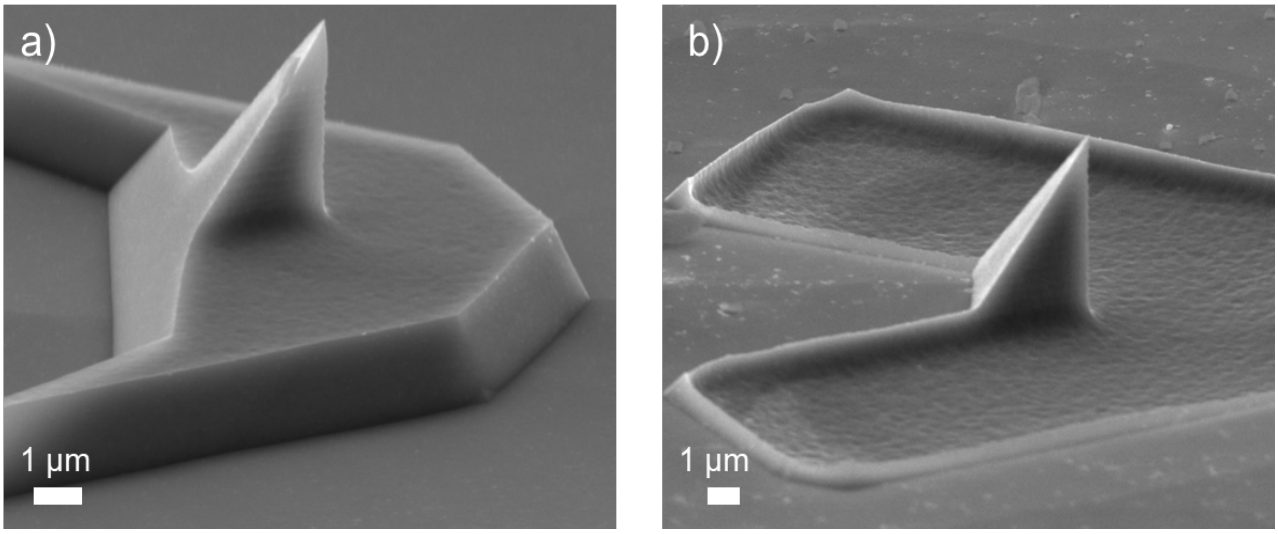


Figure 6.6: Tip obtained after TMAH etching, a) when silicon is not dry etched to expose underlying oxide in SOI wafer and b) silicon is dry etched to the expose underlying oxide in SOI wafer.

The etch rate of (100) oriented silicon wafer in 25 wt% TMAH is 350 nm/min at 70°C. The top layer of SOI wafer was 10 µm and we require 3 µm thick cantilever. Thus, the tip height was set to be 7 µm which was achieved by 20 minutes of etching in 25 wt% TMAH at 70°C. The sloped side of the tip formed has an angle of 54.7° with the (100) surface, thus it is classified as (111) plane. Due to the presence of oxide on one side of the silicon trench, that area is not etched by TMAH. Once the oxide is removed by BOE, the resulting tip has one side with 54.7° slope, while the other side is perpendicular to the surface. Figure 6.7 shows the SEM image of the resulting tip. The tip apex is ~ 95 nm without oxidation sharpening and the tip height is 7 µm.

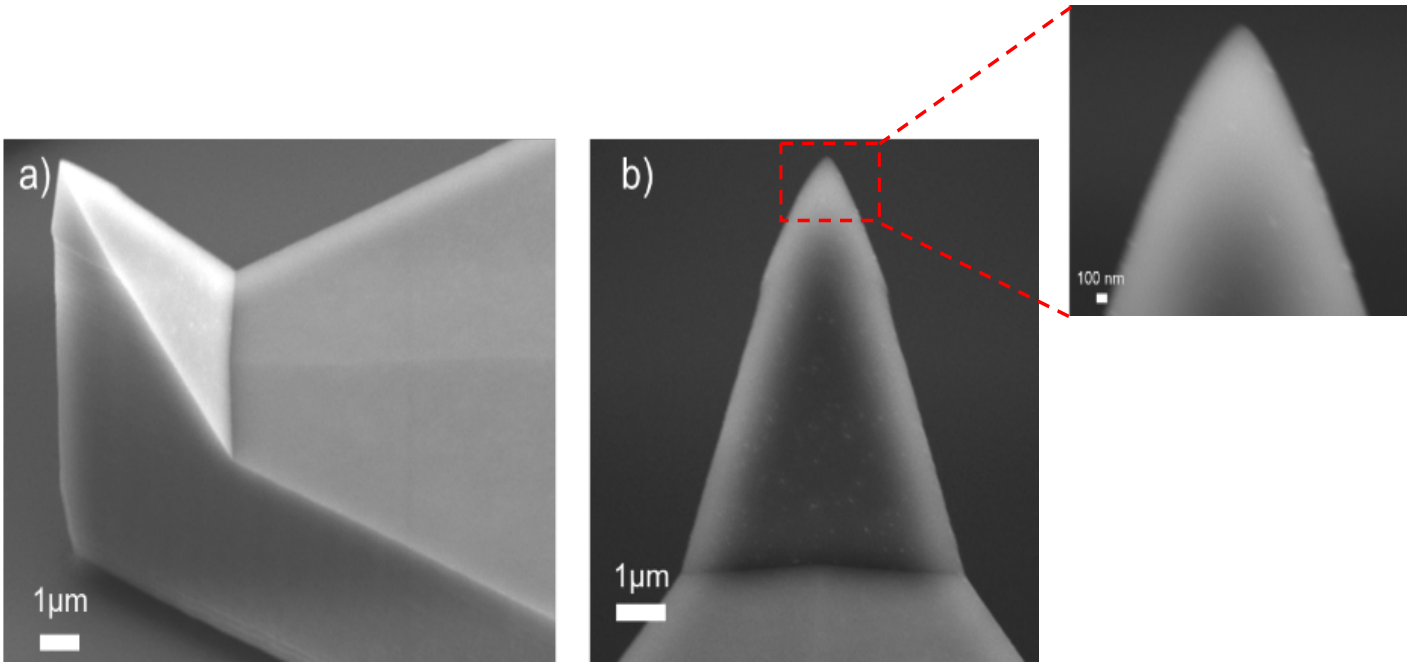


Figure 6.7: SEM image of tetrahedral tip after TMAH etching.

Due to the large width (10 µm) of the tip mask, the cantilever does not require precise alignment, and the tip can be easily patterned to be on the edge of the cantilever. Figure 6.8 shows the sample after cantilever patterning and subsequent RIE. The cantilever height is 3 µm and the length is 400 µm.

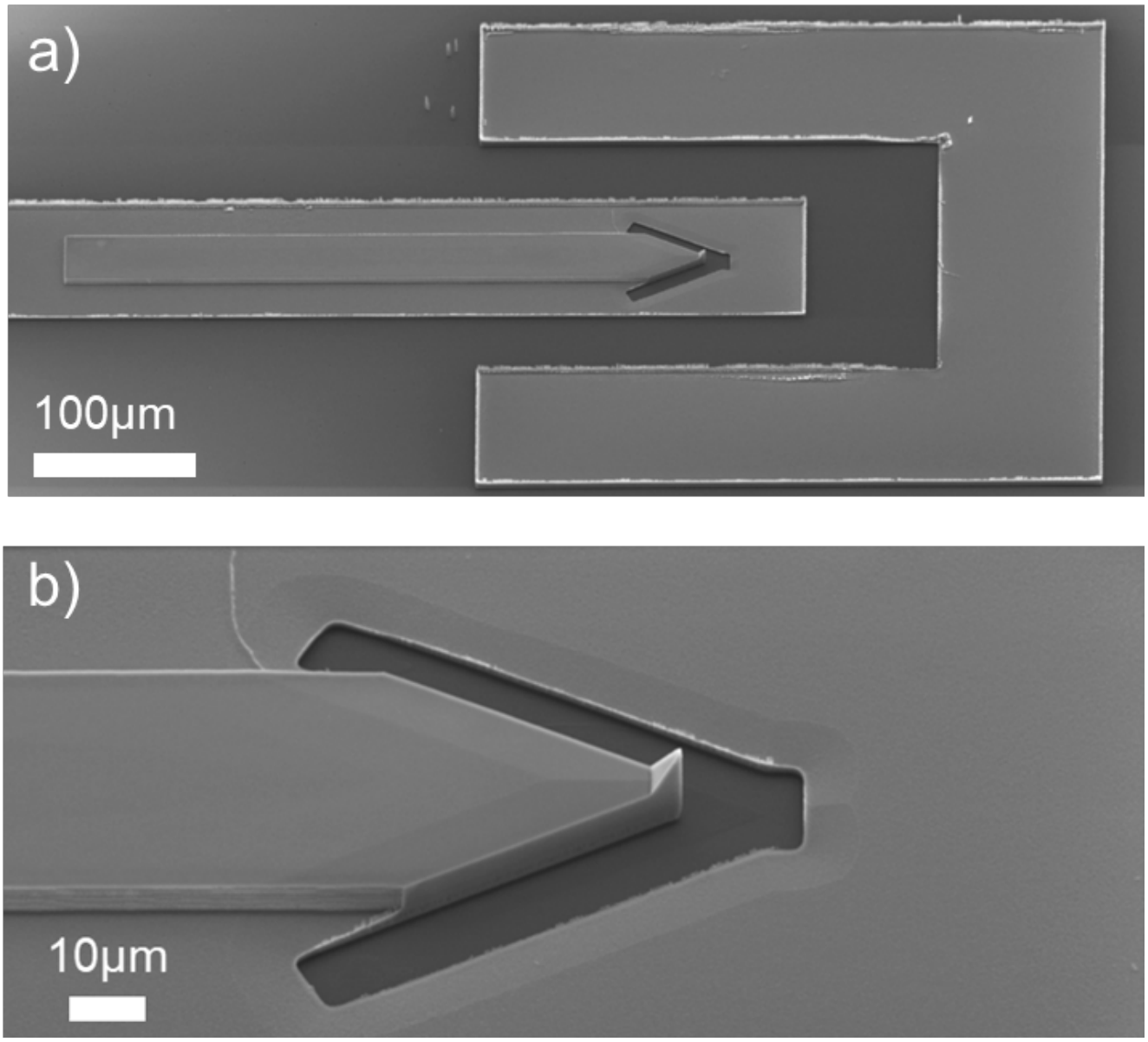


Figure 6.8: SEM image of tetrahedral tip after cantilever patterning. a) top view; b) tilted view.

6.3. FABRICATION OF TETRAHEDRAL TIP BY ION MILLING

The fabrication technique detailed in section 6.2 requires the use of LPCVD nitride mask to prevent the top silicon surface from oxidation. However, the formation of LPCVD nitride is a complicated and expensive process and not readily available in many research laboratories. Other materials such as PECVD nitride are not able to withstand the high temperature annealing required for

thermal oxidation, and PECVD nitride is much less resistant to KOH or TMAH etching than LPCVD nitride. Another issue with the previous method is the "bird-beak" that refers to the lateral oxidation of the silicon beneath the nitride mask and affects the final tip apex sharpness.

Though it is possible to use SOI wafer without a nitride layer and oxidize the silicon surface along with sidewalls, the subsequent removal of the oxide from the surface by RIE will almost certainly remove some sidewall oxide. In this section we have developed a novel method, which allows for removal of only surface oxide mask without effecting the sidewall oxide necessary to form vertical tip. The process uses angled ion milling of the oxidized silicon surface.

6.3.1. Experiment

The process flow for our developed method is shown in figure 6.9. First an SOI wafer with 15 μm thick top layer is cleaned by acetone and sonication (figure 6.9 a), followed by HMDS and photoresist coating. The resist is chosen to be NLOF 2035 which is patterned by photolithography using 375 nm laser, 220 mJ/cm^2 dose and -10 defocus (figure 6.9 b). After development, the resist acts as a mask to etch silicon using a combination of pseudo-Bosch (C_4F_8/SF_6: 40/20 sccm, RF: 50W, ICP:1200W, 10mTorr, 15C) and standard Bosch etching for 75 cycles (Etch: 20 W RF power, 1000 W ICP power, SF_6/C_4F_8 flow 160/1 sccm, 25 mTorr, 6s; Passivation: 5 W RF power, 1000 W ICP power, SF_6/C_4F_8 flow 1/160 sccm, 20 mTorr, 6s). The reason for two recipes to etch silicon is the same as that stated in section 6.2, i.e. to obtain smooth sidewall on top of the tip which later assists in oxidation sharpening (figure 6.9 c). Next the resist is removed by PG-remover, and the sample undergoes thermal oxidation at 1000°C for 3 hours which results in ~200 nm oxide formed (figure 6.9 d). The steps described so far are almost identical to those mentioned in section 6.2 (except for hard mask patterning). However, unlike the method stated in section 6.2, the oxide is formed on the top surface of the (100) wafer as well as the trench sidewalls. In order to remove

the oxide from only the top surface, while allowing the sidewall oxide to remain intact, ion milling is performed at an angle (figure 6.9 e). Once the oxide is removed from the surface, the sample undergoes TMAH etching (figure 6.9 f) and oxide removal (figure 6.9 g) to form the tetrahedral tip.

After tip formation, 15 μm thick AZ4620 resist is coated on the silicon wafer which serves as protection layer for the newly formed tip and is patterned for cantilever fabrication (figure 6.9 h). The cantilever is fabricated by etching 3 μm silicon by Bosch etching for 12 cycles (Etch: 20 W RF power, 1000 W ICP power, SF_6/C_4F_8 flow 160/1 sccm, 25 mTorr, 6s; Passivation: 5 W RF power, 1000 W ICP power, SF_6/C_4F_8 flow 1/160 sccm, 20 mTorr, 6s) (figure 6.9 i).

Finally, the handle is fabricated. First both front and backside of the sample are coated with 15 μm thick AZ4620 resist. The front side coating acts as a protective layer for tip and cantilever during handle fabrication while the backside layer is patterned to form handle (figure 6.9 j). After development, the sample is hard baked at 120°C for 5 minutes. During the subsequent RIE the resist acts as a mask against 700 cycles of Bosch etching (Etch: 20 W RF power, 1000 W ICP power, SF_6/C_4F_8 flow 160/1 sccm, 25 mTorr, 6s; Passivation: 5 W RF power, 1000 W ICP power, SF_6/C_4F_8 flow 1/160 sccm, 20 mTorr, 6s) to form the handle (figure 6.9 k). Finally, the resist is removed from both front and backside of the sample using PG remover, and the probe is released (figure 6.9 l).

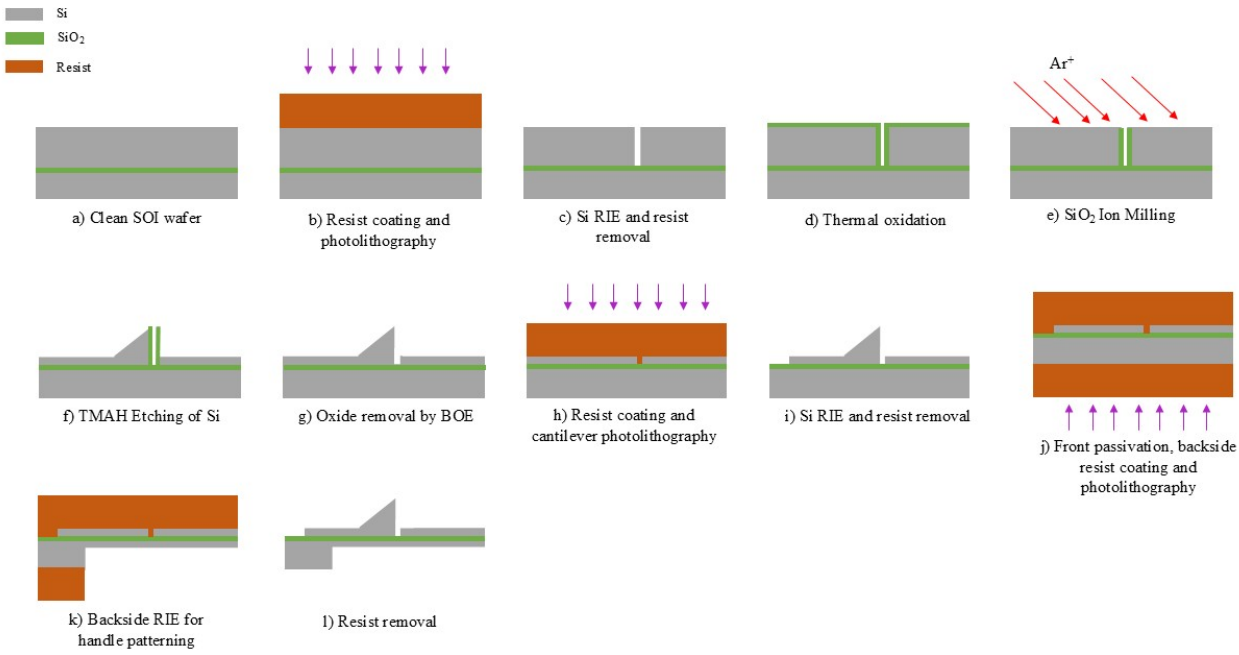


Figure 6.9: Process flow for fabrication of tetrahedral tip by ion milling.

*6.3.2. **Results and Discussion***

The pattern design for tip fabrication was the same as the one that was optimized in section 6.2 The width of the V-shaped mask was fixed at 10 µm, the length was 60 µm and the opening angle was 50°. Since we require that the ion milling process should only etch the top surface, while allowing the sidewall to remain intact, the ion bean should be at an inclination from the sample surface so that the sidewalls are not exposed to the energetic ions. It is known that the etch rate of any material is affected by the angle between the beam and the sample surface [296]. For this reason, the etch rate of thermal oxide was tested at various tilt angles between the beam and the surface. The beam voltage was set at 400 V, and the current was fixed at 190 mA. The results for etch rate of thermal oxide are shown in table 6.1.

Angle between beam and surface	Etch rate (nm/min)
20°	19.3
30°	24
40°	28.6
50°	28.3
60°	31.6
70°	28.6
75°	20
80°	11

Table 6.1: Etch rate of thermal oxide at various tilt angles between ion beam and sample surface.

Next, the patterned sample was etched at each angle, according to the etch rate obtained in table 6.1. We found that when the angle between the beam and sample surface was between 90° and 60°, no tip was formed after TMAH etching due to the sidewall oxide being etched away. However, when the angle was 50° some sidewall passivation began and tip was formed after TMAH etching, although the tip sidewall was not vertical since some of the sidewall oxide was etched during ion milling. Figure 6.10 shows the SEM image of the tip formed after TMAH etching for 20 minutes, when the angle between the beam and sample surface is 50°. It is proposed that the sidewall roughness observed after TMAH etching originates from localized oxide removal during the ion milling step or barely adequate oxide thickness. Once oxide in some random spot on the sidewall

is consumed during TMAH etching, the exposed silicon in these regions is rapidly etched by TMAH, amplifying the roughness as the silicon etching rate is ~1000× that of oxide.

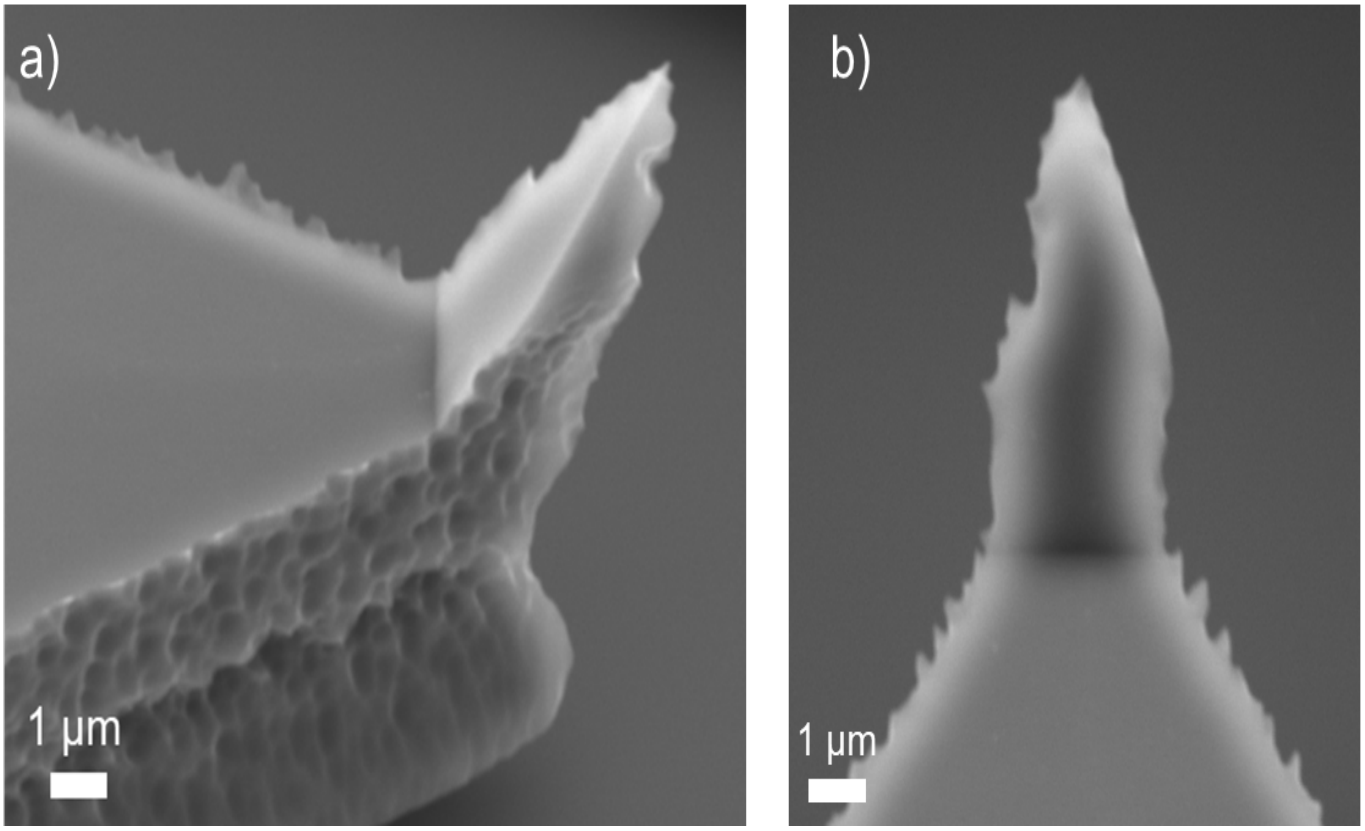


Figure 6.10: SEM image of tip formed after TMAH etching, when tilt angle between ion beam and sample surface is 50°.

Once the tilt angle is between 40° to 20°, most of the sidewall oxide was preserved and tetrahedral tips were obtained after TMAH etching. However, the apex of the tips formed was not uniform for all tilt angles. Instead, the apex increased with decrease in tilt angle between 40° and 20°, with the smallest apex being obtained at 40° tilt. The average apex was < 50 nm without oxidation sharpening. We suspect that the reason for this increase in apex is due to slight broadening of the V-shaped mask due to ion bombardment at certain angles. Figure 6.11 shows the tip formed using 40° tilt between sample and ion beam, while figure 6.12 shows the uniformity across the array

when tips are fabricated using ion beam milling method. As mentioned above, the average apex for the tips fabricated using this method is < 50 nm with an error of ±10 nm.

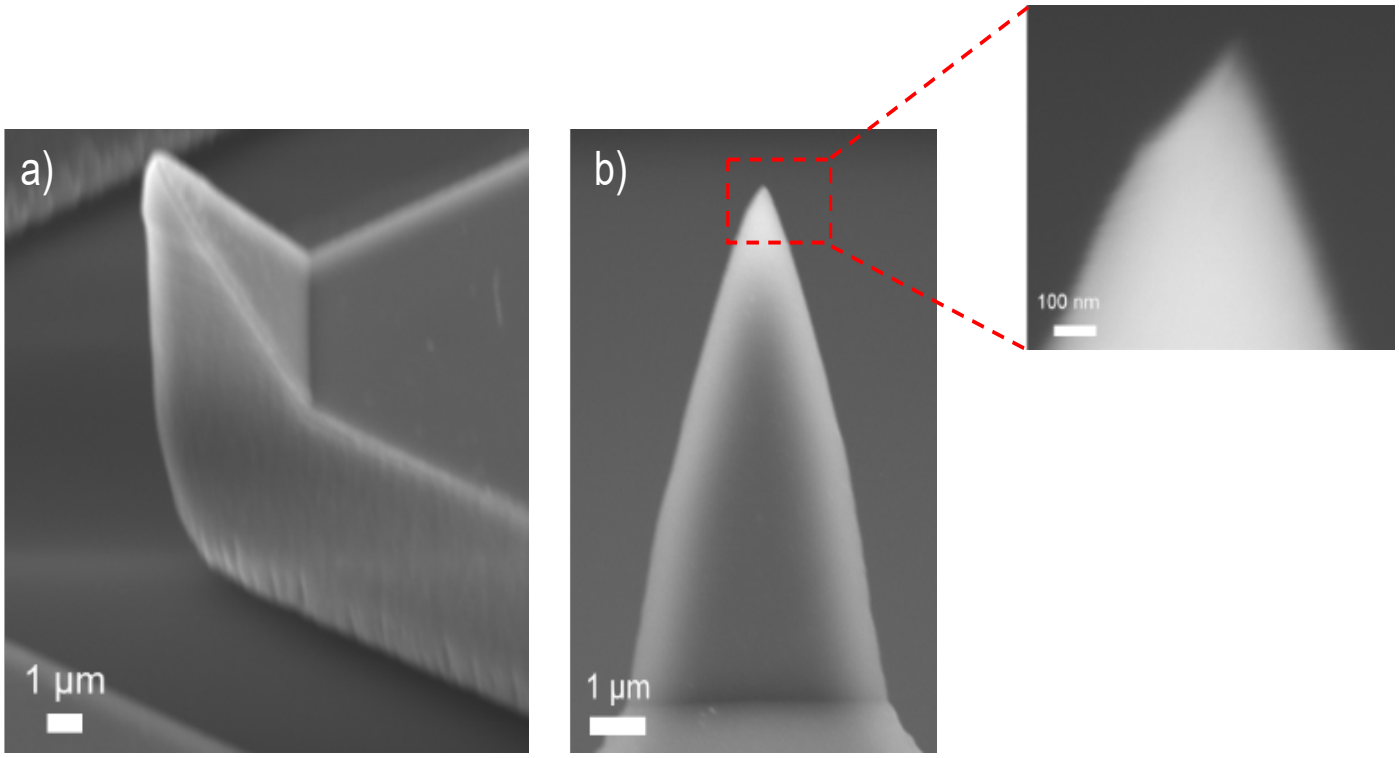


Figure 6.11: SEM image of tip formed after TMAH etching, when tilt angle between ion beam and sample surface is 40°.

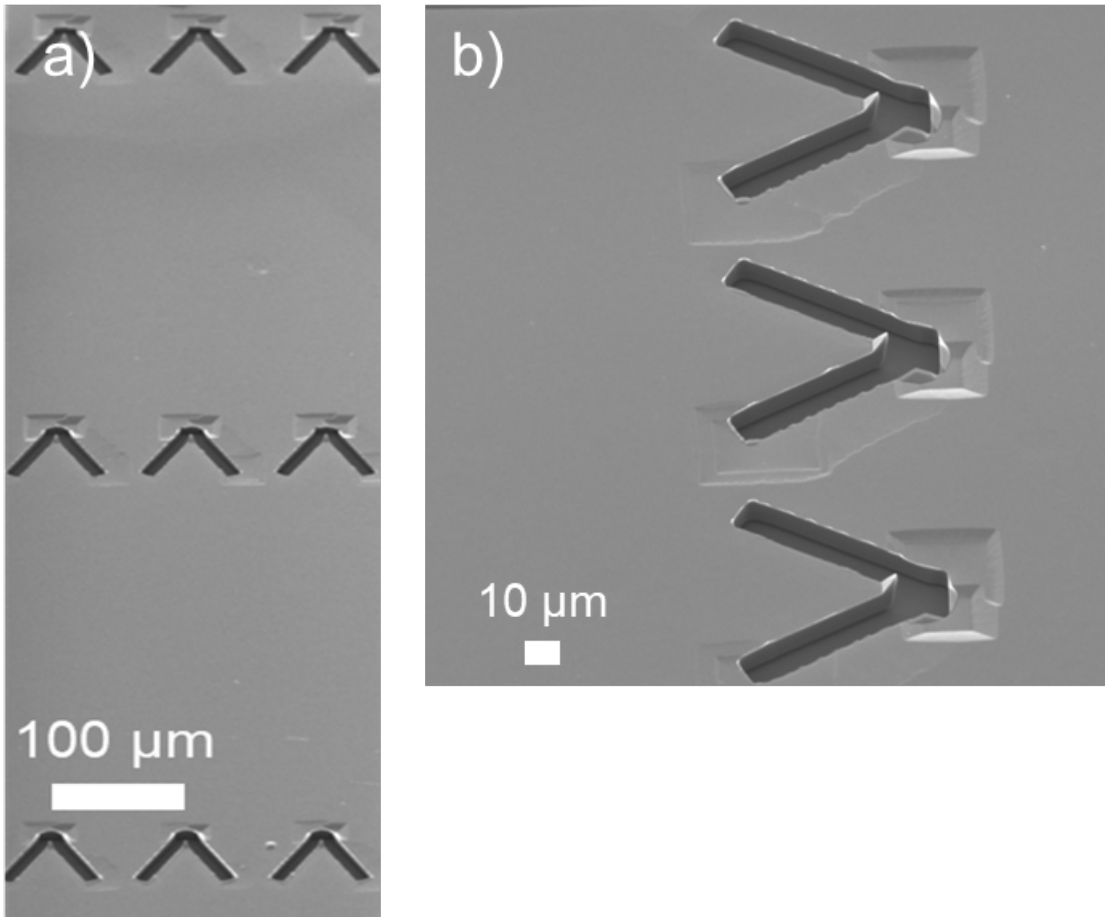


Figure 6.12: SEM image showing uniformity across array after TMAH etching, when angle between ion beam and sample surface is 40°.

Following the fabrication of tetrahedral tip, the cantilever and handle are fabricated by the same method described in section 6.2. Figure 6.13 shows cantilever fabricated for the tip shown in figure 6.11. The tip apex after cantilever fabrication is ~ 50 nm without oxidation sharpening, which shows the ability to achieve excellent tip apex using careful ion milling of SOI wafer.

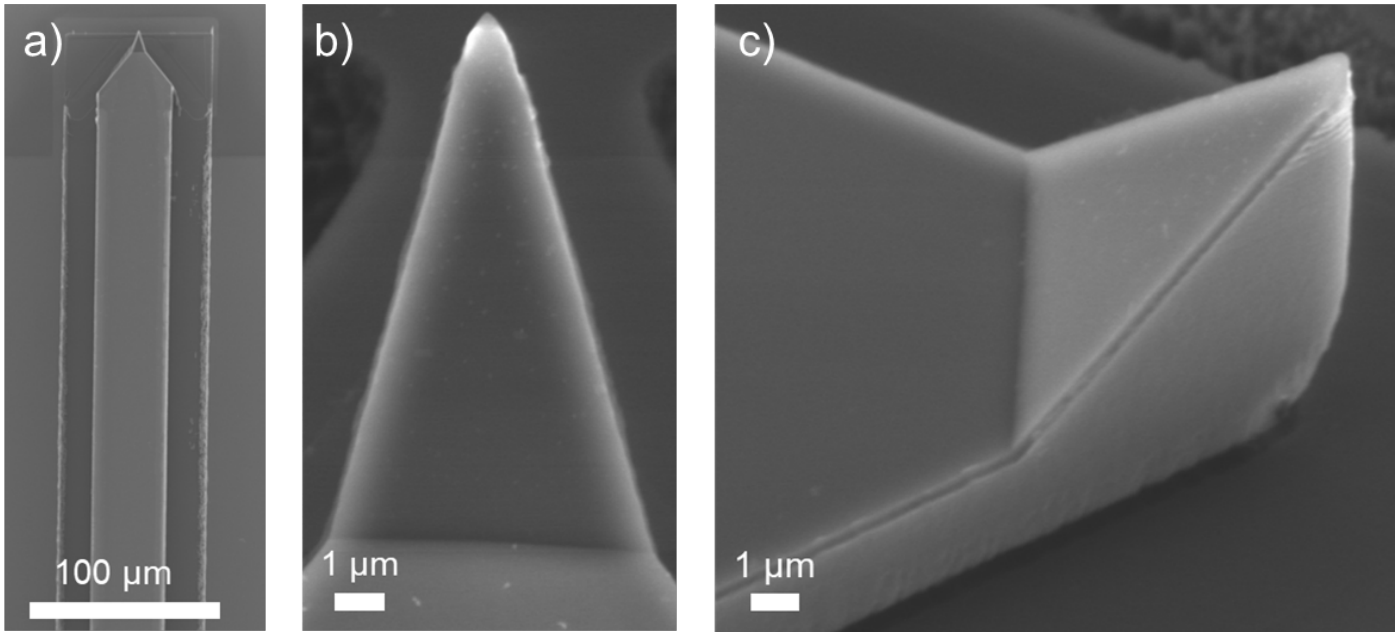


Figure 6.13: SEM image for cantilever fabricated on tip shown in figure 6.11.

6.4. CONCLUSION

In this work we have used two methods to fabricate tetrahedral AFM tips. In the first method, LPCVD nitride is used as a mask to prevent oxidation of the silicon surface. However, this method requires high cost and not readily available LPCVD nitride as the masking material. Thus we developed a novel method which uses commonly available SOI wafers. During the oxidation step, both the trench sidewalls and surface of the silicon wafer are oxidized. However, by careful ion milling of the sample using tilted ion beam, the surface oxide can be removed without affecting the sidewall oxide necessary to provide perpendicular sidewall for the tetrahedral tip. For our work the lowest apex was obtained when the angle between the sample surface and the ion beam was 40 ° and was less than 50 nm without oxidation sharpening. The apex achieved by angled ion milling is much smaller than that using LPCVD nitride mask.

CHAPTER 7: CONCLUSION AND FUTURE WORK

This work focuses on the fabrication of high aspect ratio AFM tips using silicon and diamond apex. The major findings of this work are stated below:

1. High aspect ratio diamond AFM tips are fabricated using RIE. In the first method, diamond is etched in O_2/CHF_3 plasma and cone shaped tip is formed by using shrinking Al_2O_3 mask. It is found that the lateral etching of the mask is proportional to its vertical etching rate. Thus, when patterning 700 nm thick diamond, mask size should be at least 450 nm in diameter. Additionally, to prevent diamond apex from becoming blunt during the fabrication of silicon base, mask thickness is increased such that after diamond RIE, the apex is made of Al_2O_3 which then acts as a mask during Pseudo-Bosch etching of silicon. Here, the mask thickness must be carefully adjusted so diamond apex is exposed after fabrication of silicon base. Using this approach we have fabricated AFM tips with aspect ratio of 9.63 with an average apex of 29.5 nm.
2. The second method for diamond tip fabrication is designed to reduce the strict limitations of mask dimensions stated in the above process. In this method, the base of the AFM tip is fabricated before the diamond tip fabrication. For this purpose, we designed a novel method based on T-shaped mask. First the wider part of the T-shaped mask is used to pattern the silicon base. This top mask is then selectively removed by removing the oxide on which it sits, and the narrower part of the mask is used to pattern the diamond film. In this case, O_2/C_4F_8 plasma is used to pattern the 300 nm thick diamond. Using this process, we are able to achieve aspect ratio of 7.5 and diamond tip apex of ~10 nm.
3. High aspect ratio tips with silicon apex have also been fabricated. For this purpose, we used (111) oriented silicon wafer, which is first dry-etched before undergoing wet

anisotropic etching in TMAH or surfactant-added-TMAH. We studied the effects of several design and process parameters. First, we investigated the effect of mask shape and dry etching height on the shape and apex diameter of the tip. We found that dry-etch height of at least 30 μm is necessary to obtain high aspect ratio tip structure. We also found that circular mask provided optimal tip width required to sustain imaging for long periods of time. Additionally, we studied the effect of two types of non-ionic surfactants on the etching profile of the silicon AFM tip. We concluded that when 1000 ppm Triton X-405 is added to 25 wt% TMAH, the resulting tip has the highest aspect ratio (13.8) and sharpest apex (< 9 nm). However, the smoothest surface is obtained when 1000 ppm Triton X-100 is added to 25 wt% TMAH.

4. We have also studied the effects of surfactant concentration on the etching profile of (111) silicon wafer when etched in 25 wt% TMAH at 70°C. We found that etching in pure 25 wt% TMAH results in low aspect ratio structures, while a small amount of non-ionic surfactant can drastically improve the aspect ratio by changing the anisotropy. In this work we have used non-ionic Triton X-100 and Triton X-405, which have same chemical composition of both their polar head group and PEO chain. However, Triton X-405 has a longer PEO chain compared to Triton X-100. We found that at low surfactant concentration e.g. 1 ppm, the lack of surfactant molecules leads to non-uniform etching for both surfactants. However, this issue is mitigated with increase in surfactant concentration. We have also found that at high surfactant concentration (≥ 100 ppm) Triton X-100, having smaller PEO chain length provides better etch rate suppression than Triton X-405 which has longer chain length. However, Triton X-405 provides much smoother sidewalls due to longer chain lengths facilitating hydrogen bubble removal. At all surfactant concentrations

tested, both surfactant are capable of producing high aspect ratio tips. Additionally, the tail-like feature which appears due to wafer miscut is significantly reduced with increased surfactant concentration and is the least pronounced when using 1000 ppm Triton X-100.

5. Two methods were developed for tetrahedral AFM tip fabrication. The Si_3N_4 mask method yields good tip shapes but requires costly LPCVD nitride**.** The ion milling method eliminates this requirement by using tilted ion beams to remove only surface oxide, achieving sharper apexes (< 50 nm) than the nitride-based method. This approach offers a cost-effective, high-precision alternative for tetrahedral tip fabrication using standard SOI wafers.
6. The cost of the tips fabricated using the proposed methods is summarized in Table 7.1. Our results demonstrate that both diamond and silicon AFM tips produced in this work can be fabricated at significantly lower cost compared to commercially available alternatives. The main factor contributing to this cost reduction is the fabrication approach. Most commercial diamond tips are produced using focused ion beam (FIB) processing, where Ga^+ ions are implanted into the diamond to define the tip mask. This is inherently a serial process, requiring precise alignment and multiple deposition steps, which increases fabrication time and expense. In contrast, the method developed in this study employs shrinking masks deposited across an entire wafer using electron-beam evaporation. Owing to the parallel nature of both e-beam evaporation and reactive ion etching (RIE), several hundred diamond tips can be fabricated simultaneously, leading to substantial improvements in scalability and cost efficiency. Additionally, our tips produce lower apex and higher aspect ratios than commercially available tips due to the innovative process flows developed in this work.

DIAMOND			
	Tip-1 (shrinking mask)	***Tip-2(T-shaped mask)***	***Commercial***
Apex (nm)	29	10	10 – 50
Aspect ratio	10	7.5	2 – 6
Cost (C$)	11	14	350 – 700
SILICON			
	Si(111)	***Tetrahedral***	***Commercial***
Apex (nm)	< 10	< 50	< 20
Aspect ratio	11.4 – 14	NA	7 – 9
Cost (C$)	7	7.5	25 – 70

Table 7.1: Apex, cost and aspect ratio of AFM probes fabricated using this work versus commercially available diamond and silicon AFM tips.

In the future, probe testing should be done by fabricating cantilever and handle for diamond and Si(111) AFM tips. For the fabrication of high aspect ratio tips using (111) silicon wafer, effects of different types of surfactants in KOH can be studied and compared to the results obtained in this work.

Additionally, effects of other etchant gases, such as $O_2/CHF_3/Ar$ can be explored for diamond etching. During our work we also found reasonable etching of Al_2O_3 in both O_2/CHF_3 and O_2/C_4F_8 plasma. This effect has not been previously studied to the best of our knowledge and should be further studied.

REFERENCES

(1) Debnath, K.; Arimoto, H.; Husain, M. K.; Prasmusinto, A.; Al-Attili, A.; Petra, R.; Chong, H. M.; Reed, G. T.; Saito, S. Low-loss silicon waveguides and grating couplers fabricated using anisotropic wet etching technique. *Frontiers in Materials* **2016**, *3*, 10.

(2) Voigtländer, B. Introduction. In *Atomic Force Microscopy*, Springer International Publishing, 2019; pp 1-13.

(3) Binnig, G.; Rohrer, H.; Gerber, C.; Weibel, E. Surface studies by scanning tunneling microscopy. *Physical review letters* **1982**, *49* (1), 57.

(4) Wilson, H. A. B. R. A. *Scanning Tunneling Microscopy (STM)* https://chem.libretexts.org/Bookshelves/Analytical_Chemistry/Supplemental_Modules_%28Analytical_Chemistry%29/Microscopy/Scanning_Probe_Microscopy/03_Basic_Theory/01_Scanning_Tunneling_Microscopy_%28STM%29 (accessed).

(5) Binnig, G.; Quate, C. F.; Gerber, C. Atomic force microscope. *Physical review letters* **1986**, *56* (9), 930.

(6) Albrecht, T. R.; Grütter, P.; Horne, D.; Rugar, D. Frequency modulation detection using high-Q cantilevers for enhanced force microscope sensitivity. *Journal of applied physics* **1991**, *69* (2), 668-673.

(7) Zhong, Q.; Inniss, D.; Kjoller, K.; Elings, V. Fractured polymer/silica fiber surface studied by tapping mode atomic force microscopy. *Surface Science Letters* **1993**, *290* (1-2), L688-L692.

(8) Giessibl, F. J. Atomic resolution of the silicon (111)-(7× 7) surface by atomic force microscopy. *Science* **1995**, *267* (5194), 68-71.

(9) Jalili, N.; Laxminarayana, K. A review of atomic force microscopy imaging systems: application to molecular metrology and biological sciences. *Mechatronics* **2004**, *14* (8), 907-945.

(10) Hoogenboom, B. AFM in liquids. Springer Verlag, 2012.

(11) Radmacher, M.; Fritz, M.; Hansma, P. K. Imaging soft samples with the atomic force microscope: gelatin in water and propanol. *Biophysical journal* **1995**, *69* (1), 264-270.

(12) Sugimura, H.; Uchida, T.; Kitamura, N.; Masuhara, H. Scanning tunneling microscope tip-induced anodization for nanofabrication of titanium. *The Journal of Physical Chemistry* **1994**, *98* (16), 4352-4357.

(13) Tseng, A. A. Advancements and challenges in development of atomic force microscopy for nanofabrication. *Nano Today* **2011**, *6* (5), 493-509.

(14) Sugimoto, Y.; Jelinek, P.; Pou, P.; Abe, M.; Morita, S.; Perez, R.; Custance, O. Mechanism for room-temperature single-atom lateral manipulations on semiconductors using dynamic force microscopy. *Physical review letters* **2007**, *98* (10), 106104.

(15) Meyer, G.; Amer, N. M. Novel optical approach to atomic force microscopy. *Applied physics letters* **1988**, *53* (12), 1045-1047.

(16) Voigtländer, B. Forces between tip and sample. *Atomic Force Microscopy* **2019**, 161-176.

(17) Xu, S.; Arnsdorf, M. F. Electrostatic force microscope for probing surface charges in aqueous solutions. *Proceedings of the National Academy of Sciences* **1995**, *92* (22), 10384-10388.

(18) Passeri, D.; Dong, C.; Reggente, M.; Angeloni, L.; Barteri, M.; Scaramuzzo, F. A.; De Angelis, F.; Marinelli, F.; Antonelli, F.; Rinaldi, F. Magnetic force microscopy: Quantitative issues in biomaterials. *Biomatter* **2014**, *4* (1), e29507.

(19) Nader Jalili and Karthik, L. A review of atomic force microscopy imaging systems: application to molecular metrology and biological sciences. *Mechatronics* **2004**, *14* (8), 907-945. DOI: https://doi.org/10.1016/j.mechatronics.2004.04.005.

(20) Voigtländer, B. Static atomic force microscopy. *Atomic Force Microscopy* **2019**, 199-208.

(21) Ludwig, T.; Kirmse, R.; Poole, K.; Schwarz, U. S. Probing cellular microenvironments and tissue remodeling by atomic force microscopy. *Pflügers Archiv-European Journal of Physiology* **2008**, *456*, 29-49.

(22) Zhang, Y.; Zhao, H.; Zuo, L. Contact dynamics of tapping mode atomic force microscopy. *Journal of sound and vibration* **2012**, *331* (23), 5141-5152.

(23) Maghsoudy-Louyeh, S.; Kropf, M.; Tittmann, B. Review of progress in atomic force microscopy. *The Open Neuroimaging Journal* **2018**, *12* (1).
(24) Marti, O.; Drake, B.; Hansma, P. Atomic force microscopy of liquid-covered surfaces: Atomic resolution images. *Applied Physics Letters* **1987**, *51* (7), 484-486.
(25) Bennewitz, R. Friction force microscopy. In *Fundamentals of Friction and Wear on the Nanoscale*, Springer, 2014; pp 3-16.
(26) Marsden, A. J.; Phillips, M.; Wilson, N. R. Friction force microscopy: a simple technique for identifying graphene on rough substrates and mapping the orientation of graphene grains on copper. *Nanotechnology* **2013**, *24* (25), 255704.
(27) García, R. *Amplitude modulation atomic force microscopy*; John Wiley & Sons, 2011.
(28) Voigtländer, B. Amplitude Modulation (AM) Mode in Dynamic Atomic Force Microscopy. *Atomic Force Microscopy* **2019**, 209-229.
(29) Yasumura, K. Y.; Stowe, T. D.; Chow, E. M.; Pfafman, T.; Kenny, T. W.; Stipe, B. C.; Rugar, D. Quality factors in micron-and submicron-thick cantilevers. *Journal of microelectromechanical systems* **2000**, *9* (1), 117-125.
(30) Tamayo, J.; Humphris, A.; Owen, R.; Miles, M. High-Q dynamic force microscopy in liquid and its application to living cells. *Biophysical journal* **2001**, *81* (1), 526-537.
(31) Rodrıguez, T. R.; García, R. Theory of Q control in atomic force microscopy. *Applied Physics Letters* **2003**, *82* (26), 4821-4823.
(32) Garcıa, R.; Perez, R. Dynamic atomic force microscopy methods. *Surface science reports* **2002**, *47* (6-8), 197-301.
(33) Voigtländer, B. Intermittent Contact Mode/Tapping Mode. *Atomic Force Microscopy* **2019**, 231-253.
(34) Cleveland, J.; Anczykowski, B.; Schmid, A.; Elings, V. Energy dissipation in tapping-mode atomic force microscopy. *Applied Physics Letters* **1998**, *72* (20), 2613-2615.
(35) Salapaka, M.; Chen, D. J.; Cleveland, J. Linearity of amplitude and phase in tapping-mode atomic force microscopy. *Physical Review B* **2000**, *61* (2), 1106.
(36) Landau, L. D.; Lifshitz, E. M. *Mechanics: Volume 1*; Elsevier Science, 1976.
(37) Hölscher, H.; Schwarz, U. D. Theory of amplitude modulation atomic force microscopy with and without Q-control. *International Journal of Non-linear mechanics* **2007**, *42* (4), 608-625.
(38) Eaton, P.; Batziou, K. Artifacts and practical issues in atomic force microscopy. *Atomic Force Microscopy: Methods and Protocols* **2019**, 3-28.
(39) Mesa, B.; Magonov, S. Novel diamond/sapphire probes for scanning probe microscopy applications. In *Journal of Physics: Conference Series*, 2007; IOP Publishing: Vol. 61, p 770.
(40) Niedermann, P.; Hänni, W.; Morel, D.; Perret, A.; Skinner, N.; Indermühle, P.-F.; Buffat, P.-A. CVD diamond probes for nanotechnology. *Applied Physics A* **1998**, *66*, S31-S34.
(41) Bhushan, B.; Palacio, M.; Kwak, K. J. Thermally-treated Pt-coated silicon AFM tips for wear resistance in ferroelectric data storage. *Acta materialia* **2008**, *56* (16), 4233-4241.
(42) Xie, H.; Onal, C.; Régnier, S.; Sitti, M. Nanomechanics of AFM Based Nanomanipulation. In *Atomic Force Microscopy Based Nanorobotics: Modelling, Simulation, Setup Building and Experiments*, Springer Berlin Heidelberg, 2012; pp 87-143.
(43) Tortonese, M. Cantilevers and tips for atomic force microscopy. *IEEE engineering in medicine and biology magazine* **1997**, *16* (2), 28-33.
(44) Patil, A.; Sippel, J.; Martin, G. W.; Rinzler, A. G. Enhanced functionality of nanotube atomic force microscopy tips by polymer coating. *Nano Letters* **2004**, *4* (2), 303-308.
(45) *OLTESPA-R3*. https://sfr.ca/products/oltespa-r3 (accessed 2024).
(46) Hafner, J. H. Probes in scanning microscopies. In *Nanotribology and Nanomechanics: An Introduction*, Springer, 2005; pp 117-139.

(47) Strahlendorff, T.; Dai, G.; Bergmann, D.; Tutsch, R. Tip wear and tip breakage in high-speed atomic force microscopes. *Ultramicroscopy* **2019**, *201*, 28-37.
(48) Hafner, J. H.; Cheung, C. L.; Lieber, C. M. Growth of nanotubes for probe microscopy tips. *Nature* **1999**, *398* (6730), 761-762.
(49) Cheng, B.; Yang, S.; Li, W.; Li, S.; Shafique, S.; Wu, D.; Ji, S.; Sun, Y.; Jiang, Z. Controlled growth of a single carbon nanotube on an AFM probe. *Microsystems & nanoengineering* **2021**, *7* (1), 80.
(50) Wilson, N. R.; Macpherson, J. V. Carbon nanotube tips for atomic force microscopy. *Nature nanotechnology* **2009**, *4* (8), 483-491.
(51) Temiryazev, A. Pulse force nanolithography on hard surfaces using atomic force microscopy with a sharp single-crystal diamond tip. *Diamond and related materials* **2014**, *48*, 60-64.
(52) *Nano diamond tips*. https://tipsnano.com/catalog/afm-special/scd/dep01/#:~:text=The%20conductive%20diamond%20coating%20is,reflectance%20of%20the%20laser%20beam (accessed).
(53) Erdemir, A.; Martin, J. M. Superior wear resistance of diamond and DLC coatings. *Current Opinion in Solid State and Materials Science* **2018**, *22* (6), 243-254.
(54) Agrawal, R.; Moldovan, N.; Espinosa, H. An energy-based model to predict wear in nanocrystalline diamond atomic force microscopy tips. *Journal of Applied Physics* **2009**, *106* (6).
(55) Rabe, U.; Turner, J.; Arnold, W. Analysis of the high-frequency response of atomic force microscope cantilevers. *Applied Physics A: Materials Science & Processing* **1998**, *66* (7).
(56) Bhushan, B.; Marti, O. Scanning probe microscopy–principle of operation, instrumentation, and probes. *Springer handbook of nanotechnology* **2010**, 573-617.
(57) Walters, D.; Cleveland, J.; Thomson, N.; Hansma, P.; Wendman, M.; Gurley, G.; Elings, V. Short cantilevers for atomic force microscopy. *Review of Scientific Instruments* **1996**, *67* (10), 3583-3590.
(58) Kaemmer, S. B. Introduction to Bruker's ScanAsyst and PeakForce Tapping AFM Technology. Bruker: 2009.
(59) Bruker. PeakForce Tapping How AFM Should Be — for 10 Years and Counting. Bruker.
(60) Cui, A.; Deng, M.; Ye, Y.; Wang, X.; Hu, Z. Principles and Basic Modes of Atomic Force Microscopy. In *Atomic Force Microscopy for Energy Research*, CRC Press, 2022; pp 1-43.
(61) Gutierrez, J.; Mondragon, I.; Tercjak, A. Quantitative nanoelectrical and nanomechanical properties of nanostructured hybrid composites by PeakForce tunneling atomic force microscopy. *The Journal of Physical Chemistry C* **2014**, *118* (2), 1206-1212.
(62) Su, C.; Shi, J.; Hu, Y.; Hu, S.; Ma, J. Method and apparatus of using peak force tapping mode to measure physical properties of a sample. Google Patents: 2016.
(63) Alsteens, D.; Dupres, V.; Yunus, S.; Latge, J.-P.; Heinisch, J. J.; Dufrene, Y. F. High-resolution imaging of chemical and biological sites on living cells using peak force tapping atomic force microscopy. *Langmuir* **2012**, *28* (49), 16738-16744.
(64) Gazze, S.; Hallin, I.; Quinn, G.; Dudley, E.; Matthews, G.; Rees, P.; Van Keulen, G.; Doerr, S.; Francis, L. Organic matter identifies the nano-mechanical properties of native soil aggregates. *Nanoscale* **2018**, *10* (2), 520-525.
(65) Murrell, M.; Welland, M.; O'Shea, S.; Wong, T.; Barnes, J.; McKinnon, A.; Heyns, M.; Verhaverbeke, S. Spatially resolved electrical measurements of SiO2 gate oxides using atomic force microscopy. *Applied physics letters* **1993**, *62* (7), 786-788.
(66) Ruskell, T. G.; Workman, R. K.; Chen, D.; Sarid, D.; Dahl, S.; Gilbert, S. High resolution Fowler-Nordheim field emission maps of thin silicon oxide layers. *Applied physics letters* **1996**, *68* (1), 93-95.
(67) O'shea, S.; Atta, R.; Murrell, M.; Welland, M. Conducting atomic force microscopy study of silicon dioxide breakdown. *Journal of Vacuum Science & Technology B: Microelectronics and Nanometer Structures Processing, Measurement, and Phenomena* **1995**, *13* (5), 1945-1952.

(68) Pan, C.; Shi, Y.; Hui, F.; Grustan-Gutierrez, E.; Lanza, M. History and Status of the CAFM. *Conductive Atomic Force Microscopy: Applications in Nanomaterials* **2017**, 1-28.
(69) Krause, O. Fabrication and Reliability of Conductive AFM Probes. *Conductive Atomic Force Microscopy: Applications in Nanomaterials* **2017**, 29-44.
(70) Jiang, L.; Weber, J.; Puglisi, F. M.; Pavan, P.; Larcher, L.; Frammelsberger, W.; Benstetter, G.; Lanza, M. Understanding current instabilities in conductive atomic force microscopy. *Materials* **2019**, *12* (3), 459.
(71) John, N. S.; Kulkarni, G. Gold-coated conducting-atomic force microscopy probes. *Journal of nanoscience and nanotechnology* **2005**, *5* (4), 587-591.
(72) Bhaskaran, H.; Sebastian, A.; Despont, M. Nanoscale PtSi tips for conducting probe technologies. *IEEE Transactions on Nanotechnology* **2008**, *8* (1), 128-131.
(73) Su, P.-J.; Liu, B. H. Ion-beam-sputter deposited titanium nitride thin films for conductive atomic force microscope probes. *Thin Solid Films* **2013**, *529*, 317-321.
(74) Frammelsberger, W.; Benstetter, G.; Stamp, R.; Kiely, J.; Schweinboeck, T. Simplified tunnelling current calculation for MOS structures with ultra-thin oxides for conductive atomic force microscopy investigations. *Materials Science and Engineering: B* **2005**, *116* (2), 168-174.
(75) Bussmann, E.; Williams, C. Sub-10 nm lateral spatial resolution in scanning capacitance microscopy achieved with solid platinum probes. *Review of scientific instruments* **2004**, *75* (2), 422-425.
(76) Trenkler, T.; Hantschel, T.; Stephenson, R.; De Wolf, P.; Vandervorst, W.; Hellemans, L.; Malavé, A.; Büchel, D.; Oesterschulze, E.; Kulisch, W. Evaluating probes for "electrical" atomic force microscopy. *Journal of Vacuum Science & Technology B: Microelectronics and Nanometer Structures Processing, Measurement, and Phenomena* **2000**, *18* (1), 418-427.
(77) Trenkler, T.; Hantschel, T.; Vandervorst, W.; Hellemans, L.; Kulisch, W.; Oesterschulze, E.; Niedermann, P.; Sulzbach, T. Characterization of conductive probes for Atomic Force Microscopy. In *Design, Test, and Microfabrication of MEMS and MOEMS*, 1999; SPIE: Vol. 3680, pp 1168-1179.
(78) Ando, T. High-speed atomic force microscopy and its future prospects. *Biophysical reviews* **2018**, *10* (2), 285-292.
(79) Ando, T.; Kodera, N.; Takai, E.; Maruyama, D.; Saito, K.; Toda, A. A high-speed atomic force microscope for studying biological macromolecules. *Proceedings of the National Academy of Sciences* **2001**, *98* (22), 12468-12472.
(80) Ando, T. HS-AFM System and Optimized Instrumental Components. In *High-Speed Atomic Force Microscopy in Biology: Directly Watching Dynamics of Biomolecules in Action*, Springer, 2022; pp 37-83.
(81) Uchihashi, T.; Kodera, N.; Ando, T. Guide to video recording of structure dynamics and dynamic processes of proteins by high-speed atomic force microscopy. *nature protocols* **2012**, *7* (6), 1193-1206.
(82) Adams, J. D.; Erickson, B. W.; Grossenbacher, J.; Brugger, J.; Nievergelt, A.; Fantner, G. E. Harnessing the damping properties of materials for high-speed atomic force microscopy. *Nature nanotechnology* **2016**, *11* (2), 147-151.
(83) De Wolf, P.; Snauwaert, J.; Clarysse, T.; Vandervorst, W.; Hellemans, L. Characterization of a point-contact on silicon using force microscopy-supported resistance measurements. *Applied physics letters* **1995**, *66* (12), 1530-1532.
(84) De Wolf, P. Two-dimensional carrier profiling of semiconductor structures with nanometer resolution. 1998.
(85) Clarysse, T.; Vanhaeren, D.; Hoflijk, I.; Vandervorst, W. Characterization of electrically active dopant profiles with the spreading resistance probe. *Materials Science and Engineering: R: Reports* **2004**, *47* (5-6), 123-206.
(86) Schulze, A.; Eyben, P.; Hantschel, T.; Vandervorst, W. Scanning Spreading Resistance Microscopy (SSRM): High resolution 2D and 3D carrier mapping of semiconductor nanostructures. 2017.

(87) Schulze, A.; Eyben, P.; Mody, J.; Paredis, K.; Wouters, L.; Celano, U.; Vandervorst, W. Mapping conductance and carrier distributions in confined three-dimensional transistor structures. *Electrical Atomic Force Microscopy for Nanoelectronics* **2019**, 71-106.
(88) Niedermann, P.; Hänni, W.; Blanc, N.; Christoph, R.; Burger, J. Chemical vapor deposition diamond for tips in nanoprobe experiments. *Journal of Vacuum Science & Technology A: Vacuum, Surfaces, and Films* **1996**, *14* (3), 1233-1236.
(89) Hantschel, T.; Demeulemeester, C.; Eyben, P.; Schulz, V.; Richard, O.; Bender, H.; Vandervorst, W. Conductive diamond tips with sub-nanometer electrical resolution for characterization of nanoelectronics device structures. *physica status solidi (a)* **2009**, *206* (9), 2077-2081.
(90) Hantschel, T.; Conard, T.; Kilpatrick, J.; Cross, G. Diamond Probes Technology. *Electrical Atomic Force Microscopy for Nanoelectronics* **2019**, 351-384.
(91) Buzio, R. Exploring Mesoscale Contact Mechanics by Atomic Force Microscopy. *Scanning Probe Microscopy in Nanoscience and Nanotechnology 3* **2013**, 55-75.
(92) Ducker, W. A.; Senden, T. J.; Pashley, R. M. Direct measurement of colloidal forces using an atomic force microscope. *Nature* **1991**, *353* (6341), 239-241.
(93) Cappella, B.; Dietler, G. Force-distance curves by atomic force microscopy. *Surface science reports* **1999**, *34* (1-3), 1-104.
(94) Preuss, M.; Butt, H.-J. Direct measurement of particle− bubble interactions in aqueous electrolyte: dependence on surfactant. *Langmuir* **1998**, *14* (12), 3164-3174.
(95) Wang, X.; Ryu, K. S.; Bullen, D. A.; Zou, J.; Zhang, H.; Mirkin, C. A.; Liu, C. Scanning probe contact printing. *Langmuir* **2003**, *19* (21), 8951-8955.
(96) Wang, X.; Liu, C. Multifunctional probe array for nano patterning and imaging. *Nano letters* **2005**, *5* (10), 1867-1872.
(97) Cho, J. H.; Lee, D. H.; Shin, H. S.; Pattanayek, S. K.; Ryu, C. Y.; Cho, K. Exploiting poly (dimethylsiloxane)-modified tips to evaluate frictional behavior by friction force microscopy. *Langmuir* **2004**, *20* (26), 11499-11503.
(98) Yu, Q.; Qin, G.; Darne, C.; Cai, C.; Wosik, W.; Pei, S.-S. Fabrication of short and thin silicon cantilevers for AFM with SOI wafers. *Sensors and Actuators A: Physical* **2006**, *126* (2), 369-374.
(99) Grow, R. J.; Minne, S. C.; Manalis, S. R.; Quate, C. F. Silicon nitride cantilevers with oxidation-sharpened silicon tips for atomic force microscopy. *Journal of Microelectromechanical Systems* **2002**, *11* (4), 317-321.
(100) Xu, K.; Liu, Y. Studies of probe tip materials by atomic force microscopy: a review. *Beilstein Journal of Nanotechnology* **2022**, *13* (1), 1256-1267.
(101) Tanasa, G.; Kurnosikov, O.; Flipse, C.; Buijnsters, J.; van Enckevort, W. Diamond deposition on modified silicon substrates: Making diamond atomic force microscopy tips for nanofriction experiments. *Journal of applied physics* **2003**, *94* (3), 1699-1704.
(102) Tao, Z.; Bhushan, B. Surface modification of AFM silicon probes for adhesion and wear reduction. *Tribology Letters* **2006**, *21*, 1-16.
(103) Doris, B. B.; Hegde, R. I. Improved atomic force microscopy imaging using carbon-coated probe tips. *Applied physics letters* **1995**, *67* (25), 3816-3818.
(104) Pal, P.; Sato, K. *Silicon wet bulk micromachining for MEMS*; CRC Press, 2017.
(105) Kawakatsu, H.; Saya, D.; Kato, A.; Fukushima, K.; Toshiyoshi, H.; Fujita, H. Millions of cantilevers for atomic force microscopy. *Review of Scientific Instruments* **2002**, *73* (3), 1188-1192.
(106) Albrecht, T.; Akamine, S.; Carver, T.; Quate, C. Microfabrication of cantilever styli for the atomic force microscope. *Journal of Vacuum Science & Technology A: Vacuum, Surfaces, and Films* **1990**, *8* (4), 3386-3396.
(107) De Wolf, P.; Snauwaert, J.; Hellemans, L.; Clarysse, T.; Vandervorst, W.; D'Olieslaeger, M.; Quaeyhaegens, D. Lateral and vertical dopant profiling in semiconductors by atomic force microscopy

using conducting tips. *Journal of Vacuum Science & Technology A: Vacuum, Surfaces, and Films* **1995**, *13* (3), 1699-1704.
(108) Hantschel, T.; Niedermann, P.; Trenkler, T.; Vandervorst, W. Highly conductive diamond probes for scanning spreading resistance microscopy. *Applied Physics Letters* **2000**, *76* (12), 1603-1605.
(109) Moldovan, N.; Dai, Z.; Zeng, H.; Carlisle, J. A.; Jacobs, T. D.; Vahdat, V.; Grierson, D. S.; Liu, J.; Turner, K. T.; Carpick, R. W. Advances in manufacturing of molded tips for scanning probe microscopy. *Journal of microelectromechanical systems* **2011**, *21* (2), 431-442.
(110) Uetsuka, H.; Yamada, T.; Shikata, S. ICP etching of polycrystalline diamonds: Fabrication of diamond nano-tips for AFM cantilevers. *Diamond and Related Materials* **2008**, *17* (4-5), 728-731.
(111) Obraztsov, A. N.; Kopylov, P. G.; Loginov, B. A.; Dolganov, M. A.; Ismagilov, R. R.; Savenko, N. V. Single crystal diamond tips for scanning probe microscopy. *Review of Scientific Instruments* **2010**, *81* (1).
(112) Tsigkourakos, M.; Hantschel, T.; Arstila, K.; Vandervorst, W. Diamond nano-particle seeding for tip moulding application. *Diamond and related materials* **2013**, *35*, 14-18.
(113) Williams, O. A.; Douhéret, O.; Daenen, M.; Haenen, K.; Ōsawa, E.; Takahashi, M. Enhanced diamond nucleation on monodispersed nanocrystalline diamond. *Chemical Physics Letters* **2007**, *445* (4-6), 255-258.
(114) Heyer, S.; Janssen, W.; Turner, S.; Lu, Y.-G.; Yeap, W. S.; Verbeeck, J.; Haenen, K.; Krueger, A. Toward deep blue nano hope diamonds: heavily boron-doped diamond nanoparticles. *ACS nano* **2014**, *8* (6), 5757-5764.
(115) Tsigkourakos, M.; Hantschel, T.; Bangerter, C.; Vandervorst, W. Electrical probing of B-doped diamond seeds embedded into the interfacial layer of a conductive diamond film. *physica status solidi (a)* **2014**, *211* (10), 2284-2289.
(116) Afandi, A.; Howkins, A.; Boyd, I. W.; Jackman, R. B. Nanodiamonds for device applications: An investigation of the properties of boron-doped detonation nanodiamonds. *Scientific Reports* **2018**, *8* (1), 3270.
(117) Hantschel, T.; Pape, U.; Slesazeck, S.; Niedermann, P.; Vandervorst, W. Mounting of molded AFM probes by soldering. In *Materials and Device Characterization in Micromachining III*, 2000; SPIE: Vol. 4175, pp 62-73.
(118) Shibata, T.; Maruno, K.; Nagai, M.; Kawashima, T.; Mineta, T.; Makino, E. Fabrication and Characterization of AFM Probe Integrated with High-Aspect-Ratio Diamond Tip. *Key Engineering Materials* **2012**, *523*, 569-574.
(119) McKenzie, W.; Pethica, J.; Cross, G. A direct-write, resistless hard mask for rapid nanoscale patterning of diamond. *Diamond and related materials* **2011**, *20* (5-6), 707-710.
(120) Li, L.; Bayn, I.; Lu, M.; Nam, C.-Y.; Schröder, T.; Stein, A.; Harris, N. C.; Englund, D. Nanofabrication on unconventional substrates using transferred hard masks. *Scientific reports* **2015**, *5* (1), 7802.
(121) Ziegler, J. F.; Ziegler, M. D.; Biersack, J. P. SRIM–The stopping and range of ions in matter (2010). *Nuclear Instruments and Methods in Physics Research Section B: Beam Interactions with Materials and Atoms* **2010**, *268* (11-12), 1818-1823.
(122) Flierl, C.; White, I.; Kuball, M.; Heard, P.; Allen, G.; Marinelli, C.; Rorison, J.; Penty, R.; Chen, Y.; Wang, S. Focused ion beam etching of GaN. *MRS Internet Journal of Nitride Semiconductor Research* **1999**, *4*, 769-774.
(123) Cabrini, S.; Kawata, S. *Nanofabrication handbook*; CRC press Boca Raton, FL, 2012.
(124) Xu, Y.; Matsumoto, N. Flexible and in situ fabrication of nanochannels with high aspect ratios and nanopillar arrays in fused silica substrates utilizing focused ion beam. *RSC Advances* **2015**, *5* (62), 50638-50643.
(125) Watson, J. H. An effect of electron bombardment upon carbon black. *Journal of Applied Physics* **1947**, *18* (2), 153-161.
(126) Watson, J. H. Specimen contamination in electron microscopes. *Journal of Applied Physics* **1948**, *19* (1), 110-111.

(127) Christy, R. W. Formation of thin polymer films by electron bombardment. *Journal of applied physics* **1960**, *31* (9), 1680-1683.
(128) Christy, R. Conducting thin films formed by electron bombardment of substrate. *Journal of Applied Physics* **1962**, *33* (5), 1884-1888.
(129) Crozier, P.; Hagen, C. High-resolution electron-beam-induced deposition. *Nanofabrication: Fundamentals and Applications* **2008**, 399-430.
(130) Guise, O.; Ahner, J.; Yates, J.; Levy, J. Formation and thermal stability of sub-10-nm carbon templates on Si (100). *Applied physics letters* **2004**, *85* (12), 2352-2354.
(131) Utke, I.; Moshkalev, S.; Russell, P. *Nanofabrication using focused ion and electron beams: principles and applications*; Oxford University Press, 2012.
(132) De Angelis, F.; Liberale, C.; Coluccio, M.; Cojoc, G.; Di Fabrizio, E. Emerging fabrication techniques for 3D nano-structuring in plasmonics and single molecule studies. *Nanoscale* **2011**, *3* (7), 2689-2696.
(133) Lau, Y.; Chee, P.; Thong, J.; Ng, V. Properties and applications of cobalt-based material produced by electron-beam-induced deposition. *Journal of Vacuum Science & Technology A: Vacuum, Surfaces, and Films* **2002**, *20* (4), 1295-1302.
(134) Iijima, S. Helical microtubules of graphitic carbon. *nature* **1991**, *354* (6348), 56-58.
(135) Dai, H.; Hafner, J. H.; Rinzler, A. G.; Colbert, D. T.; Smalley, R. E. Nanotubes as nanoprobes in scanning probe microscopy. *Nature* **1996**, *384* (6605), 147-150.
(136) Xu, Z.; Fang, F.; Dong, S. Carbon Nanotube AFM Probe Technology. *Electronic Properties of Carbon Nanotubes* **2011**, 105.
(137) Nishijima, H.; Kamo, S.; Akita, S.; Nakayama, Y.; Hohmura, K. I.; Yoshimura, S. H.; Takeyasu, K. Carbon-nanotube tips for scanning probe microscopy: Preparation by a controlled process and observation of deoxyribonucleic acid. *Applied Physics Letters* **1999**, *74* (26), 4061-4063.
(138) Edgeworth, J. P.; Burt, D. P.; Dobson, P. S.; Weaver, J.; Macpherson, J. V. Growth and morphology control of carbon nanotubes at the apexes of pyramidal silicontips. *Nanotechnology* **2010**, *21* (10), 105605.
(139) Fang, F.; Xu, Z.; Dong, S.; Zhang, G. High aspect ratio nanometrology using carbon nanotube probes in atomic force microscopy. *CIRP annals* **2007**, *56* (1), 533-536.
(140) Deng, Z.; Yenilmez, E.; Reilein, A.; Leu, J.; Dai, H.; Moler, K. A. Nanotube manipulation with focused ion beam. *Applied Physics Letters* **2006**, *88* (2).
(141) Park, B. C.; Jung, K. Y.; Song, W. Y.; O, B. h.; Ahn, S. J. Bending of a carbon nanotube in vacuum using a focused ion beam. *Advanced Materials* **2006**, *18* (1), 95-98.
(142) Fang, F.; Xu, Z.; Zhang, G.; Hu, X. Fabrication and configuration of carbon nanotube probes in atomic force microscopy. *CIRP annals* **2009**, *58* (1), 455-458.
(143) Lai, W.-C.; Chin, S.-C.; Chang, Y.-C.; Chen, L.-Y.; Chang, C.-S. Lattice-resolved frictional pattern probed by tailored carbon nanotubes. *Nanotechnology* **2009**, *21* (5), 055702.
(144) Wei, X.; Chen, Q.; Liu, Y.; Peng, L. Cutting and sharpening carbon nanotubes using a carbon nanotube 'nanoknife'. *Nanotechnology* **2007**, *18* (18), 185503.
(145) Marcus, R.; Ravi, T.; Gmitter, T.; Chin, K.; Liu, D.; Orvis, W.; Ciarlo, D.; Hunt, C.; Trujillo, J. Formation of silicon tips with< 1 nm radius. *Applied Physics Letters* **1990**, *56* (3), 236-238.
(146) Tang, B.; Sato, K.; Tanaka, H.; Gosalvez, M. Fabrication of sharp tips with high aspect ratio by surfactant-modified wet etching for the AFM probe. In *2011 IEEE 24th International Conference on Micro Electro Mechanical Systems*, 2011; IEEE: pp 328-331.
(147) Weber, J.; Yuan, Y.; Kühnel, F.; Metzke, C.; Schätz, J.; Frammelsberger, W.; Benstetter, G. n.; Lanza, M. Solid Platinum Nanoprobes for Highly Reliable Conductive Atomic Force Microscopy. *ACS Applied Materials & Interfaces* **2023**, *15* (17), 21602-21608.
(148) Willson, C.; Stewart, M. Photoresists. *Encyclopedia of Materials: Science and Technology* **2001**, 6973-6977.

(149) Franssila, S.; Tuomikoski, S. MEMS lithography. In *Handbook of Silicon Based MEMS Materials and Technologies*, Elsevier, 2015; pp 427-443.
(150) Diez, S. The next generation of maskless lithography. In *Emerging Digital Micromirror Device Based Systems and Applications VIII*, 2016; SPIE: Vol. 9761, p 976102.
(151) Paul, P.; Bach, C. Industrial maskless aligner: new levels of flexibility in lithography. In *Novel Patterning Technologies 2023*, 2023; SPIE: p PC1249705.
(152) *Maskless Laser Lithography*. https://heidelberg-instruments.com/core-technologies/maskless-laser-lithography/ (accessed).
(153) McCord, M. A.; Rooks, M. J. Handbook of microlithography, micromachining, and microfabricaiton Vol. *Rai-Choudhury, ed.,(IEE, London, 1997)* **1997**, 139-249.
(154) Manfrinato, V. R.; Zhang, L.; Su, D.; Duan, H.; Hobbs, R. G.; Stach, E. A.; Berggren, K. K. Resolution limits of electron-beam lithography toward the atomic scale. *Nano letters* **2013**, *13* (4), 1555-1558.
(155) Hatzakis, M. Electron resists for microcircuit and mask production. *Journal of the electrochemical society* **1969**, *116* (7), 1033.
(156) Nishida, T.; Notomi, M.; Iga, R. I. R.; Tamamura, T. T. T. Quantum wire fabrication by e-beam elithography using high-resolution and high-sensitivity e-beam resist ZEP-520. *Japanese journal of applied physics* **1992**, *31* (12S), 4508.
(157) Olynick, D.; Cord, B.; Schipotinin, A.; Ogletree, D.; Schuck, P. Electron-beam exposure mechanisms in hydrogen silsesquioxane investigated by vibrational spectroscopy and in situ electron-beam-induced desorption. *Journal of Vacuum Science & Technology B, Nanotechnology and Microelectronics: Materials, Processing, Measurement, and Phenomena* **2010**, *28* (3), 581-587.
(158) Cui, Z. Nanoscale Pattern Transfer by Deposition. In *Nanofabrication: Principles, Capabilities and Limits*, Springer, 2024; pp 299-325.
(159) Köhler, M. Isotropic Etching. In *Encyclopedia of Microfluidics and Nanofluidics*, Li, D. Ed.; Springer US, 2008; pp 877-884.
(160) House, D.; Li, D. Anisotropic Etching. In *Encyclopedia of Microfluidics and Nanofluidics*, Li, D. Ed.; Springer US, 2008; pp 47-49.
(161) Nojiri, K. *Dry etching technology for semiconductors*; Springer, 2015.
(162) Popov, O. A. *High density plasma sources: design, physics and performance*; Elsevier, 1996.
(163) Cardinaud, C.; Peignon, M.-C.; Tessier, P.-Y. Plasma etching: principles, mechanisms, application to micro-and nano-technologies. *Applied Surface Science* **2000**, *164* (1-4), 72-83.
(164) Schaible, P.; Metzger, W.; Anderson, J. Reactive ion etching of aluminum and aluminum alloys in an rf plasma containing halogen species. *Journal of Vacuum Science and Technology* **1978**, *15* (2), 334-337.
(165) Shiomi, H. S. H. Reactive ion etching of diamond in O2 and CF4 plasma, and fabrication of porous diamond for field emitter cathodes. *Japanese Journal of Applied Physics* **1997**, *36* (12S), 7745.
(166) Milne, J. P. Oxygen plasma reactive ion etching of tetrahedral amorphous carbon. *Japanese journal of applied physics* **1996**, *35* (12A), L1550.
(167) Xu, J.; Lu, K.; Fan, D.; Wang, Y.; Xu, S.; Kubo, M. Different etching mechanisms of diamond by oxygen and hydrogen plasma: a reactive molecular dynamics study. *The Journal of Physical Chemistry C* **2021**, *125* (30), 16711-16718.
(168) Yun, D. Y.; Choi, W. S.; Park, Y. S.; Hong, B. Effect of H2 and O2 plasma etching treatment on the surface of diamond-like carbon thin film. *Applied Surface Science* **2008**, *254* (23), 7925-7928.
(169) Hausmann, B. J.; Khan, M.; Zhang, Y.; Babinec, T. M.; Martinick, K.; McCutcheon, M.; Hemmer, P. R.; Lončar, M. Fabrication of diamond nanowires for quantum information processing applications. *Diamond and Related Materials* **2010**, *19* (5-6), 621-629.
(170) Tsubouchi, N.; Mokuno, Y.; Shikata, S. Characterizations of etch pits formed on single crystal diamond surface using oxygen/hydrogen plasma surface treatment. *Diamond and Related Materials* **2016**, *63*, 43-46.

(171) Hicks, M.-L.; Pakpour-Tabrizi, A. C.; Jackman, R. B. Diamond etching beyond 10 μm with near-zero micromasking. *Scientific Reports* **2019**, *9* (1), 1-6.
(172) Lee, C.; Choi, H.; Gu, E.; Dawson, M.; Murphy, H. Fabrication and characterization of diamond micro-optics. *Diamond and Related Materials* **2006**, *15* (4-8), 725-728.
(173) Lee, C.; Gu, E.; Dawson, M.; Friel, I.; Scarsbrook, G. Etching and micro-optics fabrication in diamond using chlorine-based inductively-coupled plasma. *Diamond and Related Materials* **2008**, *17* (7-10), 1292-1296.
(174) Ando, Y.; Nishibayashi, Y.; Kobashi, K.; Hirao, T.; Oura, K. Smooth and high-rate reactive ion etching of diamond. *Diamond and Related Materials* **2002**, *11* (3-6), 824-827.
(175) Tran, D.; Grotjohn, T.; Reinhard, D.; Asmussen, J. Microwave plasma-assisted etching of diamond. *Diamond and related materials* **2008**, *17* (4-5), 717-721.
(176) Otterbach, R.; Hilleringmann, U. Reactive ion etching of CVD-diamond for piezoresistive pressure sensors. *Diamond and related materials* **2002**, *11* (3-6), 841-844.
(177) Tran, D.; Fansler, C.; Grotjohn, T.; Reinhard, D.; Asmussen, J. Investigation of mask selectivities and diamond etching using microwave plasma-assisted etching. *Diamond and Related Materials* **2010**, *19* (7-9), 778-782.
(178) Craigie, C.; Sheehan, T.; Johnson, V.; Burkett, S.; Moll, A. J.; Knowlton, W. Polymer thickness effects on Bosch etch profiles. *Journal of Vacuum Science & Technology B: Microelectronics and Nanometer Structures Processing, Measurement, and Phenomena* **2002**, *20* (6), 2229-2232.
(179) Aydinoglu, F.; Pan, A.; Zhu, C.; Cui, B. Effect of oxygen plasma cleaning on nonswitching pseudo-Bosch etching of high aspect ratio silicon pillars. *Journal of Vacuum Science & Technology B, Nanotechnology and Microelectronics: Materials, Processing, Measurement, and Phenomena* **2020**, *38* (1), 012804.
(180) Cui, Z. Nanoscale Pattern Transfer. *Nanofabrication: Principles, Capabilities and Limits* **2008**, 211-266.
(181) Whetten, T. J.; Armstead, A. A.; Grzybowski, T. A.; Ruoff, A. L. Etching of diamond with argon and oxygen ion beams. *Journal of Vacuum Science & Technology A: Vacuum, Surfaces, and Films* **1984**, *2* (2), 477-480.
(182) Walsh, M. E.; Hao, Y.; Ross, C. A.; Smith, H. I. Optimization of a lithographic and ion beam etching process for nanostructuring magnetoresistive thin film stacks. *Journal of Vacuum Science & Technology B: Microelectronics and Nanometer Structures Processing, Measurement, and Phenomena* **2000**, *18* (6), 3539-3543.
(183) Neureuther, A.; Liu, C.; Ting, C. Modeling ion milling. *Journal of Vacuum Science and Technology* **1979**, *16* (6), 1767-1771.
(184) Nayak, A. P.; Logeeswaran, V.; Islam, M. S. Wet and dry etching. *University of California, Davis* **2011**.
(185) Gosálvez, M. A.; Zubel, I.; Viinikka, E. Wet etching of silicon. In *Handbook of silicon based MEMS materials and technologies*, Elsevier, 2010; pp 447-480.
(186) Tjerkstra, R. W. Isotropic etching of silicon in fluoride containing solutions as a tool for micromachining. **1999**.
(187) Kasparian, J.; Elwenspoek, M.; Allongue, P. Digital computation and in situ STM approach of silicon anisotropic etching. *Surface science* **1997**, *388* (1-3), 50-62.
(188) Gosálvez, M.; Sato, K.; Foster, A.; Nieminen, R.; Tanaka, H. An atomistic introduction to anisotropic etching. *Journal of Micromechanics and Microengineering* **2007**, *17* (4), S1.
(189) Seidel, H.; Csepregi, L.; Heuberger, A.; Baumgärtel, H. Anisotropic etching of crystalline silicon in alkaline solutions: I. Orientation dependence and behavior of passivation layers. *Journal of the electrochemical society* **1990**, *137* (11), 3612.
(190) Bean, K. E. Anisotropic etching of silicon. *IEEE Transactions on electron devices* **1978**, *25* (10), 1185-1193.
(191) Tabata, O.; Asahi, R.; Funabashi, H.; Shimaoka, K.; Sugiyama, S. Anisotropic etching of silicon in TMAH solutions. *Sensors and Actuators A: Physical* **1992**, *34* (1), 51-57.

(192) Sakaino, K.; Kawabata, Y.; Adachiz, S. Etching characteristics of Si (100) surfaces in an aqueous NaOH solution. *Journal of The Electrochemical Society* **2000**, *147* (4), 1530.
(193) Noor, M. M.; Bais, B.; Majlis, B. Y. The effects of temperature and KOH concentration on silicon etching rate and membrane surface roughness. In *ICONIP'02. Proceedings of the 9th International Conference on Neural Information Processing. Computational Intelligence for the E-Age (IEEE Cat. No. 02EX575)*, 2002; IEEE: pp 524-528.
(194) Yang, C.-R.; Chen, P.-Y.; Yang, C.-H.; Chiou, Y.-C.; Lee, R.-T. Effects of various ion-typed surfactants on silicon anisotropic etching properties in KOH and TMAH solutions. *Sensors and Actuators A: Physical* **2005**, *119* (1), 271-281.
(195) Lapadatu, D.; Kittilsland, G.; Nese, M.; Nilsen, S. M.; Jakobsen, H. A model for the etch-stop location on reverse-biased pn junctions. *Sensors and Actuators A: Physical* **1998**, *66* (1-3), 259-267.
(196) Tang, B.; Sato, K. Advanced surfactant-modified wet anisotropic etching. *Microelectromechanical systems and devices. IntechOpen* **2012**, 131.
(197) Sato, K.; Uchikawa, D.; Shikida, M. Change in orientation-dependent etching properties of single-crystal silicon caused by a surfactant added to TMAH solution. *Sensors and Materials(Japan)* **2001**, *13* (5), 285-291.
(198) Tang, B.; Shikida, M.; Sato, K.; Pal, P.; Amakawa, H.; Hida, H.; Fukuzawa, K. Study of surfactant-added TMAH for applications in DRIE and wet etching-based micromachining. *Journal of Micromechanics and Microengineering* **2010**, *20* (6), 065008.
(199) Zubel, I. Anisotropic etching of Si. *Journal of Micromechanics and Microengineering* **2019**, *29* (9), 093002.
(200) Duan, X. Microfabrication: using bulk wet etching with TMAH. **2005**.
(201) Hines, M. A. In search of perfection: Understanding the highly defect-selective chemistry of anisotropic etching. *Annual review of physical chemistry* **2003**, *54* (1), 29-56.
(202) Chan, M. W.; McCoy, C. D.; Wodin-Schwartz, S.; Warren, C. G.; Vijayaraghavan, A. MEMS KINEMATIC CLAMP FOR REPEATABLE PRECISION ALIGNMENT.
(203) Li, W.; Zhao, X.; Li, Y.; Ji, Y.; Peng, H.; Liu, L.; Yang, Q. Laboratory investigations on the effects of surfactants on rate of penetration in rotary diamond drilling. *Journal of Petroleum Science and Engineering* **2015**, *134*, 114-122.
(204) Pal, P.; Sato, K.; Gosalvez, M. A.; Kimura, Y.; Ishibashi, K.-I.; Niwano, M.; Hida, H.; Tang, B.; Itoh, S. Surfactant adsorption on single-crystal silicon surfaces in TMAH solution: orientation-dependent adsorption detected by in situ infrared spectroscopy. *Journal of microelectromechanical systems* **2009**, *18* (6), 1345-1356.
(205) Finne, R.; Klein, D. A Water-Amine-Complexing Agent System for Etching Silicon. *Journal of the Electrochemical Society* **1967**, *114* (9), 965.
(206) Schroder, H.; Obermeier, E.; Horn, A.; Wachutka, G. K. Convex corner undercutting of {100} silicon in anisotropic KOH etching: The new step-flow model of 3-D structuring and first simulation results. *Journal of Microelectromechanical systems* **2001**, *10* (1), 88-97.
(207) Seidel, H.; Csepregi, L.; Heuberger, A.; Baumgärtel, H. Anisotropic etching of crystalline silicon in alkaline solutions. Part 2: Influence of dopants. **1989**.
(208) Gosálvez, M.; Nieminen, R. Surface morphology during anisotropic wet chemical etching of crystalline silicon. *New Journal of Physics* **2003**, *5* (1), 100.
(209) Garcia, S. P.; Bao, H.; Hines, M. A. Etchant anisotropy controls the step bunching instability in KOH etching of silicon. *Physical review letters* **2004**, *93* (16), 166102.
(210) Gosálvez, M.; Xing, Y.; Hynninen, T.; Uwaha, M.; Foster, A.; Nieminen, R.; Sato, K. Faster simulations of step bunching during anisotropic etching: formation of zigzag structures on Si (1 1 0). *Journal of Micromechanics and Microengineering* **2007**, *17* (4), S27.

(211) Madou, M. Physical and Chemical Vapor Deposition—Thin Film Properties and Surface Micromachining. *Fundam. Microfabr. nanotechnology. Vol. II, Manuf. Tech. Microfabr. Nanotechnol*, 391-508.
(212) Nasir, F.; Pan, A.; Cui, B. Fabrication of high aspect ratio diamond tip using reactive ion etching. *Diamond and Related Materials* **2025**, *152*, 111950.
(213) Chung, K.-H.; Lee, Y.-H.; Kim, D.-E. Characteristics of fracture during the approach process and wear mechanism of a silicon AFM tip. *Ultramicroscopy* **2005**, *102* (2), 161-171.
(214) Gołek, F.; Mazur, P.; Ryszka, Z.; Zuber, S. AFM image artifacts. *Applied surface science* **2014**, *304*, 11-19.
(215) Kinoshita, Y.; Naitoh, Y.; Li, Y. J.; Sugawara, Y. Fabrication of sharp tungsten-coated tip for atomic force microscopy by ion-beam sputter deposition. *Review of Scientific Instruments* **2011**, *82* (11).
(216) Steen, J.; Hayakawa, J.; Harada, T.; Lee, K.; Calame, F.; Boero, G.; Kulik, A.; Brugger, J. Electrically conducting probes with full tungsten cantilever and tip for scanning probe applications. *Nanotechnology* **2006**, *17* (5), 1464.
(217) So/rensen, A.; Hvid, U.; Mortensen, M.; Mo/rch, K. Preparation of platinum/iridium scanning probe microscopy tips. *Review of scientific instruments* **1999**, *70* (7), 3059-3067.
(218) Lee, H. W.; Kim, S. H.; Kwak, Y. K.; Han, C. S. Nanoscale fabrication of a single multiwalled carbon nanotube attached atomic force microscope tip using an electric field. *Review of Scientific Instruments* **2005**, *76* (4).
(219) ***Diamond Coated AFM Tips***. https://www.nanoworld.com/search/products?term=DIAMOND (accessed).
(220) Olbrich, A.; Ebersberger, B.; Boit, C.; Niedermann, P.; Hänni, W.; Vancea, J.; Hoffmann, H. High aspect ratio all diamond tips formed by focused ion beam for conducting atomic force microscopy. *Journal of Vacuum Science & Technology B: Microelectronics and Nanometer Structures Processing, Measurement, and Phenomena* **1999**, *17* (4), 1570-1574.
(221) Adams, D.; Vasile, M.; Mayer, T.; Hodges, V. Focused ion beam milling of diamond: effects of H 2 O on yield, surface morphology and microstructure. *Journal of Vacuum Science & Technology B: Microelectronics and Nanometer Structures Processing, Measurement, and Phenomena* **2003**, *21* (6), 2334-2343.
(222) Kim, H. J.; Moldovan, N.; Felts, J. R.; Somnath, S.; Dai, Z.; Jacobs, T. D.; Carpick, R. W.; Carlisle, J. A.; King, W. P. Ultrananocrystalline diamond tip integrated onto a heated atomic force microscope cantilever. *Nanotechnology* **2012**, *23* (49), 495302.
(223) Sandhu, G.; Chu, W. Reactive ion etching of diamond. *Applied physics letters* **1989**, *55* (5), 437-438.
(224) Villalpando, I.; John, P.; Porro, S.; Wilson, J. Hydrogen plasma etching of diamond films deposited on graphite. *Diamond and related materials* **2011**, *20* (5-6), 711-716.
(225) Leech, P. W.; Reeves, G.; Holland, A. Reactive ion etching of diamond in CF4, O2, O2 and Ar-based mixtures. *Journal of materials science* **2001**, *36*, 3453-3459.
(226) Zheng, Y.; Liu, J.; Zhang, R.; Cumont, A.; Wang, J.; Wei, J.; Li, C.; Ye, H. Fast smoothing on diamond surface by inductively coupled plasma reactive ion etching. *Journal of Materials Research* **2020**, *35* (5), 462-472.
(227) Zheng, Y.; Ye, H.; Liu, J.; Wei, J.; Chen, L.; Li, C. Surface morphology evolution of a polycrystalline diamond by inductively coupled plasma reactive ion etching (ICP-RIE). *Materials Letters* **2019**, *253*, 276-280.
(228) Hicks, M.-L.; Pakpour-Tabrizi, A. C.; Jackman, R. B. Diamond Etching Beyond 10 μ m with Near-Zero Micromasking. *Scientific Reports* **2019**, *9* (1), 15619.
(229) Mehedi, H. a.; Mille, V.; Achard, J.; Brinza, O.; Gicquel, A. Effect of the process parameters of inductively coupled plasma reactive ion etching on the fabrication of diamond nanotips. *physica status solidi (a)* **2014**, *211* (10), 2343-2346.

(230) He, H.; Zhang, J.; Yang, J.; Yang, F. Silicon tip sharpening based on thermal oxidation technology. *Microsystem Technologies* **2017**, *23*, 1799-1803.
(231) Toros, A.; Kiss, M.; Graziosi, T.; Mi, S.; Berrazouane, R.; Naamoun, M.; Plestina, J. V.; Gallo, P.; Quack, N. Reactive ion etching of single crystal diamond by inductively coupled plasma: State of the art and catalog of recipes. *Diamond and Related Materials* **2020**, *108*, 107839.
(232) Nemanich, R. J.; Carlisle, J. A.; Hirata, A.; Haenen, K. CVD diamond—Research, applications, and challenges. *Mrs Bulletin* **2014**, *39* (6), 490-494.
(233) Nguyen, V. T. H.; Jensen, F.; Hübner, J.; Leussink, P.; Jansen, H. On the formation of black silicon in SF6-O2 plasma: The clear, oxidize, remove, and etch (CORE) sequence and black silicon on demand. *Journal of Vacuum Science & Technology A* **2020**, *38* (4).
(234) Lee, Y.; Zhou, Z. H.; Danner, D. A.; Fryer, P. M.; Harper, J. Chemical sputtering of Al2O3 by fluorine-containing plasmas excited by electron cyclotron resonance. *Journal of applied physics* **1990**, *68* (10), 5329-5336.
(235) Tegen, S.; Moll, P. Etch characteristics of Al2O3 in ICP and MERIE plasma etchers. *Journal of The Electrochemical Society* **2005**, *152* (4), G271.
(236) Saito, S.; Sugita, K.; Tonotani, J. Effect of CHF3 addition on reactive ion etching of aluminum using inductively coupled plasma. *Japanese journal of applied physics* **2005**, *44* (5R), 2971.
(237) Li, H.; Belkind, A.; Jansen, F.; Orban, Z. An in situ XPS study of oxygen plasma cleaning of aluminum surfaces. *Surface and Coatings Technology* **1997**, *92* (3), 171-177.
(238) Ekinci, H.; Soltani, M.; Jahed, N. M.; Zhu, X.; Cui, B.; Pushin, D. Effect of annealing on the structural, optical and surface properties of chromium oxide (Cr2O3) thin films deposited by e-beam evaporation for plasma etching applications. *Journal of Alloys and Compounds* **2021**, *875*, 160087.
(239) Blalock, G. T. Removal of carbon-based polymer residues with ozone, useful in the cleaning of plasma reactors. Google Patents: 1995.
(240) Xie, L.; Zhou, T. X.; Stöhr, R. J.; Yacoby, A. Crystallographic orientation dependent reactive ion etching in single crystal diamond. *Advanced Materials* **2018**, *30* (11), 1705501.
(241) Cui, Z. Nanoscale Pattern Transfer by Etching. *Nanofabrication: Principles, Capabilities and Limits* **2017**, 267-304.
(242) Zhu, X.; Wang, Z.; Zhu, C.; Shen, J.; Shokouhi, B.; Ekinci, H.; Cui, B. Multi-step plasma etching of high aspect ratio silicon nanostructures for metalens fabrication. *Journal of Vacuum Science & Technology B* **2024**, *42* (3).
(243) Bourget, L.; Brucker, G.; Feaver, M.; Hill, G.; Ichihashi, Y.; Koai, K.; Larson, A.; Le Tiec, C.; Martinez, L.; Pokidov, I.; et al. *MKS Instruments Handbook 2nd Edition Semiconductor Devices and Process Technology by the Office of the CTO*; 2017.
(244) Arstila, K.; Hantschel, T.; Demeulemeester, C.; Moussa, A.; Vandervorst, W. Microfabricated diamond tip for nanoprobing. *Microelectronic engineering* **2009**, *86* (4-6), 1222-1225.
(245) Oesterschulze, E.; Scholz, W.; Mihalcea, C.; Albert, D.; Sobisch, B.; Kulisch, W. Fabrication of small diamond tips for scanning probe microscopy application. *Applied physics letters* **1997**, *70* (4), 435-437.
(246) Macintyre, D.; Chen, Y.; Lim, D.; Thoms, S. Fabrication of T gate structures by nanoimprint lithography. *Journal of Vacuum Science & Technology B: Microelectronics and Nanometer Structures Processing, Measurement, and Phenomena* **2001**, *19* (6), 2797-2800.
(247) Akis, R.; Ayubi-Moak, J. S.; Faralli, N.; Ferry, D. K.; Goodnick, S. M.; Saraniti, M. The upper limit of the cutoff frequency in ultrashort gate-length InGaAs/InAlAs HEMTs: A new definition of effective gate length. *IEEE Electron Device Letters* **2008**, *29* (4), 306-308.
(248) Zhu, M.; Xie, Y.; Shao, J.; Chen, Y. Nanofabrications of T shape gates for high electron mobility transistors in microwaves and THz waves, a review. *Micro and Nano Engineering* **2021**, *13*, 100091.
(249) Cui, B.; Veres, T. High resolution electron beam lithography of PMGI using solvent developers. *Microelectronic engineering* **2008**, *85* (5-6), 810-813.

(250) Fouad, M.; Yavuz, M.; Cui, B. Nanofluidic channels fabricated by e-beam lithography and polymer reflow sealing. *Journal of Vacuum Science & Technology B* **2010**, *28* (6), C6I11-C16I13.
(251) Nasir, F.; Cui, B. Fabrication of high aspect ratio AFM tips by surfactant added TMAH etching. *Sensors and Actuators A: Physical* **2025**, *388*, 116477.
(252) Sanders, W. C. *Atomic Force Microscopy: Fundamental Concepts and Laboratory Investigations*; CRC Press, 2019.
(253) Shikida, M.; Sato, K.; Tokoro, K.; Uchikawa, D. Differences in anisotropic etching properties of KOH and TMAH solutions. *Sensors and Actuators A: Physical* **2000**, *80* (2), 179-188.
(254) Kumar, S. S.; Mukhiya, R. CMOS Compatible Wet Bulk Micromachining for MEMS Applications. In *Micromachining*, IntechOpen, 2019.
(255) Lyshevski, S. E. *Nano- and Micro-Electromechanical Systems: Fundamentals of Nano- and Microengineering, Second Edition*; CRC Press, 2018.
(256) Nijdam, A. J.; Van Suchtelen, J.; Berenschot, J. W.; Gardeniers, J. G.; Elwenspoek, M. Etching of silicon in alkaline solutions: a critical look at the {1 1 1} minimum. *Journal of crystal growth* **1999**, *198*, 430-434.
(257) Fujita, H.; Mita, Y. Nanoelectromechanical Systems. *Nanofabrication Handbook* **2012**, 369-394.
(258) Oosterbroek, R. E.; Berenschot, J. W.; Jansen, H. V.; Nijdam, A. J.; Pandraud, G.; van den Berg, A.; Elwenspoek, M. C. Etching methodologies in< 111>-oriented silicon wafers. *Journal of microelectromechanical systems* **2000**, *9* (3), 390-398.
(259) Swarnalatha, V.; Pal, P.; Pandey, A. K.; Narasimha Rao, A. V.; Xing, Y.; Tanaka, H.; Sato, K. Systematic study of the etching characteristics of Si {111} in modified TMAH. *Micro & Nano Letters* **2020**, *15* (1), 52-57.
(260) Chung, I. J.; Murfett, D.; Hariz, A.; Haskard, M. Fabrication of high aspect ratio silicon micro-tips for field emission devices. *Journal of materials science* **1997**, *32*, 4999-5003.
(261) Burt, D.; Dobson, P.; Donaldson, L.; Weaver, J. A simple method for high yield fabrication of sharp silicon tips. *Microelectronic Engineering* **2008**, *85* (3), 625-630.
(262) Pradeep Narayanan, S.; Raghavan, S. Solid silicon microneedles for drug delivery applications. *The International Journal of Advanced Manufacturing Technology* **2017**, *93*, 407-422.
(263) Zubel, I.; Kramkowska, M. The effect of isopropyl alcohol on etching rate and roughness of (1 0 0) Si surface etched in KOH and TMAH solutions. *Sensors and Actuators A: Physical* **2001**, *93* (2), 138-147.
(264) Yang, C.-R.; Yang, C.-H.; Chen, P.-Y. Study on anisotropic silicon etching characteristics in various surfactant-added tetramethyl ammonium hydroxide water solutions. *Journal of Micromechanics and Microengineering* **2005**, *15* (11), 2028.
(265) Tang, B.; Sato, K.; Gosálvez, M. A. Sharp silicon tips with different aspect ratios in wet etching/DRIE and surfactant-modified TMAH etching. *Sensors and Actuators A: Physical* **2012**, *188*, 220-229.
(266) Porter, M. R. *Handbook of surfactants*; Springer, 2013.
(267) Ashok, A.; Pal, P. Silicon micromachining in 25 wt% TMAH without and with surfactant concentrations ranging from ppb to ppm. *Microsystem Technologies* **2017**, *23*, 47-54.
(268) Gosalvez, M.; Tang, B.; Pal, P.; Sato, K.; Kimura, Y.; Ishibashi, K. Orientation-and concentration-dependent surfactant adsorption on silicon in aqueous alkaline solutions: explaining the changes in the etch rate, roughness and undercutting for MEMS applications. *Journal of Micromechanics and Microengineering* **2009**, *19* (12), 125011.
(269) Tang, B.; Sato, K. Formation of silicon nano tips using post SAM-based wet etching. In *2011 16th International Solid-State Sensors, Actuators and Microsystems Conference*, 2011; IEEE: pp 602-605.
(270) Pal, P.; Sato, K. A comprehensive review on convex and concave corners in silicon bulk micromachining based on anisotropic wet chemical etching. *Micro and Nano Systems Letters* **2015**, *3*, 1-42.

(271) Tan, B.; Huang, M.; Wei, J. Effects of mask patterns optimization and silicon surface preparation for anisotropic silicon etching. In *2005 7th Electronic Packaging Technology Conference*, 2005; IEEE: Vol. 2, p 4 pp.
(272) Farahani, R. K.; Bagheri, A. The interaction of the surface active ionic liquid with nonionic surfactants (Triton X-100 and Triton X-405) in aqueous solution by using tensiometry method. *Journal of Molecular Liquids* **2022**, *345*, 118260.
(273) Goh, S. C. K.; Guo, T. X.; Chuan, K.; Tan, C. S. Formation of 45° Silicon (110) Surface Using Triton Xn Surfactants in Potassium Hydroxide for Infrared Applications. *ECS Journal of Solid State Science and Technology* **2018**, *7* (12), Q259.
(274) Pal, P.; Sato, K. Various shapes of silicon freestanding microfluidic channels and microstructures in one-step lithography. *Journal of Micromechanics and Microengineering* **2009**, *19* (5), 055003.
(275) Zubel, I.; Barycka, I. Silicon anisotropic etching in alkaline solutions I. The geometric description of figures developed under etching Si (100) in various solutions. *Sensors and Actuators A: Physical* **1998**, *70* (3), 250-259.
(276) Ekinci, H.; Dey, R. K.; Cui, B. Two-step potassium hydroxide etching to enhance aspect ratio in trench fabrication. *Journal of Vacuum Science & Technology B* **2019**, *37* (6).
(277) Ekinci, H.; Cui, B.; Pushin, D. Fabrication of sub-micron trenches with surfactant-added KOH. In *2020 IEEE 20th International Conference on Nanotechnology (IEEE-NANO)*, 2020; IEEE: pp 172-175.
(278) Yacoot, A.; Koenders, L. Aspects of scanning force microscope probes and their effects on dimensional measurement. *Journal of Physics D: Applied Physics* **2008**, *41* (10), 103001.
(279) Sato, K.; Shikida, M.; Matsushima, Y.; Yamashiro, T.; Asaumi, K.; Iriye, Y.; Yamamoto, M. Characterization of orientation-dependent etching properties of single-crystal silicon: effects of KOH concentration. *Sensors and Actuators A: Physical* **1998**, *64* (1), 87-93.
(280) Zubel, I.; Kramkowska, M. Analysis of interaction of surfactant molecules with Si (hkl) planes on the basis of anisotropic etching in alkaline solutions. *Acta Physica Polonica A* **2009**, *116* (S).
(281) Rola, K. P.; Zubel, I. Impact of alcohol additives concentration on etch rate and surface morphology of (100) and (110) Si substrates etched in KOH solutions. *Microsystem technologies* **2013**, *19*, 635-643.
(282) Sundaram, K. B.; Vijayakumar, A.; Subramanian, G. Smooth etching of silicon using TMAH and isopropyl alcohol for MEMS applications. *Microelectronic engineering* **2005**, *77* (3-4), 230-241.
(283) Zubel, I.; Rola, K.; Kramkowska, M. The effect of isopropyl alcohol concentration on the etching process of Si-substrates in KOH solutions. *Sensors and Actuators A: Physical* **2011**, *171* (2), 436-445.
(284) Zubel, I.; Rola, K.; Zalewska, J. Behavior of tensioactive compounds in the solutions for silicon anisotropic etching. In *Electron Technology Conference 2013*, 2013; SPIE: Vol. 8902, pp 630-638.
(285) Jeon, J. S.; Raghavan, S.; Sperline, R. P. Behavior of polyethylene oxide based nonionic surfactants in silicon processing using alkaline solutions. *Journal of The Electrochemical Society* **1995**, *142* (2), 621.
(286) Wilke, N.; Reed, M. L.; Morrissey, A. The evolution from convex corner undercut towards microneedle formation: theory and experimental verification. *Journal of Micromechanics and Microengineering* **2006**, *16* (4), 808.
(287) Smiljanić, M. M.; Lazić, Ž.; Radjenović, B.; Radmilović-Radjenović, M.; Jović, V. Evolution of Si crystallographic planes-etching of square and circle patterns in 25 wt% TMAH. *Micromachines* **2019**, *10* (2), 102.
(288) Tokoro, K.; Uchikawa, D.; Shikida, M.; Sato, K. Anisotropic etching properties of silicon in KOH and TMAH solutions. In *MHA'98. Proceedings of the 1998 International Symposium on Micromechatronics and Human Science.-Creation of New Industry-(Cat. No. 98TH8388)*, 1998; IEEE: pp 65-70.
(289) Jeon, J. S.; Raghavan, S.; Carrejo, J. P. Effect of temperature on the interaction of silicon with nonionic surfactants in alkaline solutions. *Journal of The Electrochemical Society* **1996**, *143* (1), 277.
(290) Akamine, S.; Barrett, R.; Quate, C. Improved atomic force microscope images using microcantilevers with sharp tips. *Applied Physics Letters* **1990**, *57* (3), 316-318.

(291) Fischer, U. C.; Koglin, J.; Fuchs, H. The tetrahedral tip as a probe for scanning near-field optical microscopy at 30 nm resolution. *Journal of Microscopy* **1994**, *176* (3), 231-237.
(292) Best Practices for Critical Dimension Measurements by AFM: Probe Selection and Data Analysis. In *Asylum Research* Oxford Instruments: Vol. 2025.
(293) Barycka, I.; Zubel, I. Silicon anisotropic etching in KOH-isopropanol etchant. *Sensors and Actuators A: Physical* **1995**, *48* (3), 229-238.
(294) Abidin, U.; Majlis, B. Y.; Yunas, J. Fabrication of pyramidal cavity structure with micron-sized tip using anisotropic KOH etching of silicon (100). *Jurnal Teknologi (Sciences & Engineering)* **2015**, *74* (10).
(295) Plummer, J. D.; Griffin, P. B. *Integrated Circuit Fabrication: Science and Technology*; Cambridge University Press, 2023.
(296) Xu, X.; Della Ratta, A. D.; Sosonkina, J.; Melngailis, J. Focused ion beam induced deposition and ion milling as a function of angle of ion incidence. *Journal of Vacuum Science & Technology B: Microelectronics and Nanometer Structures Processing, Measurement, and Phenomena* **1992**, *10* (6), 2675-2680.

APPENDIX A: SUPPLEMENTARY INFORMATION – DIAMOND SHRINKING MASK

This section details the processing steps for fabrication of high aspect ratio diamond tips using shrinking mask (chapter 3)

1. Spin coat ~ 70 nm thick ZEP resist using undiluted ZEP at spin speed of 1000 RPM. Bake at 180°C for 5 minutes
2. EBL: Circular patterns with diameter 800 nm, dose 500 μC/cm^2, current 8 nA, shot pitch 10 nm. Develop in ZED-N50 for 90 seconds, rinse in IPA for 30 seconds and drying with N_2.
3. Deposit 550 nm Al_2O_3 using e-beam evaporation.
4. Liftoff using Remover PG at 80°C with sonication for 20 – 25 minutes
5. Diamond RIE using O_2/CHF_3: 47/5 sccm, RF: 50 W, ICP:1000 W, 10 mTorr for 13 minutes (measured etch rate: 53 nm/min). After diamond etching, apex should be Al_2O_3. Diamond etching recipe can be optimized according to system and diamond film properties. Some examples of possible optimizations are listed below:
    - In case of low diamond etching rate → increase percentage of O_2 (total gas flow constant at 52 sccm).
    - In case of high Al_2O_3 etching rate (low selectivity) → increase percentage of CHF_3 (total gas flow constant at 52 sccm).
    - In case of sidewall profile being too vertical → decrease RF power.
6. Si etching using non-switching pseudo-Bosch etching to etch to 9 μm Si. C_4F_8/SF_6: 40/20 sccm, RF: 20 W, ICP: 1200 W, 10 mTorr, 15°C for 25 minutes.

APPENDIX B: SUPPLEMENTARY INFORMATION – DIAMOND T-SHAPED MASK

This section details the processing steps for fabrication of high aspect ratio diamond tips using T-shaped mask (chapter 4)

1. Deposit 350 nm a-Si on diamond (SiH_4: 500 sccm; RF: 15 W; pressure: 1000 mTorr; temp: 250°C)
2. Deposit 100 nm PECVD SiO_2 (SiH_4/N_2O: 170/710 sccm; RF: 20 W; pressure: 1000 mTorr; temp: 330°C)
3. Spin coat resists
    a. PMMA A4: 2000 RPM; bake at 180°C for 10 minutes; second spin at 2000 RPM; bake at 180°C for 10 minutes (total thickness: 500 nm)
    b. PMGI: 5000 RPM; bake at 180 °C for 5 minutes (total thickness: ~ 80 nm)
    c. ZEP undiluted: 2000 RPM; bake at 180 C for 3 minutes (total thickness: 500 nm)
4. EBL: circular patterns with diameter 250 nm (PMMA) and 500 nm (ZEP), dose: 2000 $\mu C/cm^2$ (PMMA) and 300 $\mu C/cm^2$ (ZEP) current: 8 nA, shot pitch: 10nm.
    a. Develop ZEP in ZED-N50 for 90 seconds followed by rinse in IPA for 30 seconds and drying with nitrogen gas.
    b. Develop PMGI in MF319 for 60 seconds followed by rinse in DI water for 30 seconds and drying with nitrogen gas.
    c. Develop PMMA in MIBK:IPA for 90 seconds followed by rinse in IPA for 30 seconds and drying with nitrogen gas.

5. Etch SiO_2 by C_4F_8/O_2: 40/5 sccm; RF: 100 W; ICP: 2500 W; 10mTorr ; 50°C.
6. Etch a-Si by SF_6: 160 sccm ; RF: 10 W ; ICP: 1000 W ; 15 mTorr ; 15°C
    - Etch through the a-Si, allowing the Al_2O_3 to deposit on diamond in next step.
7. Etch PMMA in O_2 plasma O_2: 100 sccm, RF: 100 W; ICP: 2500 W; 10mTorr ; 40 °C
8. Deposit 300 nm Al_2O_3 by e-beam evaporation (deposition rate: 1 Å/s)
9. 15 minutes O_2/SF_6 clean before RIE
10. Etch SiO_2 by C_4F_8/O_2: 40/5 sccm; RF: 100 W; ICP: 2500 W; 10mTorr ; 50°C.
11. Etch a-Si by standard Bosch:
    - Etch: 20 W RF, 1000 W ICP, SF_6 / C_4F_8 : 160/1 sccm, 25 mTorr, 6s.
    - Passivation: 5 W RF, 1000 W ICP, SF_6/C_4F_8 :1/160 sccm, 20 mTorr, 6s.
12. Etch diamond by O_2/C_4F_8:52/3 sccm; 50 W ; 1000 W ; 10mTorr ; 40°C.
13. 15 minutes O_2/SF_6 clean before RIE.
14. Etch Si by Bosch to required base height.
    - Etch: 20 W RF, 1000 W ICP power, SF_6/C_4F_8 : 160/1 sccm, 25 mTorr, 5s.
    - Passivation: 5 W RF, 1000 W ICP power, SF_6/C_4F_8 : 1/160 sccm, 20 mTorr, 6s.
    - In case of negative taper during RIE, increase passivation time.
15. 1-minute O_2 Plasma cleaning to remove fluorocarbon before BOE: O_2: 100 sccm, RF: 100 W; ICP: 2500 W; 10mTorr ; 40 C.
16. Remove SiO_2 by 1:10 BOE for 10 minutes (with stirring).
17. Etch diamond by O_2/C_4F_8:50/5 sccm; 50 W ; 1000 W ; 10mTorr ; 40°C to form apex.
    - Optimization of diamond etching recipe can be done using the same method explained in appendix A.

APPENDIX C: SUPPLEMENTARY INFORMATION – Si TIP

This section details the processing steps for fabrication of high aspect ratio Si tips using Si(111) (chapter 5).

1. Clean Si wafer using acetone and O_2 plasma.
2. Deposit 1 μm PECVD SiO_2 (SiH_4/N_2O: 170/710 sccm; RF: 20 W; pressure: 1000 mTorr; temp: 330°C).
3. Spin coat 1 μm S1811 resist at 3000 RPM.
4. Photolithography: circular patterns diameter 15 μm, laser 405 nm, dose: 105 mJ/cm^2, defocus: 0.
    - Develop in MF319 for 60 seconds, followed by rinsing in DI water for 30 seconds and drying with N_2.
5. Etch SiO_2 by C_4F_8/O_2: 40/5 sccm; RF: 100 W; ICP: 2500 W; 10mTorr ; 50°C.
6. Etch Si by standard Bosch to 30 μm.
    - Etch: 20 W RF, 1000 W ICP, SF_6 / C_4F_8 : 160/1 sccm, 25 mTorr, 6s.
    - Passivation: 5 W RF, 1000 W ICP, SF_6/C_4F_8 :1/160 sccm, 20 mTorr, 6s.
7. 1-minute O_2 Plasma cleaning to remove fluorocarbon: O_2: 100 sccm, RF: 100 W; ICP: 2500 W; 10mTorr ; 40 C.
8. Etch Si in 25 wt% TMAH + 1000 ppm Triton X-405 for 13 – 15 minutes or until mask falls off.

APPENDIX D: SUPPLEMENTARY INFORMATION – TETRAHEDRAL TIP

This section details the processing steps for fabrication of tetrahedral Si tips (chapter 6).

1. Clean SOI wafer using acetone and O_2 plasma.
2. Spin coat 3 μm AZ Nlof 2035 resist at 3000 RPM, bake at 110°C for 90 seconds
3. Photolithography: V-shaped patterns with width: 15 μm, length: 60 μm, opening angle: 50° laser 375 nm, dose: 220 mJ/cm^2, defocus: -10
    - Post exposure bake at 110°C for 90 seconds
    - Develop in MF319 for 60 seconds, followed by rinsing in DI water for 30 seconds and drying with N_2.
4. Etch Si by non-switching pseudo-Bosch etching for 1 μm.
    - C_4F_8/SF_6: 40/20 sccm, RF: 50W, ICP:1200W, 10mTorr, 15°C
5. Etch Si by standard Bosch to expose oxide of SOI wafer.
    - Etch: 20 W RF, 1000 W ICP, SF_6 / C_4F_8 : 160/1 sccm, 25 mTorr, 6s.
    - Passivation: 5 W RF, 1000 W ICP, SF_6/C_4F_8 :1/160 sccm, 20 mTorr, 6s.
6. Remove remaining resist using Remover PG for 15 – 20 minutes.
7. Perform thermal oxidation of Si at 1000°C for 3 hours (~ 180 – 200 nm thermal oxide).
8. Remove surface oxide using ion milling
    - Angle between surface and ion beam: 40°.
9. Etch Si in 25 wt% TMAH for 30 minutes.
    - Before etching native oxide is removed by placing the sample in 1:50 HF for 30 – 45 seconds.

- After TMAH etching, sidewall oxide is removed by placing the sample in 1:10 HF for 5 – 7 minutes.

10. After tip fabrication, coated the front side of the sample with 15 μm thick AZ4620 resist by spin coating at 1000 rpm, bake at 100°C for 90 seconds.
11. Photolithography: cantilever pattern aligned with tip, laser 405 nm, dose: 1000 mJ/cm^2, defocus: 0
    - Develop in AZ400K 1:4 developer for 3 – 4 minutes
12. Etch Si by standard Bosch for 3 – 4 μm to fabricate cantilever.
    - Etch: 20 W RF, 1000 W ICP, SF_6 / C_4F_8 : 160/1 sccm, 25 mTorr, 6s.

Passivation: 5 W RF, 1000 W ICP, SF_6/C_4F_8 :1/160 sccm, 20 mTorr, 6